Simulation of Nuclear Observables in Inertial Confinement Fusion Experiments

Aidan Joseph Crilly

April 2020

Submitted in partial fulfilment of the requirements for the degree of
Doctor of Philosophy of Imperial College London

Department of Physics
Imperial College London
Prince Consort Road
London SW7 2AZ

Declaration

I hereby certify that the work reported in this thesis is my own work, unless acknowledged or cited with a suitable reference provided.

Aidan J. Crilly
April 2020

Copyright

Abstract

The neutrons and gamma rays created in nuclear reactions provide a way to measure conditions in Inertial Confinement Fusion (ICF) experiments. Interpretation of nuclear measurements requires detailed theoretical models and numerical simulations. This thesis presents a computational study of the nuclear observables based on radiation hydrodynamics simulations of ICF experiments. Current measurement techniques are replicated to highlight their strengths and shortcomings. Novel analyses are developed to measure conditions in experiments which are currently unmeasured.

Novel features of the scattered and high energy neutron spectrum are investigated. The neutron backscatter edge spectral shape is shown to be determined by the scattering rate weighted ion velocity distribution. A spectrum model is developed, tested and shown to infer currently unmeasured values for fluid velocity and temperature in the dense DT fuel. For magnetised spherical implosions, secondary DT neutrons exhibit yield increases and spectral anisotropy. The alpha knock-on component of the tertiary neutron spectrum shows sensitivity to hotspot transparency.

Images of the DT primary and scattered neutrons are calculated for several radiation hydrodynamics simulations. The primary neutron image shape analysis is shown to be robust against differential attenuation effects. The use of multiple energy gates to measure areal density within different angular ranges is demonstrated. Activation diagnostics are shown to have finite angular resolution due to the extended nature of the hotspot.

The time history of fusion gamma rays is found to be correlated to the rate of mechanical work performed on the hotspot. The length of peak delays between fusion and carbon gamma rays indicate the degree of burn truncation. Images of carbon gamma rays can be used to measure large scale asymmetries in the remaining ablator.

Combining and expanding on nuclear measurements allows a more complete picture of hydrodynamic conditions. This will aid in understanding and improving ICF experiments.

Role of the Author

The research in this thesis relies on many numerical codes developed at the Centre for Inertial Fusion Studies (CIFS) at Imperial College London. The radiation-magnetohydrodynamic code Chimera/Gorgon has been developed by many over the course of many years. The atomic physics code SpK was created and developed by Dr Nicolas Niasse [134]. Further development by the author is presented in this thesis. Namely the inclusion of pressure ionisation and ionisation potential depression models. The inverse ray trace neutron transport code AKED was initially created by Dr Brian Appelbe and has been further developed by many at the group [115]. The author has developed the code by: improving the inverse ray trace algorithm; including angular smoothing to the rays; including Gaussian energy spectra to the rays and including the effects of fluid velocity on neutron scattering. The 1D discrete ordinates transport code Minotaur is entirely the work of the author. The Chimera simulations analysed in this thesis were performed by Dr Kris McGlinchey [119, 120], Dr Chris Walsh [181, 184], Dr Jon Tong [174] and the author.

Many external collaborations have been enacted during the course of this research. Tomographic reconstruction techniques developed by Dr Volegov [177–179], and others, at LANL are used to process neutron images created by the author. To complement theoretical work on the backscattered neutron spectrum at OMEGA, LILAC simulations were provided to the author by Owen Mannion at the LLE.

Some of the research contained which this thesis has been published by the author. It will be indicated when chapters contain content from these publications. The publications can be found at the following references [42, 43]. Permissions for any external copyrighted material used can be found in the Permissions section at the end of the thesis.

Acknowledgements

First and foremost, I would like to thank Professor Jeremy Chittenden. Without his guidance, insight and knowledge this thesis would not have been possible. His supervision granted the freedom to explore ideas while still always providing advice and direction. This made for a truly enjoyable three and a half years of research. I am also incredibly grateful to Dr Brian Appelbe, his expertise and enthusiasm have been invaluable throughout my PhD. I apologise for wrecking his whiteboard with all my questions and half-formed ideas.

I have had the good fortune to have fantastic office mates throughout my time at Imperial. Whether sharing a coffee or a pint (or cheese), it has been great to engage in both the pointless chat and the scientific discussion. In particular, I am grateful to Jerry's students Kris, Chris, Cat and Jon who showed me the ropes when I started. To those with whom I have gone on conference, thank you for entertaining evenings and weekends. To all the lovely folk of the Plasma Group, thank you for the tea breaks, Hyde Park football and pub visits.

To my parents, I am very thankful for your love and support. While it might have gone over my head when I was younger, your lesson to always "put in the effort" was put to good use during my PhD.

Finally, I owe a great debt to Immy for making life outside work so enjoyable.

I am grateful for the funding provided towards this research by the Lawrence Livermore Academic Partnership program.

Contents

List of Tables

List of Figures

1 Introduction

1.1 Nuclear Fusion

Nuclear fusion is the combination of light nuclei to form heavier nuclei, releasing energy if the products are more stable than the reactants. Stars derive their energy from fusion reactions, first fusing hydrogen to form helium and then fusing heavier elements up until iron. The energy released per nuclear reaction, Q, is given by the binding energy difference between the reactants and products. The binding energy per nucleon peaks around iron (Z=26). Elements heavier than iron can split to form lighter nuclei while releasing energy, which is known as nuclear fission.

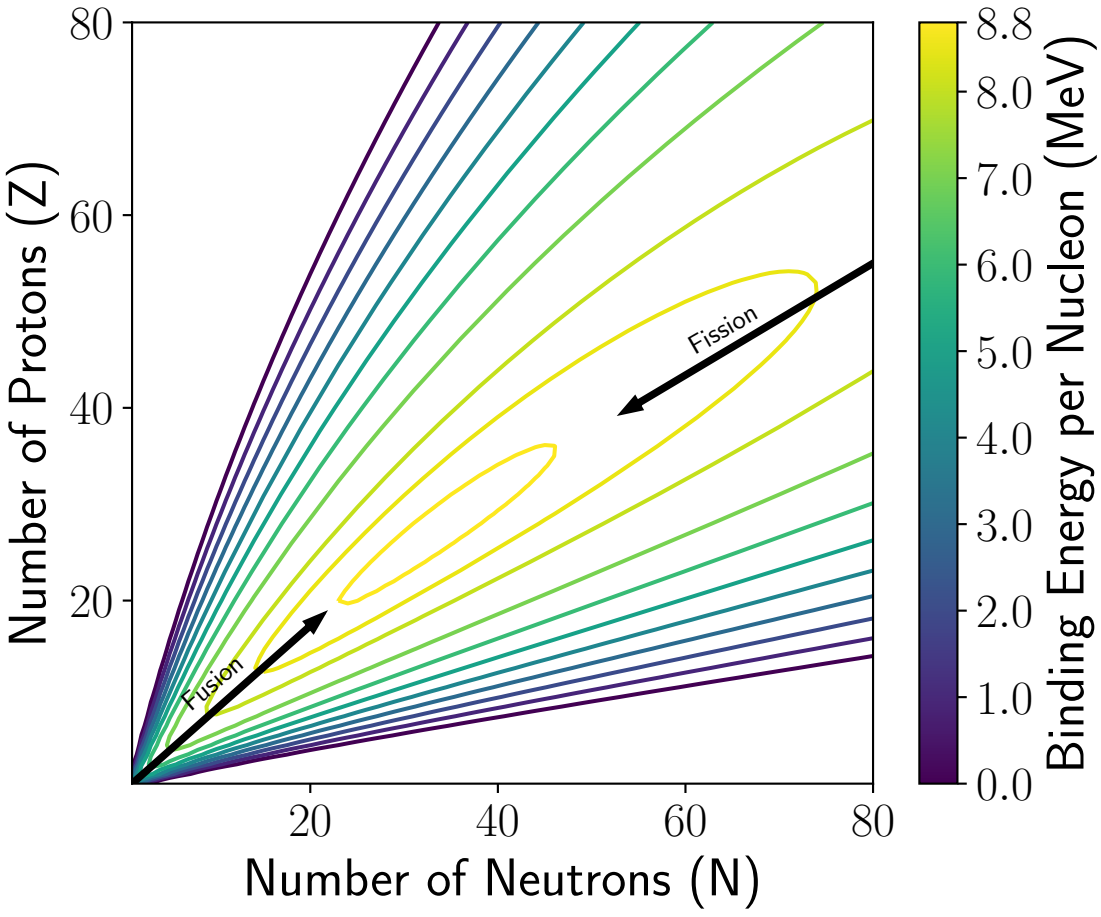

Figure 1.1: Contour plot of the binding energy per nucleon as a function of the number of neutrons and protons as approximated by the semi-empirical mass formula [149].

The electrostatic repulsion between nuclei must be overcome in order for fusion to occur. This introduces a barrier transparency term, $\mathcal{T}$, to the cross section for fusion reactions, which is often written as [8]:

$$\sigma(E) = \frac{S(E)}{E}\mathcal{T} = \frac{S(E)}{E}\exp\left(-\sqrt{\frac{E_G}{E}}\right) , \tag{1.1}$$

where E_G is the Gamow energy and S is the astrophysical S-factor, which depends on the nuclear physics of the reaction and generally has a weaker energy dependence than the Gamow factor. Thus, reactants with energies much less than the Gamow energy have a low probability of reaction. In order to sustain a high rate of fusion reactions a self-maintaining population of nuclei with sufficient energy is needed. If the reactants are in thermal equilibrium then large temperatures are needed and therefore the reactants will be in a plasma state. For example, in p-p fusion $E_G = 493$ keV which requires temperatures significantly higher than the ionisation energy of 13.6 eV. If some fraction of the energy created in the fusion reactions can be coupled back to the reactants, maintaining or raising the temperature, then a self-sustaining thermonuclear burn can occur. The reaction rate is also increased by raising the number density, n, of the fusing plasma which raises the collision frequency of nuclei ($\nu_{col} = n\sigma v$ where v is the relative velocity of the reactants). The total volumetric reaction rate, R_{ab}, for a species a colliding with a species b is given by integrating over the normalised distribution of relative velocities, $f(v)$:

$$R_{ab} = \frac{1}{1+\delta_{ab}} n_a \langle \nu_{col,b} \rangle = \frac{1}{1+\delta_{ab}} n_a n_b \int_0^\infty \sigma(E) v f(v) dv = \frac{n_a n_b}{1+\delta_{ab}} \langle \sigma v \rangle , \tag{1.2}$$

where the Kronecker delta, δ_{ab}, accounts for double counting if the species are identical. This formula separates the density dependence ($\propto n^2$) from the temperature dependence which resides inside the reactivity, $\langle \sigma v \rangle$.

Performing nuclear fusion on Earth as a source of energy is a great scientific and engineering task. It has great potential due to the high energy density of fusion fuel (greater than a million times that of fossil fuels), little to no nuclear waste and no greenhouse gas emission. Controlled nuclear fusion also presents a unique scientific challenge in understanding the physics occurring at the extreme conditions reached. For example kinetic and hydrodynamic instabilities, properties of dense plasma, and transport phenomena are areas of active research within the nuclear fusion community.

When selecting fusion fuel candidates: a low Gamow energy E_G, a high S-factor and high Q value are desirable. Hydrogen isotopes have the lowest Gamow energy due to their singular charge. The reaction of deuterium (D) and tritium (T) ($E_G = 1182$ keV) has a large S due to a broad ^{5}He resonance as well as a large $Q = 17.6$ MeV due its stable products, the doubly magic alpha particle and a neutron. Most fusion experiments to date currently use or aim to use DT as their primary fusion energy source. The DT

fusion reaction proceeds as follows:

$$D + T \rightarrow \alpha\,(3.5\text{ MeV}) + n\,(14.1\text{ MeV})\ , \tag{1.3}$$

where the bracketed terms in the above expression denote the partition of Q given to each product in the centre of mass frame in accordance with energy-momentum conservation. The high energy alpha particle will transfer its energy back to the reactants through Coloumb collisions with other charged particles; this allows thermonuclear temperatures to be maintained. The neutron has a much smaller cross section for interaction with the reactants so leaves the reaction region after no or few interactions, allowing it to be used as a heat source for the working fluid of the reactor.

The final consideration is how to confine the fusing plasma for sufficient time such that the energy released exceeds the energy delivered to form the plasma. In stars the confinement is achieved almost indefinitely by gravitational forces. Terrestrially, there are two main approaches: magnetic and inertial. In magnetic confinement fusion (MCF) magnetic fields are employed to restrict the plasma constituents to travelling along field lines. In inertial confinement fusion (ICF) the plasma is confined by its own inertia. The ICF approach is the subject of this research.

1.2 Inertial Confinement Fusion

In inertial confinement fusion a dense, hot plasma is assembled by implosion. In order for the assembled fusing plasma to achieve thermonuclear burn conditions, the fusion reaction time must be faster than all energy loss timescales in the system. The fusion time scale, τ_{fus}, and power density, W_{fus}, can be related to the reactivity as defined in Eq. 1.2:

$$\tau_{\text{fus}} = \frac{1}{n\langle\sigma v\rangle}\ ,\ W_{\text{fus}} = R_{DT}E_\alpha = \frac{1}{4}n^2\langle\sigma v\rangle E_\alpha\ , \tag{1.4}$$

where n is the total ion number density and R_{DT} is the DT reaction rate as defined in Eq. 1.2. We have used a 50:50 DT mixture and we assume the neutron escapes the system and only the alpha particle deposits its energy, $E_\alpha = 3.5$ MeV.

There are three processes which can prevent thermonuclear burn conditions being met: radiative losses, hydrodynamic disassembly and thermal conduction losses. Each of these sets a constraint on the physical parameters of the fusing plasma. Measurement of these parameters is essential in understanding the plasma's proximity to thermonuclear burn. The theory and simulation of measurement in ICF experiments is the focus of this thesis. For context, a brief simplified overview of the fundamental requirements for thermonuclear conditions in ICF will be given here. More detailed descriptions can be found in the literature [8, 111].

Firstly we will consider radiative losses by considering bremsstrahlung[1] in power balance with alpha heating. To do this we consider a uniform volume of fusing DT

[1] Bremsstrahlung or braking radiation is the electromagnetic radiation produced during the deceleration of one charged particle by another.

plasma which traps all alpha particles. We will approximate the plasma as optically thin to obtain the maximal radiative losses:

$$W_b \equiv C_b n^2 \sqrt{T_b} = \frac{1}{4} n^2 \langle \sigma v \rangle (T_b) E_\alpha \equiv W_\alpha \ , \tag{1.5}$$

where C_b is the bremsstrahlung constant ($C_b = 5.34 \times 10^{-37}$ W m^3 keV$^{-1/2}$ for n in m^{-3} and T_b in keV) and W_b is the total bremsstrahlung power density. Due to the density squared dependence of both processes, the power matching condition above uniquely defines a temperature, $T_b = 4.3$ keV, above which alpha heating dominates. Here we have also assumed the radiation is produced only by the DT plasma. However, in reality other higher atomic number elements can become mixed into the hot DT. These more efficient radiators can increase the losses, increasing the required temperature for alpha heating to dominate.

Secondly we will consider the hydrodynamic disassembly time. To do this a spherical volume, V, with radius R, uniform density, ρ, and temperature, T, is considered. This volume will expand due to a rarefaction wave moving at the isothermal sound speed[2], $c_s = \sqrt{2k_B T/m_f}$ where m_f is the average ion mass of the fuel [8]. By considering the burning volume as only the unrarefied region, the confinement time scale is given by [53]:

$$\tau_{\text{con}} = \int_0^{R/c_s} \frac{(R - c_s t)^3}{R^3} dt = \frac{R}{4c_s} \ . \tag{1.6}$$

Comparing the fusion and confinement times, we obtain:

$$\frac{\tau_{\text{con}}}{\tau_{\text{fus}}} = \langle \sigma v \rangle \frac{nR}{4c_s} = \frac{\langle \sigma v \rangle}{4 m_f c_s} \cdot \rho R \ . \tag{1.7}$$

Hence, a large areal density, ρR, is required in order to provide sufficient inertia to confine the fusing plasma. This time scale ratio can be simply related to the fractional burn up of DT, Φ. This quantity is defined as the ratio of the number of fusion reactions occurring in the confinement time and the initial number of DT pairs:

$$\Phi \equiv \frac{N_{\text{fus}}}{N_{DT}^0} = \frac{1}{N_{DT}^0} R_{DT} V \tau_{\text{con}} = \frac{1}{N_{DT}^0} \frac{nV}{4} \frac{\tau_{\text{con}}}{\tau_{\text{fus}}} = \frac{1}{2} \frac{\tau_{\text{con}}}{\tau_{\text{fus}}} = \frac{\langle \sigma v \rangle}{8 m_f c_s} \rho R \equiv \frac{1}{H_B} \cdot \rho R \ . \tag{1.8}$$

Here we have ignored fuel depletion so the above expression is only true in the low burn limit, $\Phi \ll 1$. The temperature which minimises the burn parameter, H_B, is found to be $T = 39$ keV, which is considerably greater than the bremsstrahlung limit derived in Eq. 1.5. Evaluating the ρR constraint at this minimum while including an approximate correction to include the burn depletion effect [53] we find:

$$\rho R = \frac{8 m_f c_s}{\langle \sigma v \rangle} \frac{\Phi}{1 - \Phi} \approx 73 \frac{\Phi}{1 - \Phi} \text{ kg/m}^2 \ . \tag{1.9}$$

[2]The wave can be approximated as isothermal at burning temperatures due to the high thermal conductivity smoothing out temperature changes brought about by decompression [8, 53].

It is worth considering this condition for the case of solid density DT ($\rho_{DT,\text{solid}} = 225$ kg/m^3). For a 30% burn up fraction, the mass of DT required and the resultant energy released in the form of neutrons are found to be 2.5 kg and 20 TJ (equivalent to 50 kilotons of TNT), respectively. It is abundantly clear that a much smaller mass of DT is required and hence DT must be compressed to very high densities to reach the ρR constraint. A mass of 1 mg is needed to obtain 100 MJ of fusion energy at 30% burn up fraction, which requires a compression of $\rho/\rho_{DT,\text{solid}} \approx 1500$ to match the areal density given in Eq. 1.9. Spherical convergence is preferable for reaching these high compressions as it minimises the convergence ratio ($CR = R_{\text{initial}}/R_{\text{final}}$) needed compared to other geometries and confinement is equal in all directions. A lower convergence ratio allows a more asymmetric implosion to be tolerated as asymmetries are amplified by convergence.

Up to this point a uniform spherical volume has been considered. However, there is an issue with using this as an ICF target design. The specific heat capacity of DT plasma is $c_{DT} = 0.11$ MJ/keV/mg thus compressing and heating 1 mg of fuel to sufficient temperatures requires a few MJs of energy. This reduces the maximum possible energy gain and increases the driver energy required. However, if a small fraction of the fuel ($\sim 2\%$) is heated and the majority is compressed at low temperatures, the energy requirement is reduced significantly. The hot fuel reaches thermonuclear burn conditions and self-heats. The burn is then propagated into the cold, dense fuel surrounding it. This *hotspot ignition* scheme reduces the energy requirements, thus increasing the possible energy gain. It is the central design philosophy behind current ICF experiments. The ignition and burn propagation processes have yet to be achieved experimentally but have been the subject of theoretical and computational research [8, 53, 111, 174].

This leads on to our final energy loss mechanism: thermal conduction losses. Once the central hotspot and surrounding fuel layer have formed, the large temperature gradient will create an outward heat flux into the cold fuel. This heat flux is balanced by an inward enthalpy flux in the form of mass ablation. While this mechanism does not reduce the pressure in the hotspot [14], it does increase the mass of the hotspot and consequently the temperature is reduced. The consequent reduction in alpha heating can prevent the hotspot from reaching self-heating conditions. By assuming that cold and hot fuel are stationary and isobaric, and that there is some heat front sweeping cold fuel into the hotspot at a velocity u_{abl}, an expression can be found for the hotspot heating rate including the effects of alpha heating, radiative losses and mass ablation. Using the following thermodynamic relations for internal energy, E, and pressure, P:

$$E = Mc_{DT}T = \rho V c_{DT} T, \tag{1.10}$$

$$P = \frac{2}{3}\frac{E}{V} = \frac{2}{3}\rho c_{DT} T, \tag{1.11}$$

we obtain the following equations [14, 91]:

$$-M_{\rm hs}c_{DT}\dot{T}_{\rm hs} = c_{DT}T_{\rm hs}\dot{M}_{\rm hs} - \dot{E}_{\rm hs} \ , \tag{1.12}$$

$$\dot{E}_{\rm hs} = \frac{3}{2}S_{\rm hs}Pu_{abl.} + V_{\rm hs}\frac{\rho_{\rm hs}^2}{m_f^2}\left(\frac{1}{4}\langle\sigma v\rangle E_\alpha - C_b\sqrt{T_{\rm hs}}\right) \ , \tag{1.13}$$

$$\dot{M}_{\rm hs} = S_{\rm hs}\rho_{\rm sh}u_{abl} = S_{\rm hs}\left(\frac{3}{2}\frac{P}{c_{DT}T_{\rm sh}}\right)u_{abl} \ , \tag{1.14}$$

which can be combined to find the rate of temperature change of the hotspot:

$$\frac{\dot{T}_{\rm hs}}{T_{\rm hs}} = -\frac{S_{\rm hs}}{V_{\rm hs}}\left[\frac{T_{\rm hs}}{T_{\rm sh}} - 1\right]u_{abl} + \frac{\rho_{\rm hs}}{m_f^2 c_{DT}T_{\rm hs}}\left(\frac{1}{4}\langle\sigma v\rangle E_\alpha - C_b\sqrt{T_{\rm hs}}\right) \ , \tag{1.15}$$

where V is volume, S surface area, E internal energy and P pressure. Subscripts 'hs' and 'sh' denote the hotspot and cold fuel shell respectively. Dotted quantities are used to denote time derivatives. Small surface area to volume ratios are preferable in order to minimise thermal conductive cooling of the hotspot[3]. A constraint on the ablation velocity can be made by ensuring the hotspot does not cool ($\dot{T}_{hs} > 0$):

$$u_{abl} < \frac{\Psi}{3}\frac{\rho R_{\rm hs}}{m_f}\frac{\frac{1}{4}\langle\sigma v\rangle E_\alpha - C_b\sqrt{T_{\rm hs}}}{m_f c_{DT}T_{\rm hs}\left(\frac{T_{\rm hs}}{T_{\rm sh}} - 1\right)}, \text{ where } \Psi \equiv \frac{V_{\rm hs}}{S_{\rm hs}}\cdot\frac{3}{R_{\rm hs}} \ , \tag{1.16}$$

where Ψ quantifies the symmetry of the hotspot by comparing the surface area to volume ratio to the spherical case such that $\Psi = 1$ for a perfectly spherical hotspot and $\Psi < 1$ for asymmetric hotspots. Here we have again assumed the fuel is optically thin and all alpha particles stop. The alpha particles can deposit their energy in the hotspot, thus raising the temperature without increasing the ablation velocity. If, however, alpha particles deposit their energy in the fuel shell then this can increase the ablation velocity. The region in which they deposit their energy is dependent on the hotspot temperature and areal density. Figure 1.2 shows the alpha range at different densities and temperatures. It is noted that $\rho R_{hs} \sim 3$ kg/m^2 is needed to ensure hotspot self-heating at low temperatures.

With this considered, the different regimes of hotspot heating and cooling can be seen through Eq. 1.16. This is shown in Fig. 1.3. At sufficiently low temperatures, radiative losses dominate and the hotspot is destined to cool. Depending on the ablation velocity, which is driven by both alpha and thermal energy being deposited in the shell, the hotspot can self-heat or cool. For the ablation velocity driven by thermal conduction it can be shown that $u_{abl} \propto T_{\rm hs}^{\frac{5}{2}}$ [14]. This defines a region in which mass ablation cools the hotspot indefinitely thus preventing ignition. We will refer to this as quenching the hotspot. At high temperatures, mass ablation can cool the hotspot but not extinguish it as eventually a stable temperature ($\dot{T}_{\rm hs} = 0$) is reached at a lower ablation rate.

In summary, the requirements for hotspot self-heating and confinement are:

[3]For a detailed computational study of this effect see the thesis of Dr Taylor [171].

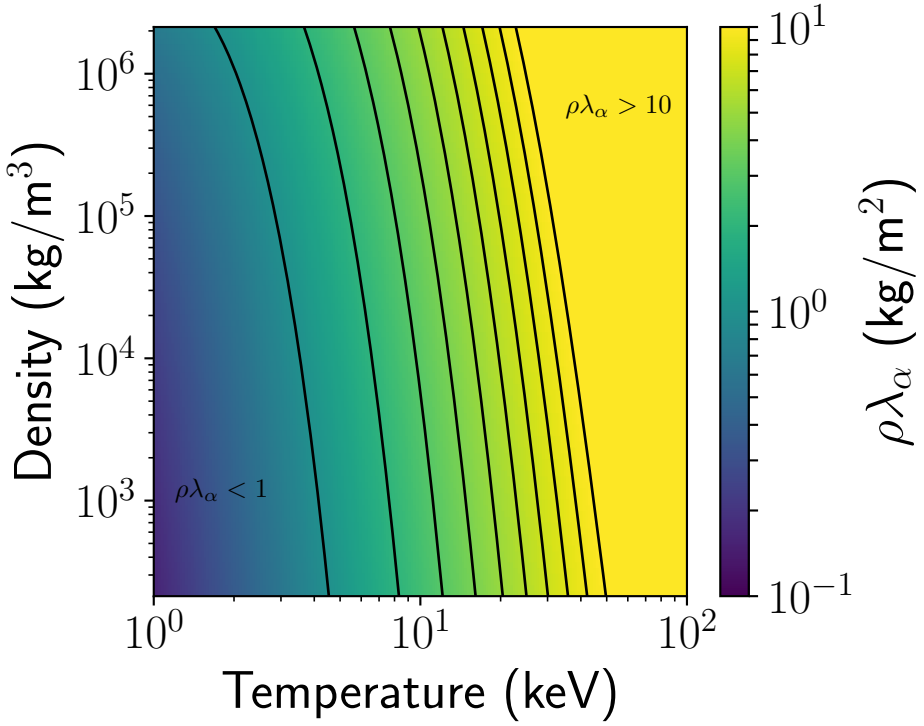

Figure 1.2: The 3.5 MeV alpha range in kg/m^2 as calculated from expressions provided by Fraley et al. [53] for a range of density and temperatures. Black contours run from 1 to 10 kg/m^2 in steps of 1 kg/m^2. This calculation includes the slowing on ions and electrons.

1. The hotspot temperature must be sufficiently high such that alpha heating dominates over radiative cooling. In the case of pure DT optically thin bremsstrahlung loss, the temperature must exceed 4.3 keV. This can be extended to say that high atomic number mix into the hot fuel must be prevented as this will increase the radiative losses.

2. The areal density of the whole capsule must be sufficiently high in order to prevent hydrodynamic disassembly before substantial thermonuclear burn has occurred. For 30% burn up the areal density of the whole capsule must be ≈ 30 kg/m^2.

3. Dependent on the hotspot temperature, the rate at which cold fuel mass is ablated into the hotspot must be low enough to prevent uncontrolled cooling. This mass ablation can be driven by thermal conduction and alpha heating. If the hotspot has $\rho R \sim 3$ kg/m^2 and $T \lesssim 10$ keV then the majority of alphas deposit their energy in the hotspot, reducing the ablation velocity. For sufficiently high hotspot temperatures $T \gtrsim 20$ keV then thermal conduction driven mass ablation cannot reduce the hotspot temperature indefinitely so no longer can cause failure.

With these established end goals, the implosion and drive of ICF capsules will be outlined. There are two methods for driving capsules, direct and indirect drive, involving the direct and indirect irradiation with laser energy. As the name suggests, direct drive

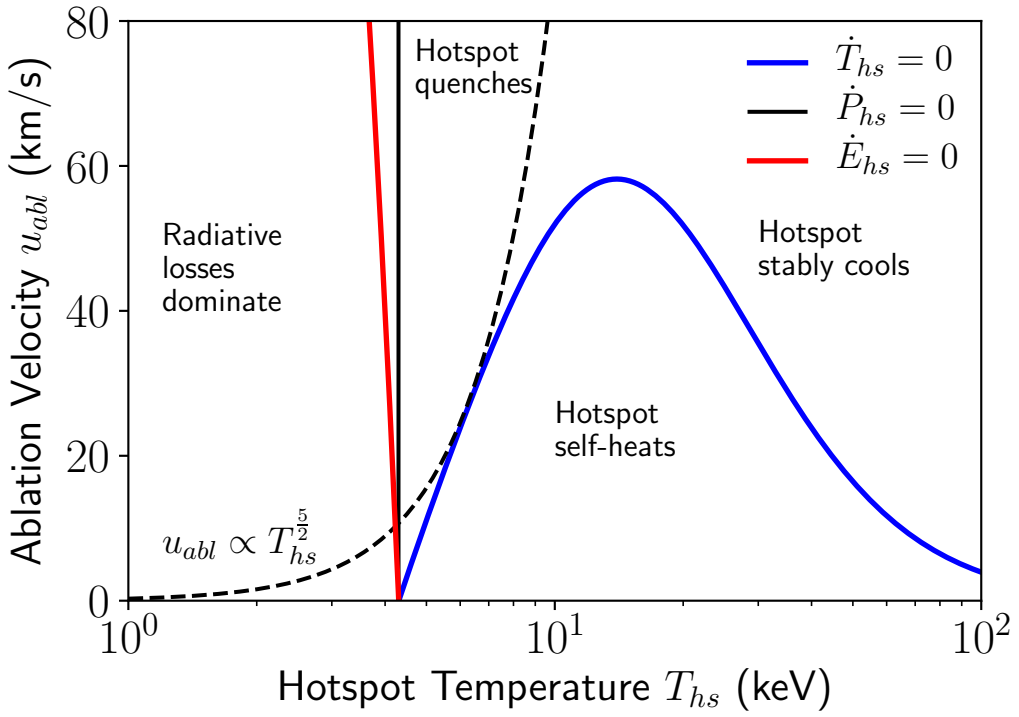

Figure 1.3: Plot of ablation velocity limit for hotspot self-heating in static hotspot-shell model. The ablation velocity, u_{abl}, at which $\dot{T}_{\rm hs} = 0$, $\dot{P}_{\rm hs} = 0$ and $\dot{E}_{\rm hs} = 0$ are plotted against hotspot temperature, T_{hs}, for $\Psi = 1$, $\rho R_{\rm hs} = 4$ kg/m^2 and $T_{\rm sh} = 500$ eV based on Eqs. 1.12 to 1.16. Since the hotspot areal density is sufficiently high to stop alphas, we will consider the mass ablation to be thermal conduction dominated. The dashed black line shows the thermal ablation velocity derived by Betti [14], this defines the paths the hotspot will move through depending on its initial temperature.

involves firing many beams of a laser directly at the capsule, while indirect drive involves the laser being used to heat a hohlraum[4] surrounding the capsule, creating a thermal X-ray bath. The irradiation produces pressure on the capsule through ablation, effectively creating a spherically converging rocket. The need to form a central hotspot leads to capsule designs of the general form seen in Fig. 1.4. The spherical piston formed by the converging shell compressively heats the central region to ignition conditions. To maximise gain, ignition should be reached once all kinetic energy has been converted to internal energy at the stagnation point.

The initial drive phase of an ICF capsule is complex, involving launching multiple shocks through the ablator and fuel. These shocks can be merged in different locations, the number of shocks changed or the strength of the shocks altered to control the in-flight adiabat (entropy). Varying the adiabat controls the balance between stability and compressibility of the implosion. A higher adiabat is more stable with respect to hydrodynamic instabilities but less compressible. The main drive ablates mass from the ablator creating inward pressure through the reaction force. The peak implosion

[4]In the most general terms, a hohlraum, literally 'hollow space' in German, is a cavity in which the walls are in thermal equilibrium with the radiation field contained within the cavity.

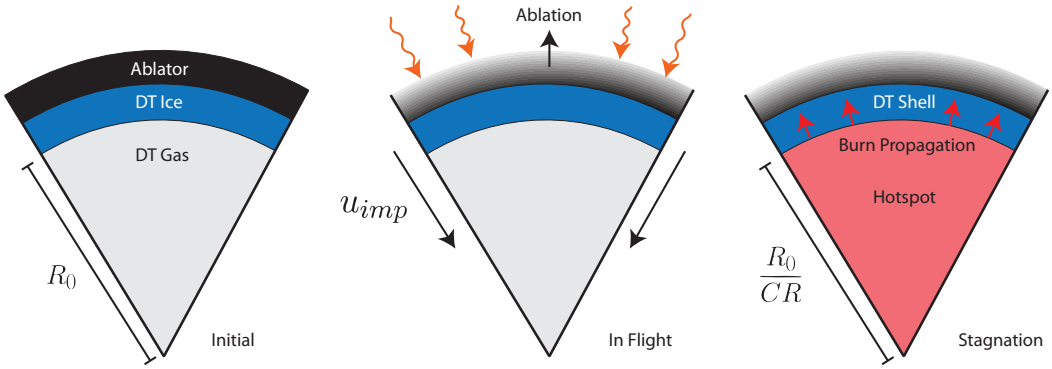

Figure 1.4: General spherical capsule design aiming for central hotspot ignition. The initial configuration includes an ablator and DT ice spherical shell of inner radius R_0 with the remainder of the capsule full of DT gas. Radiation incident on the ablator creates ablation pressure which accelerates the capsule inwards to an implosion velocity, u_{imp}. The kinetic energy is converted to internal energy until stagnation is reached. The capsule has then reached a convergence ratio, CR, sufficient to both heat and compress the fuel to ignition conditions.

velocity is reached after sufficient mass has been ablated at the exhaust velocity, u_{ex}, as shown by the Tsiolkovsky rocket equation:

$$u_{imp} = u_{ex} \ln\left(\frac{m_0}{m_\mathrm{f}}\right) \ , \tag{1.17}$$

where m_0 and m_f are the initial and final masses respectively and u_{imp} is the implosion velocity.

Once the shell has reached its peak implosion velocity, the capsule enters the deceleration phase. The kinetic energy of the shell is converted into internal energy of the hotspot therefore slowing the shell. To explore dynamic evolution of the shell and hotspot during deceleration and stagnation, the isobaric system of Equations 1.12 - 1.15 are modified to include the work done by an imploding incompressible shell moving at u_hs. First, the mechanical work performed by the shell on the hotspot is included:

$$\dot{E}_\mathrm{hs} = W_{mech} + W_{abl} + W_\alpha + W_{rad} \ , \tag{1.18}$$

$$\dot{E}_\mathrm{hs} = -u_\mathrm{hs} P S_\mathrm{hs} + \frac{3}{2} u_{abl} P S_\mathrm{hs} + \frac{1}{4} n_\mathrm{hs}^2 \langle\sigma v\rangle E_\alpha V_\mathrm{hs} - Q_{rad} V_\mathrm{hs} \ . \tag{1.19}$$

Second, the motion of the hotspot due to the shell and ablation is included along with the associated change in hotspot mass due to ablation:

$$\dot{R}_\mathrm{hs} = u_\mathrm{hs} + u_{abl} \ , \tag{1.20}$$

$$\dot{u}_\mathrm{hs} = \frac{P S_\mathrm{hs}}{M_\mathrm{sh}} \ , \tag{1.21}$$

$$u_{abl} = k \frac{T_{hs}^{5/2}}{R_\mathrm{hs} \rho_\mathrm{sh}} \ , \tag{1.22}$$

$$\dot{M}_\mathrm{hs} = S_\mathrm{hs} \rho_\mathrm{sh} u_{abl} \ . \tag{1.23}$$

Finally, the temperature change due to the changing mass and internal energy of the hotspot is found:

$$\dot{T}_{\rm hs} = \frac{\dot{E}_{\rm hs}}{M_{\rm hs} c_{DT}} - T_{\rm hs} \frac{\dot{M}_{\rm hs}}{M_{\rm hs}} \ . \tag{1.24}$$

The ablation velocity Eq. 1.22 is taken from the work of Betti *et al.*, where the expressions for k can be found [14]. The fuel depletion effect is not included in the model. The radiation loss term, Q_{rad}, has been modified to include the optical depth of the hotspot. This reduces the energy loss rate from radiation, especially at lower temperatures. In terms of the black body function, B_ν, and free-free opacity, κ_ν^{ff}, Q_{rad} is given by:

$$Q_{rad} = \frac{S_{\rm hs}}{V_{\rm hs}} \pi \int_0^\infty dh\nu \ B_\nu \left[1 + \frac{2}{\tau_\nu^2} \left((1+\tau_\nu) e^{-\tau_\nu} - 1 \right) \right], \ \tau_\nu = 2\kappa_\nu^{ff} R_{\rm hs} \ . \tag{1.25}$$

This correctly obtains the optically thin and thick limits. For simplicity radiation reabsorbed by the shell will be neglected in this model.

Given initial conditions the system of ODEs can be integrated numerically. We will consider the system from the beginning of stagnation where the shell is free-falling. By varying the initial velocity of the shell ($u_{\rm hs}$), the response of the system can be explored. The results are presented in Fig. 1.5, for the following initial conditions:

$$M_{tot} = 0.15 \text{ mg}, \ M_{\rm hs}(t=0) = 0.02 M_{tot},$$
$$T_{\rm hs}(t=0) = 500 \text{ eV}, \ R_{\rm hs}(t=0) = 500 \ \mu\text{m} \ .$$

The initial velocity of the shell was varied from 200 to 450 km/s giving shell kinetic energies, $KE_{\rm sh}$, between 3 and 15 kJ. For the implosions velocities less than 400 km/s, radiative losses lead to an inefficient system where the peak internal energy of the hotspot is less than shell kinetic energy. At 400 km/s, the hotspot begins to appreciably self-heat thus beginning to overcome radiative losses and thermal conductive cooling. However it is not sufficient to propagate the burn through the shell with only $\sim 20\%$ of the DT mass entering the hotspot. A 50 km/s increase in the implosion velocity drastically alters the behaviour; the temperature rapidly increases ($\ddot{T}_{\rm hs} > 0$) before the stagnation time, $\sim 90\%$ of the shell mass is ablated into the hotspot, and the internal energy reaches 16 $\times$ the shell kinetic energy. The increased pressure and low remaining shell inertia leads to a rapid disassembly leading to a shorter burning period.

In summary, in order for the capsule to reach the requirements for successful hotspot ignition and burn, the drive must accelerate the capsule to high implosion velocities while maintaining a high density (low adiabat) DT fuel layer. Due to cooling from both ablation of dense DT fuel and re-expansion, reaching hotspot temperatures of 4.3 keV is not sufficient for runaway self-heating. Fuel ablation is however required to reduce the hotspot's transparency to alphas (by increasing the $\rho R_{\rm hs}$) and also propagate the burn once the hotspot has ignited.

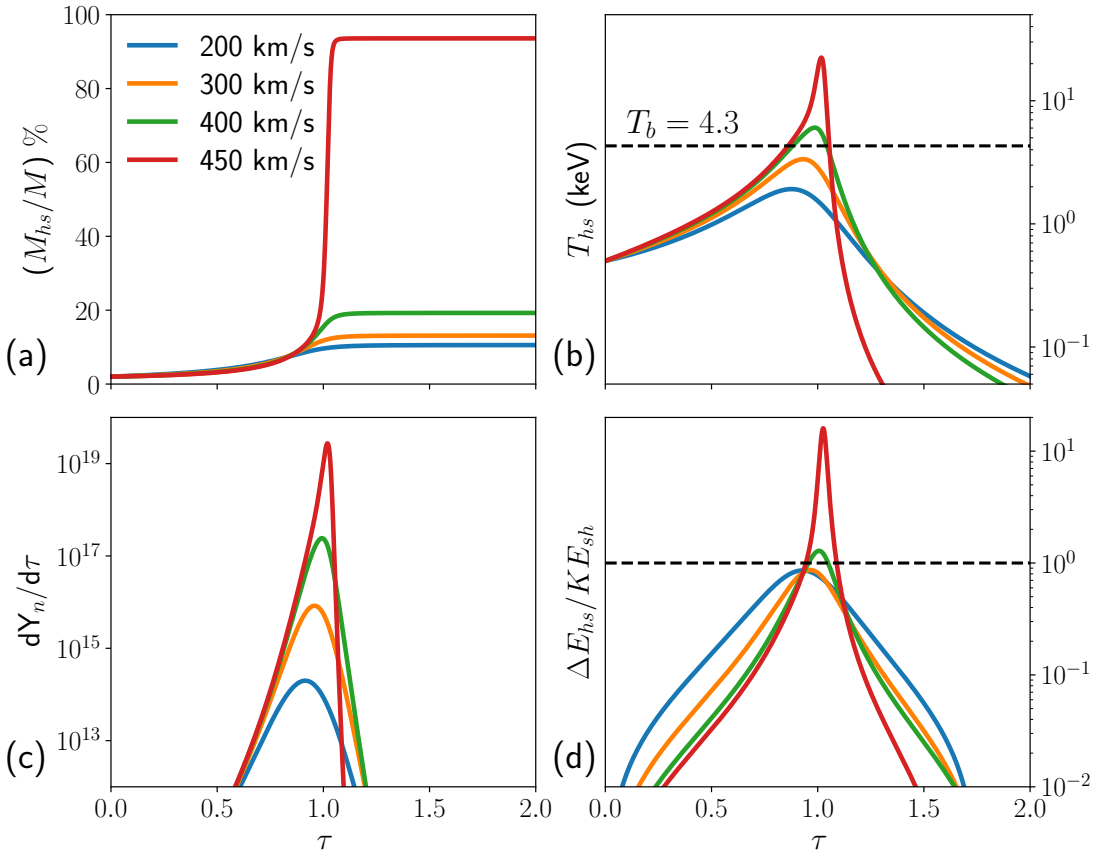

Figure 1.5: Evolution of hotspot compressed by an imploding shell with various initial implosion velocities including the effects of mechanical work, mass ablation, alpha heating and radiative losses. All plots are plotted with the normalised time $\tau \equiv \frac{u_{imp}}{R_0} t$ as the abscissa; (a) shows the percentage of the DT mass within the hotspot with an initial value of 2%, (b) shows the hotspot temperature with the optically thin bremsstrahlung limit from Eq. 1.5 shown, (c) shows the DT neutron production rate, and (d) shows the increase in the hotspot internal energy over the initial kinetic energy of the shell.

1.2.1 Current Experiments

We will now turn our attention towards current ICF experiments, the shortcomings of the simplistic analysis presented so far, the physical processes preventing thermonuclear burn conditions from being achieved, and the diagnostics used to measure the capsule conditions around stagnation.

1.2.1.1 National Ignition Facility

The National Ignition Facility (NIF) contains the world's most energetic laser (1.8 MJ) [79] and uses the indirect drive approach to drive cyrogenic layered DT capsules to stagnation pressures as high as $\sim$ 360 Gbar [108], the highest achieved pressure in a laboratory experiment. The first ICF experiments began at NIF in 2010 with the National Ignition Campaign. The capsule and laser pulse design have been altered over time to increase the stability of the implosion, reaching higher experimental fusion

yields at the price of reducing the maximum obtainable or 'clean' yield (as predicted by spherically symmetric calculations). All designs include a hohlraum made of a high atomic number material, typically gold (Au) or depleted uranium (DU), to convert the laser energy to X-rays. X-rays are absorbed by the capsule ablator by atomic processes, heating it and causing ablation. A diagram of the indirect drive concept and the recent capsule designs used at NIF are shown in Fig. 1.6. A feature included in the experimental designs which has not been discussed in the preceding analysis is the presence of a high atomic number dopant in the ablator. The dopant shields the fuel from high energy non-Planckian M-band X-rays made in the hohlraum, therefore preventing preheating of the fuel which would limit the compressibility. The dopant element depends on what can be successfully entrained within the ablator and is generally included at the few atomic percent level. The high density carbon (HDC) ablator designs can use a much shorter laser pulse due to its 3.35× higher density than CH plastic as this reduces the thickness of ablator and therefore the first shock transit time [105].

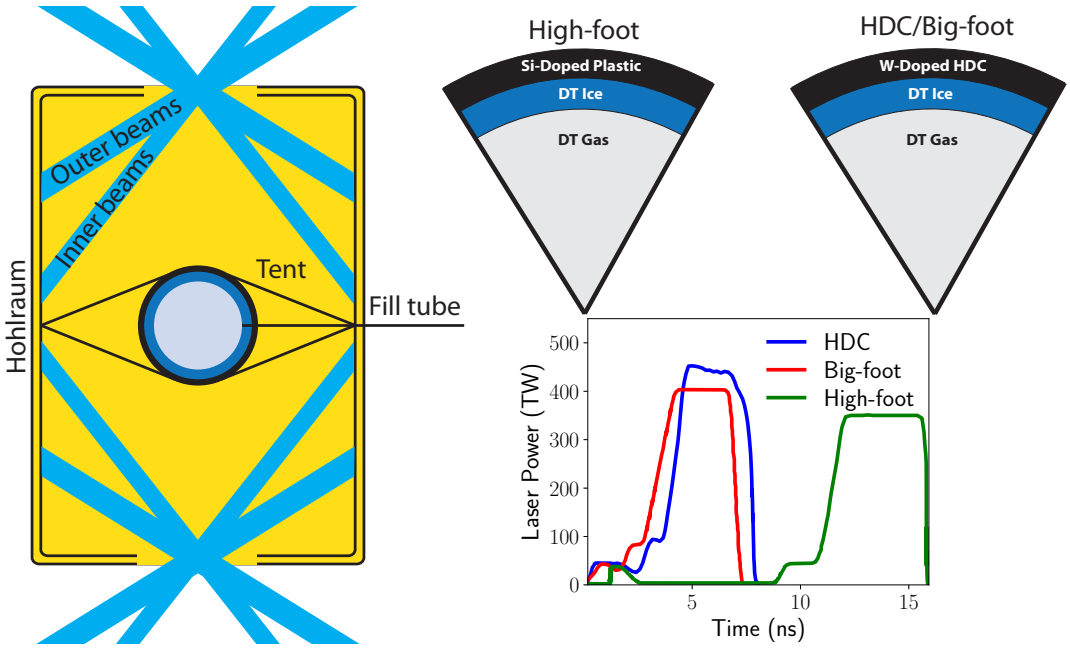

Figure 1.6: (Left) Diagram of the hohlraum-target geometry including the capsule support tent and fuel fill tube. The 192 NIF laser beams are split between the two laser entrance holes and between inner and outer beams. (Right) Diagrams of the capsule and pulse designs modelled in this work, the dimensions are not given as these can vary between shots. There are differences in ablator (plastic vs high density carbon (HDC)) and dopant type as well as laser drive shape [26, 108, 139]. For scale, capsule outer diameters are $\sim$ 2 mm and hohlraums are approximately 6 by 10 mm at NIF.

Various degradation mechanisms cause experiments to achieve lower fusion yields than predicted. Asymmetries in the radiation drive will cause an asymmetric implosion creating inefficiency in the form of residual kinetic energy (RKE)[188]. As the X-rays can be absorbed and re-emitted many times inside the hohlraum before striking the capsule, these radiation asymmetries are generally limited to lower mode numbers. As

the drive asymmetries are projected onto the spherical surface of the capsule they can be decomposed into spherical harmonics. The axisymmetric even modes (labelled $P2, P4$, etc.) were studied in more detail in earlier experiments due to the cylindrical symmetry of the hohlraum. However, low odd modes, mostly $L = 1$, have been identified as a significant source of RKE in recent analyses of experiment and simulation [60, 75, 116, 152, 162]. The tent used to support the capsule within the hohlraum imparts a perturbation to the capsule surface as the X-ray drive causes the tent to explode [161]. This perturbation is amplified by hydrodynamic instabilities and convergence producing a region of low areal density through which bubbles of hot fuel from the hotspot can escape [119, 120]. The fill tube used to feed DT into the capsule creates a perturbation which launches a jet of ablator material across the hotspot at stagnation [37, 120, 161]. This ablator material contains the high atomic number dopant so is an effective radiator causing energy loss [48]. Hydrodynamic instabilities seeded by surface roughness, volumetric defects such as voids and particulates on the capsule surface will grow, causing fuel-ablator mix and potentially feed-through to the hotspot; this induces ablator mix and increases radiative losses [37, 141, 142]. Even if these hydrodynamic instabilities do not entrain ablator into the hotspot, the cold fuel spikes and hot fuel bubbles created increase thermal conductive cooling and are a source of RKE [34].

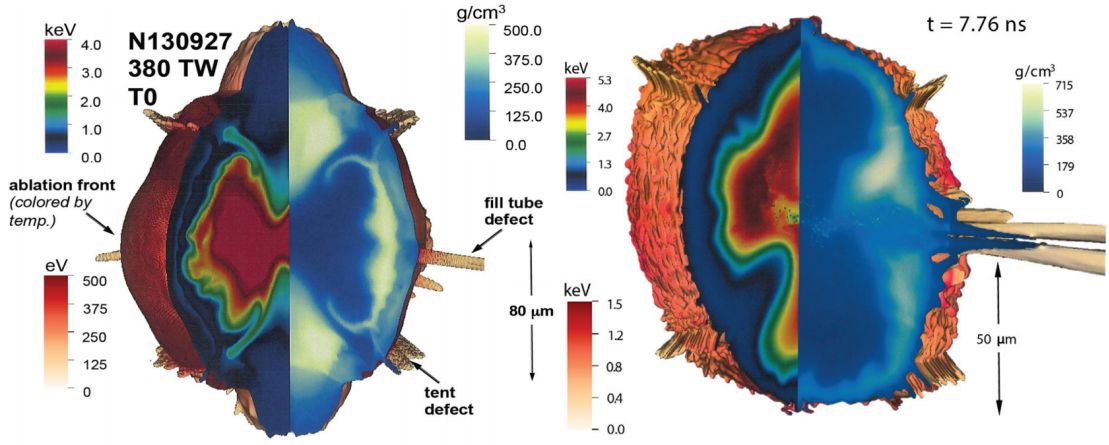

Figure 1.7: 3D radiation hydrodynamics simulations of (left) the High-foot shot N130927 which obtained a fuel gain greater than 1 [90] (figure from [38]) and (right) the HDC shot N161023 (figure from [39]) showing the density and temperature close to peak neutron production. The deleterious effects of the tent, fill tube and radiation drive asymmetries can be seen. Figures reproduced from (left) "Capsule modeling of high foot implosion experiments on the National Ignition Facility", D. S. Clark *et al.*, CC-BY license, (2017) [38] and (right) "Modeling and projecting implosion performance for the National Ignition Facility", D. S. Clark *et al.*, © IAEA, (2018) [39].

Detailed 3D radiation hydrodynamics simulations including the current understanding of perturbation sources can be used to assess the relative importance of various degradation mechanisms, to improve understanding of experimental results and to identify any possible missing perturbation sources. Examples of high fidelity simulations performed post-shot at Lawrence Livermore National Laboratory (LLNL) are shown in

Fig. 1.7. The aim of these simulations is to reproduce experimental observables through introducing known perturbation sources.

Another approach to improve understanding of degradation mechanisms is through radiation hydrodynamics simulations with idealised perturbations and asymmetries applied. The aim is not to reproduce a particular experiment but to investigate the observable effects and failure mechanisms produced. This knowledge can inform both experiment and simulation to explain discrepancies between prediction and observation [34, 42, 120, 174].

1.2.1.2 OMEGA

The OMEGA laser at the Laboratory for Laser Energetics (LLE) uses 60 laser beams to deliver up to 40 kJ directly to the target [16]. For direct drive experiments, the configuration of beams aims to uniformally irradiate a spherical capsule with UV light.

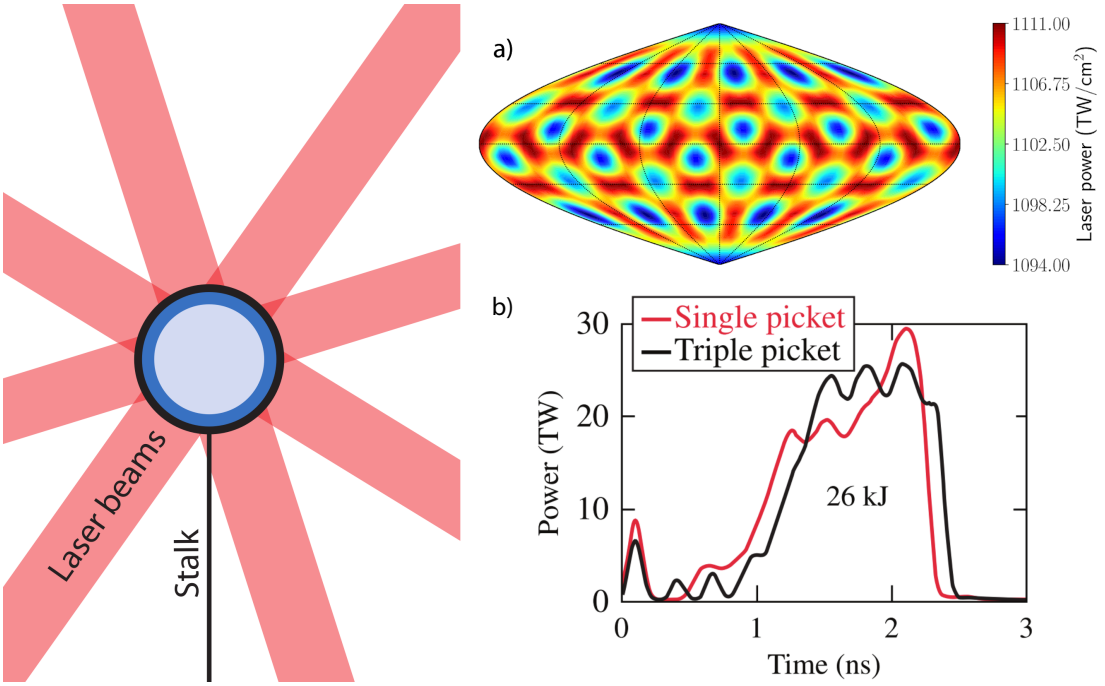

Figure 1.8: (Left) Diagram of the laser irradiation directly on the capsule which is held in place by the stalk. At OMEGA capsule outer diameters are $\sim$ 1 mm or less. (Right) **a)** Skymap of the laser intensity on the surface of the capsule with uniform equal power in the 60 OMEGA beams. This was calculated using the view factor software VISRAD [113]. **b)** Two laser pulse designs, the single and triple picket, used for ICF experiments at OMEGA, figure reprinted with permission from Regan *et al.* , Phys. Rev. Lett., 117, 025001, 2016. © 2020 by the American Physical Society.

As the radiation is in the optical range, a dopant is no longer required to shield the fuel and the ablator used is typically plastic. As the ablated plasma at sufficient density can be opaque to optical light, the laser energy is deposited further from the target than in indirect drive. More precisely, the critical electron number density, n_c, at which the

plasma becomes opaque to a laser of frequency ω_l is given by:

$$n_c = \frac{m_e \epsilon_0 \omega_l^2}{e^2} \ , \tag{1.26}$$

where m_e is the electron mass, e is the electron charge and ϵ_0 is the vacuum permittivity. Beams at non-normal incidence are refracted away before they can reach the critical surface. Electrons heated by the laser must then transport the energy to higher densities to cause ablation. Beyond the driver differences, summarised in Fig. 1.8, the principles of ICF are the same for direct drive as indirect drive.

Drive asymmetry in direct drive is influenced by the beam geometry so typically includes higher modes than one would expect from indirect drive [19]. A tent is not required and instead the capsule is held in place by a stalk which seeds a perturbation which is the subject of active research [62, 63]. Target offsets from the centre of the target chamber can induce mode 1 drive asymmetries [116, 146].

1.3 Experimental Nuclear Diagnostics

Evaluating the degradation mechanisms in play within experiments requires a wide range of measurements. However, ICF experiments present a challenging environment in which to perform measurements. The short timescales (hundreds of picoseconds), the small lengthscales (tens of micrometres) and the high background environment require complex diagnostics to handle these constraints. In this work we will focus on measurements of products of nuclear reactions and therefore will be observing close to stagnation when fusion reactions have an appreciable rate. The diagnostics used in current ICF experiments and their capabilities will be summarised here as context for the modelling presented in this work, which aims to simulate the physical phenomena being measured. Analysis of measured data involves solving an inverse problem, many of which do not have a unique solution and require an optimization problem to be solved. High dimensional optimization is difficult and therefore *ad-hoc* or simplified physical models are often used in experimental data analysis which belie the true complexity of the underlying physical system. By both modelling the physical system and the observable signals we can evaluate the effectiveness of the measurements in capturing the physical system. Novel measurements and data analysis techniques which could increase the effectiveness can also be investigated.

1.3.1 Neutron

Neutrons are produced in fusion reactions and can undergo elastic and inelastic nuclear scattering events within the capsule, altering the neutron's energy and direction of travel. Both energy spectra and time-gated images of neutron flux outside the target are measured.

1.3.1.1 Spectrometers

There are two methodologies for measurement of neutron energy spectra: time of flight and magnetic recoil.

Neutron time of flight spectrometers (nToFs) use velocity dispersion to separate the different neutron energies in time. In other words, the faster neutrons arrive first and the slower later. Then, the arrival time at the nToF relates to a specific neutron energy. If the detector has a light transit time, t_c, from the target, then the arrival time, t, and kinetic energy, K_n, of the incident neutron are given by:

$$t = \frac{t_c}{\beta_n} \ , \tag{1.27}$$

$$K_n = (\gamma_n - 1)m_n, \ \gamma_n = \frac{1}{\sqrt{1-\beta_n^2}} \ , \tag{1.28}$$

where β_n and m_n are the velocity and mass of the neutron, respectively, defined in a system of units where the speed of light $c = 1$. The time of production of a neutron can also alter the arrival time at a detector. However if the detector is positioned far enough away then the transit time is much larger than the range of production times and the neutrons can be assumed to have been made at the same instant. Then a distribution of neutron flux in arrival time, $f(t)$, can be converted to an energy distribution, $f(K_n)$, through a Jacobian:

$$f(K_n) = f(t)\left|\frac{\partial t}{\partial K_n}\right| = \frac{t_c}{(\gamma_n\beta_n)^3 m_n} f(t) \ . \tag{1.29}$$

As the Jacobian is increasing with decreasing energy, for constant time resolution the energy resolution increases with decreasing energy. This is due to the velocity dispersion increasing at lower energies.

The neutrons are not directly detected but via conversion to light either through traditional scintillators based on organic molecules [74, 116] or quartz-based Cherenkov radiators [125]. This introduces neutron energy dependent detector efficiency and a non Dirac-delta instrument response function. For a perfect delta function IRF the Eq. 1.29 is correct. However the IRF convolves the signal and, as deconvolution is an ill-posed problem, fitting to experimental data, $f(t')$, is therefore done through a forward fitting process [74]. The measured neutron flux as a function of detection time, t', is given by:

$$f(t') = \int_{t_c}^{\infty} f(K_n(t))s(K_n(t))a(K_n(t))\frac{(\gamma_n\beta_n)^3 m_n}{t_c} R(K_n, t'-t)dt + B(t') \ , \tag{1.30}$$

where s is the sensitivity of the detector at a given neutron energy, R is the energy dependent IRF, a is the beam-line attenuation and B is an additional background term. Here we have introduced the detection time t' which due to the IRF is not equal to the neutron arrival time t. By an appropriate non-linear fitting routine the physical model $f(K_n)$ can be fit to the experimental data $f(t')$. The additional background term is due to scattering of neutrons from parts of the experiment not including the capsule e.g.

the target chamber. Using a well collimated and shielded line of sight can minimise this background contribution [116].

The Magnetic Recoil Spectrometer (MRS) uses an alternative energy differentiation mechanism by using incident neutron flux to knock on charged particles and measure the recoil particle energy distribution [54]. A large separation is included between the recoil particle source, usually a CH or CD foil placed near the implosion, and the magnetic spectrometer. This creates a small range of acceptance angles to the spectrometer and thus only the forward scattered recoil particles are measured. Once inside the spectrometer, the dispersion of the charged particles travelling through the magnetic field can be mapped to a charged particle energy. Due to the focussing on forward scattering, this charged particle energy can then be mapped onto a neutron energy. As there is no reliance on time dispersion, MRS has the potential to perform a time-resolved measurement using a single detector, although this has not been accomplished at the time of writing [57].

The traditional analysis of the DT fusion neutron spectrum is to extract the thermal temperature of reacting ions from the width of the peak. This standard analysis was first outlined by Brysk in 1973 [23], although there have been many advances in the description and analysis of the DT peak [5, 132]. A notable addition is the measurement of a fluid velocity of reacting ions through a shift in the peak centroid [5, 132], which has been realised experimentally [75, 116, 118]. This analysis also revealed that the apparent ion temperature extracted from the DT peak includes a significant contribution from fluid velocity variance induced Doppler broadening. This was verified by the difference in measured apparent DT and DD ion temperatures [61]. Separately, the scattered neutron spectrum is used to measure an areal density, ρR, through a scattered yield measurement [42, 95].

1.3.1.2 2D Imaging

Similar to the neutron spectrometers, neutrons are not directly imaged but must be converted to light first. In the case of the Neutron Imaging System (NIS) at NIF [72, 123, 187] this is done by a scintillator after the neutrons have passed through an aperture array. Both penumbral and pinhole images are created by this array allowing calibration and subsequent image reconstruction [123]. There are currently three operational lines of sight (LoS), one polar with (θ-ϕ) coordinates (5.25-225) and two equatorial at (90-315) and more recently (90-213) [51]. Currently, only the (90-315) LoS can take two energy-gated images. The time dispersion effect is used to allow different time gates on the imaging systems to measure different neutron energies. All three LoSs capture images of neutrons between 13-17 MeV - this energy range is dominated by the primary DT fusion neutrons. Primary neutron images map out a set of line integrals of T(D,n)α reaction[5] rate with an attenuation factor due to scattering and other interactions. The

[5]Here we introduce the compact nuclear reaction notation. A reaction A+b which produces c+D is denoted A(b,c)D, where the convention is that the highest mass particles are in the upper case positions.

primary image, I_p, with orthogonal image plane coordinates, x and y, and attenuation length, τ, is given by:

$$I_p(x,y) = \int_0^\infty dz\ R_{DT}(x,y,z)e^{-\tau(x,y,z)}\ , \tag{1.31}$$

where z is the coordinate normal to the image. The image is processed to extract information about the spatial source distribution, R_{DT}, while generally assuming uniform or zero attenuation factor. Limited LoS (2 or 3 images) tomographic reconstruction has been developed by Volegov *et al.* to allow these 2D line-integrated images to be converted into 3D source distributions [177, 178]. Tomographic reconstruction will be discussed in more detail in Chapter 4.

The second image on the (90-315) LoS measures downscattered neutrons between 6-12 MeV. While this image does include neutrons from other sources, a significant proportion of the signal is due to singly scattered neutrons. To reach 6-12 MeV they must scatter within an angular range $\Delta\Omega$, leading to an image function of the form:

$$I_s(x,y) = \int_0^\infty dz\ n_i(x,y,z)e^{-\tau} \int_{\Delta\Omega} d\Omega \frac{d\sigma}{d\Omega} \int_0^\infty ds\ R_{DT}(x-s\Omega_x, y-s\Omega_y, z-s\Omega_z)e^{-\tau'}\ . \tag{1.32}$$

The rate of scattering is proportional to the neutron flux and areal density therefore subsequent analysis of this image can find the areal density spatial distribution. Considering only the images along (90-315), Casey *et al.* developed the fluence compensation technique to extract an approximate areal density image [25]. The primary image can be converted to a map of neutron fluence at the scattering site by using the most probable scattering angle and the assumption of constant brightness per unit length along the line of sight. Thus an image of areal density can be extracted from the downscattered neutron image by dividing out the neutron fluence calculated from the primary image. By combining the fluence compensation analysis with the 3D source tomography, the assumptions of a singular scattering angle and constant brightness per unit length can be removed and a 3D map of density can be reconstructed [180].

Due to the limited number of lines of sight and the spatial resolution of ~ 14 μm [72] used to measure the fusing region ~ 50 μm and the dense fuel layer ~ 100 μm, tomographic reconstruction is under-determined and therefore error prone. Shape asymmetry is also extracted from the 2D images by Legendre polynomial decomposition of the 17% contour[6]. Only low modes ($L \lesssim 4$) can be resolved so the shape asymmetry can be related to low mode drive asymmetry. The 17% contour is chosen to avoid the effects of noise while enclosing a significant fraction of the emission. This can be seen by Abel transforming Eq. 1.31 for constant attenuation factor and a source which is

[6]The coefficients of this decomposition are often labelled PN, where N is the polynomial order. The N > 0 coefficients are typically given as a fraction or percentage of P0.

axisymmetric about y and uniform within its volume:

$$I_p(x,y) = 2e^{-\tau}\int_{|x|}^{\infty}\frac{R_{DT}(r',y)r'}{\sqrt{r'^2-x^2}}dr' = 2e^{-\tau}\int_{|x|}^{X(y)}\frac{r'}{\sqrt{r'^2-x^2}}dr' \ , \tag{1.33}$$

$$I_p(x,y) = 2e^{-\tau}\sqrt{X(y)^2-x^2} \ . \tag{1.34}$$

For a uniform spherical source ($X^2 = R^2 - y^2$) the 17% contour corresponds to 98.5% of the total radius [72]. However, a Legendre polynomial decomposition in the source radius does not simply map to a image plane Legendre polynomial decomposition. For example, with source radius Legendre polynomial coefficients of $R_0 = 1$ and $R_2 = \pm 0.2$ the 17% contour has coefficients of $R_0' = 1.09, 0.90$ and $R_2' = 0.199, -0.193$ respectively. It is seen that the sign and amplitude of P2 in the source affects the inferred P0 from the image, in this case at the 10% level. While contour analysis does not require solution to a complex inverse problem, equating the inferred shape from a 2D image to the 3D source (even if axisymmetric) is incorrect.

1.3.1.3 Activation

Activation diagnostics are used to measure the yield of neutrons as well as the anisotropy of the neutron flux. The total primary DT neutron yield is typically measured by the activation of the isotope ^{63}Cu through the reaction ^{63}Cu(n,2n)^{62}Cu which has a threshold on the incident neutron kinetic energy of 10.9 MeV [33]. The radioactive product undergoes β^+ decay (which produces two 0.511 MeV γ-rays by positron annihilation) with a half-life of 9.74 minutes and thus the neutron yield above 10.9 MeV can be measured through the decay rate [41].

The anisotropy of the neutron flux over 4π solid angle is measured by the flange neutron activation diagnostics FNADs [15, 190, 191]. These use the ^{90}Zr(n,2n) reaction (activation energy $E_a = 12.0$ MeV [33]) to produce ^{89}Zr which undergo β^+ decay with a 3.27 day half-life producing metastable ^{89m}Y which de-excites via a 909.0 keV γ-ray several seconds later. The activation measurement is described by the following equation:

$$A(\hat{\Omega}) = ke^{-\lambda t}\int_{E_a}^{\infty} dE f_n(E,\hat{\Omega})\sigma_a(E) \ , \tag{1.35}$$

where k is a constant related to the number of target nuclei and target geometry, λ is the decay constant, $f_n(E,\hat{\Omega})$ is the energy spectrum of incident neutrons in direction $\hat{\Omega}$ and $\sigma_a(E)$ is the cross section for the activation process. The constant k is calibrated using reference shots where the energy spectrum is isotropic. Then in ICF experiments anisotropy in the activation, A, is due to anisotropy in $f_n(E,\hat{\Omega})$. We assume a Gaussian form for $f_n(E,\hat{\Omega})$ [23] and linear form for the activation cross section $\sigma(E) = \sigma_{a,m}(E -$

E_a) [15]. Then at $t = 0$ the activation is given by:

$$A(\hat{\Omega}) = \frac{k\sigma_{a,m}}{\sqrt{2\pi}\Delta} Y(\hat{\Omega}) \int_{E_a}^{\infty} (E - E_a) e^{-\frac{(E-E_\mu)^2}{2\Delta^2}} dE \ , \tag{1.36}$$

$$A(\hat{\Omega}) = \frac{k\sigma_{a,m}}{\sqrt{2\pi}} Y(\hat{\Omega}) \left[\sqrt{\frac{\pi}{2}} (E_\mu - E_a) \left(1 + \mathrm{erf} \left(\frac{E_\mu - E_a}{\sqrt{2}\Delta} \right) \right) + \Delta e^{-\frac{(E_\mu - E_a)^2}{2\Delta^2}} \right] \ . \tag{1.37}$$

Generally for the DT fusion peak, the mean neutron energy is $E_\mu \sim 14$ MeV with standard deviation $\Delta \sim 0.15$ MeV. Therefore, to a very good approximation the above expression simplifies to the f_n delta function limit:

$$A(\hat{\Omega}) \approx kY(\hat{\Omega})\sigma_{a,m}(E_\mu - E_a) \equiv kY(\hat{\Omega})\alpha(\hat{\Omega}) \ . \tag{1.38}$$

We now have two terms which can alter the activation measurement: the intrinsic yield anisotropy $Y(\hat{\Omega})$ and the centroid shift anisotropy $\alpha(\hat{\Omega}) = \sigma_{a,m}(E_\mu - E_a)$. The intrinsic yield anisotropy changes due to kinematic focussing and scattering. The first effect occurs if the emitting material is moving at a velocity $\vec{v}_f$ causing the lab frame flux to be focussed in the direction of travel. Scattering on the path to the detector lowers the energy of some neutrons to below the activation energy, the ones that undergo small angle scattering remain above 12 MeV. The downscatter ratio into 12 - 14 MeV is approximately ρR_{DT} (kg/m^2) $\times$ 0.86% for 50/50 DT. These downscattered neutrons prove difficult to include in simplified analysis as their direction is also altered in the scattering and their $< 2\%$ contribution will be neglected here [15]. The sum of the kinematic focussing and scattering effects gives an intrinsic yield anisotropy of the form:

$$Y(\hat{\Omega}) \approx \left(1 + 2\frac{\vec{v}_f \cdot \hat{\Omega}}{v_n} \right) \exp \left[-\frac{\sigma_s(E_\mu)\rho R(\hat{\Omega})}{\bar{m}} \right] \ . \tag{1.39}$$

The centroid shift anisotropy arises due the activation cross section energy dependence. Higher energy neutrons are more likely to cause activation and therefore anisotropic shifts in the mean neutron energy will cause activation anisotropy. The centroid of the DT peak varies due to a Doppler shift if the emitter is in motion. There are higher order effects which are neglected here [132], these will be discussed in more detail in Section 2.2.1. We will split the isotropic shifts to the centroid from the anisotropic shifts, $E_\mu = E_0 + \delta_E(\hat{\Omega})$, for clarity. We will approximate the centroid shift due to the Doppler shift classically:

$$\alpha(\hat{\Omega}) \approx \sigma_{a,m}(E_0 - E_a + m_n v_n \vec{v}_f \cdot \hat{\Omega}) \ . \tag{1.40}$$

Around E = 14 MeV, the activation cross section slope $\sigma_{a,m} = 0.30$ barns/MeV and the scattering cross section $\sigma_s = 0.79$ barns for 50/50 DT. Therefore we see the FNADs are sensitive to areal density asymmetries and bulk flows of the fusing plasma. The centroid shift due to Doppler shift can be measured using neutron spectrometers [75] and the FNADs 'velocity-corrected' such that only the areal density asymmetry contribution

remains [148].

1.3.2 Gamma Ray

Fusion reactions can create γ-rays, albeit with a low branching ratio, and are also produced in inelastic nuclear reactions such as neutron scattering. Given here are the measured reactions produced within the capsule. The associated branching ratio is given for the DT fusion reaction [81, 101, 125, 135]:

$$D + T \rightarrow {}^{5}He + \gamma \ (16.8 - 13.5 \text{ MeV}) \qquad \sim 4 \times 10^{-5} \ \gamma/DTn \ , \tag{1.41}$$

$$n + C \rightarrow n + C + \gamma \ (4.4 \text{ MeV}) \qquad \sim 1 \times 10^{-3} (\rho R_C) \ \gamma/DTn \ , \tag{1.42}$$

where ρR_C is the carbon areal density in kg/m^2. The 4.4 MeV γ-ray is produced via a transition from the first excited state to the ground state of ^{12}C – this is a very narrow resonance with width 0.01-0.02 eV [1]. Neutrons also inelastically scatter in the hohlraum and the thermomechanical package (TMP) which holds the target in the chamber, producing background γ-rays with energies < 14 MeV. There are two time-resolved γ-ray detectors at NIF, the gas Cherenkov detector (GCD) [65, 82] and the gamma ray history (GRH) [81] diagnostics. Both these diagnostics use Cherenkov radiation from electrons which have reached superluminal velocities via Compton scattering from the incident γ-ray flux. The Cherenkov production medium is a gas cell where the fill pressure can be altered to change the refractive index, n, and therefore threshold Cherenkov energy ($n\beta_e = 1$). For illustrative purposes, consider forward Compton scattering of an electron by a γ-ray of energy $E_\gamma = \zeta m_e$, the threshold refractive index for Cherenkov production is:

$$n = \frac{1}{\beta_e} = \frac{(2\zeta + 1)^2 + 1}{(2\zeta + 1)^2 - 1} \ . \tag{1.43}$$

For a 16.8 MeV DT γ-ray ($\zeta = 32.9$), the Cherenkov production medium must have a refractive index of at least 1.00045. Multiple gas cells with different refractive indices can be used to create spectral windows to remove background γ-ray signal. The high energy threshold channel can be used to measure the DT reaction rate as a function of time, giving measurements of the centroid and width of the reaction history named the nuclear bang time and burn width respectively. Recent developments to GCD have introduced a pulse dilation system to increase the time resolution to ~ 10 ps [65]. By combining two gas cells with threshold energies either side of the 4.4 MeV C inelastic scattering γ-ray, inference of ablator areal densities can be made [84]. Time shifts of the C-γ peak relative to the DT-γ peak are also observed [121].

C-γ rays can be imaged and the (90-213) NIS LoS is developing the capability to image fusion neutrons, downscattered neutrons, γ-rays and x-rays simultaneously [51]. The ability to image C-γ rays has previously been demonstrated on the other NIS LoS by moving the time gating earlier to the photon arrival time. Similar to the downscattered

neutron image, the C-γ image intensity is proportional to the neutron fluence and carbon areal density. With similar imaging techniques discussed in Section 1.3.1.2 information about the shape of the remaining ablator during neutron production can be found.

1.4 Research Aims

Bridging the gap between numerical simulation and experimental data analysis is beneficial to both areas of research. The aims of this thesis are to both improve the capability and accuracy of the numerical simulation of ICF experiments and simulate the observable signals produced. Therefore, we diagnose the simulated experiment as one would a real experiment. Weaknesses in current experimental analysis; experimental observations missing from simulated observations and novel analysis techniques can be realised. As discussed earlier, this work will focus on nuclear diagnostics. One- and three-dimensional neutron and fast ion transport codes have been developed in order to produce synthetic nuclear diagnostics based on hydrodynamic simulations. Current experimental trends across multiple diagnostics are explored through the application of various perturbations. Additionally, we investigate possible measurements and analyses which would expand the range of measurements possible in ICF experiments. While many current diagnostics measure conditions within the hotspot, we aim to directly measure the unknown conditions of the dense DT fuel and the remaining ablator during thermonuclear burn through analysis of nuclear measurements.

In Chapter 2, the background theory relevant to describing inertial confinement fusion implosions and their experimental observables is given. This includes a discussion of: radiation hydrodynamics; atomic and statistical physics; and fusion reaction products and their transport. Additionally, the numerical techniques and code used in modelling the nuclear observables as well as the implosion itself are discussed within this chapter.

In Chapter 3, results under the umbrella of neutron spectroscopy are given. These include the neutron backscatter edge, spectroscopic signals of areal density asymmetry and features of the high energy neutron spectrum. These sections present both novel analysis techniques which could be used on current experimental diagnostics as well as future developments to further increase the utility of neutron spectra.

In Chapter 4, various results from neutron imaging are presented. Activation measurements and primary and scattered neutron imaging of 3D radiation hydrodynamics simulations are investigated to highlight both potential shortcomings and successes of current analysis.

In Chapter 5, γ-ray measurements are investigated to complete our description of nuclear observables. These include both imaging and time history measurements of γ-rays made in both fusion reactions and inelastic neutron scattering.

Finally the conclusions and plans for future work are given.

2 Theory and Numerics

"One has to resort to the indignity of numerical simulations to settle even the simplest questions about it" – Philip Anderson

Content in this chapter has been reproduced from "Synthetic nuclear diagnostics for inferring plasma properties of inertial confinement fusion implosions", Physics of Plasmas 25, 122703 (2018), Crilly et al. [42] with the permission of AIP Publishing.

The complex physical behaviour of an ICF experiment is governed by the action of macroscopic systems of particles and the interaction between these systems. The systems belong to two classifications; those which are locally in equilibrium i.e. thermal, and those which are non-thermal. Generally the ions and electrons of the bulk plasma are close to thermal and hence are well described by the hydrodynamic equations. The thermodynamic properties of this plasma depends on a detailed description of the microscopic properties of the plasma's constituents. In contrast, the products of fusion reactions are far from equilibrium due to their long mean free paths. They therefore require an appropriate transport equation to describe their behaviour. Radiation emitted by the plasma or used to drive the capsule also requires a non-local treatment. Common to all these systems is the large number of particles allowing a statistical/probabilistic description through continuous $(\vec{r}, \vec{v})$ phase space distributions. The evolution of these distributions can be described generally by the Boltzmann equation [98]:

$$\frac{\partial f}{\partial t} + \vec{v} \cdot \nabla_r f + \frac{\vec{F}}{m} \cdot \nabla_v f = \left(\frac{\partial f}{\partial t}\right)_{collision} + \left(\frac{\partial f}{\partial t}\right)_{source}, \tag{2.1}$$

where f is the expectation value of finding any of the particles at location $\vec{r}$ with velocity $\vec{v}$ at time t and $\vec{F}$ is any external force felt by the particles in the system. The various collision operators and source terms will depend on the system considered. Processes which conserve particle number, e.g. scattering, will be assigned to the collision term. Non-conservative processes will be assigned to the source term. Systems of different particle types couple to each other making the modelling of ICF experiments uniquely challenging – analytic techniques cannot yield results without many simplifications and therefore numerical analysis is essential.

This chapter will describe the necessary theory needed to model ICF implosions and the resultant observable nuclear signals. First, a description of radiation hydrodynamics, which is used to model the plasma conditions in capsule implosions, will be given in Section 2.1. This will be accompanied by a description, in Section 2.1.3, of the underlying

microscopic behaviour associated with atomic physics which affects the thermodynamic and radiative properties of the hydrodynamic elements. Second, the theory describing the transport of nuclear reaction products through the bulk plasma will be given. This will be separated into neutron transport in Section 2.2.1 and fast ion transport in Section 2.2.2. The numerical methods employed to solve a given physical system will be given in the relevant section.

2.1 Radiation Hydrodynamics

2.1.1 Hydrodynamics

Hydrodynamics is centrally important to the theory and simulation of ICF. The materials in ICF targets are generally highly collisional giving conditions that are locally very close to thermodynamic equilibrium. This can be quantified by the electron and ion mean free paths (MFPs) [86] at typical ICF conditions at stagnation:

$$\lambda_e = 0.14 \ \frac{1}{\ln\Lambda}\left(\frac{n_e}{10^{30}\mathrm{m}^{-3}}\right)^{-1}\left(\frac{T_e}{1\mathrm{keV}}\right)^{2} \ \mu\mathrm{m} \ , \tag{2.2}$$

$$\lambda_i = 0.20 \ \frac{1}{\ln\Lambda}\frac{1}{Z_i^4}\left(\frac{n_i}{10^{30}\mathrm{m}^{-3}}\right)^{-1}\left(\frac{T_i}{1\mathrm{keV}}\right)^{2} \ \mu\mathrm{m} \ , \tag{2.3}$$

where $\ln\Lambda$ is the Coulomb logarithm, Z_i and T_i are the charge and temperature of the ion species i, and T_e is the electron temperature. These short MFPs ensure the majority of particles are in thermodynamic equilibrium and hence have a Maxwellian velocity distribution. There are populations in the tails which have longer MFPs and therefore are responsible for transport phenomena. However, these generally only slightly perturb the velocity distribution from Maxwellian and can be well described by local transport theory.

Hydrodynamics describes the behaviour of locally thermal populations of particles. The velocity dimensions of phase space can be integrated out such that only position and time dimensions remain. At the heart of this treatment are the three conservation laws used to form the hydrodynamic equations: conservation of mass, conservation of momentum and conservation of energy. These laws can be derived from Eq. 2.1 by taking velocity moments. Here we will simply quote the resulting inviscid hydrodynamic equations [29]:

$$\left[\frac{\partial}{\partial t} + \vec{u}\cdot\nabla\right]\rho + \rho\nabla\cdot\vec{u} = 0 \ , \tag{2.4}$$

$$\rho\left[\frac{\partial}{\partial t} + \vec{u}\cdot\nabla\right]\vec{u} = -\nabla P + \vec{F}_{ext.} \ , \tag{2.5}$$

$$\left[\frac{\partial}{\partial t} + \vec{u}\cdot\nabla\right]\epsilon + (\epsilon + P)\nabla\cdot\vec{u} = -\nabla\cdot\vec{q} + Q_{ext.} \ , \tag{2.6}$$

defining mass density ρ, fluid velocity $\vec{u}$, pressure P, internal energy ϵ, heat flux $\vec{q}$, exter-

nal energy source $Q_{ext.}$, and external force $\vec{F}_{ext.}$. The term inside the square brackets, named the advective derivative, describes the advection of hydrodynamic quantities with the fluid motion. Terms involving the divergence of the fluid velocity ($\nabla \cdot \vec{u}$) describe the change in hydrodynamic quantities due to compression/expansion. On the right hand side of the equations are terms which do not involve the macroscopic fluid motion (e.g. ∇P) or are external to the fluid itself.

A useful analytical result which can be found directly from the hydrodynamic equations are the Rankine-Hugoniot (RH) jump conditions. These relate the fluid states either side of a shock. A shock wave is a disturbance which moves faster than the local speed of sound resulting in a discontinuity in hydrodynamic properties either side of the shock. The conditions are expressions of the conservation of mass, momentum and energy across the shock in the frame comoving with the shock. The subscripts 1 and 2 will be used to denote upstream and downstream quantities respectively [40]:

$$\rho_1 u_1 = \rho_2 u_2 \ , \tag{2.7}$$

$$\rho_1 u_1^2 + P_1 = \rho_2 u_2^2 + P_2 \ , \tag{2.8}$$

$$\frac{\gamma}{\gamma - 1}\frac{P_1}{\rho_1} + \frac{1}{2}u_1^2 = \frac{\gamma}{\gamma - 1}\frac{P_2}{\rho_2} + \frac{1}{2}u_2^2 \ , \tag{2.9}$$

where γ is the heat capacity ratio. Shocks occur during many phases of ICF implosions and hence the RH relations are essential in analysing the hydrodynamic conditions. In the strong shock limit, $P_2/P_1 \gg 1$, one finds that density and velocity jumps across the shock converge to a constant value:

$$\frac{\rho_2}{\rho_1} = \frac{u_1}{u_2} \rightarrow \frac{\gamma + 1}{\gamma - 1}\left(= 4 \ \text{ for } \gamma = \frac{5}{3}\right) \ . \tag{2.10}$$

This demonstrates the need for many strong shocks to reach large compressions of the ablator and/or fuel during the initial drive. Passing many shocks also allows for lower entropy production than a single powerful shock – in the limit of a very large number of successive shocks the compression becomes effectively adiabatic [111].

The hydrodynamic equations given in Eqs. 2.4 to 2.6 are solved numerically within the code Chimera. The numerical schemes used have been detailed in previous work at Imperial College [34, 119, 134, 171]. In order to solve these equations for density, fluid velocity and internal energy, expressions are needed for the remaining unknowns. Thermodynamic relations between the pressure, temperature, density and internal energy can be derived from an appropriate equation of state, this will be briefly discussed in Section 2.1.3. The heat flux is described by Fourier's law $\vec{q} = -\kappa \nabla T$ and the thermal conductivity, κ, is calculated from local transport theory [163]. Coupling from the radiation field and fast ion species, e.g. DT fusion alphas, can be included via force densities and energy exchange rates. For detail on the coupling and transport of alphas within Chimera see the work of Dr Jon Tong [174]. Radiation transport will be discussed in the following section.

Here we have only discussed hydrodynamics, however, magnetohydrodynamics (MHD) and magnetic effects in transport can alter the behaviour of the plasma. The effects can be significant, especially if a strong magnetic field is externally applied to the target [140, 183]. For details on extended MHD effects in spherical ICF implosions as calculated by Gorgon (the MHD version of Chimera) see the work of Dr Chris Walsh [181–184].

2.1.2 Radiation Transport

Radiation is used in the drive of ICF implosions, but there is also significant self emission by the hot plasma. It therefore affects the dynamics of implosions by acting as both a source and sink of energy. Measurements of self emission are an important means for diagnosing plasma conditions in experiment.

In the absence of a material, radiation will free stream. In the presence of an interacting material, radiation will be absorbed, emitted/re-emitted and scattered. The mechanism for the materials interaction with the radiation field depends on both the material and radiation field properties. Here we will draw the distinction between photons with frequencies $\omega \gg \omega_p$ and $\omega \gtrsim \omega_p$. Electromagnetic (EM) waves with frequencies below the plasma frequency cannot propagate. Firstly, for the lower frequencies ($\omega \gtrsim \omega_p$) EM waves create collective responses in the plasma and therefore can refract strongly. These frequencies are relevant to the propagation of lasers through ICF plasmas. The laser paths are well described by the geometrical optics approximation – a description of which can be found in the work of Kaiser and references therein [97].

Secondly, for the high frequencies ($\omega \gg \omega_p$) photons interact with the medium at a photon-particle level. This regime is relevant to the transport of X-rays in ICF plasmas, which will be the focus of this section. The Boltzmann equation (Eq. 2.1) can be used to describe a population of photons with the simplification that the photons must move at the speed of light, c. The radiative transfer equation is written in terms of the radiation intensity, I_ν, which is related to f through a constant:

$$I_\nu = \frac{dE}{dAdtd\Omega d\nu} = \frac{h^4\nu^3}{c^2} f \ , \tag{2.11}$$

$$\frac{1}{c}\frac{\partial I_\nu}{\partial t} + \hat{\Omega}\cdot\nabla I_\nu = \frac{1}{c}\left(\frac{\partial I_\nu}{\partial t}\right)_{col.} + \frac{1}{c}\left(\frac{\partial I_\nu}{\partial t}\right)_{src.} \ . \tag{2.12}$$

The photon direction of travel is denoted $\hat{\Omega}$. The collision and source terms here contain the interactions of photons with matter through absorption, emission and scattering. The scattering term can be described through a double differential cross section. This gives the probability a photon of frequency ν' moving in direction $\hat{\Omega}'$ scatters to a frequency ν in direction $\hat{\Omega}$. The collision operator which conserves photon number has the form:

$$\frac{1}{c}\left(\frac{\partial I_\nu}{\partial t}\right)_{col.} = -n_s\sigma_{\nu,s}I_\nu + n_s\int d\hat{\Omega}'\int d\nu'\frac{d^2\sigma_{\nu,s}}{d\Omega d\nu}I_\nu(\vec{r},\hat{\Omega}',\nu',t) \ , \tag{2.13}$$

where n_s is the number density of scatterers, $\sigma_{\nu,s}$ is the total cross section for scattering at frequency ν and the double differential cross section appears in the integral term. The Thomson and Compton scattering of photons from single free electrons has a differential cross section given by the Klein-Nishina formula [192].

The absorption and emission of radiation are described through the opacity and emissivity. Physically, the opacity, κ_ν, is the inverse of the mean free path of a photon at a given frequency. The absorption processes which contribute to this opacity include free-free, bound-free and bound-bound electronic transitions. The (spectral) emissivity, j_ν, is due to the inverse of these absorption processes, giving the self emission of the material. These properties will be described in more detail in the following section. By definition, the opacity and emissivity introduce terms of the form:

$$\frac{1}{c}\left(\frac{\partial I_\nu}{\partial t}\right)_{src.} = -\kappa_\nu I_\nu + j_\nu \ , \tag{2.14}$$

combining Eqs. 2.12 to 2.14 we arrive at the full radiative transfer equation:

$$\left[\frac{1}{c}\frac{\partial}{\partial t} + \hat{\Omega}\cdot\nabla + (n_s\sigma_{\nu,s} + \kappa_\nu)\right] I_\nu = j_\nu + n_s \int d\hat{\Omega}' \int d\nu' \frac{d^2\sigma_{\nu,s}}{d\Omega d\nu} I_\nu(\vec{r}, \hat{\Omega}', \nu', t) \ . \tag{2.15}$$

At ICF relevant conditions, the material absorption and emission dominate over scattering for dynamically important photon energies. The small contribution from the scattering term can be approximated as an averaged absorption cross section. At very high frequencies such as γ-rays, scattering can dominate over absorption leading to drastically different behaviour.

There are two scenarios in which modelling of the radiation field is needed; radiative energy transfer influencing the hydrodynamics and exiting radiation measured by diagnostics. The full radiative transfer equation requires 7 dimensions: 3 spatial, 2 angular, 1 spectral and 1 temporal. Therefore, radiative transfer is extremely computationally expensive to solve numerically. Based on the requirements of the two modelling scenarios, simplifications to the transport equation can be made to ensure tractability.

First, we consider the radiative energy transfer influencing hydrodynamics (i.e. radiation hydrodynamics). Localised sources and beams of X-rays are uncommon in ICF plasmas, so I_ν should not rapidly vary with propagation direction $\hat{\Omega}$. Therefore, Eq. 2.15 is simplified by taking the first two angular moments to obtain the energy density, E_ν, flux, $\vec{F}_\nu$, and pressure, $\mathbf{P}_\nu$:

$$cE_\nu = \int I_\nu d\Omega, \ F_{i,\nu} = \int \hat{\Omega}_i I_\nu d\Omega, \ cP_{ij,\nu} = \int \hat{\Omega}_i\hat{\Omega}_j I_\nu d\Omega \ ,$$

$$\left[\frac{\partial}{\partial t} + \kappa_\nu c\right] E_\nu = 4\pi j_\nu - \nabla\cdot\vec{F}_\nu \ , \tag{2.16}$$

$$\left[\frac{\partial}{\partial t} + \kappa_\nu c\right] \vec{F}_\nu = -c^2\nabla\cdot\mathbf{P}_\nu \ , \tag{2.17}$$

$$\frac{dT}{dt} = \frac{1}{c_V}\int \kappa_\nu \left(cE_\nu - 4\pi\frac{j_\nu}{\kappa_\nu}\right) d\nu \ . \tag{2.18}$$

Also included is the heating equation, Eq. 2.18, of the material with temperature, T, and heat capacity at constant volume, c_V. The two moment equations involve a streaming operator which includes the absorption due to the opacity, κ_ν. On the RHS, there are sources due to divergences of fluxes and material emission, j_ν. Solution to these equations requires a closure relation for the radiation pressure tensor $\mathbf{P}_\nu$. Various closure relations are used throughout work in radiation hydrodynamics, Chimera utilises a closure and solution scheme known as $\mathrm{P}_{1/3}$ [129] with automatic flux limiting [165]. The closure is obtained by assuming an isotropic radiation field, in which case:

$$P_{ij,\nu} = \frac{1}{c}\int \hat{\Omega}_i\hat{\Omega}_j I_\nu d\Omega = \frac{I_\nu}{c}\int \hat{\Omega}_i\hat{\Omega}_j d\Omega = \frac{1}{3}\delta_{ij}\frac{4\pi I_\nu}{c} = \frac{1}{3}\delta_{ij}E_\nu \ . \tag{2.19}$$

The moment equations are also split into a number of radiation energy groups – this is known as a multigroup solution. Each group uses j_ν and κ_ν values which have been averaged across the range of energies within the group. A detailed description of the radiation transport methods and their implementation in Chimera can be found in the PhD theses of Dr Kristopher McGlinchey [119] and Dr Christopher Jennings [94].

X-ray diagnostics can measure spectra or images within certain spectral ranges and therefore detailed knowledge of the spectrum arriving at the diagnostic is required. The diagnostics are placed far from the implosion and therefore the incident X-ray flux is anisotropic. Therefore, the methods employed to solve radiation hydrodynamics are generally not well suited to this task. By restricting the paths of photons to only those which intersect the diagnostic, transport is solved only along characteristics of a single direction, $\hat{\Omega}_{det}$. X-ray diagnostics of the capsule measure high energy X-rays (several keV) for which the mean free path is long. Additionally, the material properties evolve slowly compared to the light transit time so a steady state can be assumed. Using the method of characteristics, the time-independent radiative transfer equation can be rewritten as:

$$I_\nu(\vec{r},\hat{\Omega}_{det}) = \int_0^\infty \exp\left[-\int_0^s ds'\kappa_\nu(\vec{r}-s'\hat{\Omega}_{det})\right] j_\nu(\vec{r}-s\hat{\Omega}_{det},\hat{\Omega}_{det})\ ds \ , \tag{2.20}$$

from this we will introduce a formal definition of optical depth, τ_ν, between position $\vec{r}$ and a distance s along direction $-\hat{\Omega}$:

$$\tau_\nu(s) = \int_0^s ds'\kappa_\nu(\vec{r}-s'\hat{\Omega}) \ . \tag{2.21}$$

When evaluating the radiation intensity at a diagnostic based on a hydrodynamic simulation, radiative properties are constant across grid cells. The radiation intensity exiting a cubic cell of length l and index i is given by:

$$I_{\nu,i+1/2} = \frac{j_{\nu,i}}{\kappa_{\nu,i}}\left(1-e^{-\tau_{\nu,i}(l)}\right) + I_{\nu,i-1/2}e^{-\tau_{\nu,i}(l)} \ , \tag{2.22}$$

where $I_{\nu,i-1/2}$ is the radiation intensity entering the cell at the far side. The whole

hydrodynamic simulation domain can be integrated across in this manner allowing post-processed synthetic X-ray diagnostics to be produced.

2.1.3 Atomic Physics & Statistical Mechanics

Knowledge of the structure of electronic states is required to understand the radiative properties of a material. We will first discuss how the structure and occupation of electronic states are determined through a confluence of atomic physics and statistical mechanics. A thermodynamic ensemble of quantum mechanical states must be considered in order to determine macroscopic properties. Marrying a small scale accurate quantum mechanical description with the many-body and many-species thermodynamic system is an exceedingly difficult task and a field of active research. There are two overarching approaches; the 'physical' and 'chemical' pictures. In the physical picture, one works at the level of electrons and nuclei, calculating electronic states self-consistently. Bound electronic states cause ions, atoms and molecules to emerge. An example of a solution method in the physical picture is density functional theory (DFT). However, physical picture models cannot independently describe all of parameter space due to the approximations made in their construction. The approach that we shall use is in the chemical picture. In the chemical picture, we define chemical species within the material; free electrons, bound electrons, ions, molecules, etc. Each of these species is described through its own free energy and interaction terms. The free energies can be derived from the partition functions for the grand canonical, $\mathcal{Z}$, and canonical, Q, ensembles:

$$\mathcal{Z} \equiv \sum_n \exp\left[-\beta\left(E_n - \mu N_n\right)\right] \ , \tag{2.23}$$

$$Q \equiv \sum_n \exp\left[-\beta E_n\right] \ , \tag{2.24}$$

where n labels the microscopic states within the system with energy E_n and occupancy N_n. The inverse temperature and chemical potential are denoted $\beta = 1/k_B T$ and μ, respectively. The partitioning of a thermodynamic system between the different species is determined through chemical equilibrium. A notable example of this is the Saha equation, where one considers the chemical equilibrium of ionisation between stages i and $i+1$:

$$A_i \rightleftharpoons A_{i+1} + e^- \ , \tag{2.25}$$

$$\mu_i = \mu_{i+1} + \mu_e \ , \tag{2.26}$$

$$N_a = \frac{1}{\beta}\frac{\partial}{\partial \mu_a} \log \mathcal{Z}_a \ , \tag{2.27}$$

$$\mu_a = -\frac{1}{\beta}\frac{\partial}{\partial N_a} \log Q_a \ , \tag{2.28}$$

where subscript a denotes the species a. Using Eqs. 2.27 and 2.28 one can find an expression for the chemical potential to solve the Saha ionisation equilibrium, Eq. 2.26. A benefit of the chemical picture is that it is conceptually closer to the macroscopic quantities we wish to extract. However, there are two issues which arise from this approach. Firstly, although the equations of chemical equilibrium are simpler than the many-body equations of the physical picture, one must construct models for the partition functions based on microscopic properties and interactions. For all but the simplest terms, these models are approximate in nature. Secondly, we have drawn a distinction between chemical species such as free and bound electrons where physically there is no difference in their properties and interactions. Indeed, core bound electrons and high energy free electrons do behave differently and are well described by different models. However, in the middle ground it is less clear that the distinction is meaningful. Interactions between free and bound electrons must be added back into the model after the separation of terms – a physical picture model has no such issue.

The discussion above is also relevant for the equation of state needed to close the hydrodynamic equations. Within the chemical picture, a statistical mechanical description of pressure, internal energy, heat capacity, chemical potential, entropy, etc. is possible through thermodynamic potentials. Typically, the Helmholtz free energy, $F = -k_B T \ln Q$, is used as it is useful for isothermal and isochoric processes while allowing the pressure to change. The equation of state code FEOS [100, 126], used in Chimera, is based on a series of additive Helmholtz free energy expressions. Ions and electrons are given separate free energy terms. Finally, thermodynamic quantities can be derived from the total free energy, e.g. $P = -\partial F / \partial V$.

Returning now to the Saha ionisation equilibrium, we first consider a dilute, single-species plasma where interaction terms due to free electrons can be ignored, then the grand partition functions are given by:

$$\mathcal{Z}_i = \sum_N e^{\beta\mu N} \frac{\mathcal{Q}_{ideal}^N}{N!} = \exp\left[e^{\beta\mu} \mathcal{Q}_{int} \mathcal{Q}_{trans}\right] \ , \tag{2.29}$$

$$\mathcal{Q}_{trans} = \frac{V}{\lambda_i^3}, \ \lambda_i = \sqrt{\frac{2\pi\hbar^2\beta}{m_i}} \ , \tag{2.30}$$

$$\mathcal{Q}_{int} = \sum_n g_n \exp\left[-\beta E_n\right] \ , \tag{2.31}$$

$$\mathcal{Z}_e = 1 + \exp\left[-\beta(E-\mu)\right] \ , \tag{2.32}$$

where $\mathcal{Q}$ are the single-particle partition functions, g_n and E_n are the degeneracy and energy of the discrete energy level n and λ_i is the thermal de Broglie wavelength for species i. The bound electrons are described by the ion internal partition function, $\mathcal{Q}_{int}$. Separately, the free electrons are described as a partially degenerate free electron gas through $\mathcal{Z}_e$. We have considered the ions to behave classically for translational degrees of

freedom as typically $n\lambda_i^3 \ll 1$. We can now form the Saha ionisation equation explicitly:

$$\frac{N_{i+1}N_e}{N_i} = N_e e^{-\beta\mu_e}\left(\frac{\mathcal{Q}_{int,i+1}}{\mathcal{Q}_{int,i}}\right) = N_e e^{-\beta\mu_e}\left(\frac{\sum_n g_{n,i+1}\exp\left[-\beta\epsilon_{n,i+1}\right]}{\sum_n g_{n,i}\exp\left[-\beta\epsilon_{n,i}\right]}\right)e^{-\beta I_i} \ , \quad (2.33)$$

where I_i is the ground state ionisation energy and $\epsilon_{n,i}$ are the excitation energies. The ionic translational partition functions cancel almost exactly as the ion masses only differ by a single electron mass. The chemical potential of the free electrons can be calculated for a given N_e, in the classical limit this simplifies to:

$$N_e e^{-\beta\mu_e} \to \frac{2V}{\lambda_e^3} \ . \quad (2.34)$$

To highlight the power of the Saha equation, we will present the analytical solution obtained for a classical hydrogen plasma with no bound electronic excitations. The ionisation fraction, $f_e = n_e/(n_0 + n_1) = n_e/n$, is given by:

$$\frac{f_e^2}{1-f_e} = \frac{2}{n\lambda_e^3}\frac{g_{0,1}}{g_{0,0}}\exp\left[-\beta I\right] \ , \quad (2.35)$$

therefore the ionisation fraction can be found over density-temperature space from a single algebraic expression, see Fig. 2.1. We see increased temperature drives ionisation

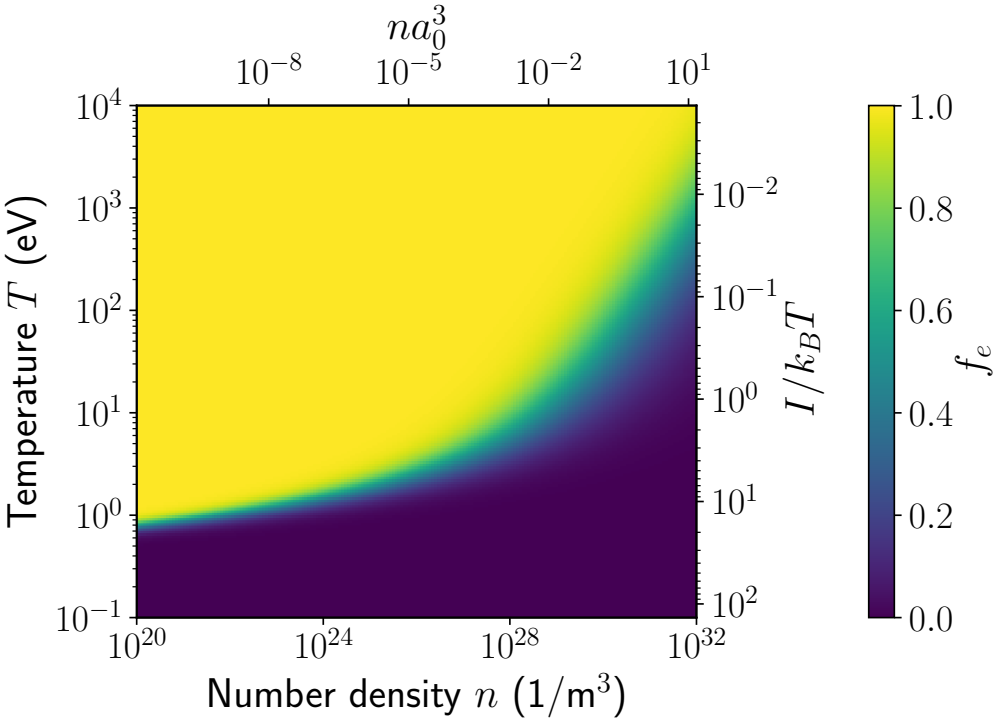

Figure 2.1: The classical ideal gas solution to the Saha equation, Eq. 2.33, for hydrogen. Plotted is the ionisation fraction $f_e = n_e/n$ against hydrogen nucleus density, n, and temperature, T. On secondary axes are the ionisation potential I/k_BT and the scaled density na_0^3 where a_0 is the Bohr radius.

and increased density drives recombination. While the Saha solution is well-behaved

over the whole space, one must remember that here we have neglected interaction terms. Therefore, the present Saha result is inaccurate at higher densities.

Given all of the ionisation and excitation energies from an atomic model, one might hope to solve the non-linear set of Saha equations for any element. Even when neglecting interaction terms, one will quickly run into difficulties. This is because the internal partition function diverges if all bound levels of an isolated atom/ion are considered. This non-physicality is a symptom of the separate treatment of bound and free electrons. In reality the highest lying bound states will be perturbed by nearby charges and become delocalised. In a simplified view, the transition between free and bound states has moved to lower energies, this process is named continuum lowering or ionisation potential depression (IPD). This rather foreign concept is related to the much more familiar screening process in plasmas. The potential of a charge is screened by the surrounding charges reducing its effect at large distances. We will consider the effect of a charged test particle placed into a plasma. In terms of the dielectric function, ϵ, in wavenumber-angular frequency $\left(\vec{k},\omega\right)$ space:

$$\phi_{\text{ext}}\left(\vec{k},\omega\right) = \epsilon\left(\vec{k},\omega\right)\phi_{\text{eff}}\left(\vec{k},\omega\right) \rightarrow \vec{D}\left(\vec{k},\omega\right) = \epsilon\left(\vec{k},\omega\right)\vec{E}\left(\vec{k},\omega\right) \ , \tag{2.36}$$

where ϕ is the electrostatic potential, $\vec{D}$ is the displacement field and $\vec{E}$ is the electric field. The response of the plasma to applied external potential, ϕ_{ext}, from the test particle results in a screened effective potential, ϕ_{eff}. From the linearised Vlasov equation including the Coulomb potential, it can be shown that one obtains a statically ($\omega = 0$) screened Coulomb potential of the form [104]:

$$\phi_{\text{eff}}(k) = \frac{q}{\epsilon_0 k^2}\frac{1}{\epsilon\left(\vec{k},0\right)} = \frac{q}{\epsilon_0}\cdot\frac{1}{k^2+\kappa^2} \rightarrow \phi_{\text{eff}}(r) = \frac{q}{4\pi\epsilon_0}\cdot\frac{1}{r}\exp(-\kappa r) \ , \tag{2.37}$$

$$\kappa^2(n_a,T) = \sum_a \frac{Z_a^2 e^2}{\epsilon_0}\frac{\partial n_a}{\partial \mu_a},\ \kappa_D^2 = \frac{\beta e^2}{\epsilon_0}\sum_a n_a Z_a^2,\ \kappa_{TF}^2 = \frac{3e^2}{2\epsilon_0}\sum_a \frac{n_a Z_a^2}{E_a^F} \ , \tag{2.38}$$

where E_a^F is the Fermi energy of species a. The response of the plasma is therefore defined through the inverse screening length, κ. The classical Debye-Hückel, κ_D, and highly degenerate Thomas-Fermi, κ_{TF}, limits of the inverse screening length are given. A consequence of the screening by the plasma is a non-zero self-energy associated with the induced electrostatic potential ($\phi_{\text{ind}} = \phi_{\text{eff}} - \phi_{\text{ext}}$). The induced electrostatic potential is due to the screening cloud and does not include the potential of the test particle itself. The total electrostatic energy of the plasma is found by summing the potential energy of all particles i, correcting for double counting:

$$U = \frac{1}{2}\sum_i Z_i e\phi(\vec{r}_i) = \frac{1}{2}\sum_i Z_i e\phi_{\text{ind}}(r=0) \equiv \sum_i \Delta_i \ , \tag{2.39}$$

from this we can find an expression for the self energy, Δ_i, by using Eq. 2.37:

$$\Delta_i = \frac{1}{2} Z_i e \phi_{\text{ind}}(r=0) = \frac{1}{2} \frac{Z_i^2 e^2}{4\pi\epsilon_0} \lim_{r\to 0} \left[\frac{1}{r} \left(e^{-\kappa r} - 1 \right) \right] = -\frac{1}{2} \frac{Z_i^2 e^2 \kappa}{4\pi\epsilon_0} \,. \tag{2.40}$$

Therefore, a free particle in a plasma has an energy of $E_i = p_i^2/2m + \Delta_i$. Since Δ_i is negative, the free continuum has shifted to lower energies. This is exactly the ionisation potential depression that was eluded to earlier. The bound states of an isolated atom which lie above Δ_i will no longer be bound if placed within a plasma. Models for $\Delta_i(n, T)$ which extend beyond the linearised result given above will be given in Section 2.1.3.1.

The dynamic version of the static continuum lowering described above is also important in plasmas. It gives rise to Stark broadening, an effect commonly considered in dense plasma X-ray line spectroscopy [71]. Additionally, this discussion will elucidate why splitting electrons into bound and free within a plasma is too simplistic. At any point in space the motion of plasma particles creates a time-varying electric potential, known as the microfield. Figure 2.2 illustrates the effect of a non-zero electric field on electron bound states at one instance. For tightly bound states, the resultant Stark shifts are perturbative and will vary in time – in a time averaged sense this effectively broadens the states. Weakly bound states may temporarily form molecular orbitals as ions draw close to each other (e.g. H_2^+ in a hydrogen plasma). Single-ion bound states

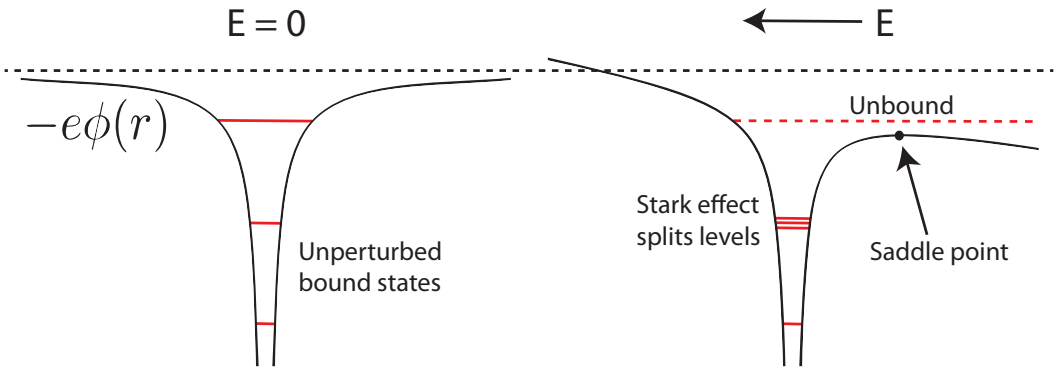

Figure 2.2: Diagram showing the various effects of an electric field on the bound states of an ion. The core states are unperturbed while higher lying states split through the Stark effect. The highest lying states, for which the electric field is strongly perturbing, are destroyed. Also shown is the potential saddle point above which states are classically unbound and below which states can quantum-mechanically tunnel out or remain bound.

can therefore be temporarily destroyed and we must include the statistical average of this effect to our chemical model. To do this we will use the occupation probability method which simply introduces a multiplicative factor, w_n, which reduces the statistical weight of bound states ($g_n \to g_n w_n$ where $0 \leq w_n \leq 1$). Following the work of Hummer and Mihalas, we define a critical field F_n^c at which the bound state n becomes

unbound. Then the probability of the survival, w_n, can be calculated from the microfield distribution function $P(F)$:

$$w_n = \int_0^{F_n^c} P(F)dF \ . \tag{2.41}$$

The microfield distribution function, $P(F)dF$, gives the probability of the ion experiencing an electric field strength in the interval $[F, F+dF]$. The microfield is isotropic in unstructured media and is defined through the statistical average of the summed electric field from all particles in the plasma. The specifics of the critical field and microfields distribution models will be given in Section 2.1.3.1.

The combined effects of pressure ionisation can be included in our chemical picture model by modifying the internal partition function. This is done through the reduced statistical weights, w_n, and shift to the continuum, Δ. An illustration showing the action of these effects on the density of states is shown in Fig. 2.3. Mathematically these effects are given by:

$$\mathcal{Q}_{int} \rightarrow \sum_n w_n g_n \exp\left[-\beta E_n\right] \ , \tag{2.42}$$

$$I_i \rightarrow I_i - \Delta \ . \tag{2.43}$$

There are more exact treatments of the theory of non-ideal plasmas which are complex and beyond the scope of this work, the author points the interested reader to the textbook of Kremp, Schlanges and Kraeft [104].

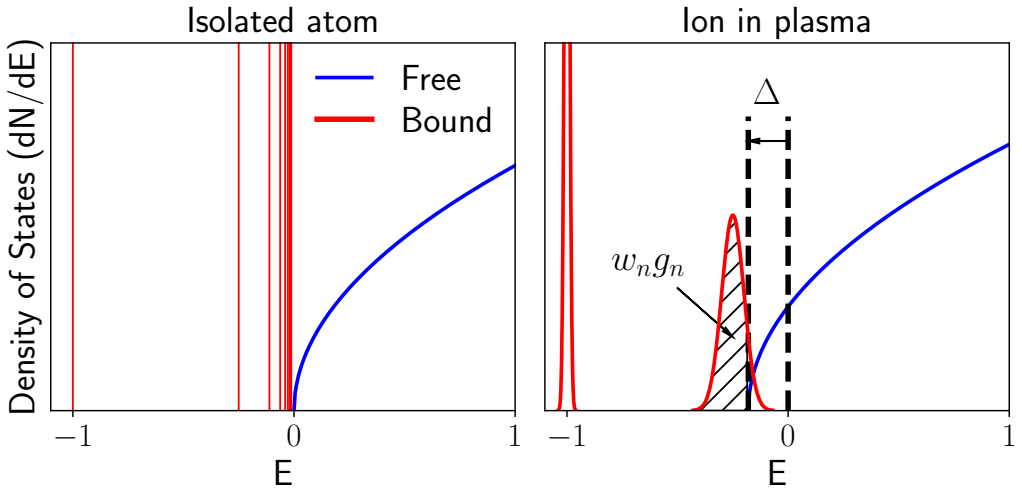

Figure 2.3: Diagrams showing the form of the density of states in the cases of an isolated atom and an ion in plasma. In a plasma the energy of the free electron continuum is lowered by Δ causing the destruction of some bound states. The statistical average of the remaining bound states are broadened by the electric microfield. A fraction of these states can become semi-bound or free resulting in a statistical weight of the bound state $w_n g_n < g_n$.

We will now begin our discussion of radiative properties. First, we note that in thermodynamic equilibrium all forward and reverse processes must balance. Therefore, the

emission of photons must balance the absorption of photons by the reverse process. The photon field is a blackbody field in thermodynamic equilibrium. Therefore, establishing equilibrium by balancing processes yields Kirchhoff's law of thermal radiation:

$$j_\nu = \kappa_\nu B_\nu \ , \tag{2.44}$$

where B_ν is the blackbody or Planckian function. Therefore, in thermodynamic equilibrium emissivity can be derived from opacity and vice-versa. While non-equilibrium conditions can arise in ICF they will not be considered. In these cases, the source function (defined as the ratio of emissivity to opacity j_ν/κ_ν) is no longer Planckian and forward and backward processes must be considered individually. However, the time-reversibility of microscopic processes can be used to relate the cross sections for forward and backward processes, even out of equilibrium.

The free-free, bound-free and bound-bound electron transitions produce/absorb photons. The theory of these processes is well-established and described within the literature [112, 153, 192]. Only a brief summary of the relevant results is given here.

Electronic transitions between bound states are described through the Einstein coefficients which detail the properties of emission and absorption from two levels of a quantum system. This system can undergo spontaneous emission (defined through the A coefficient) or interact with the present radiation field to cause photon absorption and stimulated emission (defined through the B coefficients). These processes alter the number of electrons in the lower level, j, as they are promoted to or demoted from the upper level, k. The rate equation for the level j acts to define the Einstein coefficients A and B:

$$\left(\frac{dn_j}{dt}\right) = A_{kj}n_k + (B_{kj}n_k - B_{jk}n_j)\int \frac{I_\nu}{4\pi}d\Omega \ . \tag{2.45}$$

The principle of detailed balance leads to the Einstein relations, of which we will use $g_j B_{jk} = g_k B_{kj}$. From this and the Boltzmann distribution of energy levels, one can derive the opacity for the line transition between states j and k:

$$\kappa^{\mathrm{bb}}_{jk,\nu} = \frac{h\nu_{jk}}{4\pi}\left(n_j B_{jk} - n_k B_{kj}\right) = \frac{h\nu_{jk}}{4\pi} n_j B_{jk}\left[1 - \frac{g_j n_k}{g_k n_j}\right] \ , \tag{2.46}$$

$$\frac{g_j n_k}{g_k n_j} = \exp\left[-\frac{E_k - E_j}{k_B T}\right] = \exp\left[-\frac{h\nu_{jk}}{k_B T}\right] \ , \tag{2.47}$$

it should be noted that Eq. 2.46 is true even out of thermodynamic equilibrium. The Einstein coefficients can be translated into the more familiar oscillator strength, f_{jk}, notation. The oscillator strength quantifies the quantum-mechanical correction to the classical expression based on the Larmor formula:

$$B_{jk} = \frac{\pi e^2}{\epsilon_0 m_e c h \nu_{jk}} f_{jk}\Phi(\nu) \ , \tag{2.48}$$

$$f_{jk} = \frac{2}{3}\frac{m_e}{\hbar^2} h\nu_{jk}\left|r_{jk}\right|^2 \ , \tag{2.49}$$

where r_{jk} is the dipole matrix element. We have also included the line shape function, $\Phi(\nu)$, which takes a Voigt profile[1] due to the convolution of Gaussian and Lorentzian shapes from various physical processes, e.g. Doppler and natural broadening. The stimulated and spontaneous processes are not restricted to bound-bound transitions. Therefore, all opacities must account for the effective decrease in absorption caused by stimulated emission. In thermodynamic equilibrium, this arises as a multiplicative $[1 - \exp(-h\nu/k_BT)]$ factor.

The free-free process, named bremsstrahlung, occurs within the free continuum of states so can produce/absorb photons at any energy. The total opacity of thermal bremsstrahlung for all ion species i is given by [112]:

$$\kappa_\nu^{\text{ff}} = \sum_i n_i \sigma_{i,\text{ff}} \left[1 - \exp\left(-\frac{h\nu}{k_BT}\right)\right] g_{\text{ff}}(\nu, T) \ , \tag{2.50}$$

$$\sigma_{i,\text{ff}} = \frac{4h^3c^4}{3\sqrt{3}} \alpha^5 a_0^2 \cdot n_e Z_i^2 \sqrt{\frac{m_e}{2\pi k_BT}} \cdot \frac{1}{(h\nu)^3} \ , \tag{2.51}$$

where $\alpha \approx 1/137$ is the fine structure constant, $a_0 \approx 52.9$ pm is the Bohr radius and g_{ff} is the free-free Gaunt factor. Gaunt factors are introduced to include full quantum-mechanical corrections to the semi-classical cross section expressions.

An electron transition between a bound and free state can produce photons at any energy above a threshold. The threshold energy is the energy required to promote the electron from the bound state to the lowest energy free state. Using the semiclassical photoionisation cross-section calculated by Kramer, the opacity of thermal bound-free absorption for state j is given by [153]:

$$\kappa_{j,\nu}^{\text{bf}} = n_j \sigma_{j,\text{bf}}^K \left[1 - \exp\left(-\frac{h\nu}{k_BT}\right)\right] g_{\text{bf}}(j, \nu, T) \ , \tag{2.52}$$

$$\sigma_{j,\text{bf}}^K = \begin{cases} \frac{64\pi}{3\sqrt{3}} \alpha a_0^2 \cdot \frac{\mathcal{N}_j}{Z_j^{*2}} \left(\frac{\chi_j}{h\nu}\right)^3, & h\nu \geq \chi_j, \\ 0, & h\nu < \chi_j, \end{cases} \tag{2.53}$$

where $\mathcal{N}_j$ is the principal quantum number of state j, Z_j^* is the effective screened nuclear charge seen by state j, χ_j is the energy between the bound and lowest energy free state and g_{bf} is the bound-free Gaunt factor. This cross-section has been calculated assuming hydrogenic bound states.

Given these formulae and the distribution of ionic and electronic states one can calculate the opacity. Similar expressions exist for emissivities, j_ν.

2.1.3.1 SpK

The initial numerical implementation of the theory described in the previous section was written by Dr Nicolas Niasse – the code was named SpK [134]. The author has inherited the code and has performed a number of improvements with the aim to introduce

[1] More complex line shape profiles can be produced in plasmas, see the textbook by Griem for details [71].

physical models for warm dense matter phenomena. In particular introducing pressure ionisation models to the code.

SpK is an atomic model code which uses the screened hydrogenic model (SHM) with energy levels taken from the NIST database to perform detailed configuration accounting (DCA) calculations of the state populations, free electron number density, emissivity and opacity at given conditions. Multigroup emissivity and opacity tables produced by SpK are used within the radiation-hydrodynamics code Chimera. SpK can work in local thermodynamic equilibrium (LTE) or collisional-radiative equilibrium (CRE), however, only the LTE version shall be discussed here. The Saha equations are solved iteratively using a Picard step with damping [151]. In fact, in SpK the logarithm of the Saha equations is solved as this more accurately captures the disparate scales which occur in ionic and electronic populations. With ionic stage index i and iteration index j, the Saha iterative loop has the following form [134]:

$$n_{e,j} = \bar{Z}_j n_{tot} \ , \tag{2.54}$$

$$\theta_{i+1,j} = \theta_{i,j} + \ln\left[\mathcal{Q}_{e,j}\right] + \ln\left[\frac{\mathcal{Q}_{int,i+1,j}}{n_{e,j}\mathcal{Q}_{int,i,j}}\right] - \beta(I_i - \Delta_{i,j}) \ , \tag{2.55}$$

$$f_{i,j} = \exp\left[\theta_{i,j} - \max_i(\theta_{i,j})\right] \ , \tag{2.56}$$

$$\bar{Z}_j^* = \frac{\sum_i Z_i f_{i,j}}{\sum_i f_{i,j}}, \quad n_{i,j} = \frac{f_{i,j}}{\sum_i f_{i,j}} n_{tot} \ , \tag{2.57}$$

$$\bar{Z}_{j+1} = \lambda \bar{Z}_j + (1-\lambda)\bar{Z}_j^* \ , \tag{2.58}$$

where n_{tot} is the total number of nuclei in all ionic stages, the internal and electron partition functions, $\mathcal{Q}$, take the forms given in Section 2.1.3 and Eq. 2.55 is the logarithm of the Saha equations. The ionic 'fractions', $f_{i,j}$, are constructed such that they have a maximal value of 1. This is to ensure stability over a large range of ion densities. Picard iteration (Eq. 2.58) updates the jth ionisation estimate where the damping, λ, is typically set at 90%. To initialise the iterative Saha solution, the average ionisation is estimated using a Thomas-Fermi[2] estimate [127, 150], i.e. $\bar{Z}_0 = \bar{Z}_{TF}$. The Saha loop is exited when $\bar{Z}_{j+1}$ and $\bar{Z}_j$ converge within tolerance.

Various IPD models exist and each uses different approximations to arrive at the shift in the continuum. A popular model developed by Stewart and Pyatt [164] retrieves the low coupling ($\Gamma = \frac{1}{3}\kappa_D^2 r_{ws}^2 \ll 1$, where $r_{ws} = (3/4\pi n_i)^{1/3}$) Debye limit and high coupling ion-sphere limit. This is done by ensuring continuity between the small and large radii limits of the Poisson equation. The Poisson equation solutions include the self-consistent spatial charge density distributions of ions and free electrons. The value of induced electrostatic potential at the origin is taken as the continuum shift, Δ. The

[2]In the Thomas-Fermi (TF) model, both the bound and free electrons are treated as a partially degenerate electron gas [192]. A self-consistent electron density and potential are calculated from Poisson's equation and the normalisation condition (number of electrons must equal ion charge). Approximate fits to the TF ionisation state have been performed, see More Table IV for details[127].

resulting Stewart-Pyatt model has a simple functional form:

$$\beta\Delta = \frac{\left[3(Z^*+1)\beta\Delta_D + 1\right]^{2/3} - 1}{2(Z^*+1)}, \quad \text{where:} \quad Z^* = \frac{1}{n_e}\sum_i Z_i^2 n_i \ , \tag{2.59}$$

$$\lim_{\Gamma\to 0}\Delta = \Delta_D = \frac{Ze^2}{4\pi\epsilon_0\lambda_D}, \quad \lim_{\Gamma\to\infty}\Delta = \Delta_{IS} = \frac{3}{2}\frac{Ze^2}{4\pi\epsilon_0 r_{IS}} \ , \tag{2.60}$$

where $\lambda_D \equiv 1/\kappa_D$ is the Debye length and $r_{IS} \equiv (3Z/4\pi n_e)^{1/3}$ is the ion-sphere radius. The Stewart-Pyatt IPD model has had some success [83] and some failure [36] in explaining experimental data. It is commonly used in opacity and atomic models, such as Prismspect and FLYCHK.

The pressure ionisation (PI) model used to calculate the reduced statistical weights, w_n, is based on the work of Mihalas, Hummer and Däppen [88, 89, 124]. The microfield distribution used is the Holtsmark distribution which uses the ideal gas approximation. The Holtsmark distribution is therefore correct in the $\Gamma \to 0$ limit – a derivation of the Holtsmark distribution is given in Appendix A.1.1. The Holtsmark distribution is used to find the cumulative probability of experiencing a field strength less than a critical field, F^c. This critical field is chosen such the bound state would be classically unbound i.e. the energy level lies at the saddle point as defined in Fig. 2.2.

$$w_n = \int_0^{\beta_n^c} P_H(\beta)d\beta, \quad \beta_n^c = k_n\frac{F_n^c}{F_0} \ , \tag{2.61}$$

$$F_n^c = \frac{\pi\epsilon_0 E_n^2}{Ze^3}, \quad F_0 = \frac{\bar{Z}e^2}{4\pi\epsilon_0 r_{ws}^2} = \frac{e^2 n_e}{4\pi\epsilon_0 n_i}\left(\frac{4\pi n_i}{3}\right)^{2/3} \ , \tag{2.62}$$

$$k_n = \begin{cases} 1 & \mathcal{N}_n \leq 3 \ , \\ \frac{16}{3}\left(\frac{\mathcal{N}_n}{\mathcal{N}_n+1}\right)^2\left(\mathcal{N}_n+\frac{7}{6}\right)\frac{1}{\mathcal{N}_n^2+\mathcal{N}_n+1/2} & \mathcal{N}_n > 3 \ , \end{cases} \tag{2.63}$$

where $P_H(\beta)$ is the Holtsmark microfields distribution function; F_n^c is the saddle point field for state n; k_n is the Stark ionisation factor which reduces the field required to ionise high lying states [88]; $\mathcal{N}_n$ is the principal quantum number of state n and F_0 is the field strength arising from an ion at the mean interionic separation. Numerical approximations to the Holtsmark cumulative distribution were taken from Poquérusse [143].

Including Stewart-Pyatt IPD and Holtsmark PI allows SpK to more accurately calculate thermodynamic conditions in dense plasmas. Repeating the calculation for the ionisation fraction of Hydrogen, free electrons can be obtained as the density is increased, see Fig. 2.4. We can also compare our calculation of opacity to other opacity codes at X-ray ablation relevant conditions – an example of Carbon at 1 g/cc and 100 eV is shown in Fig. 2.4. These model improvements have been used to calculate multigroup opacities to increase the accuracy of radiation hydrodynamics simulations.

While the inclusion of these two models has improved the accuracy of SpK, the models are derived within separate approximations. A more consistent approach would aim to calculate w_n and Δ from the same underlying model. This is a goal for future work on

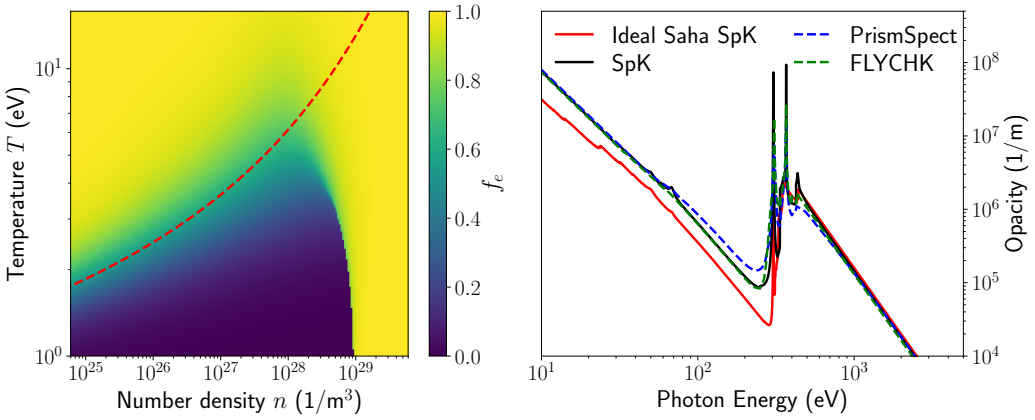

Figure 2.4: Two examples of improvements to SpK from IPD and PI models. (Left) The ionisation fraction in a hydrogen plasma as calculated by the Saha equation with non-ideal effects included. The red dashed line indicates where ideal Saha (Eq. 2.35) predicts $f_e = 0.5$. (Right) A comparison of the opacity of Carbon at 1 g/cc and 100 eV calculated by various codes.

developing SpK.

2.2 Nuclear Reaction Products

A multitude of nuclear reactions occur during an ICF implosion, the most notable of which are the fusion reactions. The products of these fusion reactions have energies orders of magnitude higher than the thermal energy of the fusing plasma. The products are either fast ions, neutrons or photons and each of these species undergo a different set of interactions after their creation. The primary fusion reactions that can occur in a fusing DT plasma are:

$$D + T \rightarrow \alpha\,(3.5\text{ MeV}) + n\,(14.1\text{ MeV}) \qquad \Gamma \sim 1\ , \tag{2.64a}$$

$$D + T \rightarrow {}^{5}\text{He} + \gamma\ (16.8 - 13.5\text{ MeV}) \qquad \Gamma \sim 4 \times 10^{-5}\ , \tag{2.64b}$$

$$D + D \rightarrow {}^{3}\text{He}\,(0.82\text{ MeV}) + n\,(2.45\text{ MeV}) \qquad \Gamma \sim 0.5\ , \tag{2.64c}$$

$$D + D \rightarrow T\,(1.01\text{ MeV}) + p\,(3.03\text{ MeV}) \qquad \Gamma \sim 0.5\ , \tag{2.64d}$$

$$T + T \rightarrow \alpha + 2n\,(+11.3\text{ MeV}) \qquad \Gamma \sim 1\ , \tag{2.64e}$$

the branching ratios, Γ, of the reactions are given on the right hand side of the above equations. The cross sections and thermal reactivities are shown in Fig. 2.5. As alluded to in the introduction, it is clear that the DT fusion reaction will be dominant with its reactivity being 2 orders of magnitude greater than the DD reaction. The energy spectra of neutrons created by these fusion reactions will be discussed in Section 2.2.1.

The fusion neutrons (also known as primary neutrons) can undergo subsequent nuclear interactions with nuclei in the background plasma. Listing those with the largest cross sections: elastic collisions with D,T and ablator materials (C,H,etc.); D(n,2n) and

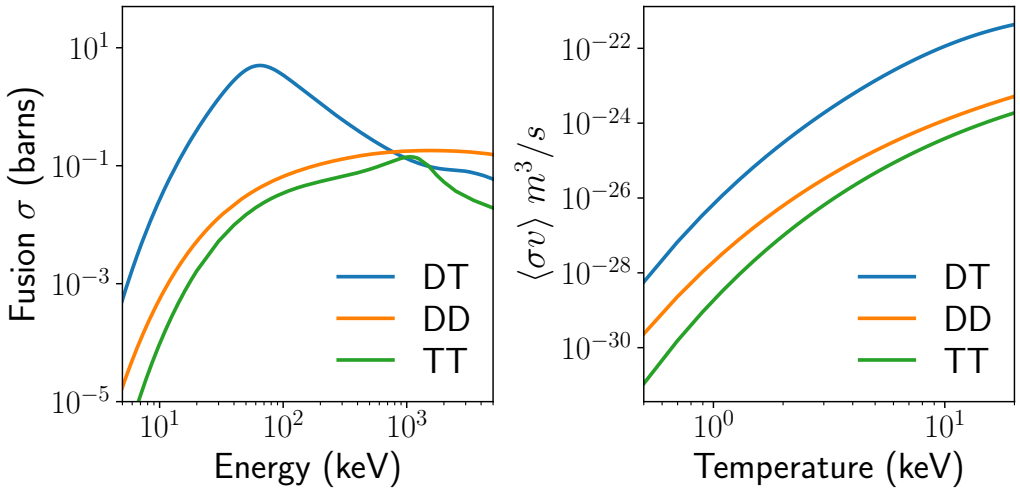

Figure 2.5: (Left) The fusion cross sections for selected reactions relevant to DT capsule fills. Cross sections are given in barns (1 barn = 10^{-28} m^2). Both DD reaction paths have been combined. The abscissa is the centre of mass energy of the collision. (Right) The corresponding thermal reactivities for experimentally relevant temperatures. Cross sections are taken from ENDF [33], Bosch-Hale reactivities are used for DT and DD [18] and the TT reactivity is calculated directly from the cross section data.

T(n,2n) reactions[3]; and inelastic scattering from C. The total cross section for neutrons interacting with H, D, T and ^{12}C as a function of incident neutron energy is shown in Fig. 2.6.

The total cross sections for neutrons at 14 MeV are of order 1 barn. Therefore, the primary DT neutrons have MFPs in 50/50 DT given by:

$$\frac{\lambda_n}{R} = \frac{1}{\sigma n_i R} = \frac{\bar{m}}{\sigma \rho R} \approx 4.2 \cdot \left(\frac{1 \text{ g/cm}^2}{\rho R} \right) . \tag{2.65}$$

Thus, for currently obtainable areal densities ($\rho R \lesssim 1$ g/cm^2) a large fraction of the primary neutrons can leave the stagnated capsule without collision. For those that collide, and therefore are lower in energy, subsequent collisions become more likely due to the increase in cross section at lower energy.

The charged particle products are presented with a Coulomb interaction cross section considerably larger than any nuclear interaction cross section. The Rutherford differential cross section is strongly peaked towards small angles:

$$\frac{d\sigma}{d\Omega} = \left(\frac{b_{90}}{1-\mu} \right)^2 , \; b_{90} = \frac{Z_1 Z_2}{8\pi\epsilon_0 K} , \tag{2.66}$$

where Z_1 and Z_2 are the charges of the colliding species, K is the kinetic energy of the

[3]No bound excited levels exist in D and T. Therefore, all inelastic interactions involve the break up of the nucleus with an energy threshold set by the binding energy. For the deuteron the triplet spin state is bound while the singlet spin state has a small positive energy – this leads to a resonance responsible for the large nH scattering cross section at low energies [13]

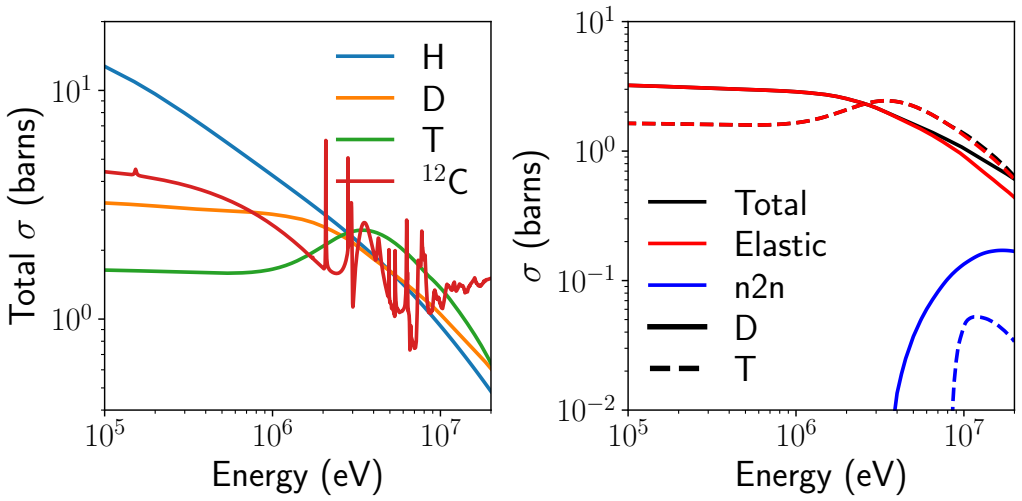

Figure 2.6: (Left) Total nuclear cross section for H, D, T and ^{12}C as a function of incident neutron energy. Cross sections values were found in the ENDF and CENDL data libraries [33, 64]. (Right) Breakdown of cross section for different reaction channels for neutron interactions with D and T. The lowest cross section reactions have been excluded from the plot, e.g. $D(n,\gamma)$ $\sigma \sim 10^{-6}$ barns.

projectile and μ is the scattering cosine.

The effect of Coulomb collisions on fast ions is well approximated by a Fokker-Planck collision operator, which will be described in detail in Section 2.2.2. However, large angle Coulomb and non-fusion nuclear collisions are still probable and these can produce additional fast ion populations. Fusion reactions can also occur between fast and background ions as the raised centre of mass energy drastically increases the cross section, see Fig. 2.5 and Eq. 1.1. Secondary fusion reactions occur when fast ions produced in a primary fusion reaction directly undergo an additional fusion reaction. For a DT plasma, the fast triton produced by the D(D,p)T reaction can undergo a T(D,n)α reaction producing a neutron in the 11.9-17.2 MeV range. Tertiary reactions, as the name suggests, involve the fusion reactions of fast ions indirectly produced by primary fusion reactions.

2.2.1 Neutron Transport

The multitude of nuclear reactions described in Section 2.2 create and modify the population of neutrons as they are born and traverse the capsule. The spatial variation, time evolution and energetic distribution of a population of neutrons within a background fluid is described by a transport equation derived from the Boltzmann equation (Eq. 2.1). The neutron transport equation is written in terms of the angular neutron flux, Ψ, which is related to the distribution, f, through a constant ($\Psi = kf$, $k = v/m_n$):

$$\frac{1}{v}\frac{\partial \Psi}{\partial t} + \hat{\Omega}\cdot\nabla\Psi = \frac{1}{v}\left(\frac{\partial \Psi}{\partial t}\right)_{col.} + \frac{1}{v}\left(\frac{\partial \Psi}{\partial t}\right)_{src.}, \tag{2.67}$$

where $\hat{\Omega} \equiv \vec{v}/v$ is the neutron direction of travel. The source term is due to fusion reactions in the background plasma. Primary reactions simply spawn neutrons independent of neutron flux. Secondary and tertiary sources are more complex but shall be placed into this term and expanded on in Section 2.2.2 on fast ion transport. All the neutron source terms will be combined into a single source term, S, which is a function of position, energy, direction and time:

$$\frac{1}{v}\left(\frac{\partial \Psi}{\partial t}\right)_{src.} = S(\vec{r}, E, \hat{\Omega}, t) \ . \tag{2.68}$$

The primary DT and DD fusion reactions are vitally important in diagnosing hotspot conditions in ICF experiments. Since they are highly exothermic $2 \rightarrow 2$ body reactions, the spectrum of neutrons is peaked close to the centre of mass neutron energy. This is due to the energy released in the reaction, $Q \sim$ MeV, being orders of magnitude larger than the pre-collision centre of mass energy, $K \sim$ keV. To illustrate the reaction kinematics from which the spectrum of fusion neutrons arises, we will consider the simple case of a homogeneous thermal fusing plasma. The velocity distribution of reacting ions are isothermal Maxwellian distributions. We introduce the reaction notation $1 + 2 \rightarrow 3 + 4$ to label particle properties (mass, energy, momenta). With particle 3 being the exiting neutron, we introduce the following standard kinematic properties [3]:

$$\vec{v}_{cm} = \frac{m_1\vec{v}_1 + m_2\vec{v}_2}{m_1 + m_2},\ \vec{v}_r = \vec{v}_1 - \vec{v}_2,\ K = \frac{1}{2}m_{12}v_r^2,\ \frac{1}{2}m_3u_3^2 = \frac{m_4}{m_3 + m_4}\left(Q + K\right) \ ,$$

then the neutron spectrum is given by the following expression:

$$dR_{12} = \frac{n_1 n_2}{1 + \delta_{12}} f_1(v_1) f_2(v_2) v_r \sigma(v_r) d^3v_1 d^3v_2 \ , \tag{2.69}$$

$$dR_{12} = \frac{n_1 n_2}{1 + \delta_{12}} N_{cm} \exp\left[-\frac{(m_1 + m_2)v_{cm}^2}{2T}\right] d^3v_{cm} N_K \exp\left[-\frac{K}{T}\right] K\sigma(K) dK \ , \tag{2.70}$$

$$R_{12}(v_3) = \frac{n_1 n_2}{1 + \delta_{12}} N_K \int_0^\infty \frac{dP_{cm}}{dv_3} K\sigma(K) \exp\left[-\frac{K}{T}\right] dK \ , \tag{2.71}$$

$$\langle \sigma v \rangle = N_K \int_0^\infty K\sigma(K) \exp\left[-\frac{K}{T}\right] dK \ , \tag{2.72}$$

$$\frac{dP_{cm}}{dv_3} = \sqrt{\frac{1}{\pi}}\sqrt{\frac{m_1 + m_2}{2T}}\frac{v_3}{u_3}\left(\exp\left[-\frac{(m_1 + m_2)}{2T}(v_3 - u_3)^2\right] - \exp\left[-\frac{(m_1 + m_2)}{2T}(v_3 + u_3)^2\right]\right), \text{ where: } \int_0^\infty \frac{dP_{cm}}{dv_3} dv_3 = 1 \ , \tag{2.73}$$

where N_i are the normalisations for the Maxwellians in i-space (e.g. $N_{cm} = \left(\frac{m_1+m_2}{2\pi T}\right)^{3/2}$) and m_{12} is the reactants' reduced mass. Equation 2.73 gives the normalised neutron production spectrum at a given K value – the second exponential function has negligible effect at physically relevant temperatures as it centred at $v_3 = -u_3$. The resultant total spectrum (Eq. 2.71) is then written as a reaction probability weighted sum over these production spectra. This is the natural variable separation since the reaction probability

($\propto n\sigma v_r$) only depends on K. Indeed the reactivity, as defined in Eq. 1.2, can be found via an integral over K, see Eq. 2.72. Figure 2.7 shows the resultant neutron production spectrum for the DT reaction at various K and T values.

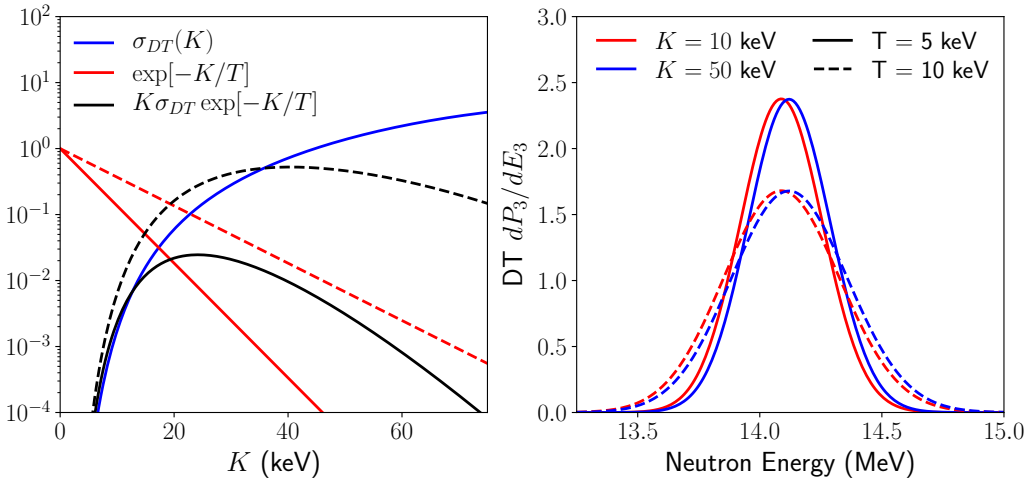

Figure 2.7: (Left) Plot showing the factors within the integrand for reactivity in Eq. 2.72 for the DT reaction. The Maxwellian and total reaction probability are plotted for two temperatures with 5 and 10 keV in solid and dashed lines respectively. The overlap of the Maxwellian and cross section creates the Gamow peak which shifts to higher K as the temperature increases. (Right) Plot showing the neutron production spectrum at two K values of 10 and 50 keV. The spectra are normalised and therefore do not take into account the increased reaction rate at higher K and T.

Here we have used classical mechanics for simplicity, however relativistically correct calculations have been performed in the literature which increase both the accuracy and complexity of the expressions [5, 132]. A DT fusion neutron moves at $\sim 0.17c$ and hence relativistic corrections are on the order of $\gamma - 1 \approx 1.5\%$. Many approximate evaluations of Eq. 2.71 have been performed, most notably the Brysk [23] and Ballabio [11] forms. These treatments involve taking moments of the neutron energy E_3 in terms of K and v_{cm} with Eq. 2.70. The moments are then used within Gaussian or modified Gaussian distributions to approximate the form of the neutron production spectrum.

While the above analysis is true for an isothermal stationary plasma, the fusing region in ICF experiments has a wide variety of hydrodynamic conditions which one must sum over. The moment approach allows the cumulants[4] of the total spectrum to be related to physical quantities of interest. A comprehensive relativistic analysis has been performed by Munro [132], the results of which are quoted here (in a unit system in which c = k

[4]The first 4 cumulants are the mean, variance, skew and kurtosis. These can be simply related to moments e.g. the variance of random variable X is given by $\langle X^2\rangle - \langle X\rangle^2$.

= 1 and the Einstein summation convention will be used):

$$w \equiv \frac{p - p_0}{E_0},\ \tau \equiv \frac{T}{m_1 + m_2},\ \kappa \equiv K \frac{dw_{cm}}{dK}\bigg|_{K=0} ,$$

$$\langle w \rangle = \langle \kappa \rangle + \langle \vec{u} \rangle_i \hat{\Omega}_i + ... \ , \tag{2.74}$$

$$\mathrm{Var}(w) = \langle \tau \rangle + \langle \mathrm{Var}(u) \rangle_{i,j} \hat{\Omega}_i \hat{\Omega}_j + ... \ , \tag{2.75}$$

$$\mathrm{Skew}(w)\,\mathrm{Var}(w)^{3/2} = 3\langle \mathrm{Cov}(\kappa, \vec{u}) \rangle_i \hat{\Omega}_i + \langle \mathrm{Cov}(\vec{u}, \vec{u}, \vec{u}) \rangle_{i,j,k} \hat{\Omega}_i \hat{\Omega}_j \hat{\Omega}_k + ... \ , \tag{2.76}$$

$$\mathrm{Kurt}(w)\,\mathrm{Var}(w)^2 = 3\,\langle \mathrm{Var}(\tau) \rangle + 6\langle \mathrm{Cov}(\tau, \vec{u}, \vec{u}) \rangle_{i,j} \hat{\Omega}_i \hat{\Omega}_j + ... \ , \tag{2.77}$$

where $\hat{\Omega}$ is the neutron emission direction, p is the lab frame neutron momentum magnitude, K is the total kinetic energy of the reactants in the centre of mass frame, and p_0 and E_0 are the neutron momentum and energy at $K = 0$. Higher order terms have been excluded for brevity. The angle brackets denote a burn average defined as follows:

$$\langle f \rangle = \frac{\int dT \int d^3u \ f(T, \vec{u}) N(T, \vec{u})}{\int dT \int d^3u \ N(T, \vec{u})} \ , \tag{2.78}$$

where $N(T, \vec{u})$ is the number of neutrons produced at temperature T and fluid velocity $\vec{u}$ summed over all positions and times.

While the derivation of the cumulants is complex, the results are physically intuitive. The mean neutron velocity at a detector along $\hat{\Omega}$ depends on the Doppler shift introduced by the fluid velocity and the kinetic energy of the reactants which must be passed onto the products. The average kinetic energy of reactants is set by the product of the cross section and the relative velocity distribution which exhibits a 'Gamow peak'. This peak arises as the cross section grows with energy, $\propto \exp(-\sqrt{E_g/K})$, but the relative velocity distribution decays, $\propto \exp(-K/T)$, see Fig. 2.7. Increasing the reactant kinetic energy K causes a shift of the neutron spectrum to higher energy. The centroid of the Gamow peak then sets $\langle \kappa \rangle$, which is named the 'Gamow shift'. The variance in the neutron velocity is due to Doppler broadening. Therefore, the variance depends on the range of centre of mass velocities due to both temperature and fluid velocity variance. The higher order cumulants depend on covariances between shift or broadening inducing mechanisms. As an illustrative example, if we consider a fusing plasma with two regions of different temperature then the combination of different width spectra will create wings therefore increasing the kurtosis. Finally the projection onto the detector LoS gives rise to LoS variation in neutron spectral cumulants. This is due to fluid velocity introducing anisotropy in the lab frame neutron spectra. There are various 'orders' at which this can occur depending on the power of fluid velocity which appears. At zeroth order are the isotropic components (e.g. $\langle \kappa \rangle$ and $\langle \tau \rangle$) which have no anisotropy. At first order are the vector components (e.g. $\langle \vec{u} \rangle$) which are proportional to the cosine between fluid velocity and detector, $\cos \zeta = \langle \hat{u} \rangle \cdot \hat{\Omega}$. At second order are the matrix components (e.g. $\langle \mathrm{Var}(u) \rangle$) which have ellipsoidal angular dependence. The eigenvectors of the matrix give the 3 principal axes and the eigenvalues give the value of the matrix component along the principal axes. Finally increasingly higher order components have

more complex angular dependences.

Experimental primary neutron spectroscopic measurements have concentrated on extracting burn-averaged quantities from the first two cumulants. For the mean, four neutron spectrometers are required to constrain the vector and isotropic components therefore allowing the burn-averaged fluid velocity and Gamow shift to be measured [75, 116]. Measurements at both NIF and OMEGA show non-zero burn-averaged fluid velocity, commonly called hotspot velocity, which indicates the presence of a low odd-mode drive asymmetry. For the variance, six neutron spectrometers are required to constrain the matrix and isotropic components [188]. The variance is often called the inferred ion temperature due to early treatments neglecting fluid velocity e.g. Brysk [23]. However the six spectral measurements do not enable separation of the temperature and fluid velocity variance effects. The smallest eigenvalue of the variance matrix is the linear combination of the temperature and isotropic fluid velocity variance. This is used as an upper bound on the burn-averaged ion temperature, $\langle\tau\rangle$. The difference between the largest and smallest eigenvalues gives the maximal inferred ion temperature asymmetry, often labelled ΔT_{ion}. A large ΔT_{ion} indicates high RKE in anisotropic flows typically attributed to low mode drive asymmetries [62]. Non-zero skew and kurtosis have been observed however analysis has been limited due their complex dependencies on physical parameters [131].

Exact numerical calculations of the relativistically correct version of Eq. 2.71 were performed by Appelbe by using tabulated data for the cross section [3, 5]. The sum over all hydrodynamic conditions can then retrieve the true neutron spectrum. This cannot be extracted from the cumulants alone as they do not constrain the functional form of the underlying distribution.

Collisions of neutrons with ions of species i, be they elastic or inelastic, are described by their appropriate double differential cross sections:

$$\left(\frac{\partial\Psi}{\partial t}\right)_{col.} = \sum_i \left[-n_i\sigma_i\Psi + n_i\int d\hat{\Omega}'\int dE'\frac{d^2\sigma_i}{d\Omega dE}\Psi(\vec{r},E',\hat{\Omega}',t)\right] \tag{2.79}$$

For elastic or inelastic scattering which preserve particle number, the double differential cross section can be reduced to a single differential cross section through conservation laws. We will consider a general $2 \rightarrow 2$ body interaction for species $i + j \rightarrow k + l$ with energy Q is released. The momenta of the products must be equal and opposite in the centre of mass (CoM) frame. Therefore the energy of the products is independent of angle in the CoM frame. Any frame transformation introduces a 1-to-1 angular dependence to the outgoing energy, simply due to the vector addition of velocities. This allows the double differential cross section (or scattering kernel) to be simplified to [169]:

$$\frac{d^2\sigma_i}{d\Omega dE} = \frac{1}{2\pi}\frac{d\sigma_i}{d\mu_c}\left|\frac{\partial\mu_c}{\partial E_k}\right|\delta(\mu_0-\mu_0^*),\ \text{where: } \mu_0 \equiv \hat{\Omega}_i\cdot\hat{\Omega}_k\ . \tag{2.80}$$

Here we have used the azimuthal symmetry of the CoM differential cross section to pull

out a factor of 2π. Subscript c is used to denote CoM quantities. For example, the lab frame scattering cosine is denoted μ_0 while the CoM frame scattering cosine is denoted μ_c. We have defined a number of kinematic parameters of interest; the energies of i and k (E_i and E_k), the scattering cosine between i and k which satisfies conservation laws (μ_0^*), and the Jacobian relating the CoM and lab frames ($g = |\partial\mu_c/\partial E_k|$).

We will work initially in the beam target frame, where species i will be the projectile, species j is the stationary target and species k is the exiting species of interest. Kinematic variables can all be written in terms of two parameters a and b:

$$a^2 \equiv \frac{m_{lk}m_{ij}}{m_k m_i}\left(1+\frac{Q}{E^*}\right), \qquad a^2 = \frac{E_{k,c}}{E_i}\ , \tag{2.81}$$

$$b^2 \equiv \frac{m_{ij}^2 m_k}{m_j^2 m_i}, \qquad b^2 = \frac{\frac{1}{2}m_k v_{cm}^2}{E_i}\ , \tag{2.82}$$

$$\text{where: } E^* = \frac{m_{ij}}{m_i}E_i = E_{i,c} + E_{j,c} \text{ and } m_{ij} = \frac{m_i m_j}{m_i + m_j}\ . \tag{2.83}$$

The right hand expressions give physical interpretations to a and b: a^2 gives the ratio of the CoM outgoing energy and the incoming energy, b^2 gives the ratio of the energy in the CoM motion of species k to the incoming energy. E^* is the same as K used in the primary spectrum analysis but we will follow the scattering literature here and use E^*.

From energy and momentum conservation laws, the kinematic parameters can be related to a and b as follows (see Appendix A.2.1):

$$E_k = (a^2 + b^2 + 2ab\mu_c)E_i\ , \tag{2.84}$$

$$\mu_0^* = \frac{1}{2b}\left[\sqrt{\frac{E_k}{E_i}} - (a^2 - b^2)\sqrt{\frac{E_i}{E_k}}\right]\ , \tag{2.85}$$

$$g(E_i) = \frac{2}{\left((a+b)^2 - (a-b)^2\right)E_i} = \frac{2}{E_{k,\max} - E_{k,\min}}\ . \tag{2.86}$$

For a uniform differential cross section, an incoming monoenergetic beam will be scattered into a uniform energy distribution between $E_{k,\max}$ and $E_{k,\min}$. For example, if we consider elastic neutron scattering from an ion with mass $m_j = Am_n$ then:

$$a = \frac{A}{A+1},\ b = \frac{1}{A+1}\ , \tag{2.87}$$

$$\therefore E_{k,\max} = E_i,\ E_{k,\min} = \left(\frac{A-1}{A+1}\right)^2 E_i = \alpha E_i\ . \tag{2.88}$$

The lower kinematic endpoint forms what is known as the *backscatter edge*, which will be the subject of Section 3.1. Another example to consider is the beam target DT fusion reaction (Q = 17.6 MeV) which describes the secondary fusion reaction of the fast triton

from the primary D(D,p)T reaction:

$$a^2 = \frac{8}{25}\left(1 + \frac{5}{2}\frac{Q}{E_i}\right), \; b^2 = \frac{3}{25} \; . \tag{2.89}$$

$$\text{For } E_i = 1.01 \text{ MeV} \rightarrow E_{k,\max} = 17.2 \text{ MeV}, \; E_{k,\min} = 11.9 \text{ MeV} \; , \tag{2.90}$$

this process, amongst others, produces a high energy neutron spectrum which will be the subject of Section 3.3.

To match the scattering kinematics notation with that of the neutron transport literature [12, 130, 167, 168]: the neutron energies are given no subscript, all masses are written as multiple of the neutron mass, primes denote pre-collision quantities and unprimed denote post-collision quantities.

The differential cross section contains the nuclear physics of scattering which is a complex problem and the complete description is beyond the scope of this work. For context, the basics of the quantum-mechanical scattering problem is outlined in Appendix A.3. The cross sections used in this work were taken from the ENDF [33] and CENDL [64] nuclear databases. In Fig. 2.8 we show the differential cross sections for the elastic scattering reactions nD and nT at a neutron energy of 14 MeV.

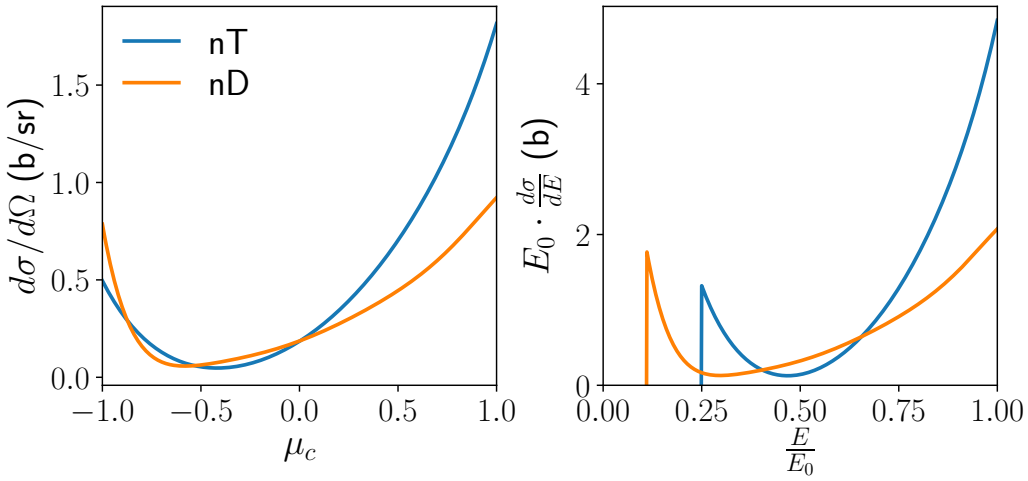

Figure 2.8: (Left) The differential cross section of elastic scattering of a 14 MeV neutron from D and T in the CoM frame as a function of scattering cosine. (Right) The differential cross section in the beam-target frame as a function of normalised energy, $E_0 = 14$ MeV. Note the backscatter edges at 1/9 and 1/4 of E_0 for D and T respectively.

In ICF the bulk ions off which the neutrons are scattering are not stationary due to thermal and non-thermal motion. While the velocities of these ions are generally much smaller than the neutrons, there is a non-negligible effect. We will consider the elastic scattering of neutrons from ions of mass Am_n. The scattering kernel must be modified in order to account for the ion motion and integrated over the distribution of ion velocities. The differential cross section can be assumed constant within the integration range due the large velocity difference between neutron and ion. Within this approximation, the

beam-target scattering kernel for a Maxwellian distribution of ion velocities is given by [12, 138]:

$$\frac{d^2\sigma}{d\Omega dE} \approx \frac{1}{2\pi}\frac{d\sigma}{d\mu_c}\left|\frac{\partial\mu_c}{\partial E}\right| D(\mu_0, E, E') \ , \tag{2.91}$$

$$D(\mu_0, E, E') = \frac{2\sqrt{EE'}}{A}\sqrt{\frac{1}{4\pi T\kappa^2}}\exp\left[-\frac{1}{4T\kappa^2}\left(\epsilon-\kappa^2\right)^2\right] \ , \tag{2.92}$$

$$\lim_{T\to 0} D(\mu_0, E, E') = \delta\left(\mu_0 - \mu_0^*\right) \ , \tag{2.93}$$

$$\epsilon \equiv E' - E, \ \kappa^2 \equiv \frac{1}{A}\left(E' + E - 2\mu_0\sqrt{EE'}\right) \ . \tag{2.94}$$

The thermal velocity distribution causes the energy-angle relationship to no longer be 1-to-1 as shown by Eq. 2.92 and Fig. 2.9. For the purpose of calculating the differential cross section the CoM frame scattering cosine, μ_c, is approximated here as the T = 0 result.

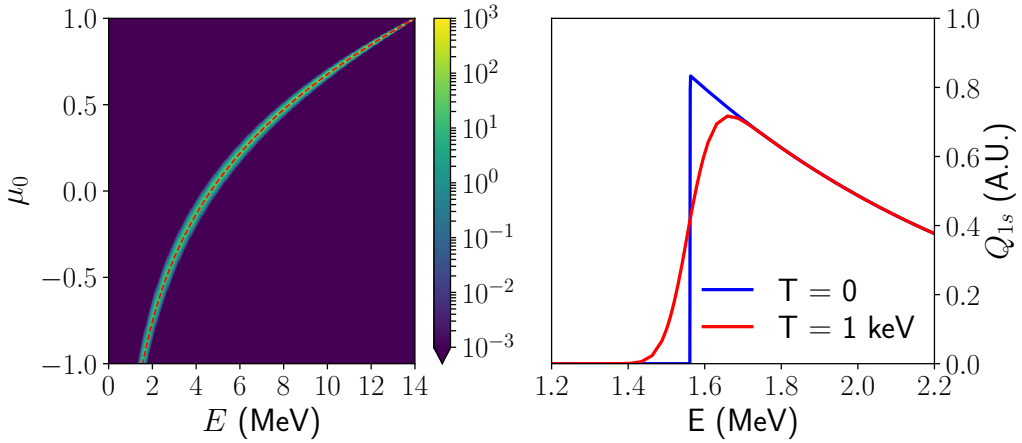

Figure 2.9: (Left) The scattering cosine energy relation for scattering of 14 MeV neutrons from thermal D ions at 1 keV. The red dashed line indicates the T = 0 relation, note the log scale of the plot. The colour scale gives the value of D as given by Eq. 2.92 for $E' = 14$ MeV. (Right) The resultant single scattered spectrum from an isotropic source around the backscatter edge. At energies E > 2.2 MeV the T = 0 and T = 1 keV results remain the same following the form shown in Fig. 2.8.

To include the bulk non-thermal motion, i.e. fluid velocity, of the scatterers we must transform our kinematic parameters from the beam target frame to the lab frame. The classical and relativistic treatment of this frame transformation are given in Appendices A.2.2 and A.2.3. Differential cross sections of the form given in Eq. 2.80 are unchanged in form but the lab frame Jacobian and quantities must be used. We will consider the classical limit first and the elastic scattering of a neutron from cold (T = 0) ions of mass Am_n and pre-collision energy E_i'. Using results derived in the appendix,

the scattering kernel is given by:

$$\frac{d^2\sigma}{d\Omega dE} = \frac{1}{2\pi}\frac{d\sigma}{d\mu_c}\frac{2}{1-\alpha}\frac{\left(1-\sqrt{\frac{E_i'}{AE}}\mu\right)}{\left(E' - 2\sqrt{\frac{E'E_i'}{A}}\mu' + \frac{E_i'}{A}\right)}\delta(\mu_0 - \mu_0^*) \ , \tag{2.95}$$

$$\mu_0^* = \frac{1}{2}\left[(A+1)\sqrt{\frac{E}{E'}} - (A-1)\sqrt{\frac{E'}{E}}\right] + \sqrt{\frac{AE_i'}{E}}\mu' - \sqrt{\frac{AE_i'}{E'}}\mu \ , \tag{2.96}$$

where μ' and μ are the cosines between the incoming neutron and the initial ion trajectory, and between the outgoing neutron and the initial ion trajectory respectively. This transformation introduces kinematic beaming as well as changing the kinematic end points. Forward scatter, $\mu_0 = 1$, still gives equal incoming and outgoing energies, $E = E'$. However, backscatter, $\mu_0 = -1$, now gives:

$$E = \left(\frac{A-1}{A+1} - \frac{2}{A+1}\sqrt{\frac{AE_i'}{E'}}\mu'\right)^2 E' \ , \tag{2.97}$$

contrasting with the beam-target results given in Eq. 2.88. The scattering cosine also now explicitly depends on neutron direction. Therefore in the lab frame the energy-angle relation is more complex and knowledge of only the neutron properties is insufficient in determining the scattering angle.

The relativistic corrections to scattering kinematics are small, this will be illustrated by considering the head-on collision between a neutron and ion for which:

$$\beta_{cm} = \frac{\gamma' m_n \beta' - m_i \beta_i'}{\gamma' m_n + m_i}, \quad \beta = \frac{\beta'(1+\beta_{cm}^2) - 2\beta_{cm}}{1 - 2\beta_{cm}\beta' + \beta_{cm}^2}, \quad K = (\gamma - 1)m_n \ . \tag{2.98}$$

The ion will be part of the bulk thermal plasma and hence $\beta_i' = v_i'/c \ll 1$. Figure 2.10 shows a comparison of relativistic and classic results for an initial neutron kinetic energy of 14 MeV. Also shown is how ion velocities alters the arrival time of backscattered neutrons, which is relevant for the resolution of nToF detectors.

Classical expressions are used in the neutron transport calculations by the codes Minotaur and AKED, see Sections 2.2.3 and 2.2.4. The relativistic kinematic corrections are included when constructing models for experimental data in Section 3.1.

There are some nuclear interactions which occur with greater than two products and thus exhibit more complex energy spectra. This is due to many distinct product distributions satisfying energy-momentum conservation compared to the single solution for the $2 \rightarrow 2$ body reactions. The final state is now dependent on the details of the interaction at a nuclear level which are generally complex. For the TT fusion reaction there are multiple possible reaction channels which contribute characteristic shapes to

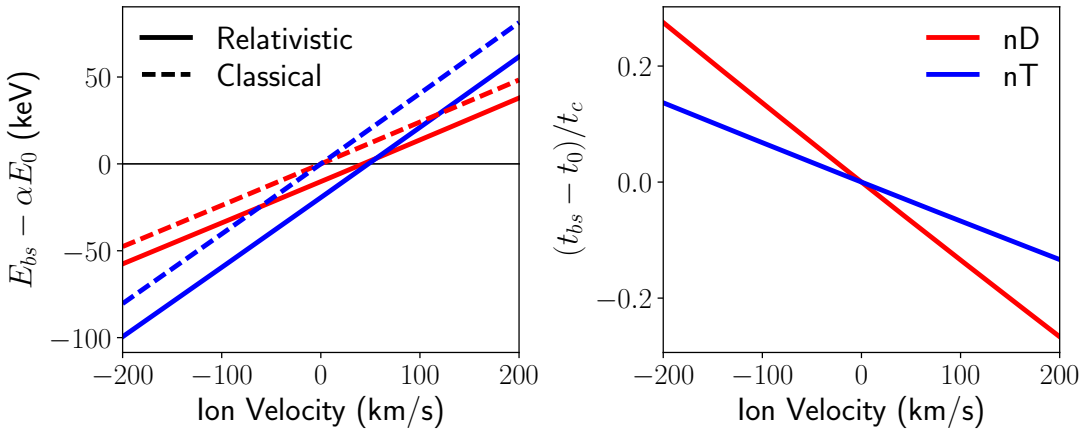

Figure 2.10: (Left) The energy shift of the backscatter edge relative to the classical beam-target result. Relativistic corrections introduce an offset of a few tens of keV without modifying the gradient significantly. (Right) The arrival time shift as a fraction of the light transit time to the nToF spectrometer. It can be seen that for a fixed time resolution that the nD edge has the potential to give a more sensitive measurement of ion velocities.

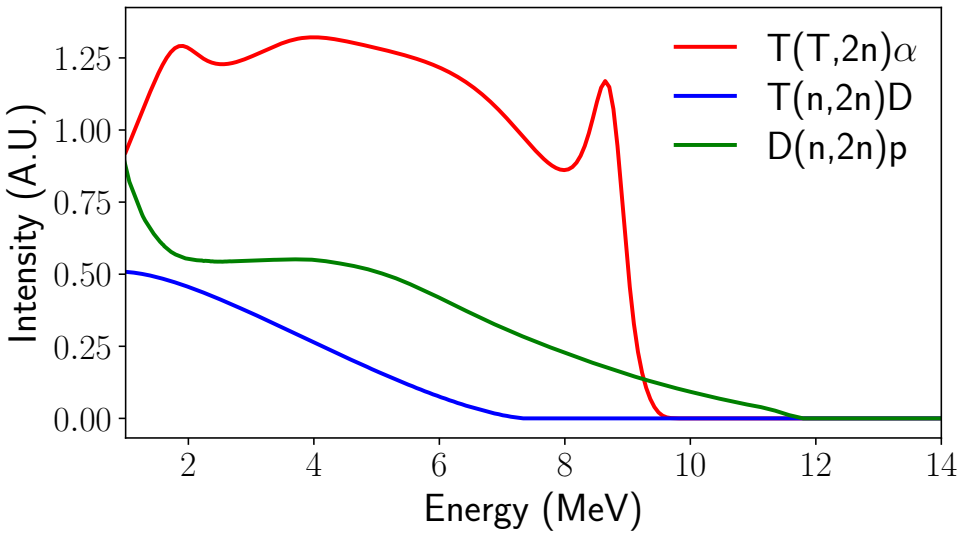

Figure 2.11: Examples of neutron spectra from the 3-product reactions present in ICF experiments. Each has been separately normalised for ease of plotting. The (n,2n) reactions are evaluated at an incident neutron energy of 14 MeV and integrated over all outgoing directions. The TT spectrum was evaluated at a temperature of 5 keV using the method developed by Appelbe [6].

the total neutron spectrum [22, 27, 96]:

$$T + T \rightarrow \alpha + 2n, \qquad Q = 11.3 \text{ MeV} , \tag{2.99}$$

$$T + T \rightarrow {}^{5}\text{He} + n, \qquad Q = 10.4 \text{ MeV} , \tag{2.100}$$

$$T + T \rightarrow {}^{5}\text{He}^{*} + n, \qquad Q = 9.2 \text{ MeV} . \tag{2.101}$$

The (n,2n) reactions pose a similar problem and differential cross sections are dependent on the nuclear physics models used. The three-body D(n,2n) reaction requires an understanding of the three-nucleon force [52] which is not well characterised. Here we will simply present the spectral shapes which are the current best estimates in Fig. 2.11.

2.2.2 Fast Ion Transport

In contrast to the bulk ions which exist in thermal equilibrium, fast ions' long mean free path requires a non-local transport description. In a similar fashion to photons and neutrons, the fast ion transport equation is derived from the Boltzmann equation (Eq. 2.1). However the external force term is non-zero due to the effect of electric and magnetic fields on the charged ion:

$$\frac{\partial f}{\partial t} + \vec{v} \cdot \nabla f + \frac{Ze}{m}\left(\vec{E} + \vec{v} \times \vec{B}\right) \cdot \nabla_v f = \left(\frac{\partial f}{\partial t}\right)_{col.} + \left(\frac{\partial f}{\partial t}\right)_{src.} . \tag{2.102}$$

The source term is due to both fusion reactions and ions knocked on by other fast species. Bulk ions can also be accelerated by electric fields into the long mean free path regime. However, this is uncommon in ICF plasmas as they are very collisional. Ion knock on sources will include a differential cross section term for a collision of species i which forms our fast ion species of interest j:

$$\left(\frac{\partial f}{\partial t}\right)_{src.} = S(\vec{r}, v, \hat{\Omega}, t) + \sum_i n_i \int d\hat{\Omega}' \int dv' \frac{d^2\sigma_{i\rightarrow j}}{d\Omega dv} v' f_i(\vec{r}, v', \hat{\Omega}', t) . \tag{2.103}$$

The primary source term, S, can be calculated in a similar way as the primary neutron source term. For a 2→2 body thermonuclear reaction, Eq. 2.71 can be used for the fast ion product.

The collision term for charged particles is problematic due to the divergence of the Coulomb potential. Classical descriptions of binary collisions of bare charges must invoke a cut off – an approach commonly invoked in high energy physics to remove divergences that exist at scales not well described by the current theory. However the idea that collisions are binary does not marry well with the concept of screening in plasmas. This can be remedied through calculating the potential of mean force which gives an effective binary potential. For a Debye plasma, the effective potential is the Debye potential which removes the long range divergence. A quantum mechanical treatment is required to describe the short scales and remove the short range divergence. These complex behaviours are hidden away in a function know as the Coulomb logarithm, $\ln \Lambda$,

which appeared briefly in Section 2.1. We can now precede with a binary collision treatment with a Coulomb logarithm attached. Inspecting the Rutherford differential cross section in Eq. 2.66, we note that small angle scattering events are much more likely than large angle ones. This allows the collision operator to be written in a Fokker-Planck form – the derivation is complex and only the results will be quoted[5]. The final simplification is to consider the collisions of fast species a with a Maxwellian population of species b [80]:

$$x_i^2 \equiv \frac{m_i v^2}{2T_i}, \quad \nu_{ab} \equiv \frac{n_b Z_a^2 Z_b^2 e^4}{4\pi\epsilon_0^2 m_a^2 v^3} \ln\Lambda \ ,$$

$$G(x) \equiv \frac{\mathrm{erf}(x) - \frac{2}{\sqrt{\pi}} x e^{-x^2}}{2x^2}, \ H(x) \equiv \mathrm{erf}(x) - G(x), \ \mathrm{erf}(x) \equiv \frac{2}{\sqrt{\pi}} \int_0^x \exp\left[-y^2\right] dy \ ,$$

$$\left(\frac{\partial f}{\partial t}\right)_{col.,ab}^{FP} = \mathcal{L}_{ab}^d(f_a) + \mathcal{L}_{ab}^s(f_a) + \mathcal{L}_{ab}^p(f_a) \ , \tag{2.104}$$

$$\mathcal{L}_{ab}^d(f_a) = \nu_{ab}^d \frac{1}{2} \frac{\partial}{\partial \mu} \left(1 - \mu^2\right) \frac{\partial f_a}{\partial \mu} \ , \tag{2.105}$$

$$\mathcal{L}_{ab}^s(f_a) = \frac{m_a}{m_a + m_b} \cdot \frac{1}{v^2} \frac{\partial}{\partial v} \left[\nu_{ab}^s v^3 f_a\right] \ , \tag{2.106}$$

$$\mathcal{L}_{ab}^p(f_a) = \frac{1}{2} \cdot \frac{1}{v^2} \frac{\partial}{\partial v} \left[\nu_{ab}^p v^4 \frac{\partial f_a}{\partial v}\right] \ , \tag{2.107}$$

$$\nu_{ab}^d = \nu_{ab} \cdot H(x_b) \ , \tag{2.108}$$

$$\nu_{ab}^s = 2x_b^2 \left(1 + \frac{m_a}{m_b}\right) \cdot \nu_{ab} G(x_b) = 2x_b^2 \nu_{ab}^* G(x_b) \ , \tag{2.109}$$

$$\nu_{ab}^p = 2\nu_{ab} \cdot G(x_b) \ . \tag{2.110}$$

This complex set of equations and definitions describe three collisional processes: angular deflection, slowing down and parallel velocity diffusion, with collision frequencies ν_{ab}^d, ν_{ab}^s and ν_{ab}^p respectively. Angular deflection acts to bring about isotropy in the velocity distribution. Slowing down reduces the speed of particles without altering their direction like a viscous drag. Parallel velocity diffusion acts to increase the variance of speeds. All these processes are a result of many successive small angle Coulomb collisions in which momentum and energy are exchanged between species. As we are interested in describing suprathermal ionic species, we must consider the behaviour of the collision frequencies at high velocities. The relative importance of the different processes is shown as a function of $x_b (= v/v_{Tb})$ in Fig. 2.12. For reference a 1.0 MeV primary triton initially has a $x_e = 0.43\sqrt{1 \text{ keV}/T_e}$ and for thermal ions $x_i \sim 43 x_e \sqrt{m_i/m_p}$.

Slowing by electrons dominates the initial behaviour of fast ion species due to the large mass difference causing $\nu_{ae}^* \gg \nu_{ae}$. Once the fast ions have slowed sufficiently to increase the collision frequency, the thermal ions can very effectively slow and thermalise any fast ion species. The slowing therefore sets the range that fast ions can travel – this was briefly discussed in the introduction with respect to alpha heating within the

[5]The interested reader should consult Helander and Sigmar [80] – the formulae in this textbook are even in SI units as an added bonus

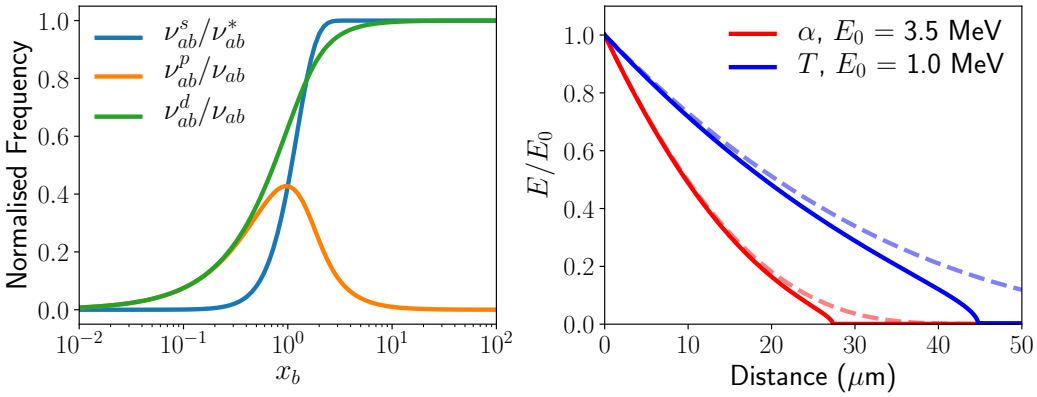

Figure 2.12: (Left) Normalised collisional frequencies as a function of the ratio of fast ion velocity to thermal velocity. Note the different normalisation for slowing down which factors out the target mass dependence. At high x_b parallel velocity diffusion can be ignored but both angular deflection and slowing down are important. However if the beam species is much more massive than the thermal species ($m_a \gg m_b$) then $\nu^*_{ab} \gg \nu_{ab}$. In this limit slowing down dominates. (Right) The effect of slowing on two common fast ion species, the alphas and tritons made in fusion reactions. A background 50/50 DT plasma at 3.0 keV and 10^{31} m^{-3} is considered. Dashed lines show slowing if only thermal electrons are considered. The Coulomb logarithm from the work of Antal and Lee was used [2].

hotspot, see Fig. 1.2. In this work, we are more concerned with the nuclear reactions which can occur in-flight. If we consider a fast D or T ion, the cross section for the DT fusion reaction peaks at ~ 0.1 MeV, as shown in Fig. 2.5. Generally, fast ions are created at energies of a few MeV and slowing down reduces their energy as they travel. This acts to increase the reaction cross section and the number of in-flight fusion reactions. Therefore, accurate modelling of fast ions and their nuclear interactions requires a good description of Coulomb collisional processes.

A significant difference between neutron and fast ion transport is the effect of electromagnetic fields. Large scale electric fields are rare in plasmas as the charges can easily move to eliminate the field. Magnetic fields are a much more common consideration and they can have a significant effect on fast ion transport. The Larmor orbits created by magnetic fields have radius and angular period given by:

$$r_L = \frac{mv_\perp}{ZeB} \tag{2.111}$$

$$\tau_L = \frac{r_L}{v_\perp} = \frac{m}{ZeB}\ , \tag{2.112}$$

where $v_\perp$ is the ion velocity perpendicular to the magnetic field B. For low B, smaller spatial and time scales will dominate and the magnetic field will have little effect. For high B, the fast particles will be confined to small, rapid Larmor orbits and their behaviour has effectively collapsed down to a single dimension along the field line. However, all realistic applications of magnetic field effects in ICF will sit in an intermediate regime. Additionally the hotspot radius, stopping distance and Larmor radius may be

of similar order causing difficulty for analytic techniques and leading to sensitivity to many parameters. Simulation of fast ion trajectories including the Lorentz force are therefore necessary. The trajectories of fast D(D,p)T tritons in various magnetic field strengths is shown in Fig. 2.13.

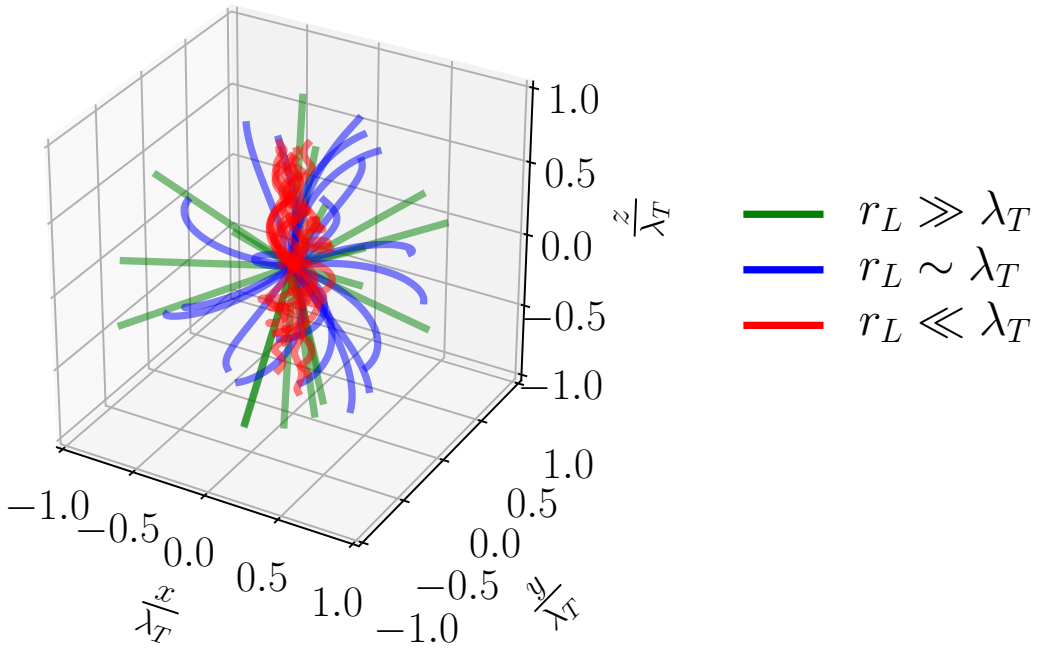

Figure 2.13: The particle trajectories of 1 MeV tritons from a point source with various magnetic field strengths applied along the z-axis. The spatial scale has been normalised by the triton stopping distance, λ_T. The triton behaviour transitions from free streaming through to confinement to the field lines. If the reactive volume is smaller than the stopping distance then one can replace λ_T with the source radius R.

The fusion reactions which occur in-flight are beam-target and therefore the spectra differ from the thermonuclear primary spectra discussed in Section 2.2.1. Instead the differential cross section and kinematic limits must be used (kinematic limits for T(D,n)α are given in Eqs. 2.89 and 2.90). The spectral shape is dependent on the fast ion flux, energy and angular distribution as well as the target ion density distribution. Figure 2.14 shows the beam-target DT spectra for various beam energy spectra produced by different physical processes. Fast tritons can be produced in D(D,p)T, nT scattering and large-angle Coulomb collisions of fusion alphas. Fast deuterons do not have a fusion source and are only created in knock-on events. The complex interplay of slowing, Larmor orbits, finite source volumes and spatial distributions make secondary and tertiary neutron spectra an interesting simulation challenge.

In this work we are focussed on the nuclear diagnostic signatures so the normally pivotal role of alpha transport in ICF will take a backstage part. Instead the focus will be on fast deuterons and tritons and their subsequent nuclear reactions. These species do not contain enough energy density to affect the hydrodynamics significantly

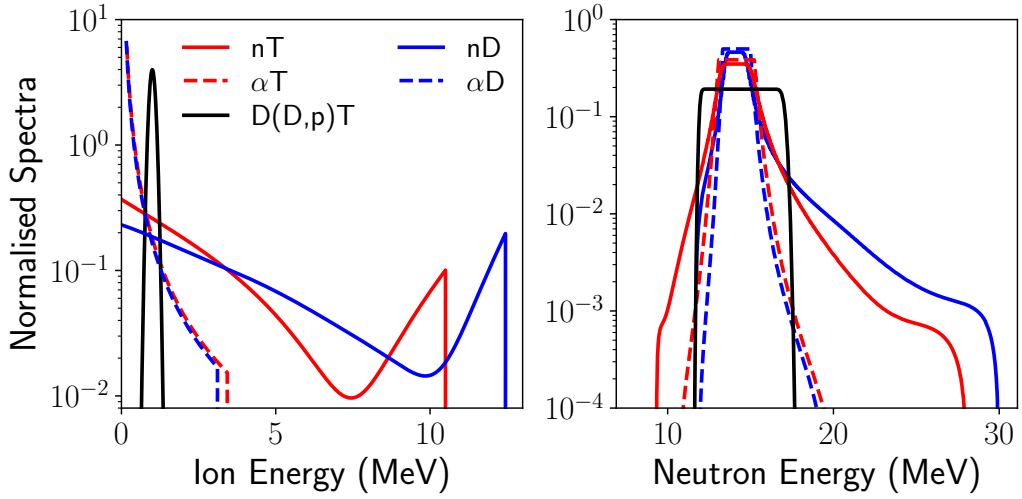

Figure 2.14: (Left) Fast ion energy spectra created by fusion reactions and the elastic collisions of neutron and alphas. For the alpha knock-on ions only the Coulomb cross section was considered (scattering angles less than 26 degrees were excluded). (Right) The resultant DT beam-target neutron spectrum assuming isotropic ion flux and differential cross section – the absolute DT reaction cross section has been included, cf. Fig. 2.5. All spectra have been normalised to have unit area for ease of comparison.

so calculation of their behaviour can be performed as a post-process. Two numerical codes have been developed to perform fast ion transport in a different number of spatial dimensions. Minotaur performs 1D spherical transport and therefore does not include magnetic field effects. AKED works in 3D and therefore will be used when magnetic fields are present.

2.2.3 Minotaur

Neutron transport including all relevant nuclear processes is an intensive numerical calculation requiring discretisation of Eq. 2.67 in position and velocity space. Invoking spherical symmetry allows multiple interaction types to be retained without restrictive calculation time. Additionally, the plasma fluid velocity is small compared to fusion neutron velocities (14 MeV neutron moves at 51,000 km/s compared to $\lesssim$ 500 km/s fluid velocities) so the transport can be assumed time independent. This approximation is on firm ground for the unscattered primary DT neutrons, which leave the capsule in $\sim$ 1 ps. However, this approximation is less valid for slow neutrons which have undergone multiple scattering. Therefore, a lower bound of 1 MeV on the neutron kinetic energy is considered. Written in its conservative form, the 1D spherical neutron transport equation is given by:

$$\left[\frac{\mu}{r^2}\frac{\partial}{\partial r}r^2 + \frac{1}{r}\frac{\partial}{\partial \mu}(1-\mu^2) + n(r)\sigma(E)\right]\Psi(r,\mu,E) = S_{ext.}(r,\mu,E) + S_{scat.}(r,\mu,E)\ , \tag{2.113}$$

where μ is the direction cosine of the neutron and r is the radius.

There are many methods for solving this equation including Legendre polynomial expansion of the angular coordinate (named P_N), discretising the angular coordinate (named discrete ordinates or S_N [6]) or stochastic Monte Carlo methods. There are merits to each method, however the anisotropic differential cross sections relevant to the problem do not favour the Legendre polynomial expansion [169]. The deterministic discrete ordinates method was opted for over the stochastic method commonly used for neutron transport in ICF plasmas [186, 189]. As the code was developed to look at diagnostic signatures in the neutron spectrum, the statistical noise introduced in a Monte Carlo solution is undesirable especially when looking at low probability events. However deterministic methods do have insidious numerical errors which must be investigated through convergence studies.

With this considered, the author developed a spherical 1D discrete ordinates multigroup neutron transport code, Minotaur. This involves discretisation of the neutron distribution over radius (index i), direction cosine (index n) and energy (index g).

First a choice must be made on how to discretise in the angular domain, $-1 \leq \mu \leq 1$. Legendre-Gaussian quadrature splits the domain into a set of nodes, μ_n, with weights, w_n, which allow integrals to be approximated as follows:

$$\int_{-1}^{1} \Psi(\mu) d\mu \approx \sum_{n=1}^{N} w_n \Psi(\mu_n), \tag{2.114}$$

$$\sum_{n=1}^{N} w_n = 2 \ . \tag{2.115}$$

If $\Psi(\mu)$ is a polynomial of degree $2N-1$, or less, then N-point Legendre-Gaussian quadrature returns the exact result of the integral. The half points are then defined through the weights with the appropriate end points:

$$\mu_{n+1/2} = \mu_{n-1/2} + w_n, \ \mu_{1/2} = -1, \ \mu_{N+1/2} = +1 \ . \tag{2.116}$$

Generally even N is chosen to avoid solving along $\mu = 0$ where the spatial derivative in Eq. 2.113 vanishes. Normal finite differencing of the angular differential in Eq. 2.113 requires uniformally spaced μ_n in order to recover the correct solution for a uniform isotropic source, $\Psi = S/n\sigma$. To allow Legendre-Gaussian discrete ordinates, angular differencing coefficients $\alpha_{n+1/2}$ are introduced which are defined as follows [109]:

$$\frac{1}{r}\frac{\partial}{\partial \mu}(1-\mu^2)\Psi\bigg|_{\mu=\mu_n} \approx \frac{2}{w_n r}\left[\alpha_{n+1/2}\Psi_{n+1/2} - \alpha_{n-1/2}\Psi_{n-1/2}\right] \ , \tag{2.117}$$

$$\alpha_{n+1/2} = \alpha_{n-1/2} - w_n\mu_n, \ \alpha_{1/2} = 0 \ . \tag{2.118}$$

These coefficients ensure that the correct solution is obtained for the uniform isotropic

[6] The abbreviation, S_N, derives from the procedure of splitting the angular domain into N straight line segments proposed by Carlson [24]. The method is a special case of the more general discrete ordinates method which has subsequently adopted the S_N label [12].

source case.

The spatial and energy domains are split with more freedom. A comment will be made here about the multigroup (energy) approximation used in Minotaur as different schemes exist in the literature [12]. The multigroup equations are found by integrating Eq. 2.113 over a finite energy ranges, the equations are then coupled through the scattering term. By performing the integration the cross sections must then be replaced by averages, for example:

$$\sigma(E)\Psi(r,\mu,E) \rightarrow \sigma_g(r,\mu)\Psi_g(r,\mu), \tag{2.119}$$

$$\sigma_g(r,\mu) \equiv \frac{\int_g \sigma(E)\Psi(r,\mu,E)dE}{\int_g \Psi(r,\mu,E)dE} \ . \tag{2.120}$$

However, rather undesirably the total cross section is now dependent on angle, μ. In Minotaur the flux is assumed to be independent of energy within each group:

$$\Psi(r,\mu,E) \approx \psi_g(r,\mu)Q(E) = \frac{\psi_g(r,\mu)}{\Delta_g} \ , \tag{2.121}$$

$$\sigma_g = \frac{1}{\Delta_g}\int_g \sigma(E)dE \tag{2.122}$$

where Δ_g is the width of the energy group. This approximation removes the angular dependence in cross sections. Suitably small energy groups must therefore be taken so that $\partial\Psi/\partial E < \Psi/\Delta_g$. Spatially we need only define radii, areas and volumes of cells – the half points of radii will be taken as the edges of cells:

$$r_{1/2} = 0, \ A_{i+1/2} = 4\pi r_{i+1/2}^2, \ V_i = \frac{4\pi}{3}\left[r_{i+1/2}^3 - r_{i-1/2}^3\right] \ . \tag{2.123}$$

By applying these discretisations to the conservative form of the neutron transport equation (Eq. 2.113) we ensure the correct conservation laws are maintained.

With the discretisation defined, the diamond differencing scheme is used to relate the fluxes at the boundaries to the centred value:

$$\Psi_{i,n,g} = \frac{1}{2}\left(\Psi_{i+1/2,n,g} + \Psi_{i-1/2,n,g}\right) = \frac{1}{2}\left(\Psi_{i,n+1/2,g} + \Psi_{i,n-1/2,g}\right) \ , \tag{2.124}$$

and the following set of discrete transport equations is obtained [12, 109]:

$$\Psi_{i,n,g} = \left[-2\mu_n A_{i-1/2} + \frac{2}{w_n}\left(A_{i+1/2} - A_{i-1/2}\right)\alpha_{n+1/2} + V_i n_i \sigma_g\right]^{-1} \times \tag{2.125}$$
$$\Big[-\mu_n\left(A_{i+1/2} + A_{i-1/2}\right)\psi_{i+1/2,n,g}$$
$$+\frac{1}{w_n}\left(A_{i+1/2} - A_{i-1/2}\right)\left(\alpha_{n+1/2} + \alpha_{n-1/2}\right)\psi_{i,n-1/2,g} + V_i S_{i,n,g}\Big], \quad \mu_n < 0 \ ,$$
$$\Psi_{i,n,g} = \left[2\mu_n A_{i+1/2} + \frac{2}{w_n}\left(A_{i+1/2} - A_{i-1/2}\right)\alpha_{n+1/2} + V_i n_i \sigma_g\right]^{-1} \times \tag{2.126}$$
$$\Big[\mu_n\left(A_{i+1/2} + A_{i-1/2}\right)\psi_{i-1/2,n,g}$$
$$+\frac{1}{w_n}\left(A_{i+1/2} - A_{i-1/2}\right)\left(\alpha_{n+1/2} + \alpha_{n-1/2}\right)\psi_{i,n-1/2,g} + V_i S_{i,n,g}\Big], \quad \mu_n > 0 \ ,$$
$$\Psi_{i,1/2,g} = \frac{2\Psi_{i+1/2,1/2,g} + (r_{i+1/2} - r_{i-1/2})S_{i,1/2,g}}{2 + n_i\sigma_g(r_{i+1/2} - r_{i-1/2})}, \ \mu_{1/2} = -1 \ , \tag{2.127}$$

where both the external and scattering source term have been bundled into $S_{i,n,g}$. Equation 2.124 gives the two diamond difference equations used to relate fluxes at both spatial and angular faces to centred values. Equations 2.125 and 2.126 give the inward and outward integration of the transport equation. Finally Eq. 2.127 is the solution for purely radially inward neutrons which is required to solve the whole system, it is often called the 'starter flux'. The solution procedure is as follows:

1. Solve for the starter flux
2. Perform inward radial sweeps, decreasing i, for $\mu_n < 0$, using the diamond difference to find $\Psi_{i,n-1/2,g}$ for the next $n+1$ sweep
3. Perform outward radial sweeps, increasing i, for $\mu_n > 0$, using the diamond difference to find $\Psi_{i,n-1/2,g}$ for the next $n+1$ sweep

For all problems considered in this work the outer boundary condition will be taken as a vacuum condition i.e. no incoming flux:

$$\Psi_{N+1/2,n,g} = 0 \text{ for } \mu_n < 0 \ . \tag{2.128}$$

The flux at the origin is isotropic and in a discrete sense this gives the following condition:

$$\left.\frac{\partial\Psi}{\partial\mu}\right|_{r\to 0} = 0 \Longrightarrow \Psi_{1/2,n-1/2,g} = \Psi_{1/2,n+1/2,g} \ . \tag{2.129}$$

A consequence of the diamond differencing scheme is a loss of positivity of the streaming operator (left hand side of Eq. 2.113). To remedy this a 'negative-flux-fixup' is employed when instances of negative flux occur [109]. This reduces the accuracy of the calculation so it preferable to choose sufficient spatial resolution to avoid this. This is parametrised through $h = \frac{n\sigma\Delta_r}{2|\mu_n|} < 1$ where Δ_r is the spatial mesh spacing.

Ignoring scattering for the time being, we can test the transport using a finite, uniform, isotropic, monoenergetic, spherical source with constant macroscopic cross section, $\Sigma = n\sigma$. This involves solving the following form of the neutron transport equation

$$\left[\mu\frac{\partial}{\partial r} + \frac{1-\mu^2}{r}\frac{\partial}{\partial \mu} + \Sigma\right]\Psi(r,\mu) = \frac{S}{2}\Theta(R-r)\ , \tag{2.130}$$

where Θ is the Heaviside function. The above equation can be solved analytically using the method of characteristics:

$$\Psi(r,\mu) = \frac{S}{2\Sigma}\left(1-\exp\left[-\Sigma l(r,\mu)\right]\right)\exp\left[-\Sigma l'(r,\mu)\right]\ , \tag{2.131}$$

$$l(r,\mu) = \begin{cases} r\mu + \sqrt{R^2 - r^2(1-\mu^2)} & r < R\ , \\ 2\sqrt{R^2 - r^2\left(1-\mu^2\right)} & r > R \text{ and } \mu > \sqrt{1-\left(\frac{R}{r}\right)^2}\ , \\ 0 & \text{elsewhere}\ , \end{cases}$$

$$l'(r,\mu) = \begin{cases} r\mu - \sqrt{R^2 - r^2(1-\mu^2)} & r > R \text{ and } \mu > \sqrt{1-\left(\frac{R}{r}\right)^2}\ , \\ 0 & \text{elsewhere}\ . \end{cases}$$

A comparison between numerical and analytic results for the first two angular moments of Ψ is shown in Fig. 2.15 for $\Sigma R = 1$. This shows good agreement for 32 angular groups used in the numerical calculation.

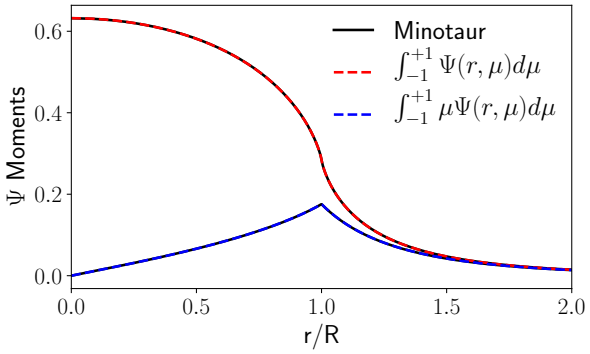

Figure 2.15: Comparing numerical and analytic transport solutions to a finite uniform isotopic spherical source of radius R within a constant macroscopic cross section $\Sigma R = 1$. The red dashed line shows the total neutron flux; the blue dashed line shows the neutron current and black lines show the equivalent results as calculated numerically by Minotaur.

Now that the streaming operator and external source term have been tested, we must now consider how to handle the anisotropic scattering source term. Commonly this is done by expanding the scattering kernel in terms of Legendre polynomials [12, 109]. However, for highly anisotropic scattering this can lead to unphysical results such as negative fluxes [169]. Instead we will use the I and I* methods outlined by Takahashi and Rusch [167–169] which performs no expansion of the scattering kernel. These methods analytically derive expressions for the 'angular transition probability', denoted I, when

the azimuthal angles are integrated out. If we consider neutron directions pre-collision, $\hat{\Omega}'$, and post-collision, $\hat{\Omega}$, with a fixed scattering cosine, μ^*, between them then the angular transition probability, abbreviated to ATP, is given by [169]:

$$\hat{\Omega}' \cdot \hat{\Omega} = \mu\mu' + \sqrt{1-\mu^2}\sqrt{1-\mu'^2}\cos(\phi - \phi') \ , \tag{2.132}$$

$$I(\mu', \mu, \mu^*) = \int d\Delta_\phi \delta(\hat{\Omega}' \cdot \hat{\Omega} - \mu^*), \quad \Delta_\phi \equiv \phi - \phi' \ , \tag{2.133}$$

$$= \frac{1}{\pi\sqrt{1-\mu^2-\mu'^2-\mu^{*2}+2\mu\mu'\mu^*}} = \frac{1}{\pi\sqrt{1-y^2}} \ , \tag{2.134}$$

$$y \equiv \frac{\mu - \mu'\mu^*}{\sqrt{1-\mu'^2}\sqrt{1-\mu^{*2}}} \ , \tag{2.135}$$

$I(\mu', \mu, \mu^*)$ is symmetric in its three parameters and obeys conservation of probability when integrated over any one of the angles. The diagrammatic interpretation and the plotted functional form are shown in Fig. 2.16. Numerically I must be integrated over the angular group widths in μ, μ' and μ^*, one of the three integrals can be performed analytically thus avoiding the singularities in I at $y = \pm 1$ [167, 168].

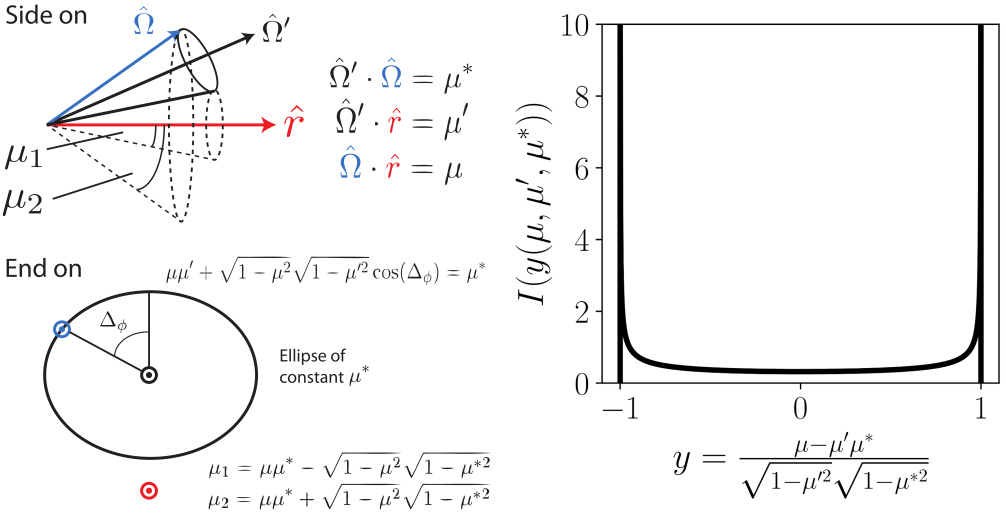

Figure 2.16: (Left) Diagram showing the geometric arrangement under consideration, the angles between $\hat{\Omega}'$ and $\hat{r}$, and $\hat{\Omega}'$ and $\hat{\Omega}$ are fixed but the azimuthal angle between $\hat{\Omega}'$ and $\hat{\Omega}$ is allowed to vary. This causes the angle between $\hat{\Omega}$ and $\hat{r}$ to change between the limits μ_1 and μ_2. (Right) The angular transition probability plotted in terms of the reduced variable y, $I(y) = \left[\pi\sqrt{1-y^2}\right]^{-1}$. The cosines in y can be interchanged due the symmetry properties of I.

Before introducing the differences between the I* and I methods, the discretisation and treatment of the scattering source in discrete ordinates will be discussed. First we will only consider downscatter since, for the relevant temperatures, the degree of upscatter is small, $E_n/T \gtrsim 10^3$. This also greatly simplifies the transport calculation as the energy groups can be swept in decreasing energy order (increasing index) a single time. The s-th scattered source term is calculated using a transport solution for the $s-1$ flux, thus a von Neumann series solution can be converged on through multiple

iterations. The discretised version of the differential cross section is often named a transfer cross section with symbol σ^t as it gives the particles transferred from a given energy/angle group to another. The scattering source is simply a sum over these transfer cross sections[7]:

$$\begin{aligned} S_{scat.,i,n,g,s} &= \int_i \int_g \int_{g'} \int_m \int_n n(r) \frac{d^2\sigma}{d\Omega dE} \Psi^{s-1}(r, \mu', E') \\ &= n_i \sum_{g' \geq g} \Delta_{g'} \sum_m w_m \sigma^t_{g,g',m,n} \Psi_{i,m,g',s-1} \ , \end{aligned} \tag{2.136}$$

where m and g' are the incoming angular and energy group.

If the lab frame differential cross section is independent of neutron direction, i.e. the target is stationary, then the I*-method can be used. This involves separating the calculation of ATP from the differential cross section. In index notation:

$$\int_g \int_{g'} \int_m \int_n \frac{d^2\sigma}{d\Omega dE} = \sum_{n^*} w_{n^*} \sigma_{g,g',n^*} I_{n^*,m,n} = \sigma^t_{g,g',m,n} \ . \tag{2.137}$$

For $2 \rightarrow 2$ body reactions, calculation of the intermediate σ_{g,g',n^*} with proper treatment of the delta function angular dependence is detailed in the report by Mori *et al.* [130]. For other reactions, such as the D(n,2n) reaction, the unit base transform is used to allow smooth interpolation over non-rectangular double differential cross section data tables – this method is detailed in the ENDF manual [175].

If the differential cross section depends on neutron direction, i.e. the target is non-stationary, then the calculation cannot be separated. The ATP and differential cross section should be calculated at the same time to avoid unnecessary numerical calculation. This is named the I-method as, rather than treating the scattering cosine as an independent variable (like in the I*-method), it is directly linked to the kinematic parameter μ_0^*. This means that I is calculated at the same time as the differential cross section:

$$\int_g \int_{g'} \int_m \int_n \frac{d^2\sigma}{d\Omega dE} = \sum_{n^*} w_{n^*} \sigma_{g,g',m,n,n^*} I_{n^*,m,n} = \sigma^t_{g,g',m,n} \ . \tag{2.138}$$

The transfer cross sections can also be position dependent if fluid velocity and temperature are spatially varying. This adds extra dimensionality to the transfer cross section calculation which then dominates computing time. Appendix B.2 describes the calculation of the transfer cross sections in detail.

To test the scattering operator in Minotaur, the constant isotropic elastic scattering of a unit monoenergetic source, $Q_0(E) = \delta(E - E_0)$, is considered. The energy spectrum for the sth scattered flux can be calculated analytically by repeated operation of the scattering kernel, this can be compared to the equivalent discrete form from Minotaur,

[7] We will introduce notation here to abbreviate the integration over the discretised space. For example, for energy group g the integral $\int_g$ is used to represented $\int_{E_g - \Delta_g/2}^{E_g + \Delta_g/2} dE$

see Fig. 2.17:

$$Q_s(E) = \int_E^{E/\alpha} \frac{2\sigma}{(1-\alpha)E'} Q_{s-1}(E')dE' \ , \tag{2.139}$$
$$= \frac{2^s\sigma^s}{(1-\alpha)^s E_0(s-1)!} \sum_{i=0}^{s} \binom{s}{i} (-1)^{i+s} \ln^{s-1}\left(\frac{E}{\alpha^i E_0}\right) \Theta\left(\frac{E}{\alpha^i} - E_0\right) \ .$$

Discrete form:

$$S_{g,s} = \sum_n w_n \sum_{g' \geq g} \Delta_{g'} \sum_m w_m \sigma^t_{g,g',m,n} S_{g',s-1} \ . \tag{2.140}$$

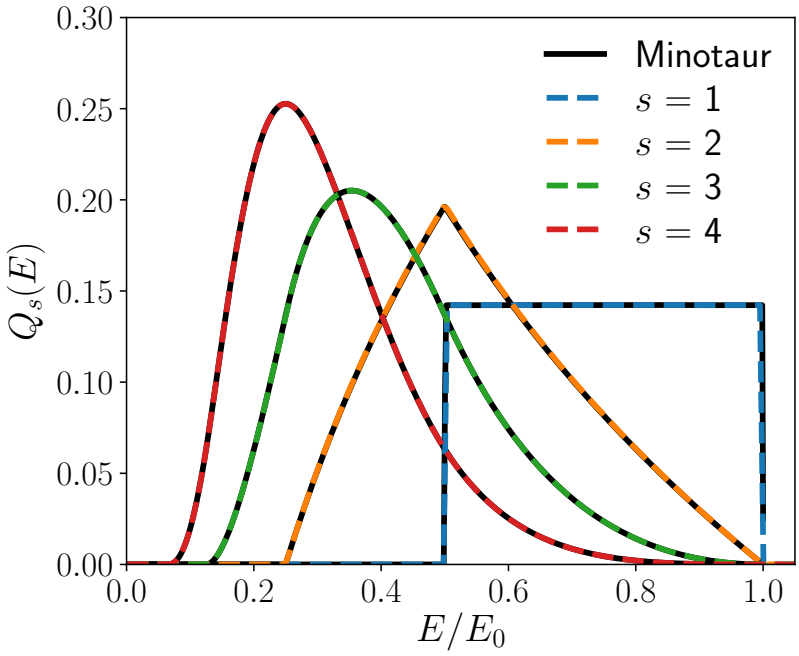

Figure 2.17: Comparison of analytic (dashed lines) and numerical (solid lines) isotropic scattering source terms as defined in Eqs. 2.139 and 2.140 with $\alpha = 0.5$ and $\sigma = 1$.

With the neutron transport numerics of Minotaur described, its practical application to 1D radiation hydrodynamics simulation of ICF experiments will be given. For this we will use a simulation of N130927 performed with Chimera [34]. Figure 2.18 shows the hydrodynamic conditions at the time of peak neutron production (known as bang time). This simulation will serve to show Minotaur can recover known neutron spectroscopic signals. In Chapter 3, we show how Minotaur has been used to highlight novel neutron spectral features.

The birth spectra of fusion neutrons for given plasma conditions were accurately calculated by Appelbe [3, 5, 6] and are included in Minotaur. Alternatively the relativistic Brysk [11, 23] spectrum can be used for the DT and DD reactions. This is less accurate but provides an analytic form for the spectra and allows more direct comparison with 3D calculations which also use this form for expedience. The Brysk form has a Gaussian

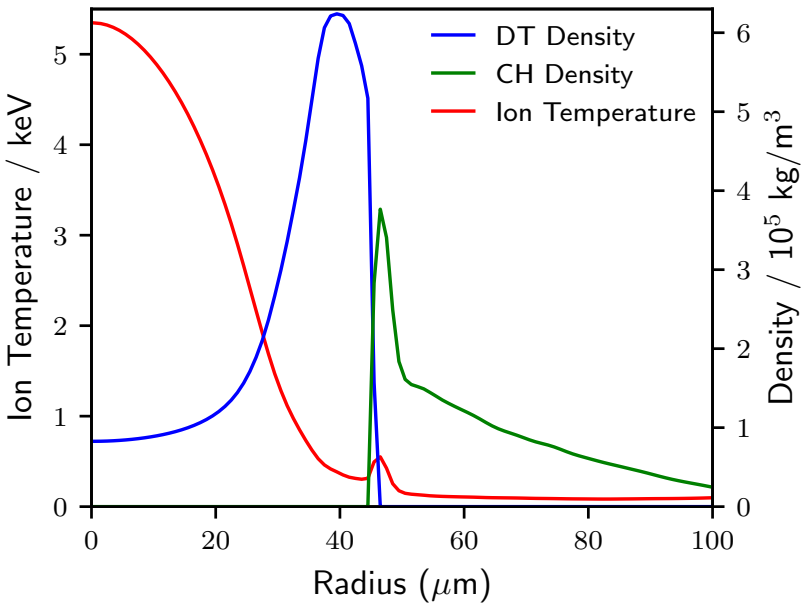

Figure 2.18: The simulated density and temperature radial profiles at bang time for High-Foot shot N130927 [34]. A neutron yield of 7.85×10^{15} was obtained without alpha-heating effects.

functional dependence:

$$Q_{\text{Brysk}}(E) = \frac{Y}{\sqrt{2\pi\sigma_b^2}} \exp\left[-\frac{\left(E-\bar{E}_b\right)^2}{2\sigma_b^2}\right] , \tag{2.141}$$

Ballabio gives expressions for the mean, $\bar{E}_b$, and variance, σ_b^2, which will be given in Appendix B.1. Most notably the Brysk model cannot capture the high energy tail present in the more accurate spectra. As most nuclear cross sections decrease with increasing energy above 14 MeV, this high energy tail is not expected to have a significant effect on the spectra at lower energies.

An example of the full 1D neutron spectrum is given calculated from the hydrodynamic simulation of N130927 in Fig. 2.19. The neutron spectrum shows several features of interest; the DT and DD peaks occurring at $\sim$ 14 and 2.5 MeV respectively, the backscatter edges either side of the DD peak and the spectrum down to 10 MeV which is dominated by scattering from D and T. These 1D neutron transport calculations give knowledge of the full detail of the spectrum for an unperturbed implosion. This calculation was run with 64 angular (Legendre-Gauss) groups and 400 energy groups which were clustered around spectral features of interest; 25 hydrodynamic time steps surrounding bang time were summed to obtain the time integrated spectrum. The scattering source term was iterated 4 times (therefore allowing quadruple scattering) before the result had converged.

Below the DT peak and down to 10 MeV, the major contribution to the spectrum is from scattering from deuterons and tritons. Scattering from the ablator and D(n,2n) provide minor additions to this region. Multiple scattering from the fuel becomes in-

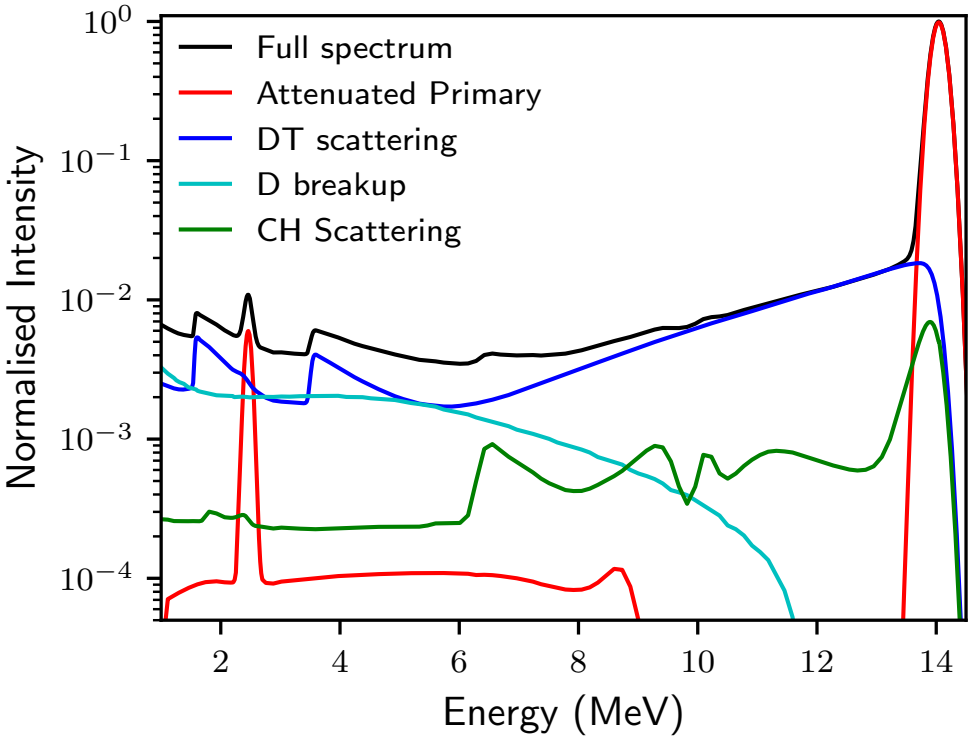

Figure 2.19: Neutron spectrum created by post-processing a 1D Chimera simulation of the High-Foot shot N130927 using Minotaur. The contributions to full spectrum, black line, from various nuclear interactions are shown. Multiple scattering events are considered in this calculation.

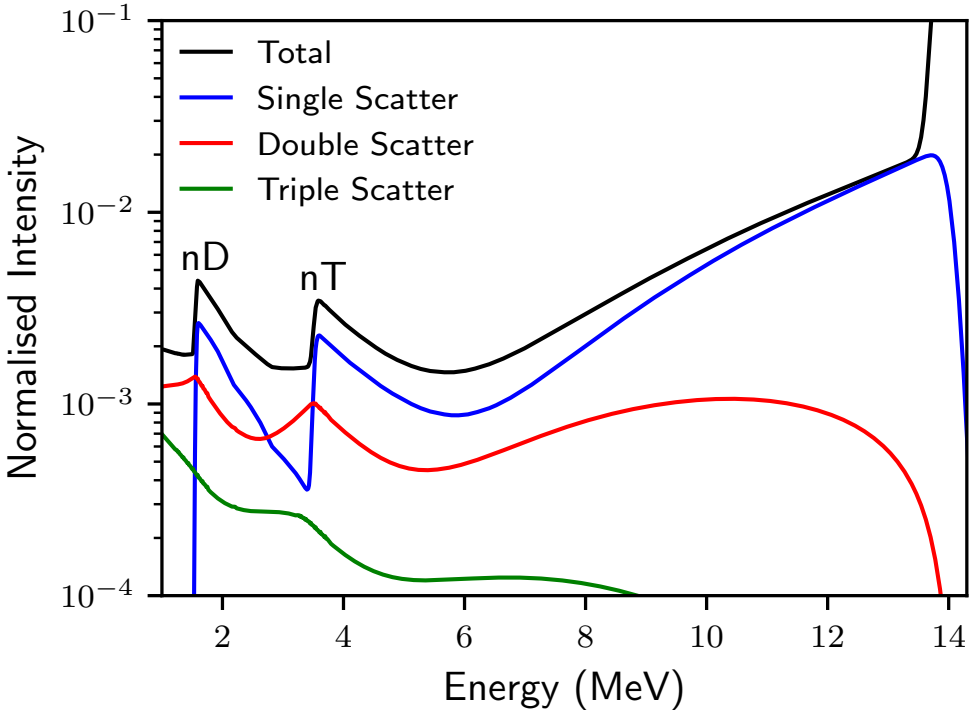

Figure 2.20: Neutron spectra produced from the down scattering of DT fusion neutrons by deuterons and tritons only. The different contributions from multiple scattering are separated out. A simple isobaric hotspot model[172, 173] was used. The spectra are normalised such that the attenuated DT peak value is unity.

creasingly important at higher areal densities. Figure 2.20 illustrates the spectral contribution of DT multiple scattering at a fuel ρR of 1 g/cm^2. For fuel areal densities relevant to current indirect drive ICF ($\leq$ 1 g/cm^2), the 10–12 MeV spectrum is predominately from single scattering from DT. This leads to fitted relations between fuel areal density and down scattered ratio (DSR) [56, 61]. The DSR is defined as the ratio of neutron yields in spectral ranges [10 MeV, 12 MeV] and [13 MeV, 15 MeV]. This can be related to the areal density in the single scatter and monoenergetic point source approximation:

$$\mathrm{DSR} = \frac{Y_{10-12}}{Y_{13-15}} \approx \frac{\rho R}{\bar{m}} \int_{10}^{12} dE \left.\frac{d\bar{\sigma}}{dE}\right|_{E'=14} = \frac{\langle\bar{\sigma}\rangle}{\bar{m}}\rho R \ , \tag{2.142}$$

where barred quantities are averaged over the fuel fractions. Negligible remaining ablator contribution has been assumed, due to both the lower ablator areal density and larger ion average mass. The DSR-ρR relationship can change due to capsule conditions deviating from the simplifying assumptions. The most erroneous of these is the point source approximation. An extended source will, on average, reduce the areal density seen by scattering neutrons. Therefore ρR in Eq. 2.142 should be replaced with the neutron averaged areal density, $\langle\rho L\rangle < \rho R$. Based on the capsule model used, DSR-ρR relations can be inferred from areal density scans in Minotaur. For two example cases, a point source in a uniform sphere and an isobaric hotspot model [172], linear $\rho\mathrm{R}_{\mathrm{DT}}$-DSR coefficients ($\sim \bar{m}/\langle\bar{\sigma}\rangle$) of 21.0 and 19.4 were found. These are in agreement with others in the literature [56, 61]. It is difficult to have a definitive $\rho\mathrm{R}_{\mathrm{DT}}$-DSR relationship as it is dependent on hotspot-fuel configuration, remaining ablator percentage and DT primary spectral shape. However realistic variation of capsule conditions in 1D do not alter the linear $\rho\mathrm{R}_{\mathrm{DT}}$-DSR coefficients by more than $\sim$ 10 %. However, multidimensional effects can be significant. This is to be expected as ρR becomes poorly defined for large 2D/3D asymmetries.

Minotaur was adapted to perform fast ion transport in tandem with neutron transport. Only unmagnetised problems can be considered due to the restriction of spherical symmetry employed in Minotaur. Following Morel [128], the Fokker-Planck collision operator (Eq. 2.104) can be recast in terms of angular flux, Ψ, and energy:

$$\left[\frac{\mu}{r^2}\frac{\partial}{\partial r}r^2 + \frac{1}{r}\frac{\partial}{\partial\mu}(1-\mu^2) + n(r)\sigma(E)\right]\Psi(r,\mu,E) = \mathcal{L}_{FP}\Psi + S_{ext.}(r,\mu,E) \ , \tag{2.143}$$

$$\mathcal{L}_{FP}\Psi = \frac{\alpha}{2}\frac{\partial}{\partial\mu}\left(1-\mu^2\right)\frac{\partial\Psi}{\partial\mu} + \frac{\partial}{\partial E}\beta\Psi + \frac{1}{2}\frac{\partial}{\partial E}\left(\gamma\frac{\partial\Psi}{\partial E}\right) \approx \frac{\partial}{\partial E}\beta\Psi \ . \tag{2.144}$$

As discussed in Section 2.2.2, slowing down is generally the dominant term for fast ions and therefore we shall neglect angular deflection and parallel diffusion ($\alpha = \gamma = 0$). A slight modification to the transport algorithm is required to include the Fokker-Planck slowing down term. Using a simple upwind scheme, the transport equation of energy

group g becomes [128]:

$$[\Omega \cdot \nabla + n(r)\sigma_g]\,\Psi_g = \bar{\beta}_{g-1\to g}\Psi_{g-1} - \bar{\beta}_{g\to g+1}\Psi_g \ , \tag{2.145}$$

$$\bar{\beta}_{i\to j} = \frac{\beta(E_i)}{(E_i - E_j)} \ , \tag{2.146}$$

$$\beta(E) = 1.303\times 10^{-35}\cdot \frac{Z_i^2 Z_t^2 m_i}{m_t E_i} n_t y(\epsilon_i)\ln\Lambda \ , \tag{2.147}$$

$$y(\epsilon_i) = \left[\mathrm{erf}(\epsilon_i) - \frac{2\epsilon_i}{\sqrt{\pi}} e^{-\epsilon_i^2}\left(1+\frac{m_t}{m_i}\right)\right] \ , \ \epsilon_i^2 = \frac{m_t E_i}{m_i T} \ , \tag{2.148}$$

subscripts i and t refer to the fast ion and target particle respectively, energies and temperatures are in MeV and number densities in m^{-3}. This forms a matrix equation with the diagonal and upper diagonal non-zero. The lowest energy 'sink' group has a boundary condition $\bar{\beta}_{g\to g+1} = 0$. At every spatial step this matrix equation is solved using LU decomposition with partial pivoting from Numerical Recipes [144]. This general method allows easier extension to higher order differencing schemes and the inclusion of the parallel diffusion term – the simple upwind scheme is positive definite but diffusive. A test problem of a point (1 μm radius) triton source in a 3 keV 50/50 DT plasma at a ion number density of 10^{31} m^{-3} is considered. The triton energy birth spectrum used was consistent with the 3 keV ion temperature. Figure 2.21 shows the results of this test which show good performance of the slowing algorithm, given its simplicity.

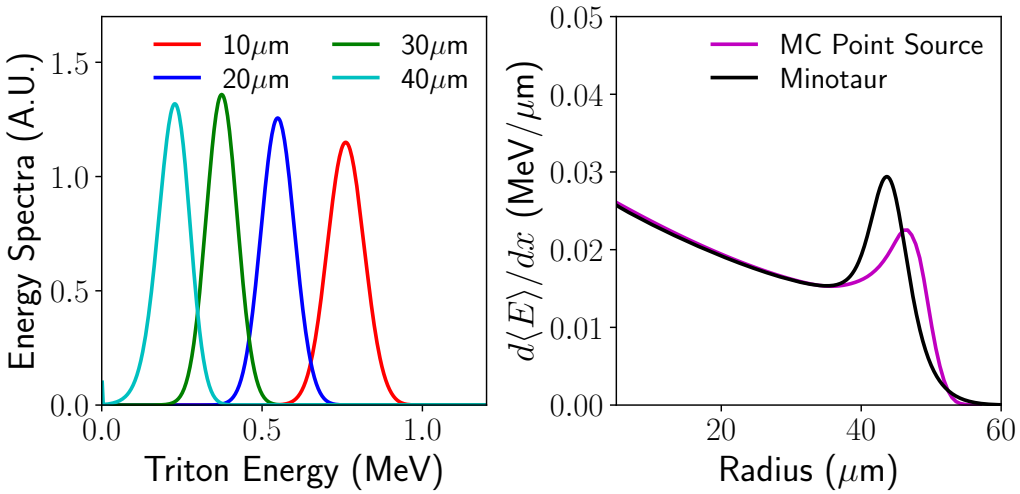

Figure 2.21: (Left) The triton spectrum at various radii showing the slowing and no strong evidence of numerical diffusion. The peak at $\sim$ 0 MeV is the sink group from which the tritons cannot leave and therefore accumulate. (Right) The averaged stopping power calculated from the mean of the triton spectrum at a given radius. A Monte Carlo (MC) point source result is shown for comparison. The Minotaur solution shows an early onset and stronger Bragg peak. Likely causes for this are the poor energy resolution at Bragg peak triton energies, the treatment of the sink group and the "ray effects" present in discrete ordinates solutions of point source problems [107].

Minotaur can perform fast ion transport of alphas, deuterons and tritons with slowing

down. Including knock-on fast ion source terms from neutrons and alphas was a simple extension of the scattering source term which exists in the neutron transport. Currently no scattering term of the same species is implemented (e.g. the effect of large-angle Coulomb scattering on the fast D and T populations). The neutrons produced by fast D and T reactions are fed back into the neutron transport[8]. The results from Minotaur's coupled neutron fast ion transport will be given in Section 3.3.

2.2.4 AKED

Numerical solution of neutron and fast ion transport in all of 6D phase space is a leviathan computational task. In order to efficiently solve these problems, the region of phase space explored must be restricted. Monte Carlo techniques statistically sample the space with many computational particles therefore estimating the underlying distribution. These stochastic methods are inherently noisy and thus low probability events experience large statistical error. Deterministic methods used in less dimensional problems (such as discrete ordinates) typically do not scale well to 3D, so new schemes are needed.

In this section, we present the code AKED[9] which uses a novel inverse ray trace method to perform neutron transport in 3D. This allows both neutron spectra and images to be calculated at multiple detector locations. Fast ion transport is performed with a more traditional Monte Carlo method as Larmor orbits cannot be handled by a ray tracing method.

The inverse ray trace is based on a solution to the transport equation using the method of characteristics. As only diagnostic signatures are of interest, only the neutrons which will arrive at the detector are tracked. This greatly reduces the size of the calculation making it tractable in 3D. The time independent form of the transport equation can be rewritten in a line integral form [12]:

$$\psi(\vec{r},\hat{\Omega},E) = \int_0^\infty \exp\left[-\sigma(E)\int_0^{s'} ds'' n(\vec{r}-s''\hat{\Omega})\right] S(\vec{r}-s'\hat{\Omega},\hat{\Omega},E)\; ds' \;,$$

where S represents both the external and nuclear interaction source terms. Solving along the detector line of sight, $(\vec{r},\hat{\Omega}) = (\vec{r}_{det},\hat{\Omega}_{det})$, now constitutes a single line integral if S is known. In practice this integral tracks neutron paths from the detector plane back through the simulation grid. The source and degree of attenuation is calculated for each grid cell intersected. For a primary source, the source term is simply the reaction rate in that grid cell. A scattering source is handled via an additional set of traces from the intersected cell to all emitting cells above an emission power threshold. This is a

[8] One can imagine a chain of neutron knock-on ions reacting to produce high energy neutrons which knock-on ions to even higher velocities. This "DT fusion accelerator" has an upper limit when the energy taken away by the neutron in the knock-on event matches the energy gained in the DT reaction. This occurs at a final neutron energy given by $E = 4Q/5\alpha$ and therefore 126 and 56 MeV for D and T respectively.

[9] AKED is a misnomer as this originally stood for Alpha Kinetic Energy Deposition, a progenitor code for alpha particle transport. The name however has stuck and I hope it doesn't change.

considerably larger calculation than for the primary source. Since each ray from an emitter to the scattering cell is independent, this calculation can be fully parallelised (AKED uses the MPICH implementation of MPI). Generally only a limited scattered energy range is of interest, allowing the calculation size to be reduced by considering only a subset of rays for which the primary neutrons downscatter into the accepted range. Figure 2.22 shows a diagram of the inverse ray trace method for primary and scattered neutrons. The details of and the improvements to the numerical raytracing in AKED will be given in Appendix B.3.

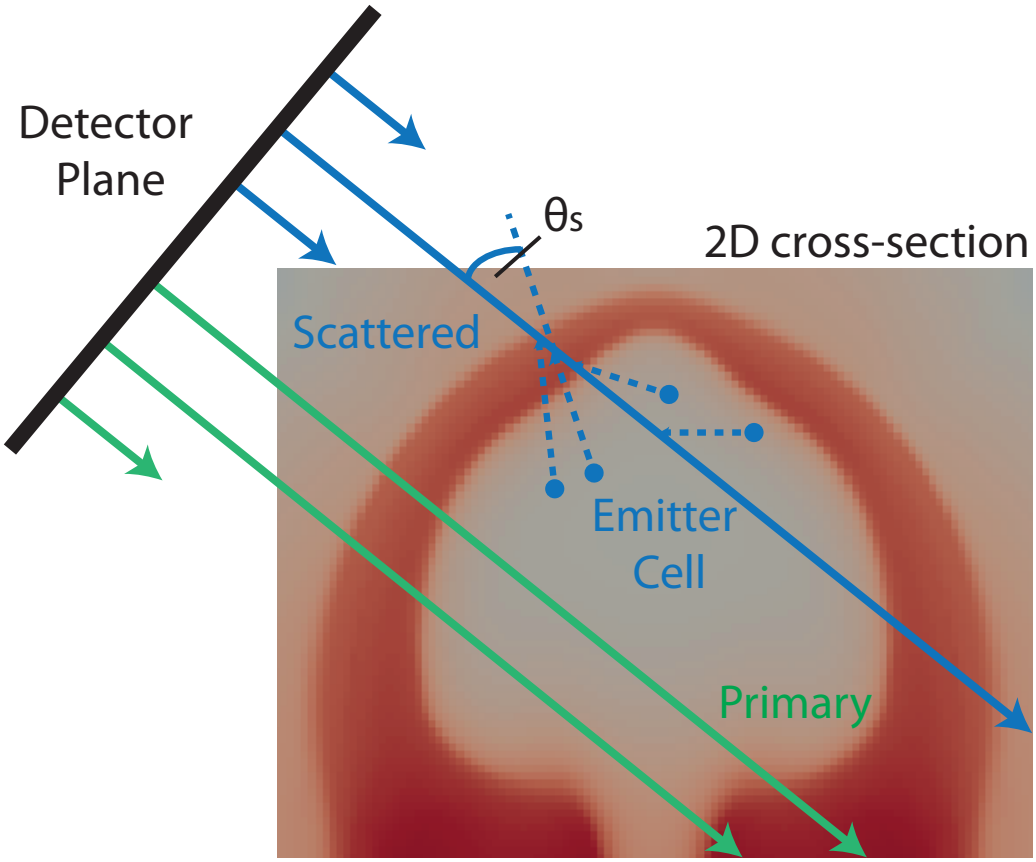

Figure 2.22: Schematic of the inverse ray trace method. In green, primary neutrons are tracked by straight rays traced back from the detector plane through the simulation grid. In blue, scattered neutrons are found by a combination of many traces. Neutrons are traced from the emitter cells to every scattering cell along the detector line of sight. The range of allowed scattering angles, $\theta_s = \cos^{-1}\mu_0$, is set by the energy gate considered.

The source term for scattering is given by a more complex expression:

$$S_{scat.}(\hat{\Omega}, E) = n_i \langle l \rangle \frac{d\sigma}{d\Omega_{lab}} \delta(\hat{\Omega} \cdot \hat{\Omega}' - \mu_0^*(E', E)) \cdot S_{emit} \Delta\Omega_{in} \ , \tag{2.149}$$

$$S_{scat.}(\hat{\Omega}, E) \approx n_i V \frac{d\sigma}{d\Omega_{lab}} \delta(\hat{\Omega} \cdot \hat{\Omega}' - \mu_0^*(E', E)) \cdot \frac{S_{emit}}{4\pi r_{e-s}^2} \ , \tag{2.150}$$

where S_{emit} is the neutron emittance of the source cell, $\Delta\Omega_{in}$ is the solid angle subtended by the scatterer cell from the emitter cell, $\langle l \rangle$ is the mean chord of rays through the

scatterer cell, V is the volume of the scatterer cell and r_{e-s} is the emitter-scatterer distance. The energy of the outgoing neutron is calculated using the elastic scattering relation for a scattering cosine, $\mu_0 = \hat{\Omega} \cdot \hat{\Omega}'$:

$$\frac{E}{E'} = \frac{\left(\mu_0 + \sqrt{\mu_0^2 + A^2 - 1}\right)^2}{(A+1)^2} \ . \tag{2.151}$$

The monoenergetic approximation for the primary DT peak is poor if resolved neutron spectra are desired. However, a multigroup method becomes computationally expensive if fine energy resolution is required. Therefore a number of approximations are made to improve the efficiency of the calculation while maintaining spectral detail. Motivated by the success of the Brysk model[11, 23] (Eq. 2.141), we consider each neutron ray to have a Gaussian energy distribution. By considering Gaussians, only three variables are required to be transported along the rays: amplitude, mean and variance. The neutron birth spectrum within each grid cell's rest frame is indeed close to Gaussian [132]. However transforming to the lab frame results in a loss of the Gaussian form of Brysk. Noting that the fluid velocity is significantly lower than the neutron velocity, the Gaussian form can be recovered via a first order binomial expansion in the ratio of fluid to neutron velocity. If we consider the lab frame neutron velocity, $\vec{v}_n$, and emitter fluid velocity, $\vec{v}_f$, with cosine μ_f between them, then transforming to the rest frame must give the Brysk neutron energy, $\bar{E}_b$:

$$E_f \equiv \frac{1}{2} m_n v_f^2, \quad \delta E = E_n - \bar{E}_b, \quad \frac{\delta E}{\bar{E}_b} \ll 1 \ ,$$

$$\bar{E}_b = \frac{1}{2} m_n \left(\vec{v}_n - \vec{v}_f\right)^2 = E_n - 2\sqrt{E_n E_f}\mu_f + E_f \ , \tag{2.152}$$

$$\delta E = 2\sqrt{\bar{E}_b E_f}\mu_f \sqrt{\left(1 + \frac{\delta E}{\bar{E}_b}\right)} - E_f \approx 2\sqrt{\bar{E}_b E_f}\mu_f \left(1 + \frac{1}{2}\frac{\delta E}{\bar{E}_b}\right) - E_f \ , \tag{2.153}$$

$$\delta E = \frac{2\mu_f\sqrt{\bar{E}_b E_f} - E_f}{1 - \mu_f\sqrt{E_f/\bar{E}_b}} \ . \tag{2.154}$$

A similar simplification can be made for the Jacobian from rest to lab frames. The lab frame neutron spectrum is then approximated by the following Gaussian form:

$$Q_b(E) = \frac{Y}{\sqrt{2\pi\sigma_b^2}} \left(1 + \frac{1}{2}\frac{\delta E}{\bar{E}_b}\right) \exp\left[-\frac{(E - (\bar{E}_b + \delta E))^2}{2\sigma_b^2}\right] \ . \tag{2.155}$$

The final primary spectrum constitutes a sum of these approximated Brysk spectra. Although the individual spectra reaching the synthetic detector possess no higher cumulants than variance, their sum will. Therefore, the moment analysis outlined by Munro [131, 132] is still possible with some error introduced. Additionally, the Gaussian form can be exploited when handling attenuation. Performing a piecewise linear fit to the total cross section centred on the spectral mean simplifies the calculation of

the neutron attenuation to a mean shift [132] and amplitude reduction.

$$Q_a(E) \propto \exp\left[-\frac{(E-\bar{E})^2}{2\sigma_b^2} - nL(\sigma_m E + \sigma_c)\right] , \tag{2.156}$$

$$Q_a(E) \propto \exp\left[-\frac{(E-\bar{E}')^2}{2\sigma_b^2}\right] \exp\left[-nL\left(\sigma_c + \sigma_m\bar{E} - \frac{1}{2}nL\sigma_m^2\sigma_b^2\right)\right] , \tag{2.157}$$

$$\bar{E}' = \bar{E} - nL\sigma_m\sigma_b^2 , \tag{2.158}$$

where nL is the line integrated number density of scatterers. Since $\sigma_m < 0$ at 14 MeV, the mean shift for primary DT neutrons is to higher energies. For scattering, the energy dependence of the differential and absolute cross section is assumed constant about the spectral mean. This allows the scattered spectrum mean and variance on the ray to be simply related to the source mean and variance via a multiplicative factor, as given by Eq. 2.151:

$$\beta = \frac{E}{E'} = \frac{\left(\mu_0 + \sqrt{\mu_0^2 + A^2 - 1}\right)^2}{(A+1)^2} = \frac{A^2 + 1 + 2A\mu_c}{(A+1)^2} , \tag{2.159}$$

$$\bar{E}_s = \beta\bar{E}, \quad \sigma_s^2 = \beta^2\sigma^2 , \tag{2.160}$$

where the mean and variance post scattering event are denoted $\bar{E}_s$ and σ_s^2 respectively. The energy reduction factor β can be modified to include the effect of scatterer fluid velocity through classical kinematics. At the present time the effect of temperature on scattering has not been included in AKED. In summary: the birth, attenuation and scattering of neutrons can be performed by manipulation of the amplitude, mean and variance of a Gaussian. This efficient treatment of the energy domain along with the efficiency of the ray trace allows for calculation of primary and singly-scattered neutron spectra from large ($\sim 10^6$ computational cells) 3D radhydro simulations.

Forming images involves summing over energy space and resolving the detector position, in the opposite fashion to the spectra. Often images are taken in restricted energy gates, e.g. 13 - 15 MeV and 6 - 12 MeV. These gates are sufficiently wide that many of the effects needed to accurately describe the spectra are not required to form these gated images e.g. the effects of fluid velocity on scattering. Therefore, images can be calculated in a more computationally efficient manner. It is worth noting here that since the 3D radhydro simulations are calculated on Cartesian grids at stagnation that they suffer from grid imprint. This presents itself as distortions along the cardinal directions of the simulation grid. A symptom of this is that images produced from these simulations can appear “boxy”. Higher spatial resolution can mitigate the grid imprint but at an increased computational cost.

Currently, only singly-scattered and un-scattered neutrons are included in the inverse ray trace method. This approximation introduces significant error at lower neutron energies as the degree of multiple scattering increases. However, features at higher neutron energies and distinct single scattering phenomena such as the backscatter edges can be

analysed within this approximation with appropriate background subtraction. Minotaur was used to benchmark the more approximate 3D ray trace calculations by ensuring agreement on a symmetric implosion, see Fig. 2.23. For expedience the multiple and ablator scattering and break-up reaction backgrounds are omitted in 3D calculations. To estimate the error in AKED, Minotaur found at 1 g/cm^2 the spectrum produced within the single scatter approximation introduces fractional error $< 30\%$ above 10 MeV causing a 20% reduction in calculated DSR. These errors increase for larger areal densities and decrease for lower.

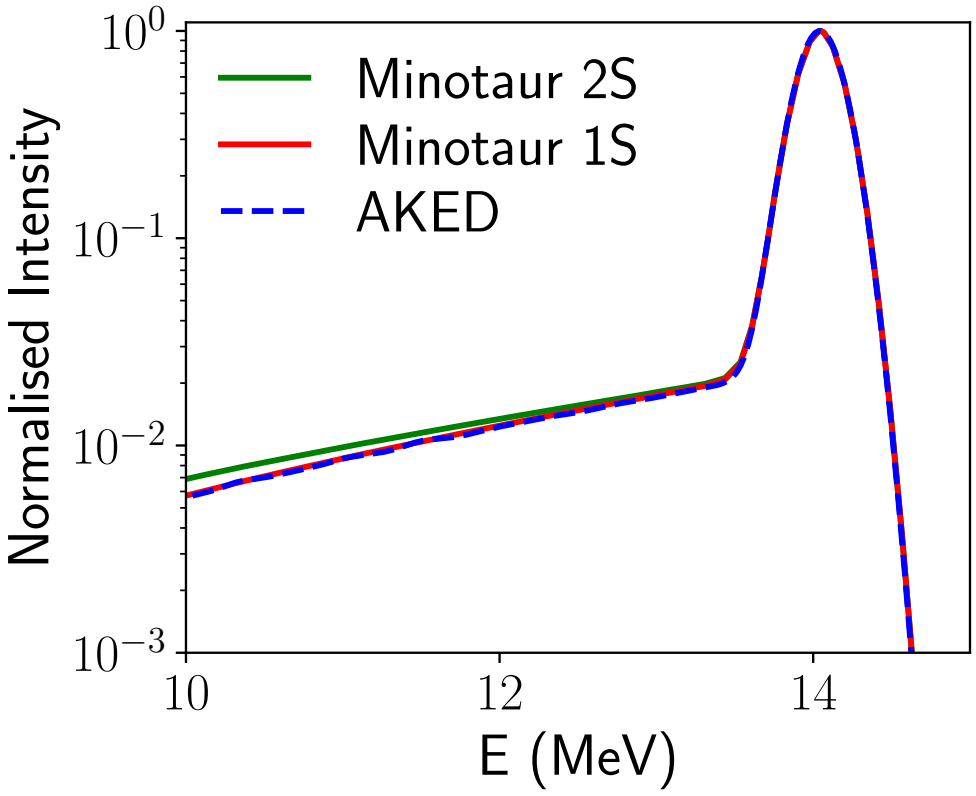

Figure 2.23: Comparison of the DT primary and singly scattered neutron spectrum from AKED and Minotaur. AKED was run in 3D with spherically symmetric hydrodynamic profiles. The equivalent calculation was performed in 1D in Minotaur with only scattering from DT considered. Excellent agreement between the codes is seen in the single scatter case (1S). The effect of double scattering (2S) on the scattered spectrum is shown by the green line.

The inverse ray trace method can also be used to calculate the γ-ray signal made by inelastic scattering of neutrons from carbon nuclei. This resembles the scattered neutron calculation however the trace back to the detector tracks the 4.4 MeV γ-rays rather than the scattered neutrons.

Fast ion transport in AKED is performed with a Monte Carlo method which uses the framework outlined by Sherlock [159]. The Lorentz force is included and the equations of motion are integrated using the standard Boris algorithm commonly used in particle-in-cell simulations. Each Boris step is followed by the collisional processes, e.g. slowing

down, and calculation of produced beam-target spectra. Figure 2.13 showed some fast ion trajectories calculated using this method. With a set of detector positions specified, the beam-target spectra can be calculated directly from the differential cross section in the T = 0, $v_f = 0$ limit or interpolated from tables calculated at a range of beam energies, plasma temperatures and fluid velocities [4].

3 Neutron Spectroscopy

Content in this chapter has been reproduced from "Synthetic nuclear diagnostics for inferring plasma properties of inertial confinement fusion implosions", Physics of Plasmas 25, 122703 (2018), Crilly et al. [42] and "Neutron backscatter edge: A measure of the hydrodynamic properties of the dense DT fuel at stagnation in ICF experiments", Physics of Plasmas 27, 012701 (2020), Crilly et al. [43], with the permission of AIP Publishing.

Typically detailed analysis of neutron spectra in ICF experiments is limited to the DT and DD peaks. In this chapter, we aim to extend spectral analysis to include features in the scattered and high energy spectrum. This will introduce techniques which could be utilised to increase our understanding of conditions within ICF experiments.

3.1 Backscatter Edge

As described in Section 2.2.1, DT fusion neutrons that undergo 180° elastic scatter from ions lose the largest fraction of their energy possible for a single scattering event. This produces a sharp edge in the neutron spectrum. For stationary target ions, the resultant edge energy is dependent only on the ion mass and incoming neutron energy. However, if the target ion has significant velocity (due to thermal or non-thermal motion) this will affect the energy of the backscattering neutron[1]. Therefore the energy spectrum of these backscattering neutrons can be related to the hydrodynamic conditions of the ions from which the scattering occurred.

3.1.1 Backscatter Edge Spectral Shape

The scattering kinematics of neutrons are affected by the velocities of ions with which they interact. In the general case, this is accounted for by a frame transformation from the beam-target frame of the neutron and stationary ion to the lab frame in which the ion is non-stationary. The backscattering geometry simplifies this transform greatly, using the notation that primed quantities are pre-collision and unprimed post-collision:

[1] One can draw an analogy with VISAR, an interferometry technique which measures the velocity of any reflector by reflecting a laser from its surface. In our case, neutrons backscatter from ions therefore measuring the velocity of the scattering medium opposite the detector.

$$v_n = \frac{A_i - 1}{A_i + 1} v'_n + \frac{2A_i}{A_i + 1} v'_{i,\parallel} \ , \tag{3.1a}$$
$$\text{Where } v'_{i,\parallel} \equiv \frac{\vec{v}'_i \cdot \vec{v}_n}{v_n} = -\frac{\vec{v}'_i \cdot \vec{v}'_n}{v'_n} \ ,$$

where subscripts indicate the particle species (n and i for neutron and ion) and A_i is the mass ratio between the ion and neutron. As the pre-collision neutron and ion velocities are uncorrelated, the mean and variance of the final neutron velocity are simply given by:

$$\langle v_n \rangle = \frac{A_i - 1}{A_i + 1} \langle v'_n \rangle + \frac{2A_i}{A_i + 1} \langle v'_{i,\parallel} \rangle \ , \tag{3.1b}$$
$$\text{Var}(v_n) = \left(\frac{A_i - 1}{A_i + 1} \right)^2 \text{Var}(v'_n) + \left(\frac{2A_i}{A_i + 1} \right)^2 \text{Var}(v'_{i,\parallel}) \ . \tag{3.1c}$$

The pre-collision neutron velocity mean and variance are determined by hotspot conditions [3, 5, 132]. The scattering medium conditions determine the pre-collision ion velocity mean and variance. Any bulk motion will cause a shift in the edge position and any variation in ion velocity, be it temperature or variance in fluid velocity, will create a broadening of the edge. Hence an analogy can be drawn between the backscatter edge moments and the moments of the primary DT fusion neutron peak. While the DT peak moments are only sensitive to the burn-weighted properties of the hotspot, the backscatter edge shape is also sensitive to the scattering rate weighted properties of the scattering medium.

The form of the backscatter edge is found by evaluating the spectrum of singly collided neutrons. This is given by the product of the uncollided or 'birth' neutron flux, Ψ_b, and the nuclear interaction differential cross section of the background ions integrated over all space, time, incoming neutron direction, $\hat{\Omega}'$, and energy, E':

$$I_{1s}(E, \hat{\Omega}) = \int d\tau_i \int d\hat{\Omega}' \int dE' \frac{d^2\sigma_i}{dE d\Omega} \Psi_b(\vec{r}, \hat{\Omega}', E') \ , \tag{3.2}$$

where $d\tau_i = n_i dV dt$ and n_i is the number density of ions of species i. By assuming energy separability, the birth neutron flux can be split into the spatial angular flux, ψ_b, and a normalised birth energy spectrum, Q_b. The resultant total spectrum of singly interacting neutrons travelling in direction, $\hat{\Omega}$, with energy, E, is then given by:

$$I_{1s}(E, \hat{\Omega}) = \int d\tau_i \int d\hat{\Omega}' \psi_b(\vec{r}, \hat{\Omega}') \int dE' \frac{d^2\sigma_i}{dE d\Omega} Q_b(E', \hat{\Omega}') \ . \tag{3.3}$$

As the densest regions of the capsule are situated outside the fusing plasma, the birth energy spectra across these regions are well represented by the averaged spectrum, supporting energy separability. Here we have also assumed no attenuation between source and scattering site. Since the DT birth spectrum width is small compared to its

mean, changes in spectral shape due to differential attenuation are small for typical ICF conditions[132]. Figure 3.1 shows the change in DT primary mean, $\langle v_n' \rangle$, and standard deviation, $\sqrt{\mathrm{Var}(v_n')}$, for density and temperature profiles taken from a LILAC[44] simulation at bang time. The mean is very close to constant ($\ll 1$ % change) and the standard deviation changes by only a few percent in the dense DT layer. This result lends credence to the energy separability approximation used in the following analysis.

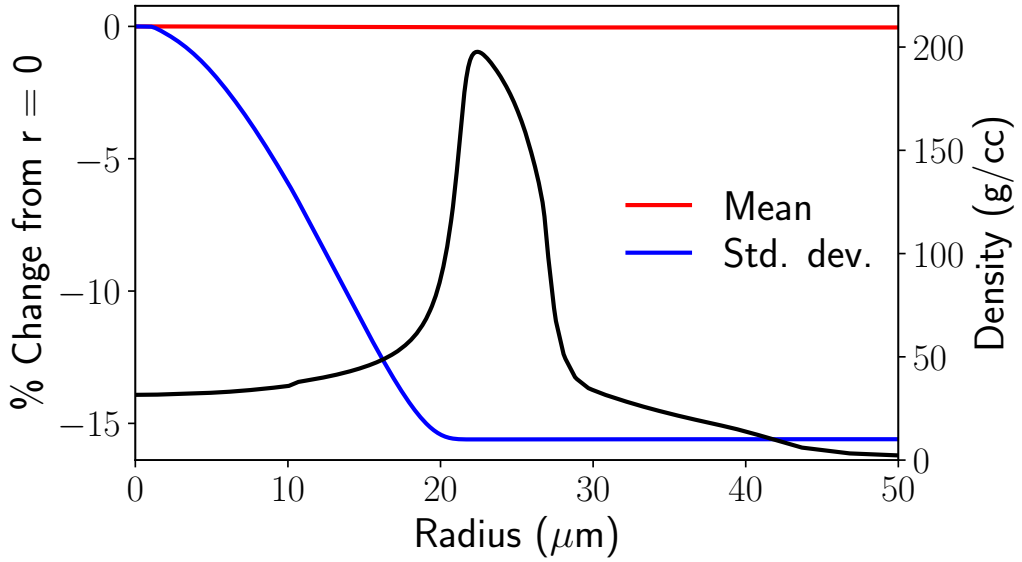

Figure 3.1: A plot of the percentage change in DT primary mean and standard deviation with radius for density and temperature profiles taken from a LILAC[44] simulation at bang time. Also shown is the density as a function of position. In the dense DT layer, changes in the primary spectrum cumulants are minimal.

Here we will consider the scattering source term as we did in Section 2.2.1. However, we will simplify the analysis by only considering backscatter events. For elastic collisions, energy and momentum conservation requires that the outgoing neutron energy is directly related to the pre-collision velocities and the scattering cosine, $\hat{\Omega}' \cdot \hat{\Omega} = \mu_0$. For a single ion velocity, the double differential cross section can therefore be written as[169]:

$$\frac{d^2\sigma_i}{dEd\Omega} = \frac{1}{2\pi}\frac{d\sigma_i}{d\mu_c}\left|\frac{\partial\mu_c}{\partial E}\right|\delta(\mu_0 - \mu^*) \ , \tag{3.4a}$$

subscript c denote terms in the centre of mass frame, μ^* is the lab frame scattering cosine which satisfies the conservation requirements. By only considering the backscatter geometry, where $\mu_0 = -1$, the neutron trajectory reduces to a single dimension and hence only depends on the parallel component of the ion velocity, as seen in Eq. 3.1a. Therefore, to include the summed total effect of a Maxwellian distribution of ion velocities,

$M(\vec{r}, v'_{i,\|})$, one integrates over $v'_{i,\|}$ with the associated distribution:

$$\frac{d^2\sigma_i}{dEd\Omega} = \int dv'_{i,\|} M(\vec{r}, v'_{i,\|}) \frac{1}{2\pi} \frac{d\sigma_i}{d\mu_c} \left| \frac{\partial \mu_c}{\partial E} \right| \delta(1+\mu^*) \ , \tag{3.4b}$$

$$\frac{d^2\sigma_i}{dEd\Omega} = \int dv'_{i,\|} M(\vec{r}, v'_{i,\|}) \left(\frac{d\sigma_i}{dE} \right)_{bs} \ . \tag{3.4c}$$

If the fluid velocity and ion temperature at coordinate $\vec{r}$ are $\vec{v}_f$ and T_i respectively, then the Maxwellian, $M(\vec{r}, v'_{i,\|})$, has mean $\vec{v}_f \cdot \hat{\Omega}$ and variance T_i/m_i.

Combining Eqs. 3.3 and 3.4c, the complete backscattering spectrum function is obtained:

$$I_{bs}(E, \hat{\Omega}) = \int dv'_{i,\|} \int d\tau_i \ \psi_b(\vec{r}, -\hat{\Omega}) M(\vec{r}, v'_{i,\|}) \int dE' \left(\frac{d\sigma_i}{dE} \right)_{bs} Q_b(E', -\hat{\Omega}) \ , \tag{3.5a}$$

note that the initial neutron direction has been set to satisfy the backscattering condition, i.e. $\hat{\Omega}' = -\hat{\Omega}$. The birth neutron flux at position $\vec{r}$ in direction $-\hat{\Omega}$ can be found via integration of the neutron production rate along chords. For a detector direction $\hat{\Omega}_{\text{det}}$, Fig. 3.2 shows the geometry of the integral expression in Eq. 3.5a.

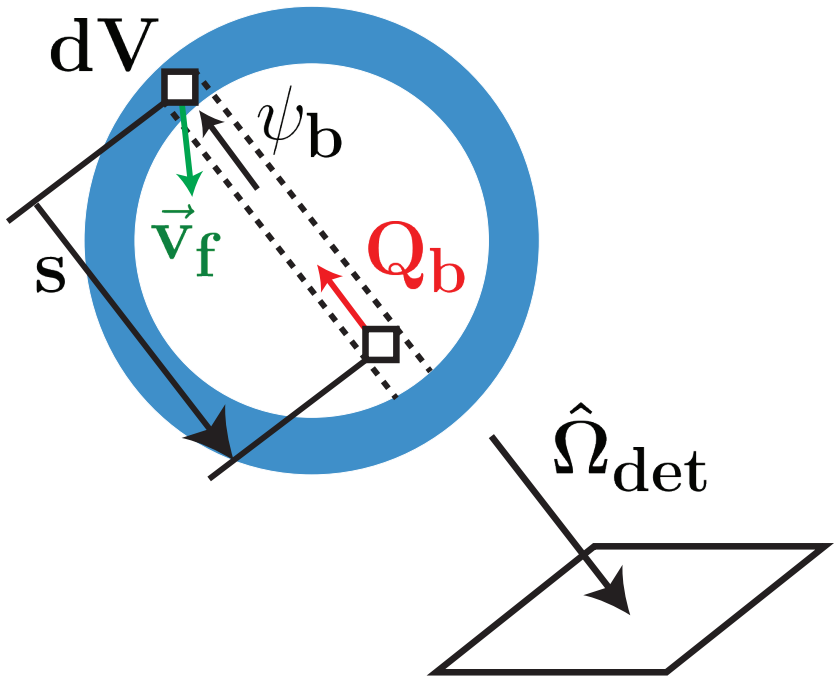

Figure 3.2: Diagram showing the geometry of the backscattered neutron source. Within the volume dV neutrons are backscattering towards the detector along the line of sight $\hat{\Omega}_{\text{det}}$. The flux of birth neutrons, ψ_b, reaching dV with energy spectrum Q_b are travelling along a chord in the direction $-\hat{\Omega}_{\text{det}}$. The ions in dV are assumed to have a Maxwellian distribution of velocities with fluid velocity $\vec{v}_f$ and temperature T_i.

Noting the separation of terms dependent on position and on neutron birth energy,

the integral can be expressed as an integral over ion velocity of two collected expressions:

$$I_{bs}(E,\hat{\Omega}) = C\int dv'_{i,\parallel} P(v'_{i,\parallel},\hat{\Omega}) Q_{bs}(v'_{i,\parallel},E,\hat{\Omega}) \ , \tag{3.5b}$$

$$\text{Where: } C = \int d\tau_i \ \psi_b(\vec{r},-\hat{\Omega}) \approx \langle \rho R/\bar{m}\rangle \, Y_n \ , \tag{3.5c}$$

$$P(v'_{i,\parallel},\hat{\Omega}) = \frac{1}{C}\int d\tau_i \ \psi_b(\vec{r},-\hat{\Omega}) M(\vec{r},v'_{i,\parallel}) \ , \tag{3.5d}$$

$$Q_{bs}(v'_{i,\parallel},E,\hat{\Omega}) = \int dE' \left(\frac{d\sigma_i}{dE}\right)_{bs} Q_b(E',-\hat{\Omega}) \ , \tag{3.5e}$$

where Y_n is the birth neutron yield and $\bar{m}$ is the average ion mass in the scattering medium.

Physically, $P(v'_{i,\parallel})$ is the normalised distribution of ion velocities seen by backscattering neutrons. This will change based on the hydrodynamic properties of the hotspot and fuel shell. Since the probability of scattering is proportional to the ion number density, $P(v'_{i,\parallel})$ will be weighted more strongly towards the densest parts of the capsule. Hence measurement of the spectral shape of the backscatter edge will allow inference of the properties of the dense fuel. This distribution is converted to a backscatter edge shape through the averaged differential cross section, Q_{bs}. This term is determined by the primary DT birth spectrum and the elastic scattering differential cross section.

In this work we will focus on the nT backscatter edge and hence the distribution of triton velocities. The theory above is general and applies for elastic scattering from any ion species. However, experimentally the nT edge is more accessible for current ICF target designs, as it has the greatest signal to background. Extra value is gained from the measurement of multiple backscatter edges. For example with both nT and nD edge measurements, separation of thermal and non-thermal broadening effects is possible due to the ion mass differences; a similar analysis exists for the DT and DD primary peaks [61, 133].

The classical expressions given in Eq. 3.1 are approximately correct however relativistic corrections are required in order to accurately find the position of the edge. This is due to the relativistic velocities of the DT primary neutrons ($\sim$ 0.17c). As shown in Fig. 2.10, for a 14 MeV neutron backscattering off a stationary triton ($A_i = 2.99...$) the classical and relativistic kinematic edges differ in energy by 20 keV, 3.483 MeV and 3.463 MeV respectively. Current nToF detectors have the energy resolution to detect these differences [116]. In this section we have only considered pure backscatter events, however scattering angles less than 180° must be considered in order to fully model the scattered neutron spectrum. This will be addressed in Section 3.1.3.1.

3.1.2 Measuring Implosion Dynamics Near Stagnation

As the capsule starts to stagnate it consists of three distinct regions: hotspot, shocked shell and free-falling shell [14]. The return shock acts as the boundary between the subsonic shocked material, composed of both the hotspot and shocked shell, and the

unshocked material, which is rapidly inflowing at the implosion velocity. The boundary between the hotspot and shocked shell will be taken as the 1 keV ion temperature contour in this work, although other definitions exist. Neutrons scatter within each of these regions and the scattering kinematics will be influenced by the different hydrodynamic properties. The relative fraction of areal density in each of these regions will determine the proportion of scattering occurring. Here we will discuss the properties for implosions with weak alpha-heating; they are still compressing during neutron production as there is insufficient heating to sustain fusion reactions during re-expansion[174]. The free-falling shell is cold ($\sim$ 100 eV) and imploding at or close to the implosion velocity ($\sim$ 300-500 km/s). The shocked shell is at a temperature of a few hundred eV and moving at several tens of km/s. Conditions within the hotspot change rapidly with radius; as the temperature drops with radius, the density rises and hence the scattering neutrons are more sensitive to conditions towards the edge of the hotspot.

Of central importance to the backscatter edge shape is the distribution of ion velocities seen by backscattering neutrons, $P(v'_{i,\|})$. In the following analysis we will relate the properties of this distribution to relevant hydrodynamic quantities. For a 1D spherical profile, Eq. 3.5d can be evaluated as follows:

$$P(v'_{i,\|}) \propto \int dt \int 4\pi r^2 dr\ n_i(r,t) \int d\mu\ \psi_b(r,\mu,t) M(r,\mu,t)\ , \tag{3.6a}$$

$$M(r,\mu,t) = \sqrt{\frac{m_i}{2\pi T_i(r,t)}} \exp\left[-\frac{m_i \left(v'_{i,\|} + v_f(r,t)\mu \right)^2}{2T_i(r,t)} \right]\ , \tag{3.6b}$$

$$\psi_b(r,\mu,t) = \int_0^\infty ds\ R_{DT}\left(\sqrt{r^2 - 2sr\mu + s^2}, t \right)\ , \tag{3.6c}$$

$$R_{DT}(r,t) = f_D f_T n_i^2(r,t) \langle \sigma v \rangle_{DT} \left(T_i(r,t) \right)\ , \tag{3.6d}$$

$$\text{where: } \mu = \hat{\Omega}' \cdot \hat{r}\ ,\ \phi_b(r,t) = \int d\mu\ \psi_b(r,\mu,t)\ ,$$

where f_D and f_T are the number fraction of D and T, $\langle \sigma v \rangle_{DT}$ is the DT reactivity[18] and the total birth flux, ϕ_b, has been defined here for later use. Using the above equations, $P(v'_{i,\|})$ can be calculated without the need for a neutron transport calculation. This method also allows for the individual contributions from the hotspot, shocked and free-falling shell to the shape of the backscatter edge to be examined separately. Within this section, subscripts HS, SS and FS will denote hotspot, shocked and free-falling shell respectively, total components will appear without a subscript.

By taking moments of Eq. 3.6a, expressions for the mean and variance, $\bar{v}$ and Δ_v^2, of

$P(v'_{i,\|})$ in terms of the appropriate average of hydrodynamic quantities are found:

$$\bar{v} = -\langle v_f \mu \rangle \ , \tag{3.7a}$$

$$\Delta_v^2 = \left\langle \frac{T_i}{m_i} \right\rangle + \langle v_f^2 \mu^2 \rangle - \bar{v}^2 \ , \tag{3.7b}$$

$$\text{Where: } \langle x \rangle = \frac{\int dt \int 4\pi r^2 dr \ n_i \int d\mu \ \psi_b \ x(r,\mu,t)}{\int dt \int dr \ 4\pi r^2 n_i \phi_b} \ , \tag{3.7c}$$

where Eq. 3.7c defines the scattering rate averaging used in Eqs. 3.7a and 3.7b for the hydrodynamic quantities.

Thus, from measurements of the backscatter edge, inferred $\bar{v}$ and Δ_v values can be interpreted in terms of the above scattering rate averaged hydrodynamic quantities. For a neutron point source, the scattering rate average reduces to:

$$\langle x \rangle_{\text{p.s.}} = \frac{\int dt \frac{dY_n}{dt} \int dr \ n_i x(r, \mu = 1, t)}{\int dt \frac{dY_n}{dt} \int dr \ n_i} \ , \tag{3.8}$$

i.e. a burn weighted areal density average, hence the quantities in Eqs. 3.7a and 3.7b can be approximated as such.

An extended neutron source reduces the contribution from the centre of the hotspot and introduces angular dependence to the neutron flux altering the effects of fluid velocity to the moments. To illustrate the angular dependence effect, we will use the uniform spherical source solution given in Eq. 2.131 (neglecting attenuation) to give average neutron directions ($\langle \mu \rangle$ and $\langle \mu^2 \rangle$) as a function of radius. These are shown in Fig. 3.3, we also show the averages for an isobaric hotspot with a parabolic temperature profile for comparison. We see that the angular averages monotonically increase the weighting of fluid velocities at larger radii. Outside the emitting region, $\langle \mu^2 \rangle$ tends to $\langle \mu \rangle^2$ as the spread of neutron directions reduces. Given that $\langle \mu \rangle < 1$, average fluid velocities inferred from $\bar{v}$ will be underestimates.

A more detailed understanding of the information contained in the backscatter edge can be found through analysis of radiation hydrodynamics simulations. In this work we will focus on simulations of the single[154] and triple[69] picket direct drive designs for OMEGA. These designs have been fielded experimentally and obtain high hotspot pressures and neutron yields[70]. In particular the triple and single picket shots 87653 and 89224 will be considered. In addition to the pulse shape differences, 89224 is a faster target (480 km/s compared to 390 km/s of 87653) leading to a higher burn-averaged ion temperature (4.8 keV compared to 3.8 keV of 87653). The simulations were performed by the 1D hydrodynamics code LILAC[44].

The triple picket design aims to minimize the shock preheating of the fuel and hence achieve a low in-flight adiabat [155]. This allows a high peak density to be achieved in the fuel shell at stagnation. Therefore an increased fraction of the neutrons will scatter in the shell compared to the hotspot. The bangtime profiles for the LILAC simulation of shot 87653 are shown in Fig. 3.4. See Fig. 3.5 for the bang time hydrodynamic conditions

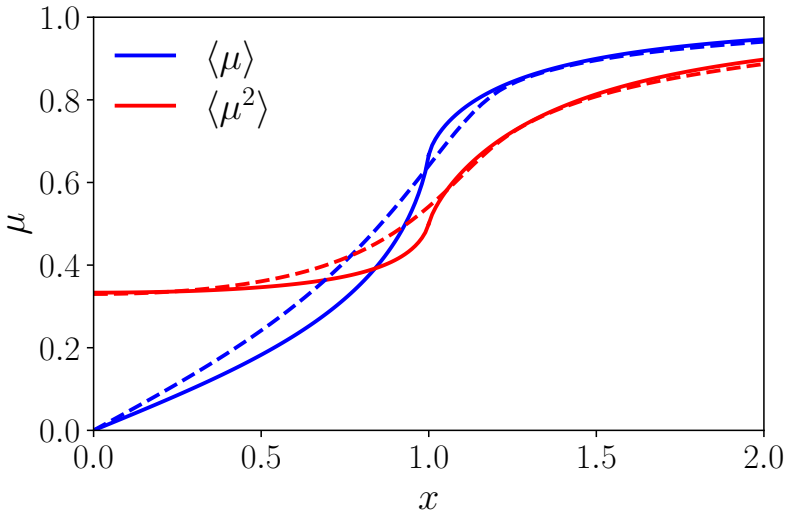

Figure 3.3: Plot showing the mean and mean of the squared neutron direction for the uniform hotspot (solid line) and isobaric parabolic temperature profile (dashed line) cases as a function of normalised radius $x = r/R$. The normalising radius, R, was set to enclose 90% of the neutron emission in the parabolic temperature profile case.

for 89224 as calculated by LILAC, this shot will be discussed further in the following paragraphs. Also shown is the angular integrated scattering rate, i.e. the averaging used in calculating $\bar{v}$ and Δ_v. It follows the density profile closely outside the hotspot, showing that an areal density average is a good approximation in this region. Comparing the scattering and burn rate it is clear that the primary and scattered neutrons sample different regions. Nearly all primary neutrons are created in the hotspot and a considerable fraction ($> 50\%$) of neutrons scatter in the shell regions. Hence the scattered neutron spectrum contains information of the hydrodynamic properties in regions of the stagnated capsule that are inaccessable via primary neutron measurements.

The dynamics of the return shock is important in determining the conditions in the shocked shell and hotspot. Figure 3.6 tracks the return shock and hotspot positions during neutron production. The Rankine-Hugoniot (RH) shock conditions (given in Eqs. 2.7 to 2.9) can be used to find the post-shock hydrodynamic properties given the upstream conditions and shock velocity. As discussed earlier, the upstream or free-falling shell has a fluid velocity close to the implosion velocity and a low temperature. An approximate set of shock conditions in the lab frame can be obtained by assuming the upstream pressure is negligible. We will relax this assumption later in this chapter but here it allows us to find the basic physical relationships brought about by the return shock:

$$v_f = \frac{\gamma - 1}{\gamma + 1} v_{imp} + \frac{2}{\gamma + 1} v_s \ , \tag{3.9}$$

$$T = \frac{2\,(\gamma - 1)}{(\gamma + 1)^2} \frac{\bar{A}}{Z + 1} \cdot m_p \left(v_{imp} - v_s\right)^2 \ . \tag{3.10}$$

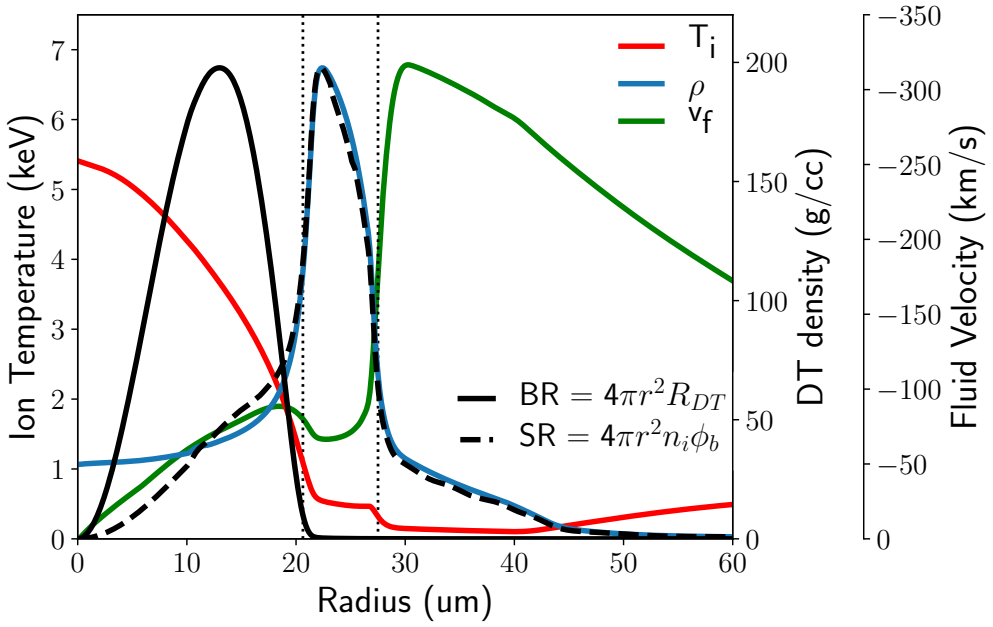

Figure 3.4: The bang time hydrodynamic (density ρ, ion temperature T_i and fluid velocity v_f), burn rate (BR) and scattering rate (SR) profiles for the LILAC simulation of shot 87653. The vertical dotted lines show the position of the hotspot edge and return shock. The hotspot edge occurs at a temperature of 1 keV and the return shock at the maximal velocity gradient.

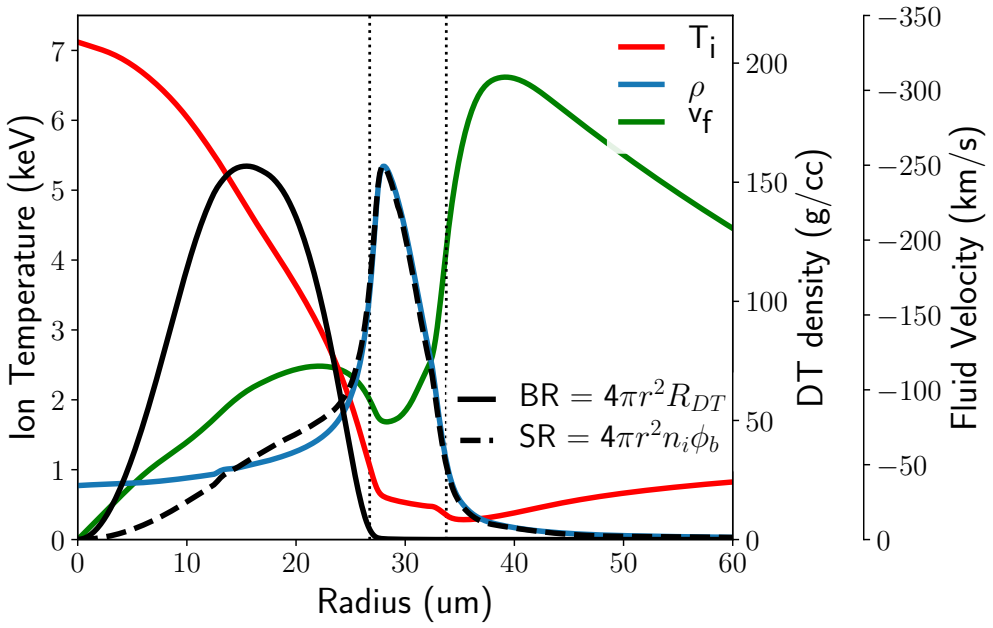

Figure 3.5: The bang time hydrodynamic (density ρ, ion temperature T_i and fluid velocity v_f), burn rate (BR) and scattering rate (SR) profiles for the LILAC simulation of shot 89224. The vertical dotted lines show the position of the hotspot edge and return shock. The hotspot edge occurs at a temperature of 1 keV and the return shock at the maximal velocity gradient. Hydrodynamic quantities on same scales as in Fig. 3.4.

The post-shock fluid velocity and temperature are v_f and T and the implosion and shock velocity are v_{imp} and v_s. We have used the strong shock limit and a fully ionised ideal gas equation of state. The neglected degeneracy corrections to the pressure are $< 10\%$ at stagnation from LILAC simulations of the two shots considered. From these equations we see that the post shock conditions are dependent on only the implosion and shock velocities. If the conditions are uniform, $\gamma = 5/3$, and the shock velocity is negligible, we can manipulate these equations to find expressions for $\bar{v}$ and Δ_v for the nT edge:

$$\bar{v} = v_f = \frac{1}{4} v_{imp} \ , \tag{3.11}$$

$$\Delta_v^2 = \frac{T}{3m_p} = \frac{\bar{A}}{32} v_{imp}^2 \ . \tag{3.12}$$

However, the hydrodynamic conditions vary spatially and temporally during neutron production as can be seen in Figs. 3.4 and 3.6. The shock conditions therefore cannot fully explain the scattering ion velocity distribution moments.

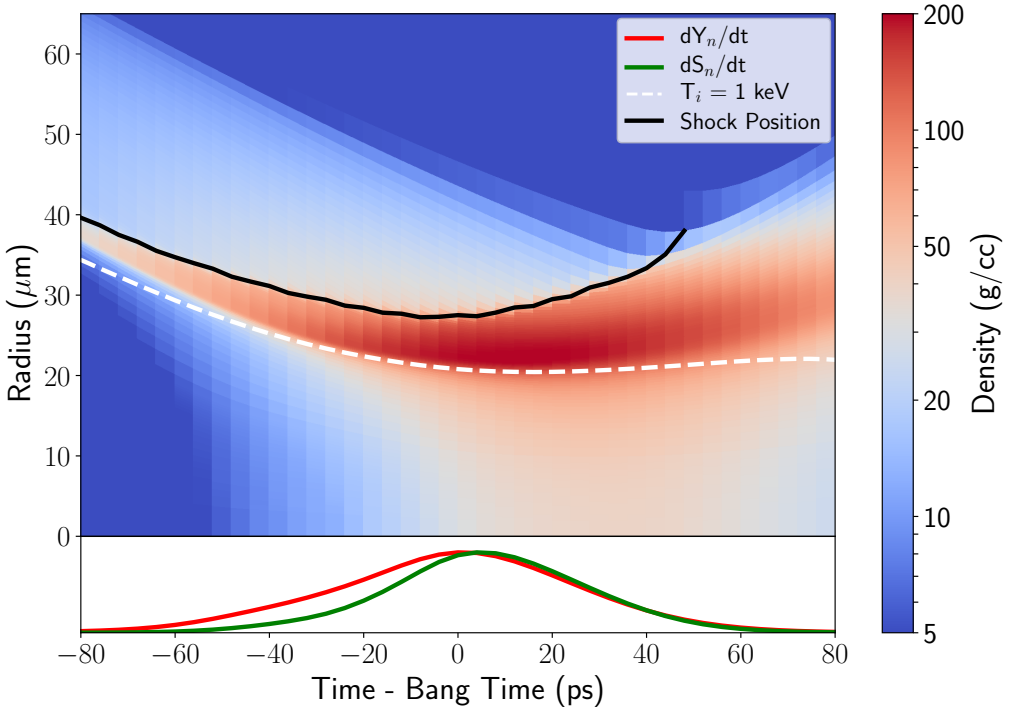

Figure 3.6: Plot showing the stagnation phase from the LILAC simulation of shot 87653. The colour plot shows the density, on a log scale, as a function of radius and time with the position of the return shock and 1 keV contour overlaid. At the bottom of the plot, the birth (red) and scattering (green) rates are shown as a function of time.

Given the capsule conditions throughout neutron production, calculation of $P(v'_{i,\parallel})$ and the resultant backscatter edge shape can be performed, see Fig. 3.7. The individual contributions to $P(v'_{i,\parallel})$ from the hotspot, shocked and free-falling shell as well as the total mean and variance are given in Table 3.1. The positive $\bar{v}$ causes an upshift in the

energy of the backscatter edge. The non-zero Δ_v causes an additional broadening of the edge over the slight broadening due to the variance in the birth neutron energy.

The single picket design uses a pre-pulse designed to increase the adiabat to reduce hydrodynamic instability growth [68]. A consequence of increased adiabat is reduced shell compressibility and hence a lower peak density is achieved in the shell at stagnation. Therefore an increased fraction of the neutrons will scatter in the hotspot compared to the shell. The calculated $P(v'_{i,\parallel})$ and backscatter edge shape for the LILAC simulation of shot 89224 are shown in Fig. 3.8. The individual contributions to $P(v'_{i,\parallel})$ from the hotspot, shocked and free-falling shell as well as the total mean and variance are given in Table 3.1.

From analysis of these two LILAC simulations some general remarks can be made about the various contributions to $\bar{v}$ and Δ_v. Differences in these quantities can then be attributed to the physical processes which govern the individual behaviour of the hotspot, shocked and free-falling shell.

Table 3.1: Relative contributions from the three regions of the capsule to the scattering ion velocity distribution for simulations of the triple and single picket shots 87653 and 89224. Data for Δ_v^2 have been converted to units of eV via the triton mass (Δ_v^2 (eV) $= m_T(\Delta_v$ (km/s))^2) to aid comparison with scattering rate averaged temperatures, $\langle T_i \rangle$.

	Hotspot	Shocked Shell	Free-Falling Shell	Total
87653 - Triple Picket				
Scatter fraction	33%	50%	17%	-
$\bar{v}$ / km/s	34	40	255	75
Δ_v^2 / eV	2878	784	555	1644
$\langle T_i \rangle$ / eV	2770	522	207	1206
89224 - Single Picket				
Scatter fraction	45%	45%	10%	-
$\bar{v}$ / km/s	45	52	252	69
Δ_v^2 / eV	3606	1107	1130	2359
$\langle T_i \rangle$ / eV	3396	544	475	1829

For $\bar{v}$, it was seen that in both cases the subsonic velocities of the hotspot and shocked shell are within 10 km/s of each other. The free-falling shell is considerably faster therefore a return shock which is less far through the fuel at bang time will cause higher $\bar{v}$ values. However generally $\lesssim 20\%$ neutrons scatter in this region so $\bar{v}$ is closer to the velocity of the shocked fuel. Using the shocked and unshocked $\bar{v}$ values[2] and Eq. 3.9, a shock velocity can be calculated as follows:

$$v_s = \frac{1}{3}\bar{v}_{FS} - \frac{4}{3}\bar{v}_{SS} \ . \tag{3.13}$$

This gives 32 and 15 km/s, radially outward, shock velocities for 87653 and 89224 respectively. These are in agreement with the shock velocities in the hydrodynamics

[2]Remembering that a minus sign is needed when switching between $\bar{v}$ and fluid velocity.

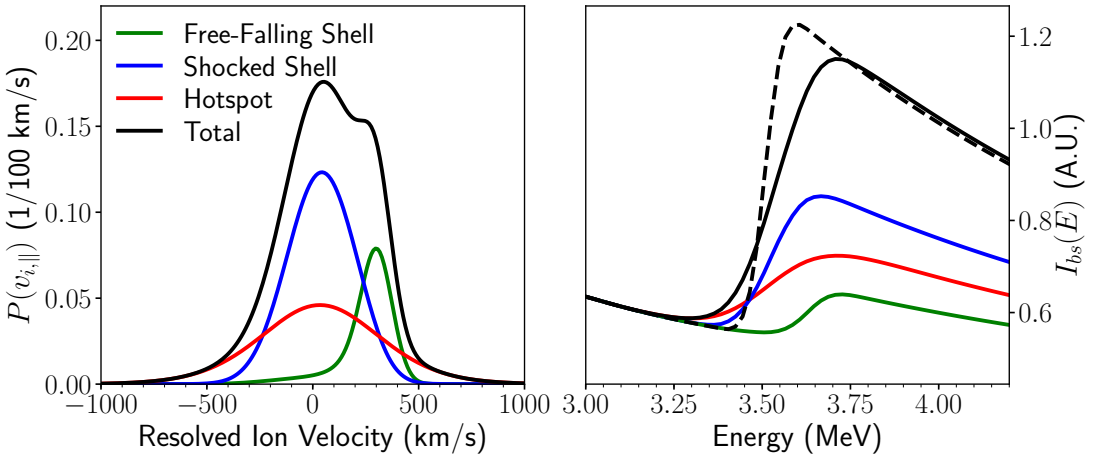

Figure 3.7: For shot 87653: the scattering triton velocity distribution as measured by backscattering neutrons (left) and the resultant single scattered spectral shape around the nT backscatter edge (right). The contributions from each region of the capsule are shown individually. (Right) The dashed black line shows the spectral shape if the velocities of the scattering ions are ignored.

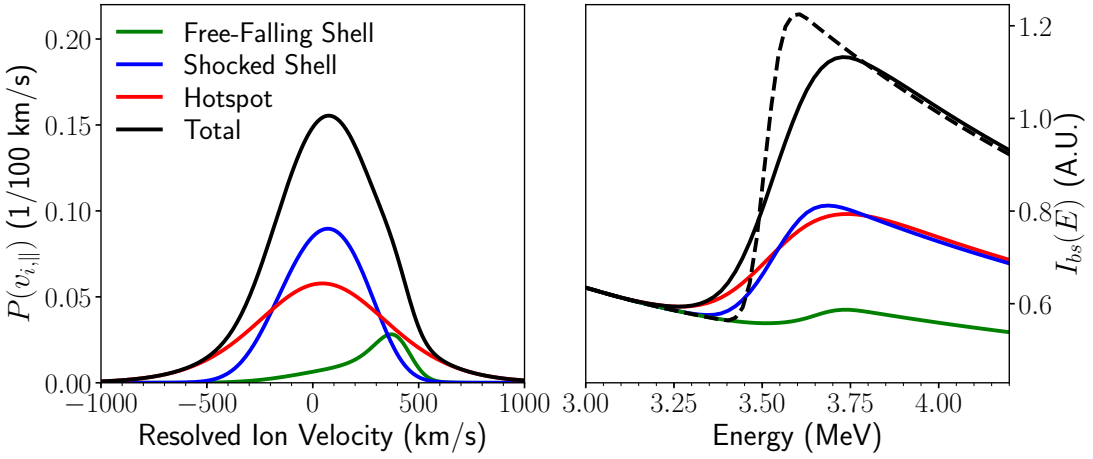

Figure 3.8: For shot 89224: the scattering triton velocity distribution as measured by backscattering neutrons (left) and the resultant single scattered spectral shape around the nT backscatter edge (right). The contributions from each region of the capsule are shown individually. (Right) The dashed black line shows the spectral shape if the velocities of the scattering ions are ignored.

simulations at bang time to within a factor of ~ 2. As the shell implodes, it performs mechanical (PdV) work on the hotspot. Loss mechanisms, such as radiative cooling, must be balanced by compressive and alpha heating. Hence a high rate of mechanical work at bang time indicates both low alpha heating and high losses. Using measurements of hotspot pressure[32] and radius, $\bar{v}$ can be used to calculate the rate of PdV work through an isobaric hotspot approximation:

$$W_{\text{mech}} = 4\pi P_{HS} R_{HS}^2 \bar{v} \ . \tag{3.14}$$

The mechanical power was found to be 4.1 (3.8) and 6.2 (7.1) TW for 87653 and 89224 respectively, where bracketed terms are those calculated directly from the hydrodynamics simulations without approximation. Hence by combining measurements from the backscatter edge and current hotspot diagnostics, the work being done on the hotspot by the imploding shell at bang time can be calculated.

For Δ_v^2, ion temperature is the dominant source of ion velocity variance in the hotspot, whereas both temperature and fluid velocity variance are significant for the shell. This leads to approximately 25% of the total Δ_v^2 being due to fluid velocity variance. For comparison, approximately 10% of the apparent ion temperature as measured by the width of the primary DT peak[5, 11, 23, 132] is due to fluid velocity variance in these simulations.

The scattering rate averaged temperature, $\langle T_i \rangle$, depends on multiple factors within the stagnating capsule. If the shell density is lower, i.e. higher stagnation adiabat, a larger fraction of neutrons will scatter within the hotspot, increasing the $\langle T_i \rangle$. Comparing the triple and single picket simulations, we find scatter weighted adiabats of 7.5 and 11.0 respectively within the shocked shell. Similar fractional change is seen in the total Δ_v^2 for these simulations. Additionally if the temperature gradient at the edge of hotspot is higher this will also cause an increase in the $\langle T_i \rangle$ of the fuel. While it's difficult to predict, with simple models, the temperature profile between hotspot and shocked shell, the return shock heating of the shell is more easily described. Again, we invoke the RH conditions using Eqs. 3.10 and 3.13:

$$T = \frac{\bar{A}}{6} m_p \left(\bar{v}_{FS} - \bar{v}_{SS} \right)^2 \ , \tag{3.15}$$

from which we obtain shocked shell temperatures of 201 and 174 eV for 87653 and 89224 respectively, a factor of ~ 3 underestimate. The assumption of negligible pre-shock pressure is the likely cause for this. Considering an ideal gas with $\gamma = 5/3$, we can obtain a more general expression for the post-shock temperature if we do not invoke a strong shock limit. To do this we will introduce the Mach number M, defined as follows:

$$M^2 \equiv \frac{v^2}{c_s^2} = \frac{\rho v^2}{\gamma P} \ , \tag{3.16}$$

where c_s is the adiabatic sound speed. The pre-shock Mach number can be used to

calculate the shock strength and the general RH jump conditions [49, 170, 192]:

$$\zeta \equiv \frac{P_{SS}}{P_{FS}} = \frac{5M_{FS}^2 - 1}{4} \ , \tag{3.17}$$

$$\frac{v_{FS}}{v_{SS}} = \frac{\rho_{SS}}{\rho_{FS}} = \frac{4\zeta + 1}{\zeta + 4} \ , \tag{3.18}$$

$$\frac{T_{SS}}{T_{FS}} = \frac{\rho_{FS}}{\rho_{SS}} \frac{P_{SS}}{P_{FS}} = \frac{\zeta + 4}{4\zeta + 1} \cdot \zeta \ . \tag{3.19}$$

The strong shock limit is given by $\zeta \to \infty$. Unfortunately we now require the pre-shock temperature in order to evaluate the post-shock temperature. From simulation, the pre-shock Mach numbers are approximately 2.2 and 1.5 at bang time for 87653 and 89224 respectively. This predicts post-shock temperatures of 486 and 710 eV by using the $\langle T_i \rangle$ of the pre-shock material (shown in Table 3.1 in the free-falling shell column and corresponding $\langle T_i \rangle$ rows). The values obtained are generally in better agreement with the $\langle T_i \rangle$ of the shocked shell from simulations, as shown in Table 3.1 in the shocked shell column and corresponding $\langle T_i \rangle$ rows. The larger inaccuracy for 89224 is likely due to the lower percentage of free-falling shell remaining during neutron production giving a larger averaged pre-shock temperature, see Fig. 3.5.

Shock physics can explain the hydrodynamic conditions either side of the return shock at any one instant. However, there are many processes occurring which are not predicted purely through the RH conditions. These include subsonic time evolution; spatial gradients in conditions pre- and post-shock; thermal conduction and mass ablation. Therefore, deviations from pure shock predictions are expected – although these predictions do provide good estimates and bounds on stagnation conditions.

The fluid velocity variance can be due to both variation in space and time. Using the 87653 simulation, we will visualise the effect of fluid velocity variance on $P(v'_{i,\parallel})$ by neglecting the thermal velocity of the ions. Calculating $P(v'_{i,\parallel})$ at bang time is used to quantify the spatial contribution and the time-integrated calculation includes both spatial and temporal components. The results are shown in Fig. 3.9. Several sources of fluid velocity variance can be identified in both the time-resolved and time-integrated results. A large source of spatial velocity variance is due to the fluid velocity jump across the return shock, this appears as a double peaked $P(v'_{i,\parallel})$. A less clear source of variance is due to the range of scattering neutron directions due to the extended source. This is especially clear in the hotspot, where $\langle \mu^2 \rangle - \langle \mu \rangle^2$ is the largest, see Fig. 3.3. The time-integrated result shows much larger variance in scattering ion velocity due to fluid velocity. This is due to deceleration of the scattering regions, on top of the spatial fluid velocity variance apparent in the time-resolved case

Estimates of the fluid velocity variance can be found using simple models which describe the dominant processes affecting the fluid velocity. To first order, the temporal variation is due to the average deceleration of the shell, $\langle a \rangle$, throughout neutron pro-

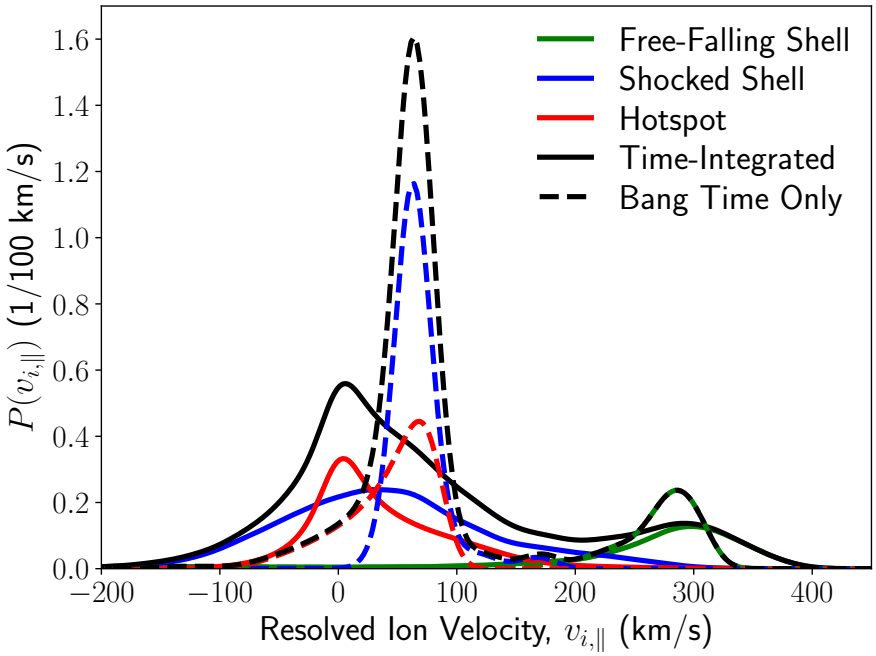

Figure 3.9: The scatter weighted triton velocity distribution from LILAC simulation of shot 87653 where the effect of temperature has been neglected. The solid lines show the time-integrated result and the components due to free-falling shell, shocked shell and hotspot. The dashed curves show the time-resolved result at bang time.

duction, this can be estimated by the following:

$$\mathrm{Var}\left(v_f\mu\right)_t \approx 300\left[\left(\frac{\langle a\rangle}{1\times10^{15}\mathrm{m/s^2}}\right)\left(\frac{BW}{100\mathrm{ps}}\right)\right]^2 \mathrm{eV}\ , \tag{3.20}$$

where BW is the nuclear burn width and the velocity variance has been converted to units of eV via the triton mass.

Spatial variations in fluid velocity in the shell are generally dominated by the difference in velocities across the return shock. This can be estimated by assuming the return shock is approximately stationary in the lab frame and satisfies the strong shock conditions. Defining the fraction of shocked areal density, χ_{sh}, and the pre-shock velocity, v_{imp}:

$$\mathrm{Var}\left(v_f\mu\right)_s \approx 300\left[\frac{9}{16}\chi_{sh}\left(1-\chi_{sh}\right)\left(\frac{v_{\mathrm{imp}}}{100\mathrm{km/s}}\right)^2\right]\mathrm{eV}\ . \tag{3.21}$$

The fraction of shocked areal density will depend on the position of the return shock through the fuel and the pre-shock velocity is determined by the implosion velocity at the beginning of the deceleration phase. The return shock position also affects $\bar{v}$, which can be approximated in a similar fashion:

$$\bar{v} \approx \frac{4-3\chi_{sh}}{4}v_{\mathrm{imp}}\ . \tag{3.22}$$

This approximation considers only the deceleration across the shock. Post-shock, the fuel continues to compress and decelerate, leading to a lower average fluid velocity than predicted by shock conditions.

A preliminary study using an ensemble of 100 LILAC simulations was made to further investigate the trends shown for the selected shots 87653 and 89224. These were post-processed to extract the scattering rate weighted ion velocity distributions. These were split into contributions from hotspot, shocked and free-falling shell therefore yielding 11 values per simulation (scatter fraction, ion velocity mean and variance for each region and the totals). It is worth noting that the total $\bar{v}$ and Δ_v are, by definition, related to the components as follows:

$$\bar{v} \equiv \chi_{HS}\bar{v}_{HS} + \chi_{SS}\bar{v}_{SS} + \chi_{FS}\bar{v}_{FS} \ , \tag{3.23}$$

$$\Delta_v^2 + \bar{v}^2 \equiv \chi_{HS}\left(\Delta_{v,HS}^2 + \bar{v}_{HS}^2\right) + \chi_{SS}\left(\Delta_{v,SS}^2 + \bar{v}_{SS}^2\right) + \chi_{FS}\left(\Delta_{v,FS}^2 + \bar{v}_{FS}^2\right) \ , \tag{3.24}$$

where the scatter fraction is denoted with χ, the total shocked fraction χ_{sh} is equal to $\chi_{HS}+\chi_{SS}$ and the sum of all three scatter fractions is 1. Without further manipulation, Fig. 3.10 shows the correlation matrix for these different values across all 100 LILAC simulations. The presence of many strong correlations and anti-correlations between the

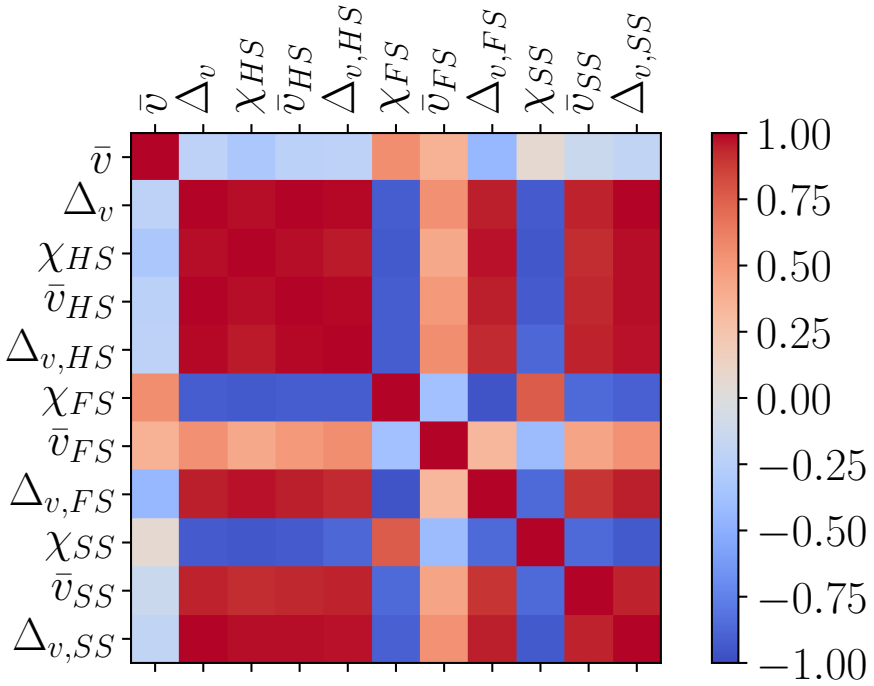

Figure 3.10: The correlation matrix of the scattering rate weighted ion velocity distribution components from 100 1D LILAC simulations. Strong correlations and anti-correlations are seen therefore suggesting a more fundamental relationship between the components. The total $\bar{v}$ stands out as the only component with poor correlations with all other components.

various components indicates a more fundamental underlying relationship between the values. There is certainly further analysis that could be performed to better understand

the physical relations between the scattering ion cumulants. Simplified hydrodynamic models, such as those described in Betti *et al.* [14] and Christopherson *et al.* [35], could aid in this analysis. These include the hotspot, shocked shell and free-falling shell components and capture the dynamics of the return shock. Alternatively, one could extract more information from the LILAC ensemble such as the average shock speed, shell deceleration and shock strength to relate with the scattering weighted quantities. Understanding these physical relations will allow a physically motivated fitting model to be constructed which goes beyond the empirical Gaussian approximation made for the scattering ion velocity distribution.

3.1.3 Neutron Spectral Shape Model

Since the nD and nT backscatter edges occur at low neutron energies, there are multiple sources of background. For the nT edge these include; TT primary neutrons, nD single scattering, the D(n,2n) and T(n,2n) break up reactions and multiple scattering. Thus a general model is required in order to evaluate the shape of the edge and backgrounds. Due to the complexity of the backgrounds at lower neutron energies, *ad-hoc* models have been opted for to fit the neutron background under the DD peak [74] and in previous work on the nT edge [42]. However, for fitting backscatter edges, the background is only constrained at lower energies after the edge, where no single scatter signal for that ion species exists. Therefore, a more constraining *ab-initio* model is favoured to ensure the spectral shape under the edge is physical.

While scattering from remaining carbon-based ablators in indirect drive experiments can contribute $\sim 1\%$ to the 10-12 MeV neutron spectrum[95], it has a much smaller contribution at lower energies, see Fig. 2.19. DT fusion neutrons elastically scattering once from carbon have a lower energy limit of 10 MeV due to carbon's high mass, $A_i \approx 12$. The highest cross section inelastic scattering, which produces a 4.4 MeV γ-ray, has a neutron lower energy limit of 6 MeV. Therefore ablator scattering can be neglected in fitting the nT edge.

3.1.3.1 Integral Model

With knowledge of the differential cross sections of the various nuclear interactions, the distribution of scattering ion velocities, and the birth neutron energy spectrum, the full scattered neutron spectrum can be approximated. The same simplifying assumptions used to obtain an expression for the spectral shape of the backscatter edge, Eq. 3.5a, can be used for a general scattering angle for elastic scattering interactions. For complex inelastic processes, such as the (n,2n) reactions, the effect of the ion velocity distribution has not been included. Since these reactions produce a broadband spectrum of neutrons for every scattering angle, the relative effect of ion velocities on the spectral shape is reduced. By assuming isotropy in areal density and birth spectrum, the single

interaction components to the spectra are given by:

$$I_{1s}(E) = \int dv'_{i,\parallel} P(v'_{i,\parallel}) \int dE' \frac{d\sigma_i}{dE}(E', v'_{i,\parallel}) Q_b(E') \ . \tag{3.25}$$

Multiple interaction events can be treated in a similar fashion to the single interaction terms, however the source term is no longer the birth neutrons and is instead replaced by the scattered neutron source. In addition, the averaged ion velocity distribution seen by neutrons undergoing multiple scatters will be different to the distribution seen by singly scattered neutrons. As the scattering rate is $\propto n_i \psi$ where ψ is the neutron flux to be scattered, the difference between the spatial and angular distribution of the birth and singly scattered neutron fluxes will alter the scattering rate weighted ion velocity distribution. Here the zeroth order approximation of stationary ions will be used:

$$I_{2s}(E) = \int dE' \frac{d\sigma_i}{dE} \left(E', v'_{i,\parallel} = 0\right) I_{1s}(E') \ . \tag{3.26}$$

The cross sections for the (n,2n) inelastic scattering processes rapidly decrease near their threshold energies, see Fig. 2.6. Therefore double inelastic scattering events can be neglected – a numerical analysis performed by Minotaur showed double inelastic events are $\sim 10^{-3}$ of the scattered signal at OMEGA cyro areal densities. The various components of the single and double scatter models are shown in Fig. 3.11a.

The primary TT neutrons contribute to the spectral background below 9 MeV. Using the ratio of the DT and TT reactivities, the TT yield is calculated from the DT yield and the inferred burn averaged ion temperature:

$$Y_{TT} = \frac{1}{2} \frac{f_T f_T \cdot \langle \sigma v \rangle_{TT}(\langle T \rangle_{DT})}{f_D f_T \cdot \langle \sigma v \rangle_{DT}(\langle T \rangle_{DT})} Y_{DT} \ . \tag{3.27}$$

The temperature dependent shape of the TT spectrum has been evaluated by Appelbe [6] and hence can be included in the model with relative ease. The single scattering of the TT neutrons is then evaluated in an identical manner to the single scattering of the DT neutrons. Figure 3.11b shows a comparison of the single scatter model with and without TT scattering against a Minotaur calculation.

The complete spectral model for the fitting of the backscatter edge includes the following contributions; single interactions (nT, nD, D(n,2n), T(n,2n)) of the DT and TT neutrons including the effects of scattering ion velocities, double interactions of the DT neutrons, and the uncollided TT neutrons. The model can be written as the following fitting function:

$$I_{bs}(E) = A_{1s} I_{1s}(E, \bar{v}, \Delta_v) + A_{2s} I_{2s}(E, \bar{v}, \Delta_v) + A_{TT} I_{TT}(E) \ . \tag{3.28}$$

The amplitudes will have the following dependencies: $A_{1s} \propto \rho\mathrm{R}$, $A_{2s} \propto (\rho\mathrm{R})^2$ and $A_{TT} \propto \exp(-\sigma\rho\mathrm{R})$. Given proper normalisation of I_{1s} to area per unit energy, areal density can be inferred via $\rho\mathrm{R} = \bar{m} A_{1s}$. The scattering terms have been written as

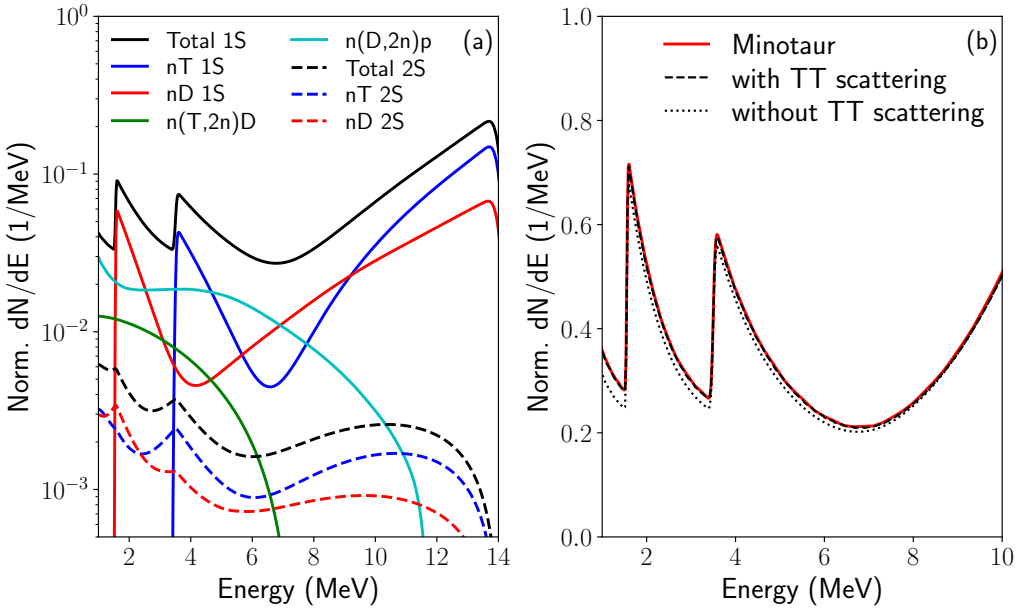

Figure 3.11: (a) Plot showing the various components of the single and double scatter model with stationary ions for a Brysk DT birth spectrum. The single scatter components are scaled such that they integrate up to their respective cross sections. (b) Plot showing a comparison between the single scatter model with and without TT scattering against a Minotaur calculation.

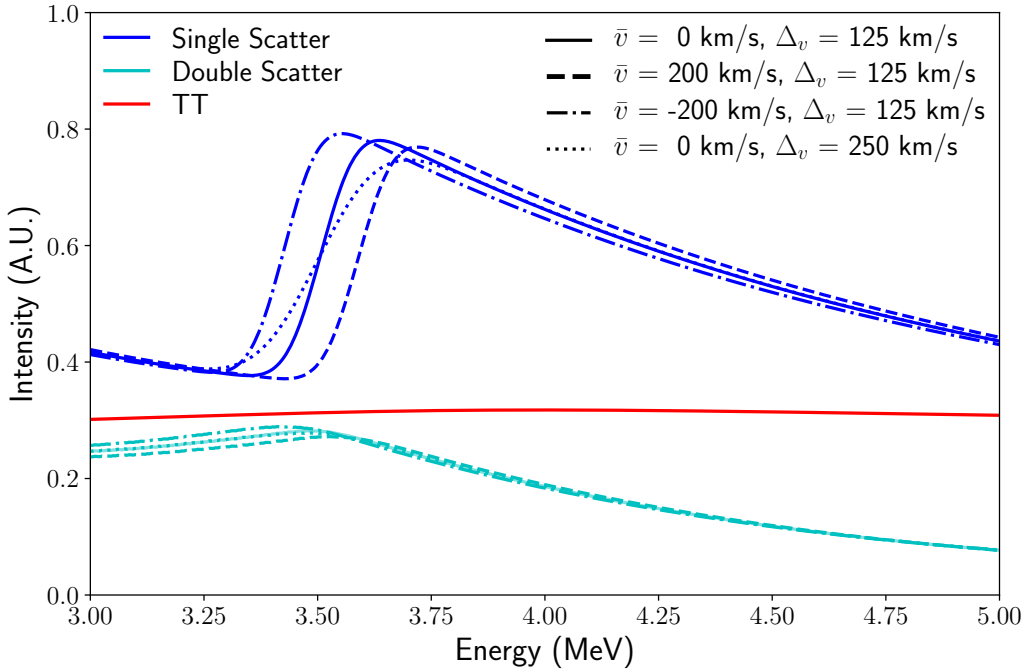

Figure 3.12: The components of the spectral model given in Eq. 3.28 for various $\bar{v}$ and Δ_v values. The scattering ion velocity distribution was assumed to have a Gaussian functional form with mean $\bar{v}$ and standard deviation Δ_v.

functions of the cumulants of the scattering ion velocity distribution, $P(v'_{i,\|})$. In order to fit experimental data some functional form needs to be assumed for $P(v'_{i,\|})$. A Gaussian approximation has been shown to produce reasonable results on synthetic data[42], also see Figs. 3.7 and 3.8. Figure 3.12 shows the various model components for various $\bar{v}$ and Δ_v values within the single Gaussian model for $P(v'_{i,\|})$. More complex models, such as three Gaussians for the hotspot, shocked shell and free-falling shell respectively, could be used to infer more information about the stagnated capsule but requires many free parameters to be set.

Experimental measurements of the underlying spectral shapes and differential cross sections have been made for a number of reactions included in this model: the nD and nT single scattering at $\sim$ 14 MeV[55]; the TT primary spectrum [27] and the D(n,2n) reaction at $\sim$ 14 MeV [52]. Theoretical models[33, 64] in agreement with these measurements are then used to cover all neutron energies. For the T(n,2n) reaction, limited neutronic experimental data are available and hence there is a larger uncertainty in its spectral shape.

3.1.3.2 Synthetic Data Comparison

Synthetic neutron spectra, which include transport effects excluded from the simplified spectral model (Eq. 3.28) can be produced based on hydrodynamic profiles. Comparisons between synthetic data and the model will serve as the first test towards experimental viability of this model.

For the first case we will consider the LILAC simulation for the shot 87653, see Figs. 3.4 and 3.7. This has a burn-averaged ρR of 218 mg/cm^2 for which the attenuation of the primary DT spectrum is $< 2\%$ and approximately 1% of scattered neutrons undergo triple scattering. Hence many of the assumptions made are valid at this areal density. The analysis of the edge was performed in a similar fashion to an experimental analysis, although in energy rather than time-of-flight space. First, the primary DT peak was fit in order to estimate the birth spectrum shape. Then non-linear least-squares fitting of the spectrum is performed using the Levenberg–Marquardt algorithm on both sides of the nT edge (between 3 and 5 MeV), extending the range previously used in Crilly *et al.*[42]. Using the $P(v'_{i,\|})$ shown in Fig. 3.7, excellent agreement is seen between the model and synthetic data with at most $\sim$ 0.5% deviation, the results are shown in Fig. 3.13. Using the single Gaussian approximation for $P(v'_{i,\|})$ showed at most $\sim$ 1% deviation between model and synthetic data. This produced best fit values of $\bar{v}$ and Δ_v of 72 and 214 km/s compared to the theoretical values of 75 and 229 km/s; the discrepancies can be attributed in part to non-Gaussian components of $P(v'_{i,\|})$.

The same analysis was followed for shot 89224, which has a burn-averaged ρR = 162 mg/cm^2. The deviation between model and synthetic data was again $\sim$ 1%. The single Gaussian model found best fit $\bar{v}$ and Δ_v values of 70 and 254 km/s compared to the theoretical values of 69 and 274 km/s. Therefore the accuracy error introduced in $\bar{v}$ and Δ_v by the approximations made is $< 10\%$. At OMEGA the timing uncertainty in the

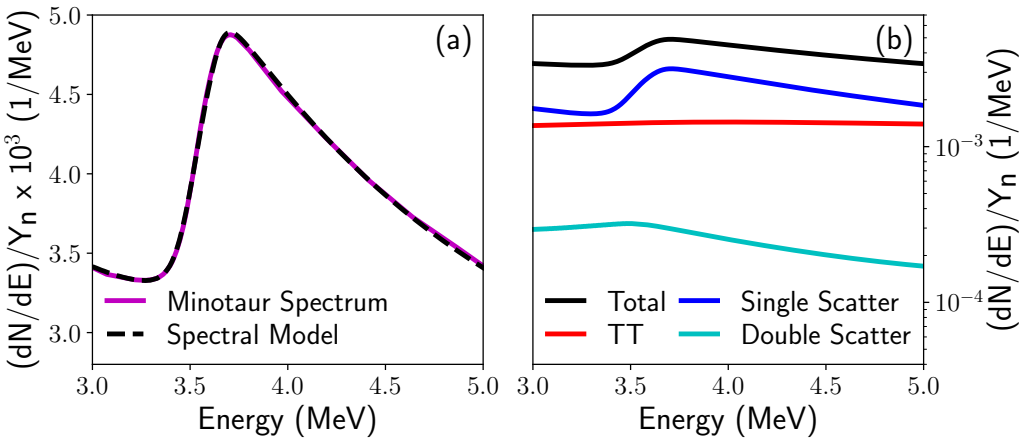

Figure 3.13: (a) A comparison of the synthetic neutron spectra calculated by Minotaur and the spectral model solution. (b) A plot showing the components of the spectral model over the fitting range. All individual components are within 10% of their equivalent neutron transport result.

nToFs is ~ 56 ps [116]. At 3.5 MeV this leads to neutron velocity (energy) uncertainty of ~ 3.5 km/s (1 keV). Given the results from synthetic data and experimental uncertainty, analysis of experimental data for similar OMEGA shots can be carried out with the model presented [117].

Higher areal densities will reduce the signal to background for the backscatter edge as well as introduce additional backgrounds and non-negligible attenuation. To test the validity of the assumptions made within the model, neutron spectra were calculated for a set of scaled isobaric profiles with ρRs of 0.25, 0.5, 0.75 and 1.0 g/cm^2. By scaling self-similar profiles it is ensured that the averaged hydrodynamic properties, e.g. burn-weighted ion temperature, of the DT fuel are unaltered between different areal densities. A pressure of 100 Gbar, central temperature of 6 keV with a parabolic spatial profile and shell temperature of 300 eV were used. Fits to the synthetic spectra are shown in Fig. 3.14. Good agreement between the total model and the synthetic spectra is found across the whole fitting range for all areal densities.

Agreement between the individual components of the fit (uncollided primary TT, single and double scattering) and the equivalent neutron transport component gives confidence that the underlying physical phenomena are well modelled. For $\rho R = 0.5$ g/cm^2, an average deviation of 14% is found between the amplitude of the single scatters in the model and the equivalent neutron transport result. At higher areal densities, triple scattering and differential attenuation cause increasing deviation between the components of the model and synthetic spectra. Therefore interpretation of the various amplitudes of the backgrounds, A_{1s}, A_{2s} and A_{TT}, in the model as physical parameters is lost. The complete model however still performs well as an ad-hoc fitting function and measurement of $\bar{v}$ and Δ_v is possible at higher areal densities.

These results suggest that the model developed in this work could be used to fit experimental spectra at 0.5 g/cm^2 (DSR $\sim 2.5\%$) and potentially up to 0.75 g/cm^2 (DSR

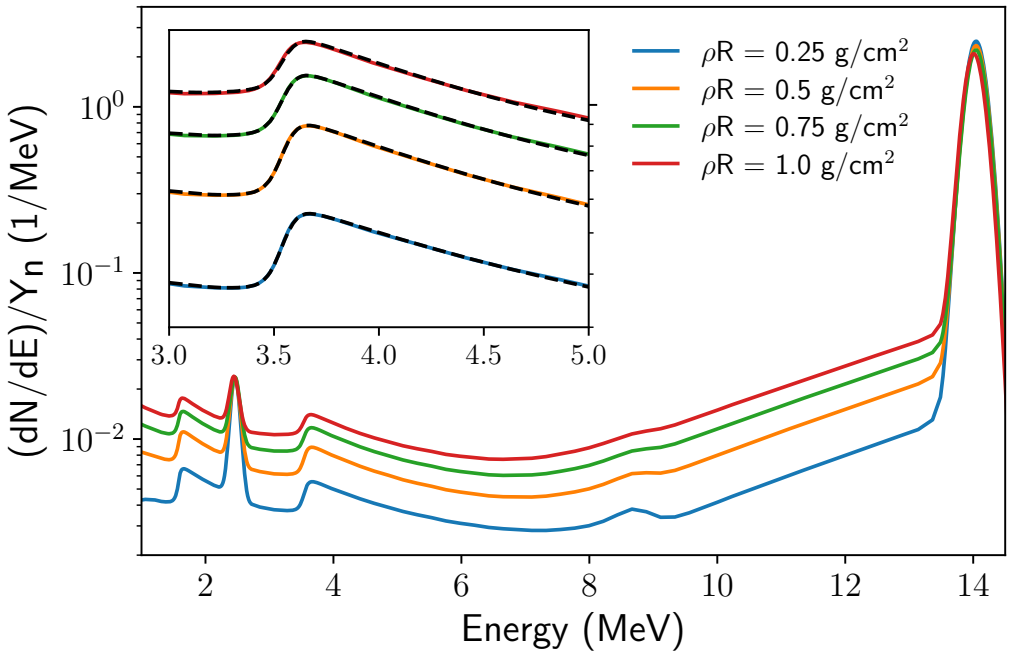

Figure 3.14: Synthetic neutron spectra calculated by Minotaur for four isobaric profiles with varying ρR. The inset plot shows more detail around the nT backscatter edge and the spectral model fits to this region in the dashed black lines.

$\sim 3.8\%$) if requirements on physicality of the underlying components of the background are relaxed. Inclusion of triple scattering and attenuation effects would allow access to even higher areal densities with confidence in the physical basis of the ab-initio model.

3.1.4 Multidimensional Effects

Whilst the preceding analysis has focussed on 1D implosions, in reality ICF experiments are subject to many instabilities and perturbations which preclude a spherical implosion. The scattered neutron spectrum will still be affected by the velocity distribution of the ions, however now different lines of sight will sample regions of the capsule with different hydrodynamic conditions. Asymmetries in the measured $\bar{v}$ would indicate asynchronous stagnation of the shell. Variation in Δ_v could be due to differences in the shell deceleration[42] and/or angular variation in fuel temperatures.

A radiation-hydrodynamics simulation performed by the code Chimera[34, 174] will be used here to illustrate how anisotropy in hydrodynamic conditions manifests within the scattering ion velocity distribution. The time integrated spectrum from a capsule implosion with a P1 asymmetry will be considered. The magnitude of the drive asymmetry, 3% P1/P0, used in the Chimera simulation caused a 60% reduction in neutron yield compared to the symmetric case and produced a 130 km/s neutron-averaged (see Eq. 2.78) hotspot velocity. A 2D slice in the x-z plane of the simulation at bang time is shown in Fig. 3.15. This presents a scenario where, when viewed along the +z axis (denoted as +z line of sight), the detected primary neutrons are shifted up in energy,

but the neutrons travelling towards the back of the capsule are down shifted. The backscattered neutrons will then receive a positive energy shift from the fluid velocity of the shell. Hence the shifts from the hotspot and from the shell are oppositely directed. When viewed along the opposite direction (−z line of sight) both the shifts act to increase the backscattering neutron energy, albeit with a different shell velocity magnitude. Combining spectra from antipodal lines of sight will allow the calculation of separate hotspot and shell velocities. The primary spectra measured constrain the spectrum of neutrons arriving at the backscattering sites. As a result no additional assumptions need to be made about the birth spectrum used to fit the edges.

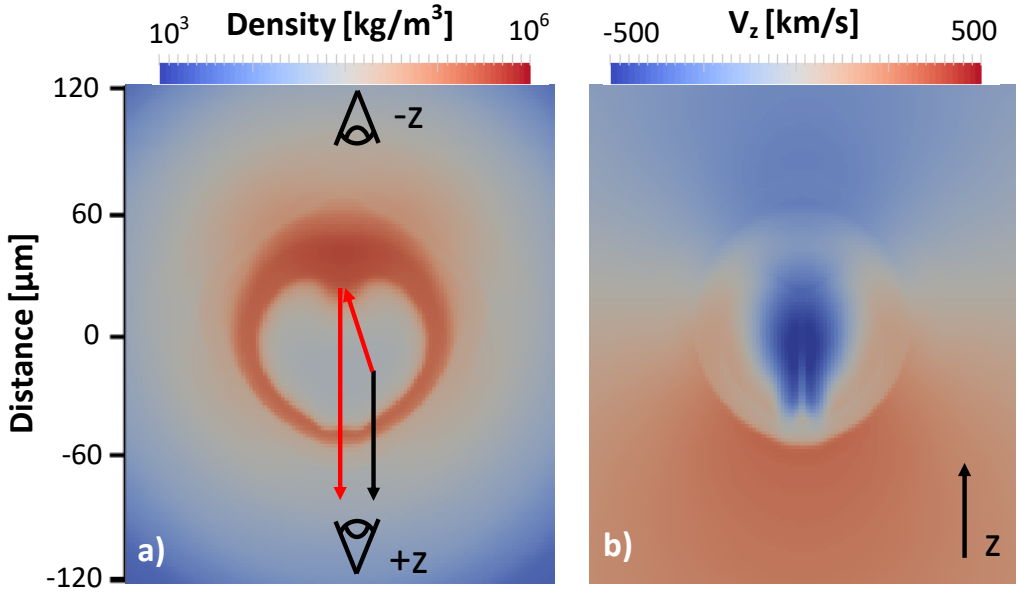

Figure 3.15: P1 simulation at bang time. **a)** Density cross section showing hotspot and perturbed dense shell. For a single fluid element, the paths of primary neutrons (black) and backscatter neutrons (red) are shown. Primaries are seen parallel to the fluid velocity, and backscattered neutrons are emitted anti-parallel to the hotspot flow. Thus they will have oppositely directed Doppler shifts. An additional up shift in energy will be caused by the fluid velocity of the shell which is parallel to the detector direction. Detector lines of sight are shown and labelled. **b)** z-component of fluid velocity within the x-z plane showing large bulk fluid velocity along -z.

The neutron transport was performed by AKED with the effects of fluid motion turned on and off to provide a comparison. Ion temperature effects on scattering are not included in AKED but will be discussed later in this section. Portions of the resulting spectra are shown in Fig. 3.16. The bulk fluid motion has produced the expected shifts of both primary and backscatter edge spectra. The Down Scattered Ratios (DSRs) predict ρR = 0.77 and 0.30 g/cm^2 along the +z and -z axes respectively. This areal density difference is mirrored in the intensity of the backscatter edges showing the mode 1 asymmetry.

Analysis performed in Crilly *et al.*[42] on these spectra used an earlier iteration of the

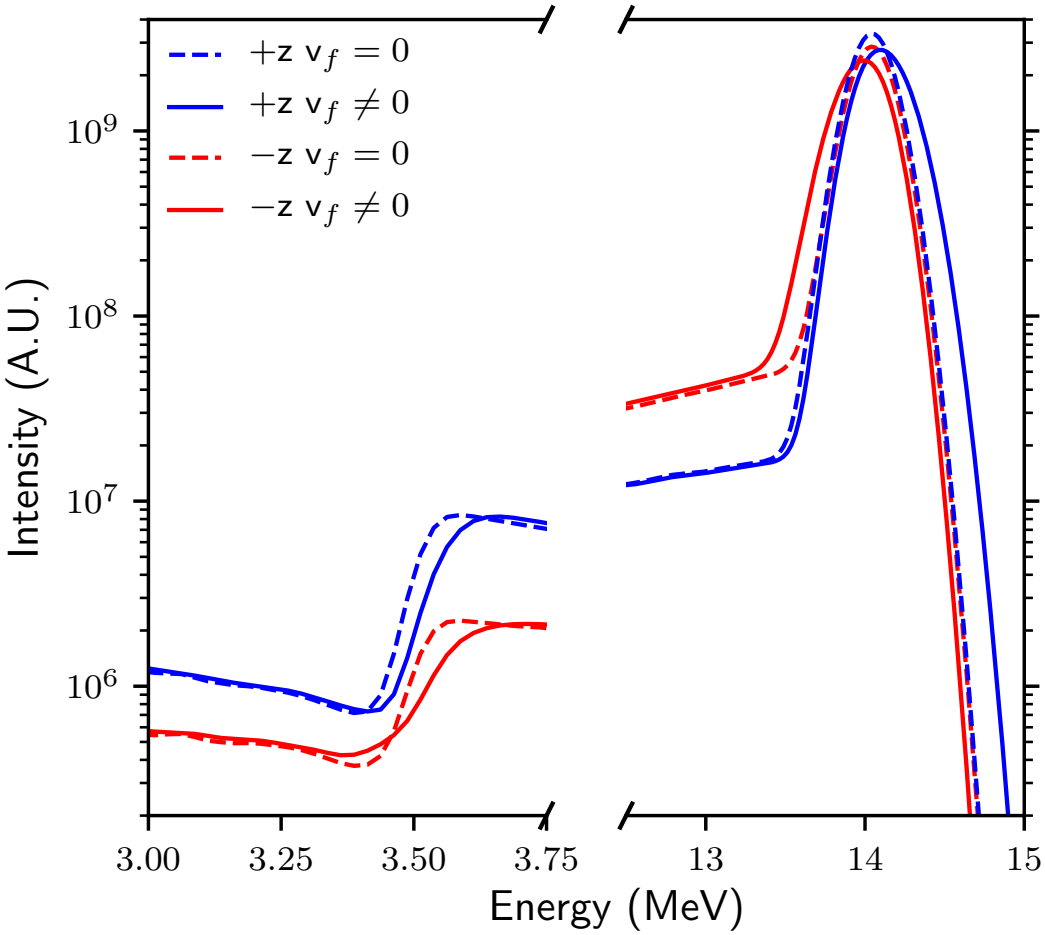

Figure 3.16: The neutron spectra produced by a P1 perturbed implosion. The +z detector line of sight is anti-parallel to the bulk fluid motion in the hotspot. Spectra along this line of sight are plotted in blue and the anti-podal line of sight in red. The spectra with the effects of fluid motion, v_f, neglected are plotted with dashed lines. Shifts and variance changes in the primary spectra are due to hotspot residual kinetic energy. For the backscatter edges, the shifts and variance changes are due to a combination of the hotspot and shell velocities.

fitting model than the one given in Eq. 3.28. This more primitive model used a Gaussian distribution of ion velocities, however the differential cross section was assumed isotropic and an ad-hoc background model was used. The derivation and detail of the model will be given in an Appendix C.2. The model was able to extract $\bar{v}$ and Δ_v values of 130/50 km/s and 40/90 km/s for the $+/-$ z lines of sight respectively. The ad-hoc background model was able to handle the areal density asymmetry present – the 1D model (Eq. 3.28) relies on spherical symmetry so cannot be used in this case.

To link these 3D results with the 1D analysis presented in previous sections, Fig. 3.17 shows the scattering ion velocity distributions as seen by two antipodal detectors along the axis of the P1 drive asymmetry. From the $+z$ direction, a faster shell is observed as this side of the capsule has been driven harder by the drive asymmetry. From the $-z$ direction, a slower shell is observed as well as the presence of a free-falling shell component. Averaged shell velocities, $\bar{v}$, of 160 and 78 km/s from $+z$ and $-z$ respectively. This agrees with the projected fluid velocity seen by neutrons with scattering angles in the range $180^o \pm 10^o$ calculated within the inverse ray trace of AKED. Asymmetry in $\bar{v}$ will create anisotropy in work done causing ineffective conversion to internal energy within the hotspot. This results in residual kinetic energy which is evident in this case due to the large hotspot velocities. The lower $\bar{v}$ values obtained by fitting the spectra (130 and 40 km/s) can be explained by the simplified nature of the fitting model. Due to the assumption of isotropic centre of mass frame scattering, the fit becomes invalid at energies above the edge where the scattering angles are less than 180^o. Therefore larger fluid velocities which create a greater shift in the kinematic edge are not well captured within this approximation.

Extending beyond previous work by the inclusion of the thermal velocity of the ions, Δ_v^2 values of 784 and 1591 eV were found from $+z$ and $-z$ respectively. The scatter weighted temperatures of 552 and 1110 eV reveal that the difference in Δ_v^2 between detectors is due to both differences in dense fuel temperatures as well as differential deceleration of the shell. In summary, large anisotropy in both $\bar{v}$ and Δ_v^2 were found therefore demonstrating the backscatter edge measurement could assist in identifying 3D asymmetries in the dense fuel.

As seen in our P1 example, centre of mass motion of the hotspot occurs in asymmetric implosions and causes the birth spectrum to be anisotropic[5, 75, 116, 132]. Backscattered neutrons were initially moving in the opposite direction to the detector line of sight. Hence knowledge of the "reverse" birth spectrum is required in order to analyse the backscatter edge. In previous work [42], also presented above, this was resolved by using antipodal detectors. However without this detector arrangement the reverse birth spectrum can be approximated if the neutron averaged fluid velocity vector is measured. This measurement is currently performed at the NIF[75] and OMEGA[116, 118] and requires at least four neutron spectrometers. For the detector measuring the backscattered neutron spectrum, a measurement of the apparent ion temperature is also required. Using the notation of Munro[132], the centroid and variance of the reverse birth spectrum

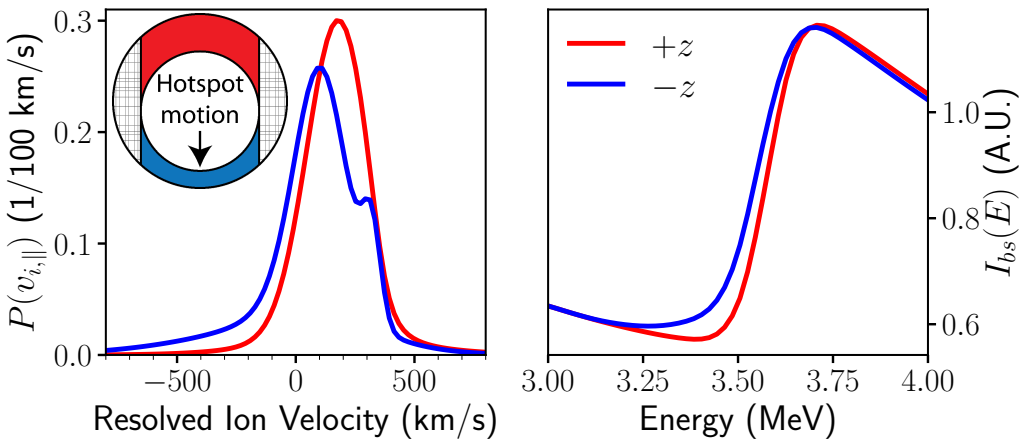

Figure 3.17: (Left) The scattering ion velocity distributions from two antipodal lines of sight for a hydrodynamics simulation of an indirect drive High Foot implosion with an imposed P1 X-ray drive asymmetry[42]. Inset is a schematic showing the regions of the implosions sampled by the different lines of sight. The $+z$ side, in red, has been driven harder due to the drive asymmetry. (Right) The resultant single scattered spectral shapes around the nT backscatter edge for the two lines of sight. Note the different shifts and slopes for the different lines of sight due to asymmetry in $\bar{v}$ and Δ_v^2 values.

can be approximated by:

$$\langle\omega\rangle_b = \langle\bar{\kappa}\rangle + \langle\vec{u}\rangle_i\hat{\Omega}_{b,i} + ... \approx \langle\bar{\kappa}\rangle - \langle u\rangle_i\hat{\Omega}_{d,i} \approx \langle\omega\rangle_d + 2\langle u\rangle_i\hat{\Omega}_{d,i} \ , \tag{3.29a}$$

$$\mathrm{Var}(\omega)_b = \langle\tau\rangle + \mathrm{Var}(\vec{u})_{ij}\hat{\Omega}_{b,i}\hat{\Omega}_{b,j} + ... \approx \mathrm{Var}(\omega)_d \ , \tag{3.29b}$$

$$\text{where: } \hat{\Omega}_{b,i} = -\hat{\Omega}_{d,i} \text{ for backscatter.}$$

Figure 3.18 shows the geometric interpretation of these relations. In the above approximations higher order terms and the effect of scattering have been neglected. Absolute errors in the inferred reverse birth spectrum have a reduced effect due to the mass difference between neutron and scattering ion, see Eq. 3.1 a-c. For example, errors in the mean birth energy are reduced by a factor of 4 for the nT edge.

Similar to the measurement of hotspot velocity, mode 1 asymmetry of the fluid velocity of the shell can be measured by 4 spectrometers if it is assumed to have the following form:

$$\vec{v}_{shell} = (\vec{v}_{asym} \cdot \hat{r} + v_{iso})\hat{r} \ . \tag{3.30}$$

The purely radial velocity is required so that the average angle between neutron and fluid velocity is the same in every line of sight. Then 4 measurements of $\bar{v}$ can be decomposed into v_{iso} and $\vec{v}_{asym}$. The isotropic component is compressive while the asymmetric part is purely residual kinetic energy. The optimal detector arrangement for this measurement is the same as for the hotspot velocity measurement. A brief discussion of optimal detector arrangements is given in Appendix C.1.

Large areal density asymmetries present an issue for the spectral background model if a broad energy range of the neutron spectrum is considered. Restricting to $\sim$ 3-5 MeV

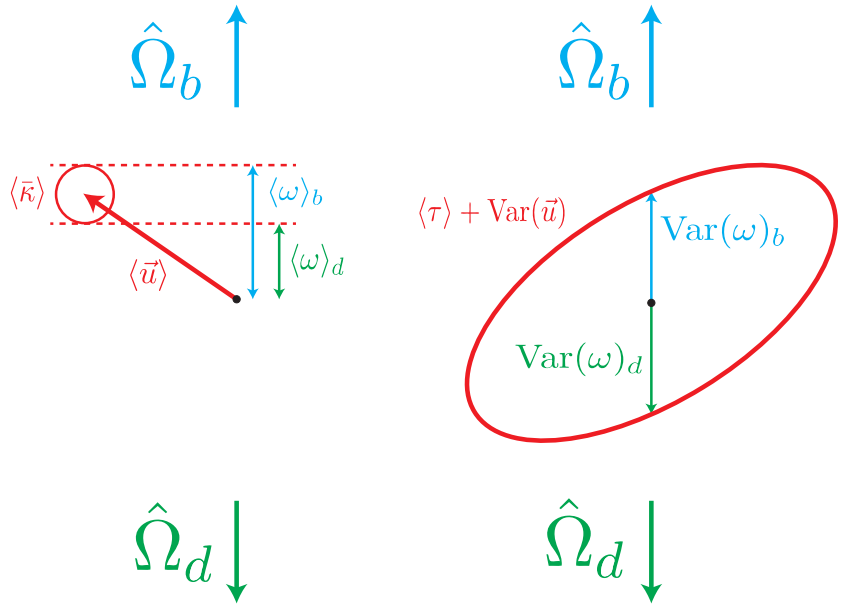

Figure 3.18: Diagrams showing how the forward and reverse DT (or DD) birth spectrum mean and variance are related. Neglecting higher order terms and scattering effect, the variances are equal whereas the means take different components of the vector component.

reduces the scattering angle range for the elastic processes (nT and nD). The large aspect ratio of hotspot size to shell thickness also acts to reduce the range of neutron averaged areal densities seen[42]. For the (n,2n) reactions a single incoming neutron energy and scattering angle produces a broad band of outgoing neutron energies. Hence near the nT edge the (n,2n) background has been produced in all 4π of solid angle, thus has a much weaker dependence on ρR asymmetries. Further development of the detailed model to include the effect of strong ρR asymmetries is required. 3D measurements of ρR from neutron spectrometers[95] or FNADs[15, 190, 191] could be used to inform this analysis.

3.2 Downscattered Spectrum from Areal Density Asymmetries

The degree of down scatter of DT fusion neutrons is often used as a measure of areal density. This is done through a DSR measurement which is converted to an areal density through a fit to 1D neutron spectra [56, 95]. To recap, the DSR is defined as the ratio of neutron yields in ranges [10 MeV, 12 MeV] and [13 MeV, 15 MeV]. When considering 3D effects, the energy-angle relation for elastic scattering is a vital reference. For stationary ions, incoming and outgoing neutron energies E' and E are related through the scattering cosine, μ_0, and ion-neutron mass ratio, A_i:

$$\frac{E}{E'} = \left(\frac{\mu_0 + \sqrt{\mu_0^2 + A_i^2 - 1}}{A_i + 1} \right)^2 . \tag{3.31}$$

The areal density traversed by the downscattering neutrons is therefore at an angle to the line of sight [95]. For a given energy range, this defines a cone of scattering over which a neutron-averaged areal density is measured, see Fig. 3.19. The line of sight areal density is only experienced by the un-scattered or low scattering angle neutrons. This draws a distinction between areal density measurements from primary neutrons, such as the FNADs, and scattered neutrons, such as the nTOFs. Energy gating and spectra can use this geometric feature of elastic scattering to measure different spatial regions of the implosion, this will be explored in Section 4.2.

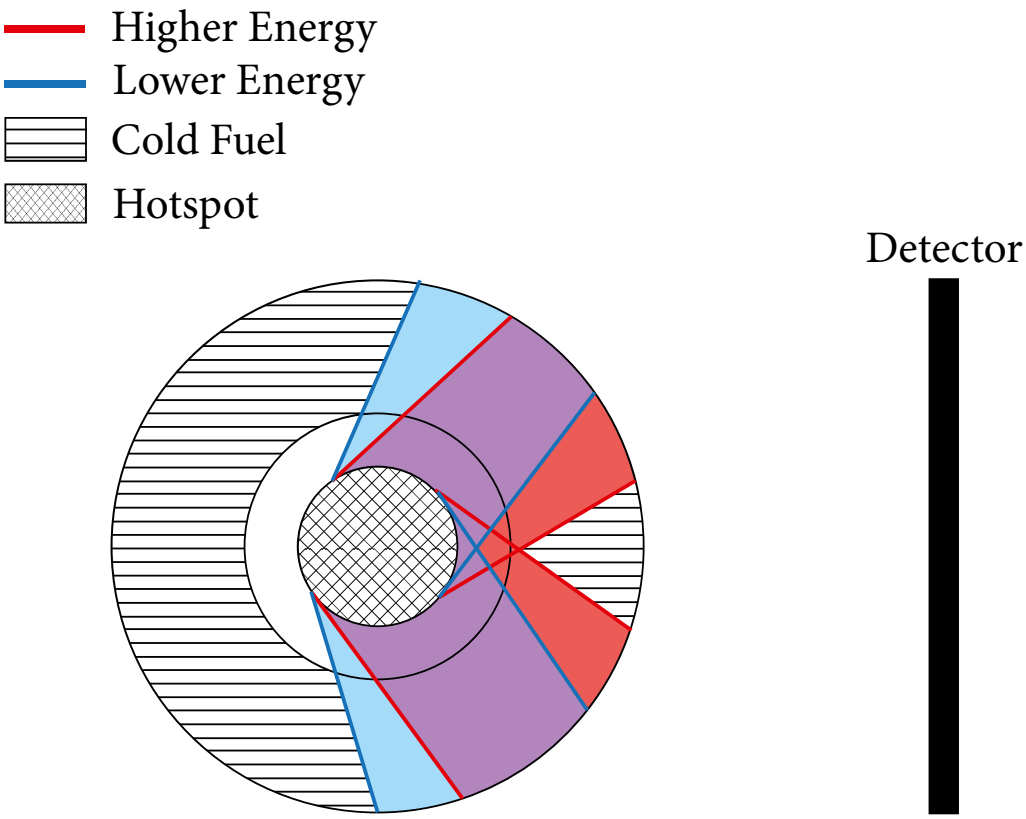

Figure 3.19: Diagram showing two scattering cones for two different energy gates. Scale of hotspot and cold fuel has been altered to emphasise the scattering cone geometry. Due to an extended source there is overlap between the available scattering regions. Higher energy scattered neutrons will sample regions at a lower angle to the detector line of sight. The reverse is true for lower energy scattered neutrons. For a 14 MeV neutron the scattering angles from D (T) down to 10 and 12 MeV are 47.5^o (59.5^o) and 31.9^o (39.5^o) respectively.

Variations in plasma conditions may influence the slope of the scattered spectrum. The shape of down scatter spectrum is set by the differential cross section, the energy distribution of the scattering neutrons and the areal density of the scattering medium. As the spectrum down to 10 MeV is dominated by elastic scattering from DT [42], changes of spectral shape in this region could indicate fuel areal density asymmetry. Reducing to the simplest case of a monoenergetic, $E' = E_0$, point source in an arbitrary

single species density distribution, the singly scattered neutron spectrum is given by:

$$I_{1s}(E,\hat{\Omega}) \propto Y_n \langle \rho R \rangle \frac{d\sigma}{d\Omega}(\mu_0(E_0,E)) \ , \tag{3.32}$$

$$\langle \rho R \rangle = \int d\phi \int d\mu \int dr \ \rho(\vec{r}) \delta(\mu - \mu_0(E_0,E)) \ , \tag{3.33}$$

where the $\langle \rho R \rangle$ integral defines the scattering cone for scattering cosine μ_0. Therefore, with knowledge of the differential cross section, the azimuthally averaged areal density at varying polar angles can be inferred. Multiple species, birth energy spectra and spatial source distributions complicate the resulting downscattered spectrum, however the underlying principle still holds.

To illustrate this effect with realistic source and areal density asymmetries, the neutron spectrum for an implosion with a P2 drive asymmetry will be considered, see Fig. 3.20. The magnitude of the drive asymmetry, 3% P2/P0, used in the Chimera simulation was such that the neutron yield was close to experimental values (3.19×10^{15} without alpha-heating). The positive P2 asymmetry created a larger ρR along the waist compared to the poles. However, due to the hotspot being greatly distorted, the areal density experienced on average by a neutron leaving the capsule differs significantly from the ρR taken from the simulation centre point.

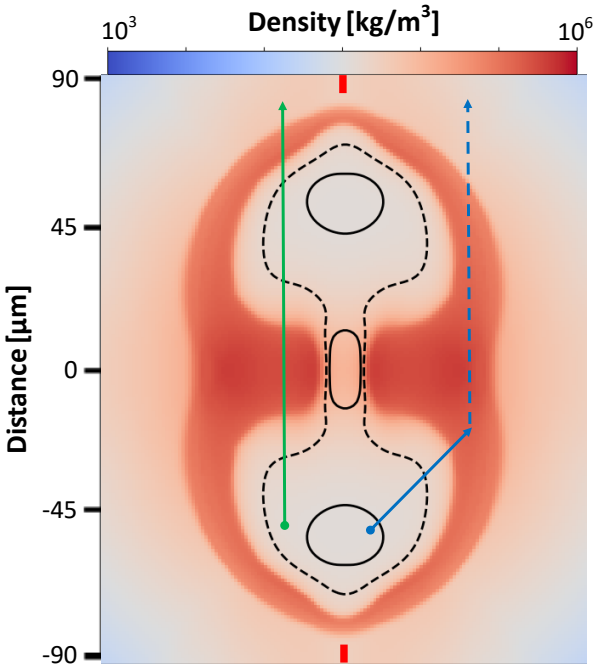

Figure 3.20: The density in the x-z plane at peak neutron production of a P2 hydrodynamics simulation. The black contours show the single (solid line) and double e-folding (dashed line) of the unattenuated primary neutron fluence. The green line shows the path of an un-scattered neutron to a polar detector. The path of a singly-scattered neutron is shown by the blue lines. The probability of scattering is proportional to the areal density along the solid blue line. The axis of symmetry is on the line connecting the vertical red ticks.

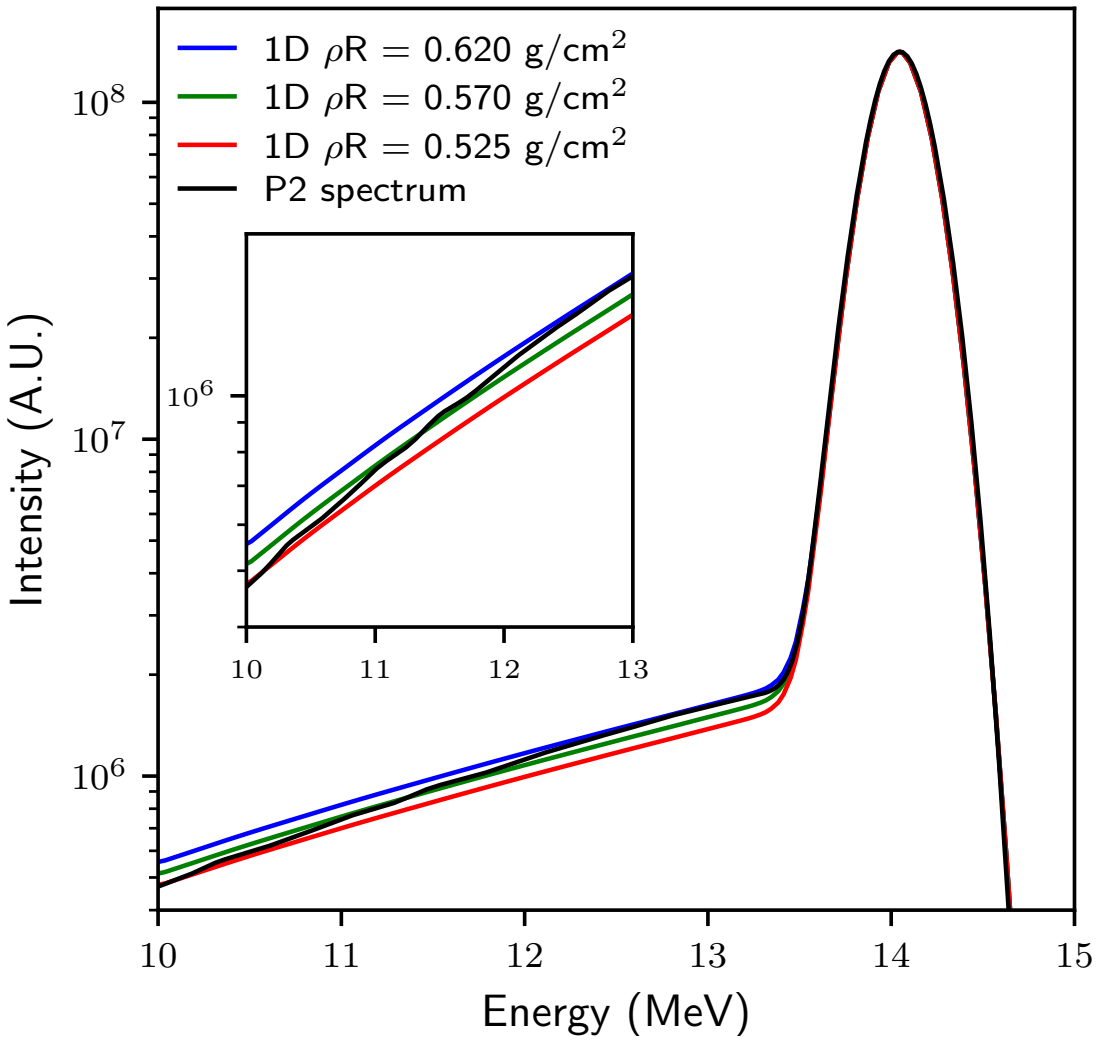

Figure 3.21: The neutron spectrum produced along the axis of symmetry by a capsule implosion with an imposed P2 perturbation, black line. The blue, green and red lines show the single downscatter spectrum for 3 different areal densities. The areal densities used in descending order are the line of sight neutron-averaged areal density, the inferred areal density from the DSR of the P2 simulation and an areal density chosen such that 1D spectrum matches that P2 spectrum at 10 MeV. Inset is a zoomed in plot over the 10-13 MeV region.

In order to infer the change in areal density with angle from neutron spectra, it was assumed that the primary spectrum measured and the birth spectrum of neutrons to be downscattered were the same. Thus by matching the measured primary spectrum, a set of calculated 1D neutron spectra would match the downscattered spectrum from the perturbed implosion when the areal densities were equal. Various 1D isobaric hotspot simulations were performed where the temperature and velocities were tailored to fit the Brysk cumulants of the primary spectrum from the P2 simulation. Due to the low neutron-averaged areal densities, the single scatter approximation used in the neutron transport is valid. For a detector viewing along the axis of symmetry, the large areal density surplus at the waist is avoided by neutrons born in the polar jets which scatter into the detector line of sight, c.f. solid blue line in Fig. 3.20. From the simulation data, it is seen that, as the scattering angle is increased from 30^o to 60^o, the neutron-averaged areal density along scattering paths decreases. Intuitively this will increase the slope in the 10 - 12 MeV range of the spectrum. Figure 3.21 shows the resultant neutron spectrum from the P2 simulation with a polar detector.

The P2 spectrum DSR infers a $\rho R = 0.57$ g/cm^2; this areal density represents the weighted sum over all scattering paths exemplified by the solid blue line in Fig. 3.20. The $\langle \rho R \rangle$ along the detector direction was found to be 0.62 g/cm^2. The 1D spectra with these areal densities intersect the P2 spectrum at different energies, see Fig. 3.21. A 1D simulation with $\rho R = 0.525$ g/cm^2 intersects close to a neutron energy of 10 MeV. This corresponds to a 15% change in ρR between the line of sight and the angular range near 10 MeV. Minotaur was used to construct single-scattering ρR-DSR relationships for the 10–11, 11–12 and 12–13 MeV regions. Applying these to the P2 neutron spectrum, $\rho R_{10\text{-}11} = 0.56$ g/cm^2, $\rho R_{11\text{-}12} = 0.58$ g/cm^2 and $\rho R_{12\text{-}13} = 0.60$ g/cm^2 were calculated. The average angles in these ranges are 49°, 41° and 31° respectively. These were weighted by the differential cross section with the assumption of a 50:50 mixture of DT.

In this way, spectra can be utilised to calculate the magnitude of neutron-averaged areal density asymmetry. As each energy range includes integration over the hotspot volume and scattering cone, the areal density from simulation centre is not accessible. At bang time the centre point areal densities are 0.4 and 2.2 g/cm^2 along the pole and across the waist respectively. This asymmetry is significantly larger than that inferred from the neutron spectrum. However, if a relatively spherical hotspot were to be surrounded by an asymmetric dense fuel distribution, the effect on the downscattered spectrum would be amplified. In experiments, the drive is often modified until the hotspot appears round in imaging [157] – the downscatter slope analysis, amongst other techniques, could be used to test whether the dense DT fuel layer is also round given the modified drive.

3.3 High Energy Neutrons

There are secondary and tertiary DT fusion reactions which can produce neutrons with energies greater than the primary DT neutrons [10]. These involve the reaction of fast

ions with the thermal population therefore reaching suprathermal reaction energies. The order, primary, secondary or tertiary, indicates how many interactions take place in the fusion reaction chain. Figure 3.22 shows the series of reaction chains relevant for DT fusion. The energies obtained can be calculated using the kinematic expressions given in Section 2.2.1.

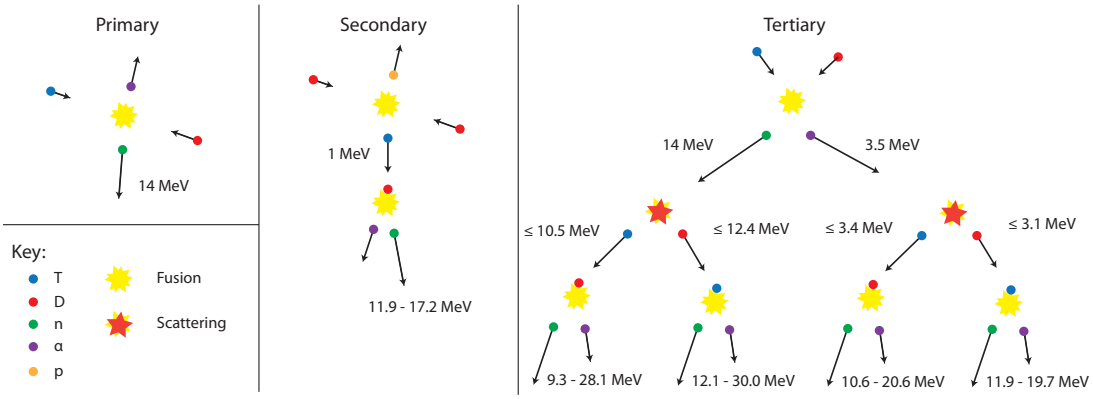

Figure 3.22: Diagrams showing the reaction chains for primary, secondary and tertiary DT fusion. Energies for fast particles in the intermediate steps are given as well as the range of energies for the final state neutrons. For the tertiaries, the neutron-mediated branch is on the left and the alpha-mediated on the right. Particle types are labelled by colour with a key in the bottom left.

3.3.1 Secondary Reactions in Magnetised Spherical Implosions

In Magnetised Linear Inertial Fusion (MagLIF) the spectral shape of secondary DT neutrons made in a magnetised DD plasma has been shown theoretically [7, 102] and experimentally [156] to depend on magnetic field strength and topology. Future plans to magnetise spherical implosions on the NIF require an assessment and measurement of the magnetic flux compression possible. Measurement of the secondary neutron spectra presents a possible mechanism for a direct magnetic field strength diagnostic. However a low areal density $\rho R \lesssim 100$ mg/cm^2 target is required in order for the triton stopping distance to be greater than the target size [147]. If this is not satisfied, nearly all tritons thermalise within the fuel and Larmor orbits will not extend the path lengths and hence will not increase the reaction probability of the tritons. Gas filled exploding or compressing pusher capsules are viable choices to remain under this areal density requirement while still producing large primary yields. The conditions from a 2D hydrodynamic simulation of a magnetised exploding pusher were used to set up a suitable test problem. The secondary neutron spectra were calculated from the averaged static hydrodynamic conditions at bang time with various burn widths enforced:

$$r = 300\ \mu\text{m},\ \rho = 1000\ \text{kg/m}^3,\ T_e = 5\ \text{keV},\ T_i = 10\ \text{keV},\ B = 2000\ \text{T}\ .$$

The spectra along two of the NIF nToF lines of sight are shown in Fig. 3.23. The magnetic field is orientated along the z-axis, (θ-ϕ) coordinates of (0-0), while Spec E and

Spec NP are along (90-174) and (18-304) respectively. Magnetising the triton orbits is seen to increase the secondary yield. This is because it extends the pathlength of tritons within the fuel. This can be quantified by the triton path average areal density. For the unmagnetised case $\langle \rho R \rangle = 22.0$ mg/cm^2 and secondary yield ratio of 3.2×10^{-3} were found – AKED and Minotaur agreed on these values to within a few percent. Magnetised tritons with burn widths of 100 ps and 200 ps gave $\langle \rho R \rangle = 29.0$ and 34.3 mg/cm^2, and yield ratios of 4.7 and 7.0×10^{-3} respectively. It is worth noting that the unmagnetised triton transit time across the fuel is 40-50 ps. The anisotropy in the spectra is due to increased path length of tritons emitted perpendicular to the field relative to those emitted parallel. Therefore, when observing the spectrum perpendicular to the field there is a larger flux of tritons parallel and anti-parallel to the line of sight. Reaction kinematics then leads to the observed double peaked spectrum. A similar reasoning can be applied to the detector parallel to the field.

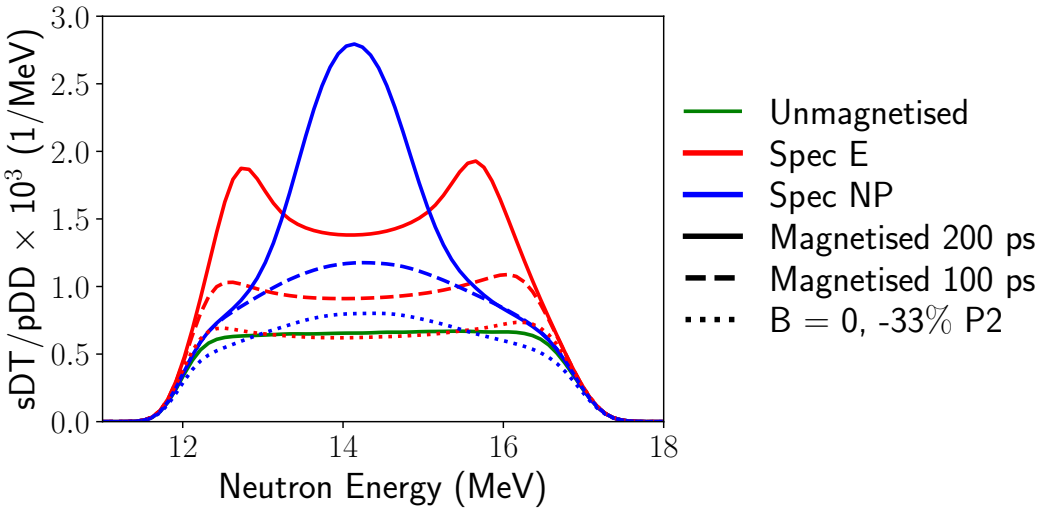

Figure 3.23: Secondary neutron spectra calculated for static idealised conditions consistent with a magnetised DD exploding pusher on the NIF. The effect of magnetising the fast triton orbits is to increase the secondary yield and to introduce anisotropy to the neutron spectra. Two burn widths of 100 and 200 ps were considered to estimate the effect of time-dependent hydrodynamic conditions. Also shown is the unmagnetised with a -33% P2 shape asymmetry applied which mimics the spectral shape of the magnetised cases.

While the results are encouraging, the secondary spectrum can also show anisotropy if an areal density asymmetry is present. For example, a negative P2 implosion[3] will create a similar spectral anisotropy as a magnetic field applied along the z-axis as shown in Fig. 3.23. Imaging diagnostics could measure the shape asymmetry and its effect on spectral anisotropy could be quantified. Finally the time-dependent case with realistic drive asymmetries and perturbations needs to be considered – this will be the subject of future work.

[3]Within the ICF community, the positive and negative P2 shapes are often referred to as 'sausage' and 'pancake' respectively. Other breakfast foods have yet to be utilised for other Legendre modes.

3.3.2 Alpha and Neutron Mediated Tertiaries

There is interest in both alpha and neutron mediated tertiaries as they could provide additional measurements of capsule conditions. The tertiaries are very sensitive to areal density ($Y_t \propto Y_p \rho R^2$) and therefore measurable yields require cryogenic implosions with DT ice layers. Work on the tertiaries has suggested that they are a possible test of stopping power models in degenerate plasmas [77, 78] and activation measurements have been performed at NIF [73]. These measurements used thulium activation diagnostics which have a threshold energy of $\sim$ 16 MeV but the cross section rapidly grows up to 20 MeV. Therefore the signal is dominated by knock-on ions and the high energy neutron yield was found to $\sim 10^{-4}$ of the total yield. In future, this analysis could proceed beyond a yield measurement to a spectral measurement in order to infer more details of the reaction in-flight process. Towards this, high energy neutron spectra were calculated using Minotaur for an OMEGA scale areal density. We will use a simple isobaric model for hotspot [171] and fuel shell with a fixed total fuel areal density. The ion and electron temperature have radial profiles given by:

$$T(r) = \begin{cases} T_c - (T_c - T_s)\left(\frac{r}{R}\right)^q & r < R \ , \\ T_s & R < r < R_{\text{fuel}} \ . \end{cases} \tag{3.34}$$

The exponent q was varied and the effect on the resultant high energy neutron spectrum was investigated. The resulting spectra for:

$$T_c = 6\text{keV},\ T_s = 500\text{eV},\ \rho R = 250\text{mg/cm}^2,\ R = 25\mu\text{m and } R_{\text{fuel}} = 30\mu\text{m} \ ,$$

with two q values (2 and 10) are shown in Fig. 3.24. It is seen that the flatter temperature profile ($q = 10$) leads to a faster population of alphas. This is due to the reduced stopping power at higher temperatures, see Fig. 2.12, meaning that the hotspot is more transparent in this case. The deuterons and tritons are then knocked on to higher energies. However, the cross section for large angle Coloumb scattering is inversely proportional to the square of the projectile energy, therefore a faster alpha population produces fewer total knock-on ions. This leads to the alpha-mediated tertiary neutrons having a larger high energy component but a reduced total yield. The rapid increase in density at the hotspot edge gives a small volume for slowing and scattering to occur. The opposite is true in the more opaque ($q = 2$) case.

The neutron-mediated tertiary neutrons do not have such a sensitivity as the primary DT neutrons are unaffected by plasma temperature in flight. Additionally, neutron scattering can occur within the shell where alphas have been ranged out. The secondaries are a $\sim$ 1 % contribution to the high energy spectra and therefore have negligible effect to the spectral shape. This test case shows spectral sensitivity to capsule conditions beyond yield and areal density. A future theoretical and computational investigation of tertiary neutron spectra could reveal a useful diagnostic tool.

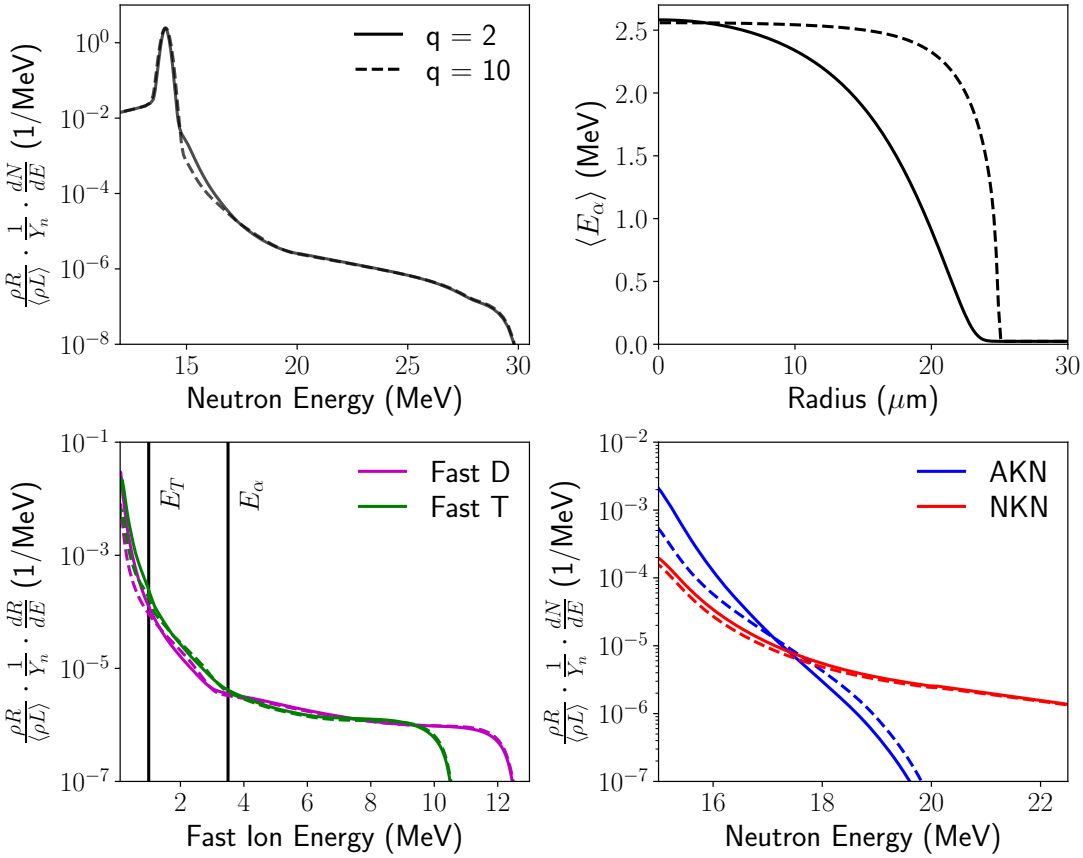

Figure 3.24: (Top Left) The high energy neutron spectrum for different values of q as defined in Eq. 3.34. The normalisation ensures that the scattered component of the spectra will line up between the two cases. A clear difference in the spectral shape occurs at $\sim$ 16 MeV. Solid lines will be used for the $q = 2$ case in all plots, similarly for the dashed line and $q = 10$. (Top Right) The average α particle energy as a function of position. The flatter temperature profile ($q = 10$) maintains a high average alpha energy to large radii. This is due to the lower stopping power at higher temperatures. (Bottom Left) The normalised fusion reaction rate as a function of fast ion energy. Above the birth alpha energy fast ions are produced by neutron knock on events. Below the birth alpha energy an increased reaction rate at $\sim$ 3 MeV is seen for $q = 10$. This is due to the higher flux of high energy alpha knock on ions. (Bottom Right) The neutron spectrum created by the DT fusion reactions of alpha knock on ions (AKN) and neutron knock on ions (NKN). The AKN spectra for $q = 2$ and 10 have distinct differences where as the NKN spectra are similar.

4 Neutron Imaging

Content in this chapter has been reproduced from "Synthetic nuclear diagnostics for inferring plasma properties of inertial confinement fusion implosions", Physics of Plasmas 25, 122703 (2018), Crilly et al. [42] with the permission of AIP Publishing.

As discussed in the Introduction, purely spherical implosions give the most efficient conversion of kinetic to internal energy. Neutron imaging gives spatial information of both the hotspot and dense fuel. It is therefore essential for measuring deleterious asymmetries in the implosion. In this chapter, we will assess the current analysis methods used in neutron imaging by using synthetic data from radiation hydrodynamics simulations.

4.1 Primary Neutron Imaging

In this section, two nuclear diagnostics which measure the spatial distribution of the primary DT neutrons are discussed. The first is traditional 2D imaging which measures the spatially resolved distribution of the line-integrated DT fusion rate. The images are used to measure the convergence and shape asymmetry of the implosion. Multiple 2D images can be used to tomographically reconstruct the 3D emitting volume. The second diagnostic considered is a system of activation measurements that create a 2D image of the yield variation, as discussed in Section 1.3.1.3. While each activation sample spatially and temporally integrates the incident neutron flux, multiple samples placed over the sphere can resolve angular variation in the primary DT neutron yield.

4.1.1 2D Imaging

As discussed in Section 1.3.1.2, primary neutron images map out a set of line integrals of T(D,n)α reaction rate with an attenuation factor due to scattering and other interactions. Scattered neutrons are lower in energy so are gated out for the primary neutron images. Two important measurements extracted from primary images are the radius and any distortion to the hotspot, as measured by the Legendre modes [72]. The radius of the hotspot is used to measure compression through the convergence ratio. Shape distortion is measured through the 17% contour. One might consider how attenuation affects this analysis. The dense fuel shell is the densest region and hence causes a large fraction of the attenuation. Due to the hotspot-shell configuration, the primary neutron images will be limb darkened by this effect.

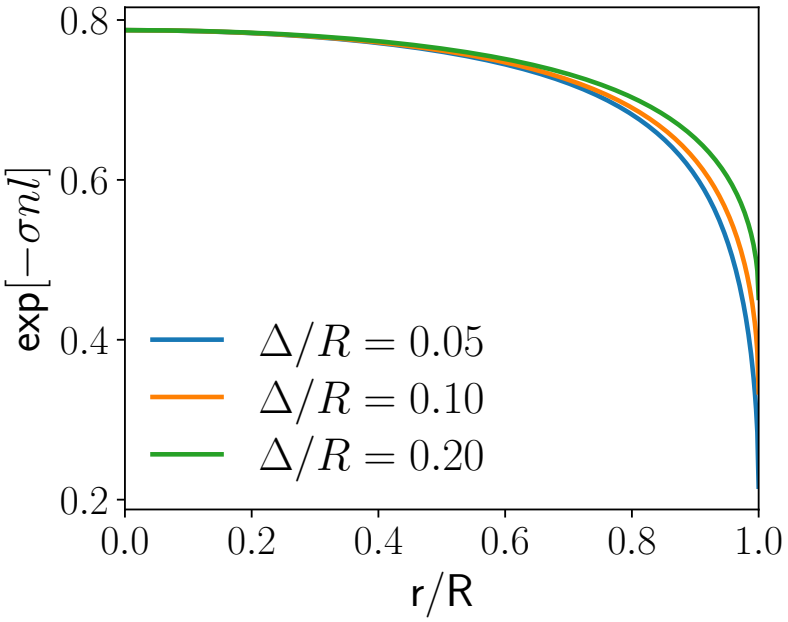

Figure 4.1: The primary image attenuation factor as a function of radius for a uniform spherical DT shell of areal density 1 g/cm^2 and thickness Δ surrounding a hotspot of radius R

To quantify this we will consider a uniform spherical DT shell of areal density 1 g/cm^2 and thickness Δ surrounding a hotspot of radius R. Figure 4.1 shows the attenuation factor as a function of image radius for various shell-hotspot aspect ratios, Δ/R. The thinnest, i.e. the highest density, shells cause the strongest limb darkening. This may lead to a small underestimate of the hotspot radius when analysing the 17% contour. For a uniform source the limb darkening causes a shift in inferred hotspot radius from 0.985 R to 0.962 R for an aspect ratio of $\Delta/R = 0.05$. Therefore for symmetric implosions the 17% contour is robust to attenuation effects.

We will now consider primary neutron images from 3D hydrodynamic simulations. To do this we will utilise a simulation with many different wavelength perturbations[1] performed with Chimera [181] – this simulation type will be referred to as "multimode". Figure 4.2 shows a density cross section at bang time and the time integrated primary neutron image, including attenuation, as calculated by AKED. Experimental images are also time integrated as the time-of-flight velocity dispersion effect is used to separate out the neutrons by energy to form gated images.

Neglecting attenuation effects could cause misidentification of darker regions as regions of low neutron production. However, the attenuation effect is likely to be marginal similar to the symmetric limb darkening analysis. To remove the conflicting effect of temporal blurring we will consider a time resolved image. This is shown for the multimode simulation in Fig. 4.3. When imaged at 1μm resolution, the level of attenuation

[1]The perturbations take the form of randomly seeded Rayleigh-Taylor velocity perturbations. These are placed at the vertices of geodesic spheres in order to uniformly perturb the whole sphere. More details can be found in thesis of Dr Taylor [171].

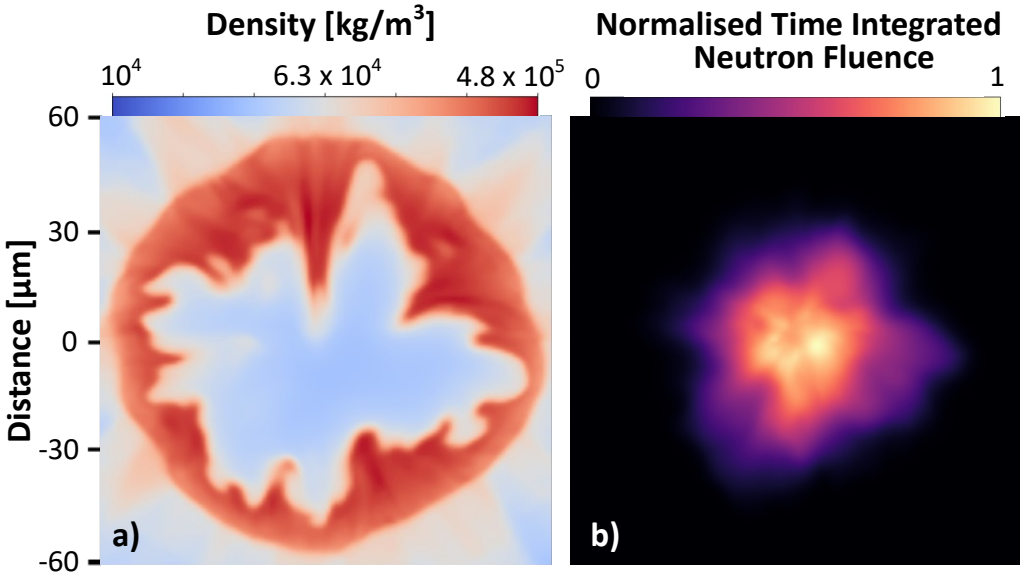

Figure 4.2: **a)** 2D y-z density slice at neutron bang time through a 3D Chimera simulation with randomly seeded Rayleigh-Taylor velocity perturbations applied [181]. The magnitude of the perturbations were set such that the neutron yield was close to experimental values (4.80×10^{15} without alpha-heating). **b)** A time integrated primary neutron image down the x-axis, through the density slice given.

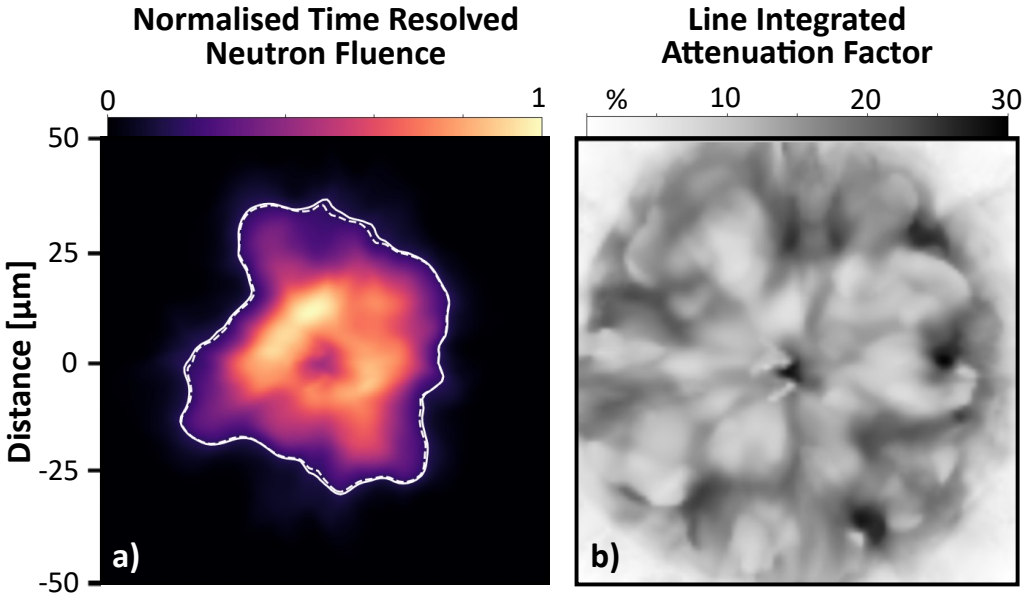

Figure 4.3: Large areal density differences can create variation in the level of attenuation for primary neutrons. Using the same simulation as used in Fig. 4.2, **a)** shows the attenuated primary neutron image down the z-axis at bang time with 1μm resolution (equal to the hydro resolution). The white lines map out the 17% contour which is used to measure hotspot shape [72]. The solid line is the contour when attenuation is neglected while for the dashed line attenuation is included. **b)** shows the spatial variation in the level of attenuation. This is defined through a line integrated attenuation factor given by one minus the ratio of the attenuated to the unattenuated flux at the detector.

is observed to vary by at most 20% within the hotspot. The shape inferred via the 17% contour with attenuation effects on and off is within 2.5μm at all points. At 5μm resolution, the variation in attenuation is reduced to below 13%. Thus the error induced by neglecting attenuation in analysis of primary images is tolerable for high mode and small amplitude low mode perturbations.

While shape analysis using the 17% contour can identify distortion of the hotspot within a plane, this is not the complete picture. Since realistic capsule implosions are perturbed in a 3D manner, ideally a 3D surface could be constructed to identify 3D asymmetries. However, due to the limited number of lines of sight, tomographic reconstruction of the neutron production is challenging. Neglecting attenuation, the problem is given by the matrix equation:

$$\mathbf{A} \cdot \vec{x} = \vec{b} \,, \tag{4.1}$$

where $\vec{x}$ and $\vec{b}$ are the source and images arranged as vectors of length M and N (generally $M > N$). The $N \times M$ matrix $\mathbf{A}$ gives the relative contribution of a source point to an image point. There are many tomographic methods for solving for the source, $\vec{x}$. However, for many techniques poor results are expected if only a few images are available. To illustrate the difficulty of this problem we will adopt a naive approach and compute the (Moore-Penrose) pseudo-inverse of $\mathbf{A}$ via singular value decomposition (SVD). We will take 3 orthogonal images of the multimode simulation (neglecting attenuation) and aim to reconstruct the 3D source. Figure 4.4 shows the results of the SVD reconstruction.

Many artefacts exist in the reconstruction, most notably the cross pattern along the detector directions. The total neutron yield has also been increased in the reconstruction by 8%. In order to obtain more accurate and efficient results a different method must be utilised. Sophisticated tomographic techniques for a small number lines of sight have been developed by Volegov *et al.* to form a 3D reconstruction of the neutron reaction rate [177–179]. These tomographic techniques employ an iterative Generalized Expectation-Maximization (or GEM) algorithm. These aim to maximise the log-likelihood with an additional potential term which prevents large differences between adjacent cells [177]. By employing an isobaric hotspot approximation, these 3D reconstructions are being used to infer burn averaged density and temperature profiles [48]. While shape analysis through the 17% contour appears robust to attenuation effects, this may not apply to the reconstructions. Further work to investigate these effects in reconstruction techniques is required. Some results from the Volegov *et al.* reconstructions will be shown at the end of Section 4.2 alongside density reconstructions from scattered neutron images.

4.1.2 4π Yield Variation

The FNADs measure the incident neutron fluence modulated by the activation cross section which possesses an energy threshold [15, 190, 191]. This system is distributed over 4π of solid angle and aims to capture the 3D nature of the areal density. Since the

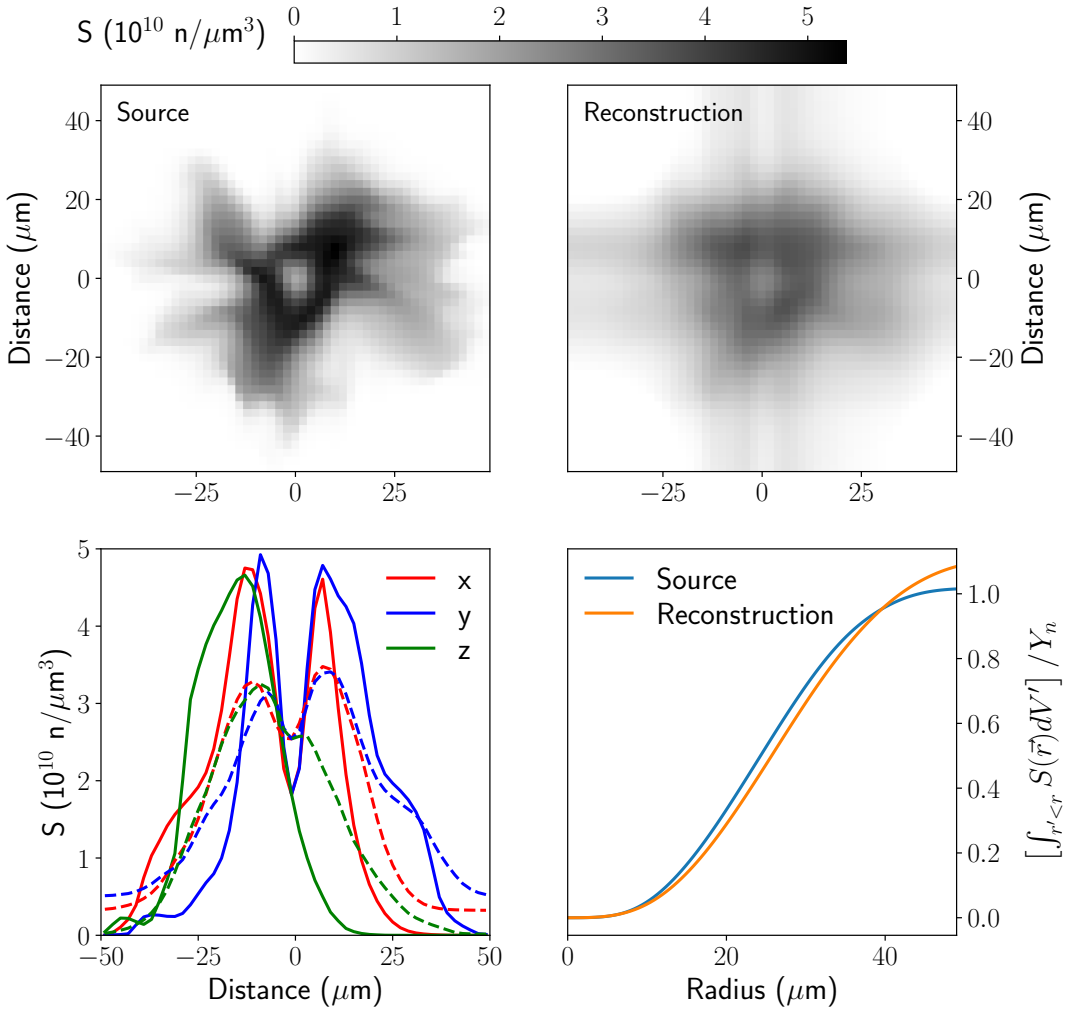

Figure 4.4: Three orthogonal images were used to perform a tomographic reconstruction of the 3D neutron production source, S. (Top) Comparison between the central x-y planes of the source and reconstructed neutron production distribution. Various reconstruction artefacts are seen. (Bottom left) Line outs through the 3D volumes along the x, y and z axes for the source (solid lines) and the reconstruction (dashed lines). (Bottom right) The cumulative radial volume integral of the fractional neutron production rate, S/Y_n.

neutron fluence is attenuated by areal density, variation in FNAD signal is correlated with capsule areal density variations. The hotspot is generally extended and therefore it is expected that the areal density variation inferred in this way is correlated with the neutron-averaged areal density. Due to the energy dependence of the activation cross section, the Doppler shifts induced by fluid velocity in the hotspot will also affect the FNADs signal [15, 148]. Flows towards an activation sample will increase the signal measured. In this work we will focus on the finite FNAD resolution due to the extended source.

The hotspot and shell can become highly distorted, this can cause a chord from an emitting cell to enter and exit the shell multiple times before exiting the capsule. This geometrically complex (non-convex) system is difficult to analyse. We will make a number of simplifying assumptions here to show the effect of an extended source. The hotspot is taken as a uniform sphere of negligible density, the shell as a uniform shell and perturbations as uniform increases in density on patches of the shell. This model is therefore purely illustrative – the results of detailed numerical calculation will be given later in this section. The loss of resolution induced by an extended source can be shown by varying the hotspot radius. Figure 4.5 shows the test case geometry and the results for two perturbation sizes.

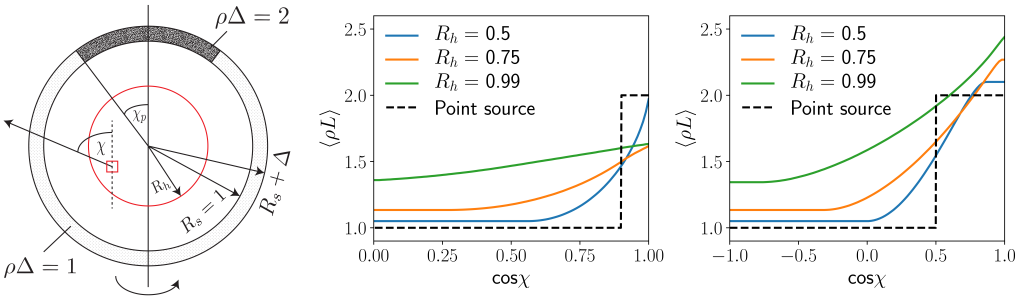

Figure 4.5: (Left) The geometry of the FNAD test problem. The source region lies within R_h, the shell starts at $R_s = 1$ and has thickness $\Delta \ll R_s$. The density perturbation lies at polar angles less than χ_p. Rays are traced from every point in the source volume out at angle χ. (Centre) The average areal density for $\cos\chi_p = 0.9$ at various hotspot radii. (Right) The average areal density for $\cos\chi_p = 0.5$ at various hotspot radii.

The extended hotspot results deviate from the point source result quite strongly even in the unperturbed region. This is because of the increased average chord length through the shell. Additionally the perturbation is smoothed out considerably by the extended source. From a geometric analysis, the last ray angle that intersects the perturbation (using the angle definitions in Fig. 4.5) is given by:

$$\sin(\chi - \chi_p) = \frac{R_h}{R_s} \,. \tag{4.2}$$

This sets the angular resolution for a given hotspot-shell radius ratio e.g. the apparent perturbation width is increased by 30° for $R_h/R_s = 0.5$. There are many differences between this simple model and realistic stagnation conditions. However, the same con-

clusions can be carried across. An extended hotspot has poorer angular resolution and an increased average chord through the shell.

We will now consider a more accurate representation of the FNAD diagnostic by post-processing a 3D hydrodynamics simulation. To form the synthetic ^{90}Zr FNADs a forward ray trace was performed from all the emitting cells along a detector direction vector. A birth spectrum was created for each emitting cell based on the temperature and fluid velocity. The areal density along the neutron path was used to attenuate the number of neutrons measured. Using the 3D multimode simulation shown in Fig. 4.2, 5000 synthetic FNADs were distributed at uniform angular intervals over 4π. The resultant measurement is given in Fig. 4.6 a). A low mode ($l, m \leq 2$) spherical harmonic fit was performed on the 19 experimental FNAD locations [190, 191], shown as coloured circles. This shows asymmetry in both the polar, l, modes and azimuthal, m, modes, see Fig. 4.6 b).

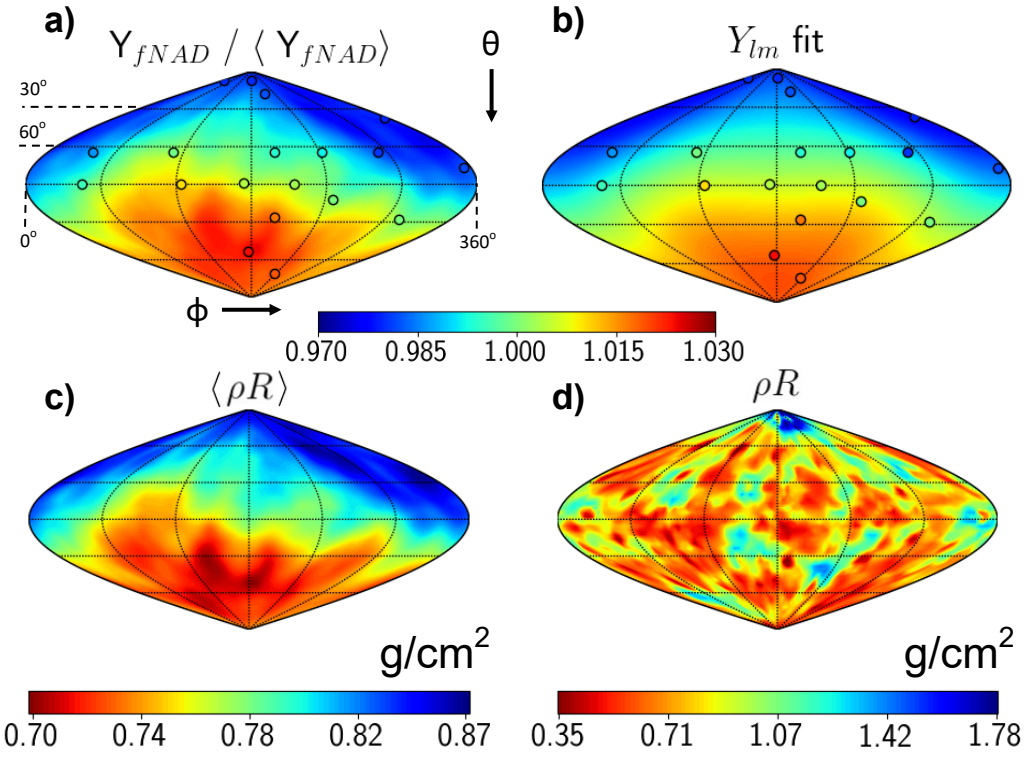

Figure 4.6: Sky maps of **a)** the synthetic FNAD signal for an implosion with multimode perturbations applied; **b)** a $l, m \leq 2$ spherical harmonic fit performed on the synthetic FNAD data sampled at the experimental detector positions; **c)** the neutron-averaged areal density and **d)** the line integrated density from the simulation centre point weighted by the burn history. Figure **a)** marks the angles of some lines of latitude and longitude for orientation. [17]

The degree of smoothing of high mode perturbations can be seen by comparing the neutron-averaged areal density (Fig. 4.6c) and the line integrated density from the simulation centre point weighted by the burn history (Fig. 4.6d). As expected, the neutron-averaged areal density shows the same features as the FNAD map. However, the map of centre point ρR weighted by the burn history is notably different. In the

$\langle \rho \mathrm{R} \rangle$ map, the high mode detail has been greatly smoothed and the magnitude of the resulting low mode alias is lower. The extended nature of the hotspot means that the bubbles and spikes seen clearly in the ρR map are sampled from multiple starting points. Spikes surrounded by emitting material thus appear spatially larger. Also, when viewed down the spike axis, the attenuation effect appears reduced due to emitting plasma surrounding the spike. Hence high mode perturbations are not resolvable, no matter the number of activation detectors, and the magnitude of the low mode sample of these perturbations is lowered. Experimental FNADs sky-maps often exhibit modes $l, m \leq 2$ of similar or larger magnitude as those found in the multimode synthetic data [15, 91]. In this multimode simulation a large polar spike produces a P1 signal in the FNADs. Possible high mode detail missed by the FNADs would be visible in well-resolved primary and scattered neutron images, e.g. Figs. 4.2 and 4.3. The neutron-averaged fluid velocity inferred from the primary spectra (29 km/s) accounts for $\approx 25\%$ of the FNAD variation. This L=1 effect exacerbates the aliasing of the high mode areal density variation, although correction of the fluid velocity effect is possible with a spectroscopic hotspot velocity measurement[148]. Performing downscattered neutron spectral measurements along the poles, the ρR_{DSR} were found to be 0.71 and 0.81 g/cm^2 respectively. These are consistent with the P1 measured in the FNADs. It should be noted that the DSR measurement samples between $\sim 30 - 60$ degrees away from the detector axis.

4.2 Scattered Neutron Imaging

Scattered neutron images can be used to identify areas of increased density as this will lead to increased scattering. However, these images contain information about both the density and the neutron flux at the scattering site. Therefore additional analysis is required to infer the scattering ion density. Fluence compensation is a technique, developed by Casey *et al.* , which can be used to approximately decouple the primary flux from scattered neutron images and therefore directly image the scatterer density [25]. The technique involves using the primary image to infer the primary fluence at the scattering locations.

Simplifying assumptions are needed to calculate the primary fluence from the primary image. First, the primary neutron emission rate is assumed to be constant along the line of sight[2]. Second, a single average scattering angle, $\bar{\theta}_s$, is used. The average angle depends on the energy gate, $[E_{\mathrm{min}}, E_{\mathrm{max}}]$, used to form the scattered neutron image. The scattered neutron spectrum within this energy gate can be used to compute $\bar{\theta}_s$. This is done by first calculating the angle of scattering of a 14 MeV neutron from the

[2]Technically, the neutron source is assumed to be separable along the line of sight direction, z, such that $S(x, y, z) = \tilde{S}(x, y)I(z)$. However this has the same effect as the constant along z assumption.

average fuel ion with a given outgoing neutron energy, E:

$$\cos\theta_s(E) = \frac{1}{2}\left[(\bar{A}+1)\sqrt{\frac{E}{14\text{ MeV}}} - (\bar{A}-1)\sqrt{\frac{14\text{ MeV}}{E}}\right] , \tag{4.3}$$

where $\bar{A}$ is the average ion mass divided by the neutron mass. The scattering angle is then averaged using the outgoing scattered neutron spectrum, $Q_s(E)$, as follows:

$$\bar{\theta}_s = \frac{\int_{E_{\min}}^{E_{\max}} \theta_s(E) Q_s(E) dE}{\int_{E_{\min}}^{E_{\max}} Q_s(E) dE} . \tag{4.4}$$

The primary fluence, $\psi_{i,j}$, is then found using $\bar{\theta}_s$ to calculate the $1/r^2$ dilution between source and scattering site:

$$\psi_{i,j} = \sum_{k,l} \frac{S_{k,l}}{4\pi r_{k,l,i,j}^2} , \tag{4.5}$$

$$r_{k,l,i,j} = \frac{\sqrt{(x_i - x_k)^2 + (y_j - y_l)^2}}{\sin\bar{\theta}_s} , \tag{4.6}$$

where $S_{i,j}$ is the primary neutron image and the image coordinate distances are x_i and y_j. Attenuation effects on the primary fluence calculation are neglected.

Dividing the scattered neutron image by the approximated primary fluence retrieves the product of the areal density seen by these scattered neutrons and the differential cross section. For a downscattered neutron image, $DSn_{i,j}$, the fluence compensated image, $\langle\rho L\sigma\rangle_{i,j}$, is given by [25]:

$$\langle\rho L\sigma\rangle_{i,j} = \frac{\bar{A} m_n}{A_p} \frac{DSn_{i,j}}{\psi_{i,j}} , \tag{4.7}$$

where A_p is the image pixel size and m_n is the neutron mass.

The simplifying assumptions of a single scattering angle and uniform brightness per unit length appear restrictive and one would like to see the effects of these approximations. However, constructing a suitable test problem is tricky, as with all scattering problems. As a test case, we will consider an unattenuated monoenergetic spherical neutron source and a spherically symmetric scattering medium with density $n_s(r)$. A scattered neutron image is made at infinity with a radial coordinate s. This leads to a scattered image per unit radius of the form:

$$P_{sn}(s) = \int d\mu \int 2\pi r^2 dr n_s(r) \delta\left(s - r\sqrt{1-\mu^2}\right) \int d\mu' \Psi(r,\mu') \int d\mu^* I(\mu',\mu,\mu^*) \frac{d\sigma}{d\Omega}(\mu^*) , \tag{4.8}$$

where I is the angular transition probability (Eq. 2.134) and Ψ is the angular neutron flux. The Dirac-δ ensures that we move along the line of sight of the detector. Figure 4.7 shows the imaging and scattering geometry.

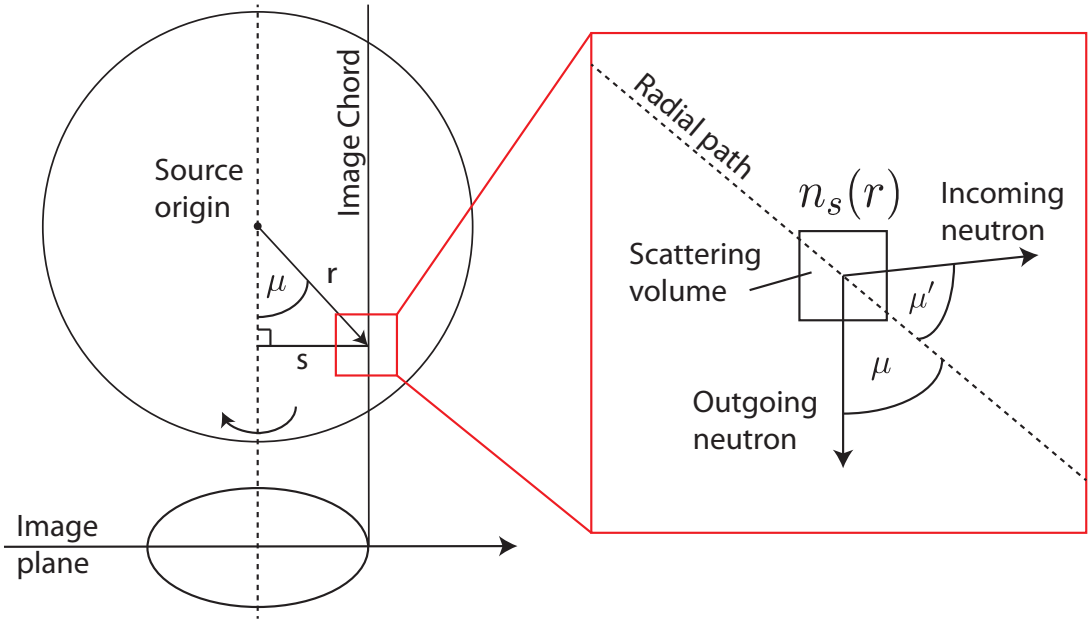

Figure 4.7: Diagrams showing the imaging and scattering geometry for the formation of scattered neutron images from a spherically symmetric source. Direction cosines, μ and μ', are defined relative to the radial path. The image radius, s, is then linked to the source radius, r, through the outgoing neutron direction, μ, as given by trigonometry: $s = r\sqrt{1-\mu^2}$.

To proceed, we will integrate out the Dirac-δ and retrieve the image intensity per unit area to reach our final expression:

$$F_{sn}(s) = \frac{P_{sn}}{2\pi s} = \int d\mu \frac{s}{(1-\mu^2)^{3/2}}\, n_s\left(\frac{s}{\sqrt{1-\mu^2}}\right) \int d\mu' \Psi\left(\frac{s}{\sqrt{1-\mu^2}}, \mu'\right) \int d\mu^* I(\mu', \mu, \mu^*) \frac{d\sigma}{d\Omega}(\mu^*) \ . \tag{4.9}$$

This integral becomes the forward Abel transform (in angular form) for constant Ψ and isotropic differential cross section. Unfortunately the differential cross section does not have a simple analytic form therefore this integral must be integrated numerically over all scattering angles. We can construct a simple numerical test to assess only the uniform brightness per unit length approximation. This will be done by including the single scattering angle approximation. The allowed scattering cosine, μ^*, will be varied to observe its effect. We will use the bang time conditions of a 1D Chimera simulation of the HDC shot n170601 to set our density and neutron flux. From this we can calculate our primary and scattered images from Eq. 4.9 and then find our fluence compensated image. The results of this test are shown in Fig. 4.8.

In this test, we see that the shape of the scattered images is very different between isotropic and peaked differential cross sections. More forward directed scattering produces images of the front of the dense DT layer, while larger scattering angles highlight the peripheries. This carries over into the fluence compensated images which become more strongly peaked at larger radii for larger scattering angle. The fluence compen-

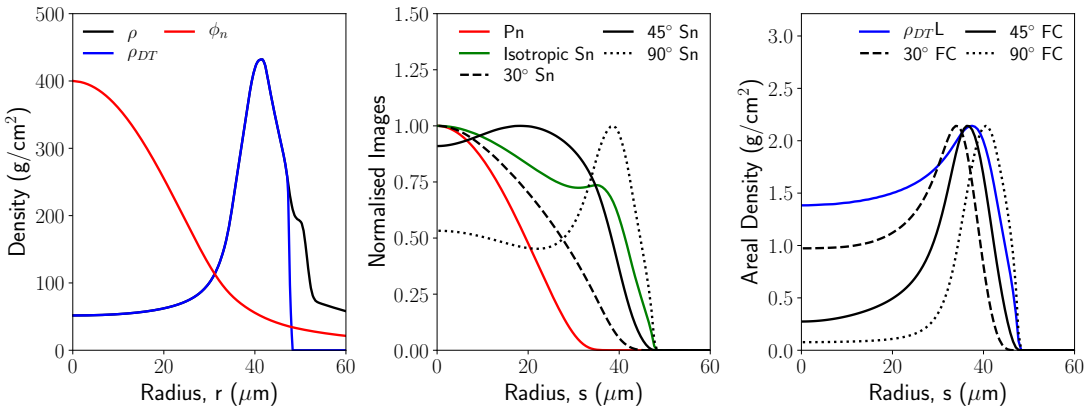

Figure 4.8: (Left) Plot showing the DT density, total density and scaled neutron flux radial profiles at bang time in the 1D Chimera simulation of the HDC shot n170601 . (Centre) Plot showing the resulting primary (Pn) and scattered (Sn) neutron images as a function of image radius, s. Three single scattering angle cases are considered (30°, 45° and 90°) shown with the black curves as well as the isotropic scattering case in green. (Right) Shown in blue is the line integrated density, ρL, as given by the forward Abel transform on the DT density, ρ_{DT}, in the left hand plot. Using the fluence compensation technique, the three single scattering angle images are converted into fluence compensated images (FC). These have been scaled to the ρL maximum.

sated images deviate strongly from the line integrated density due to the scattering geometry restriction. We can see that the assumption of uniform brightness per unit length prevents us from recovering the underlying spherical density distribution. However, we can convert the scattered image into a, more physically useful, distribution of areal density along the scattering paths. In Casey *et al.* [25], the average scattering angle is taken as 45° for which the fluence compensated image is closest to matching the position of peak ρL in this test case.

Typically, experimental images use an energy gate between 6 and 12 MeV to measure the scattered neutron image. There are many contributions to this range beyond singly scattered neutrons, see Fig. 2.19. Notably, the inelastic D(n,2n) process comprises a significant portion of signal, reaching equality with the DT elastically scattered fraction at $\sim$ 6 MeV, see Fig. 3.11. Multiple scattering also becomes important at higher areal densities, see Fig. 2.20 for the contributions of double and triple scattering to the spectrum at 1 g/cm^2. There are therefore multiple benefits to restricting the energy range at the cost of reduced signal. Sources which are difficult to describe and analyse, such as inelastic and multiple scattering, can be minimised. Also the range of allowed elastic scattering angles is reduced, leading to a more directed measurement.

If the large range of scattered neutron energies was split into multiple energy gates then different regions of the dense shell could be sampled, see Fig. 3.19. To illustrate this technique we will consider a calculation where a single spike Rayleigh-Taylor[171] velocity perturbation has been applied to an otherwise symmetric implosion at peak velocity. The neutron transport calculation was carried out with AKED. At initialisation, the maximal radial velocity of this spike was a factor of $\sim$ 2 times greater than in the

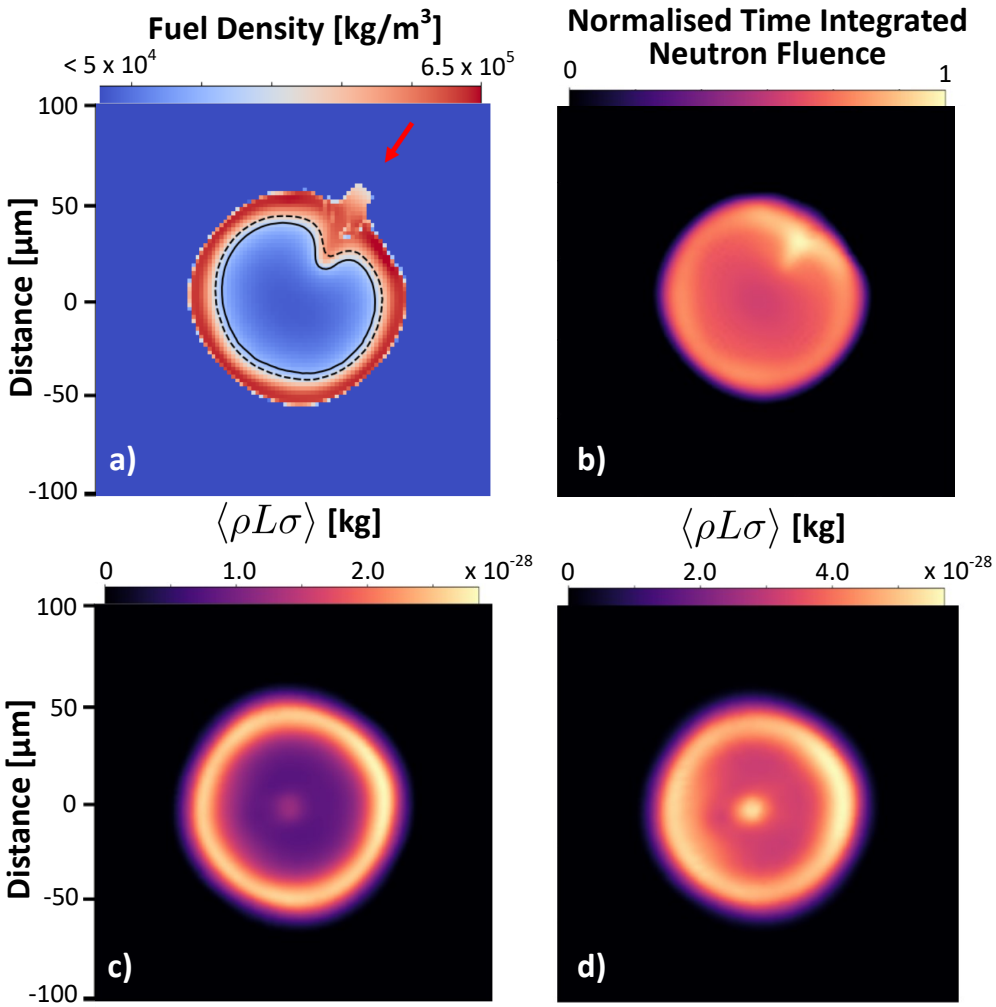

Figure 4.9: **a)** Fuel density slice in the x-y plane at bang time and the fusion reaction rate contours overlaid. The solid and dashed lines represent a single and double e-folding of the reaction rate respectively. **b)** A scattered neutron image taken down the z-axis with a 10-12 MeV gate. **c)** and **d)** Fluence compensated images showing the single spike perturbation along the detector line of sight (90^o,45^o), shown by the red arrow in **a)**. The two images correspond to two energy gates, 10.0-11.5 MeV and 11.5-13 MeV respectively. The average scattering angles inferred from the neutron spectrum are $\sim 45^o$ and 30^o respectively.

rest of the shell. Using two energy gates above 10 MeV allowed separate imaging of the spike density and the shell density at higher angles, see Fig. 4.9. The time dispersion of the neutrons would allow this technique to be applied along a single line of sight. By viewing the spike along its axis, blurring due to radial motion is avoided in the time integrated image. A time integrated scattered neutron image perpendicular to the spike axis reproduces the shape of the perturbation. The 11.5-13 MeV image can be used to estimate the areal density of the cold fuel spike and the preceding shell. Dividing out by the differential cross section evaluated at the average angle of 30^o, an areal density of ~ 2.0 g/cm^2 was obtained. An areal density of 1.8 g/cm^2 was found at bang time directly from the Chimera simulation.

Working with the Neutron Imaging Group at LANL, synthetic primary and (6-12 MeV) scattered neutron images from the multimode simulation were used in tomographic reconstruction of the neutron production and density [179]. Using AKED, time integrated images were taken along experimental NIS lines of sight to test and benchmark the reconstruction technique for use with experimental data. To aid in the comparison, the time integrated neutron production and density were calculated from the hydrodynamic simulation. When integrating up the density, each time was weighted by the total neutron production rate at that time to give the correct burn average. The 6-12 MeV window for the scattered images includes a much larger angular range ($\sim$ 30°-100°) than for the 10-13 MeV cases discussed above. This greatly increased the computational expense of the calculation, and the efficient ray trace method was essential in making this task tractable. Figure 4.10 shows the results of the reconstruction. Given this synthetic data test, the reconstruction technique has been used to analyse experimental data.

The third line of sight on the NIS will soon be upgraded to measure a scattered neutron image [179]. This will allow more accurate reconstruction of the density distribution. The synthetic data analysis can then be revisited and the new scattered image line of sight included. Carbon γ-ray images (see Section 5.1 for details) on the NIS lines of sight were also calculated using AKED for the multimode simulation – these will be the subject of future reconstruction work to measure the remaining ablator morphology.

4.3 Combined Imaging Analysis

Spectroscopic measurements regularly measure large hotspot velocities [75, 116, 148]. However, these measurements are unable to distinguish different spatial hydrodynamic profiles if they have the same integrated flow velocities. In this section we will explore two different perturbation types which can induce hotspot flows. We aim to answer the question: can imaging techniques distinguish between the different perturbations when the spectroscopic measurements cannot?

To do this we consider two scenarios: a P1 drive asymmetry and a more localised reduction in the implosion velocity, which will be named an aneurysm perturbation for reasons which will become clear. Both result in neutron spectroscopic measure-

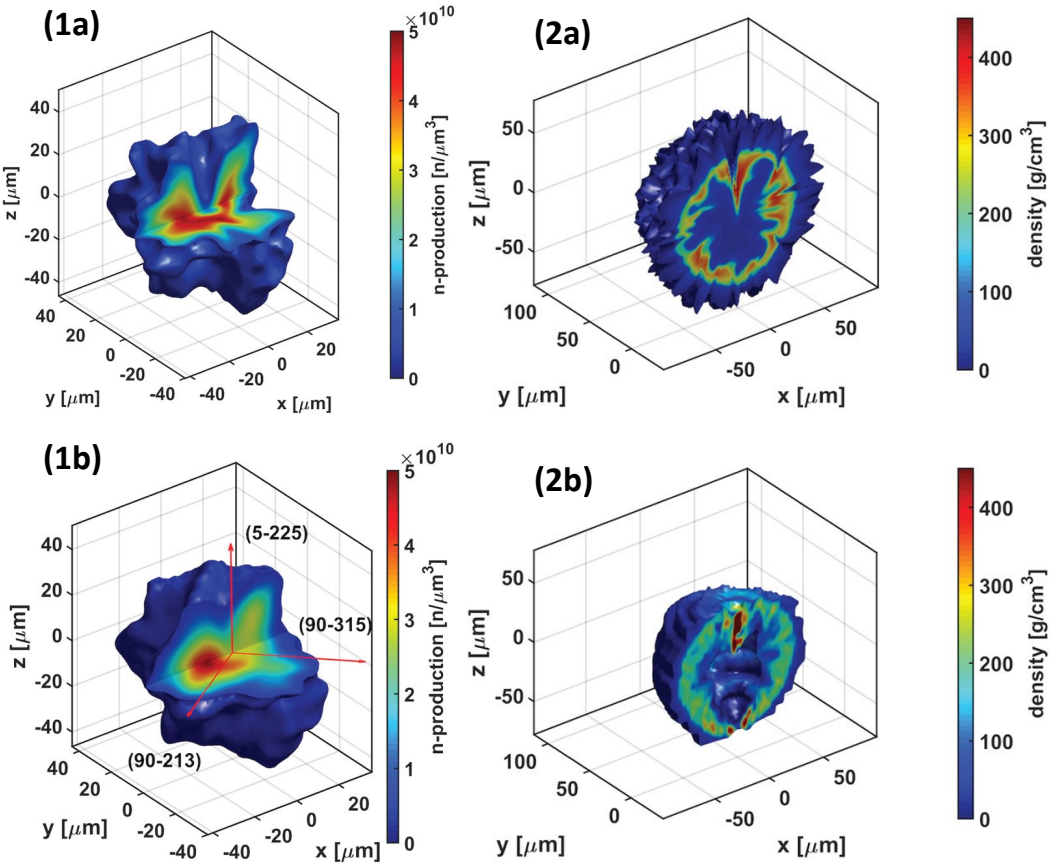

Figure 4.10: Plot (1a) shows the time integrated neutron production rate from the multimode Chimera simulation. Plot (1b) shows the reconstructed neutron production rate from 3 primary neutron images taken along experimental NIS lines of sight (shown on the figure). Plot (2a) shows the burn averaged density in the multimode simulation. Due to current experimental availability of only 1 scattered image, the density distribution must be assumed axisymmetric for the analysis to proceed. Plot (2b) shows the reconstructed density from 1 scattered neutron image using the source reconstruction in plot (1b). Reproduced from "Density determination of the thermonuclear fuel region in inertial confinement fusion implosions", Journal of Applied Physics 127, 083301 (2020), P. L. Volegov, S. H. Batha, V. Geppert-Kleinrath, C. R. Danly, F. E. Merrill, C. H. Wilde, D. C. Wilson, D. T. Casey, D. Fittinghoff, B. Appelbe, J. P. Chittenden, A. J. Crilly, and K. McGlinchey, with the permission of AIP Publishing.

ments with the axes of centroid shift, $\langle v \rangle$, and inferred ion temperature asymmetry, ΔT_i, aligned[3]. Thus without additional information these scenarios are difficult to distinguish. However, they have very different hydrodynamic behaviour at stagnation. The P1 exhibits bulk motion along the drive axis while maintaining a relatively round hotspot. The shell is more strongly compressed on the side with harder drive. The hotspot does not break out of the shell during neutron production. In contrast, the aneurysm perturbation proceeds as a normal implosion with a localised region lagging behind. Once the pressure in the hotspot builds up during stagnation, this localised region has the lowest areal density and, consequently, is forced outwards. The hotspot starts to flow out through this developing aneurysm leading to a measurable hotspot velocity in neutron spectra. Therefore the different structures of the shell and hotspot should present themselves in primary and fluence compensated images as shown in Fig. 4.11.

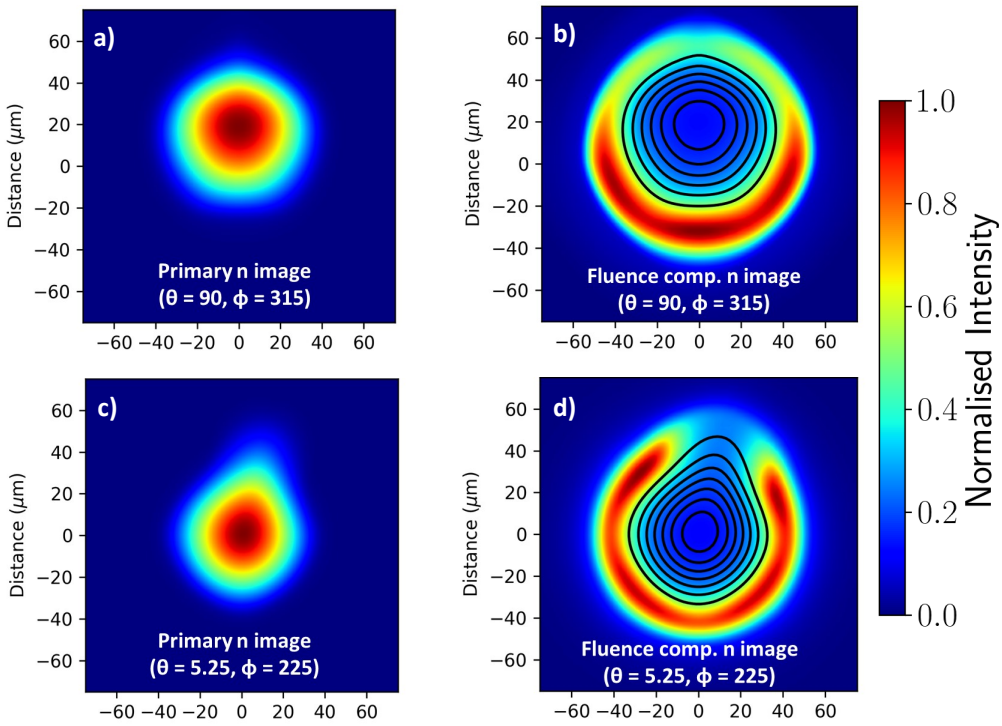

Figure 4.11: Graphs **a)** and **b)** are the primary and fluence compensated neutron images for the P1 drive asymmetry case. The drive axis is along $\theta = 0$. The contours on the fluence compensated images are the contours of the primary neutron image. Graphs **c)** and **d)** are the primary and fluence compensated neutron images for the aneurysm case. The axis of the perturbation is along $\theta = 80°$, $\phi = 30°$. The NIS polar and equatorial lines of sight were considered and the line of sight which gave the best representation of the hotspot and shell shape was used. Some slight Cartesian grid imprinting is visible but is small compared to the perturbation size.

The P1 case shows a close-to round hotspot from the primary neutron image. Its cen-

[3]In this context, I am using axes to refer to the directions given by the vector component and maximal principal axis of the matrix component of the primary spectrum cumulants. See discussion of Eqs. 2.74 to 2.77 and Appendix C.1 for detail

troid is displaced from target chamber centre by ≈ 20 μm. However, this displacement would be difficult to detect with the NIS as the final neutron image is an average of many images through many pinholes. The fluence compensated image reveals the areal density asymmetry aligned with the drive asymmetry axis. The aneurysm case shows a distorted hotspot with a 'teardrop' shape due to the outflowing hotspot. The centroid of the emission is very close to the centre. The nature of the perturbation means that for most of the shell the implosion is unperturbed, this leads to a centred implosion. This also shows up in the fluence compensated image which shows a small weak patch in the shell through which the hotspot is flowing. The imaging resolution of the primary and scattered neutron images are ~ 10 μm [176, 179]. This is sufficient to resolve the differences visible in Fig. 4.11.

Similar analysis has been performed with X-ray images by Ruby *et al.* [152]. X-ray images have the benefits of having better spatial resolution than neutron images and being time resolved (~ 100 ps), this allows a direct measurement of velocity. However, X-ray images do not measure the same behaviour of the fusing material as neutron images, even in the case of no mix. This is due to the different temperature dependencies of X-ray emissivity and nuclear reactivity. Also mix induced by the fill tube or other defects can dominate X-ray images. Then the dynamics of the mixed region rather than fusing region are measured. X-rays images also cannot measure shell conditions. Therefore, the correlation between hotspot flows and low areal density regions cannot be seen.

While these perturbations were applied in an idealised manner, the important distinction is their different extent: whole capsule (P1) vs localised (aneurysm). Potential sources of these two cases are quite different due to this fact. The P1 asymmetry could be caused by smooth top-bottom drive imbalance [114] while the aneurysm could be caused by the growth of more localised defects. These could be dust on the capsule, voids or grain boundaries in the ablator, the fill tube or stalk, surface roughness and the capsule support tent. Many tailored experiments have been performed to observe the growth of these perturbations as detailed within the comprehensive reviews by Smalyuk *et al.* and the references therein [160, 161].

5 Gamma Ray Measurements

Content in this chapter has been reproduced from "Synthetic nuclear diagnostics for inferring plasma properties of inertial confinement fusion implosions", Physics of Plasmas 25, 122703 (2018), Crilly et al. [42] with the permission of AIP Publishing.

In indirect drive implosions there is remaining ablator at stagnation. This is to prevent radiative heating of the dense DT shell which would limit compression. Most of the shots on NIF to date have used an ablator containing carbon (CH, HDC). This chapter is concerned with these shots, although the discussion of DT fusion γ rays is more general as it does not rely on a carbon-based ablator.

5.1 Imaging the Carbon Ablator via Inelastic Neutron Scattering

Fine scale hydrodynamic mix between the ablator and fuel has been suggested as a possible cause of lower than expected compressions as measured by the DSR [37]. While this mix can not be resolved at stagnation, measurements of the reduced compression of DT and carbon would lend credence to this hypothesis. The carbon γ history, the topic of the following section, can be used to measure the average ablator areal density [30, 84, 121]. However this gives no information on the spatial distribution of ablator. Imaging the carbon ablator through the 4.4 MeV γ-rays made in inelastic neutron scattering could provide this information.

Much of the analysis applied to scattered neutron imaging can be equally applied to carbon γ imaging. One key difference is that the differential cross section for γ emission is symmetric and close to isotropic, with a P2 coefficient of ~ 0.15 [64]. Within the isotropic approximation, a carbon γ image is given by:

$$I_\gamma(x,y) = \int dz \ \frac{\rho_C(\vec{r})}{m_C} \int dE \ \sigma(E)\phi_n(\vec{r},E) \ , \tag{5.1}$$

where $\phi_n \equiv \int d\mu \Psi_n$ is the total flux of neutrons, ρ_C is the carbon density, m_C the mass of a carbon nuclei and σ is the inelastic scattering cross section. As the primary DT neutron fluence is ~ 100 times greater than at other neutron energies, we will neglect other neutron energies and invoke energy separability:

$$I_\gamma(x,y) \approx \int dz \ \frac{\rho_C(\vec{r})}{m_C}\phi_n(\vec{r}) \int dE \ \sigma(E)Q_n(E) = \frac{\langle\sigma\rangle}{m_C} \int dz \ \rho_C(\vec{r})\phi_n(\vec{r}) \ , \tag{5.2}$$

where $\langle\sigma\rangle$ defines the average scattering cross section across the primary DT spectrum. For a uniform isotropic neutron flux the images shows the carbon areal density along chords. Since the carbon occupies the remaining ablator shell, we expect a limb brightened image. This is due to the largest chord residing at the inner radius of a shell. In more realistic scenarios, the total neutron flux, ϕ_n, will highlight carbon closer to the neutron source. Unlike scattered neutron images, the emission and scattering sources are separated in carbon γ imaging.

To show the effect of the neutron flux term we will consider a 1D hydrodynamic simulation of the HDC implosion N170601. Figure 5.1 shows the density, the neutron flux and their product at bang time. Also shown are the resultant carbon gamma images with and without the neutron fluence term. The effect, while subtle, is to reduce the effective emission with increasing distance from the hotspot.

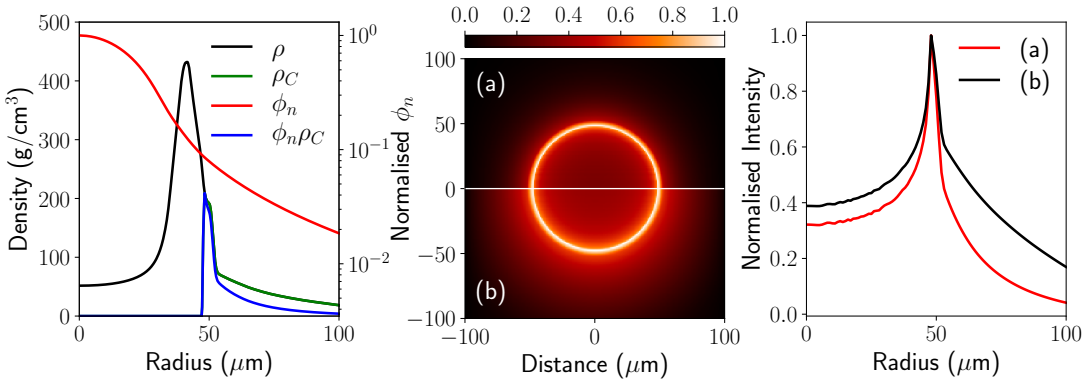

Figure 5.1: (Left) The density, neutron flux and their product as a function of radius from a 1D simulation of the HDC implosion n170601 at bang time. The neutron flux has been normalised and is plotted on the right hand log scale, all other quantities are on left linear scale. (Centre) Carbon γ-ray images constructed using a forward Abel transform. The upper half (a) takes account of the neutron flux and the lower half (b) assumes a uniform isotropic flux. Both images are normalised to their peak. (Right) Lineouts through the constructed normalised images shown in the centre plot.

For this symmetric case it is clear that the inner radius of the ablator can be found given sufficient spatial resolution. Decompression of the ablator would reduce the intensity measured and increase the thickness of the ring seen in the image.

Perturbations within the ablator can seed or feed through to the fuel creating cold fuel spikes [119]. If these ablator perturbations do not break out into the hotspot then they will not create a measurable X-ray signal. It is therefore critical to image the shape of the ablator near bang time to identify such perturbations. The remaining ablator also provides areal density to maintain confinement. Thin regions in the ablator will reduce confinement and allow early decompression.

The multimode simulation will be used as a case study for these potential further uses of carbon γ imaging. Figure 5.2 shows time integrated carbon γ images at the resolution of the simulation and with a 10 μm Gaussian filter applied to mock up potential experimental resolution. The third line of sight of NIS will soon be upgraded

to image the carbon γ rays [179]. We will use the $\sim$ 10 μm resolution reported for the neutron imaging as an estimate for γ imaging resolution [179]. The spikes created by the perturbations and the blow-off region are clearly visible. Thin regions of the ablator can also be seen. The presence of spikes still persists after the addition of a 10μm Gaussian filter.

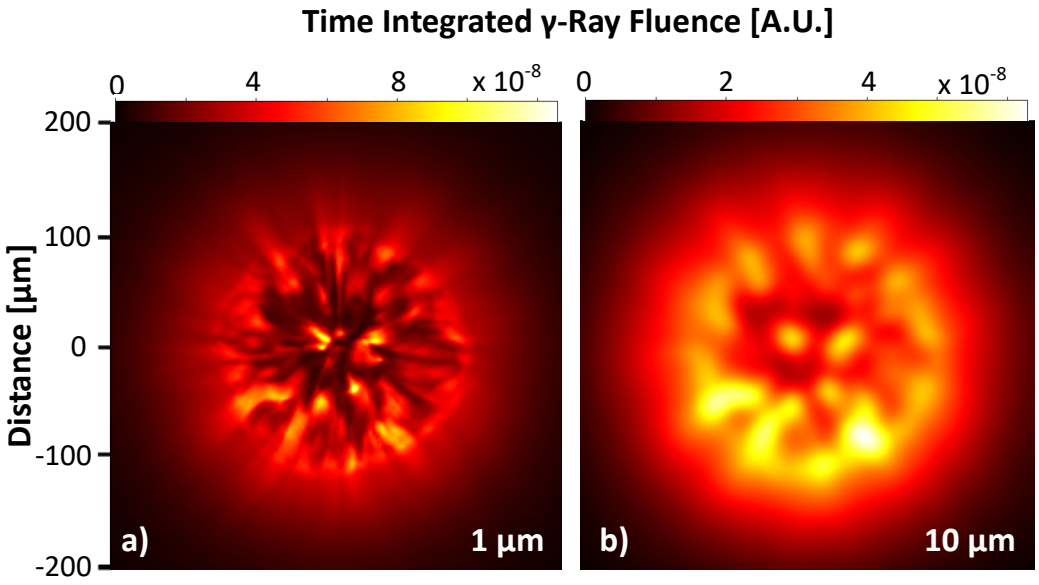

Figure 5.2: **a)** Time integrated carbon γ ray image at the resolution of the simulation (1 μm) for multimode simulation. **b)** A 10 μm Gaussian filter applied to image **a)**. Carbon spikes from all 4π of solid angle and the blow-off region are seen.

The fill tube has been experimentally observed to inject doped ablator into the hotspot, which greatly increases X-ray emission [47, 185]. There has been detailed simulation work aiming to capture the hydrodynamic behaviour of the fill tube induced mix and the resulting diagnostic signatures [39, 46, 185]. One might wonder if carbon γ imaging may be able to contribute a direct nuclear measurement of the mixed carbon to corroborate the X-ray images. To answer this question, we will be using the 3D Chimera simulation of N161023, including the fill tube and 2D radiation drive asymmetries, performed by Dr Kris McGlinchey. Other synthetic nuclear measurements from this simulation are reported in McGlinchey *et al.* [120]. Figure 5.3 shows equatorial carbon-γ images perpendicular to the fill tube jet. At the resolution of the simulation (2 μm) the injected carbon due to the fill tube is visible in the image[1]. While the mass of ablator mix induced by the fill tube is small (30 - 100 ng depending on ablator type and fill tube size [185]), the carbon is injected into the hotspot and hence experiences a very high neutron flux which increases its carbon-γ-ray production. However, at a more realistic resolution of 10 μm the fill tube mix is washed out in the image. Interplay

[1]It is worth noting that the interface tracker used in the hydrodynamics of this simulation [136] prevents movement of mix cells once they become a single isolated cell. Therefore we might expect the fill tube mix to travel further into the hotspot in reality. This has the potential to increase its carbon-γ-ray signal due to the increased neutron fluence.

between the radiation drive asymmetries (primarily P4) and the fill tube has caused ablator decompression around the fill tube which is visible as reduced carbon-γ-ray intensity. This implosion is significantly less perturbed than the multimode simulation and hence the γ-ray images more closely resembles the 1D result shown in Fig. 5.1.

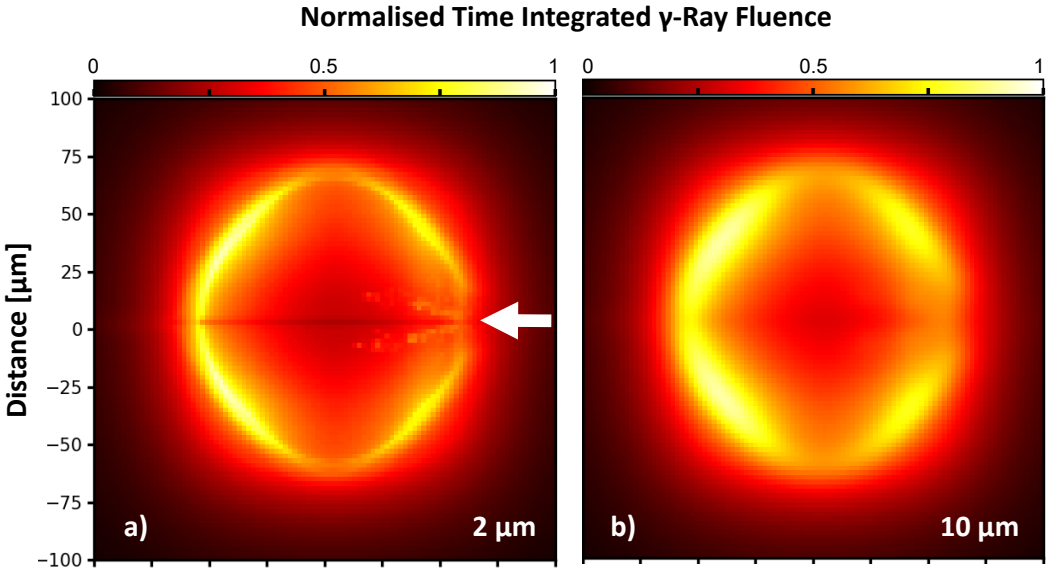

Figure 5.3: **a)** Time integrated carbon γ-ray image at the resolution of the simulation (2 μm) for a 3D simulation of NIF shot n161023 including the fill tube and radiation drive asymmetries. The position and direction of the fill tube is indicated with the white arrow. **b)** A 10 μm Gaussian filter applied to image **a)**. While the fill tube induced hotspot mix is visible in image **a)**, it is not resolved in image **b)**. The radiation drive asymmetry is primarily P4, this creates increased ablator areal density at the 45° and 135° angles which is visible in both cases.

From a computational model standpoint, the inverse ray trace has led to clear images allowing physical interpretation. Due to the low cross section, previous Monte Carlo γ-ray calculations have exhibited poor statistics leading to noisy images [20]. While this could be remedied in future calculations, the inverse ray trace by construction produces images at the resolution of the hydrodynamic grid.

5.2 Fusion and Carbon γ-ray Histories

DT fusion γ-rays can be used to track the progress of burn in time without complications from additional interactions in flight to the detector. The Gamma Reaction History (GRH) and Gas Cherenkov Detector (GCD) measure the burn history and extract the bang time and burn width which correspond to the centroid and FWHM of the fusion γ-ray production rate.

The measured burn widths are consistently higher than most simulations predict. Through numerical investigation it is found that perturbations can both elongate or truncate the burn depending on their nature [120]. Perturbations which introduce high atomic number mix, such as the fill tube, tend to lower the burn duration by reducing

the effective size of the hotspot through radiative cooling. In contrast, asymmetric implosions without mix tend to have longer burn widths. We will look at two types of asymmetry: low mode drive asymmetry (P2 and P4) and the multimode perturbation (which has been used multiple times within this thesis). The asynchronous convergence of these implosions extends the time over which mechanical work is done on the hotspot, see Fig. 5.4. We define a few timescales, beyond the burn width, to compare the different simulations. First we define the stagnation time to be when the PdV work on the hotspot goes to zero. The time difference between the stagnation time and bang time will be denoted Δt_{stag}. Secondly a PdV timescale is defined as the peak-to-trough PdV work divided by the gradient of the PdV work at stagnation, this will be denoted t_{PdV}.

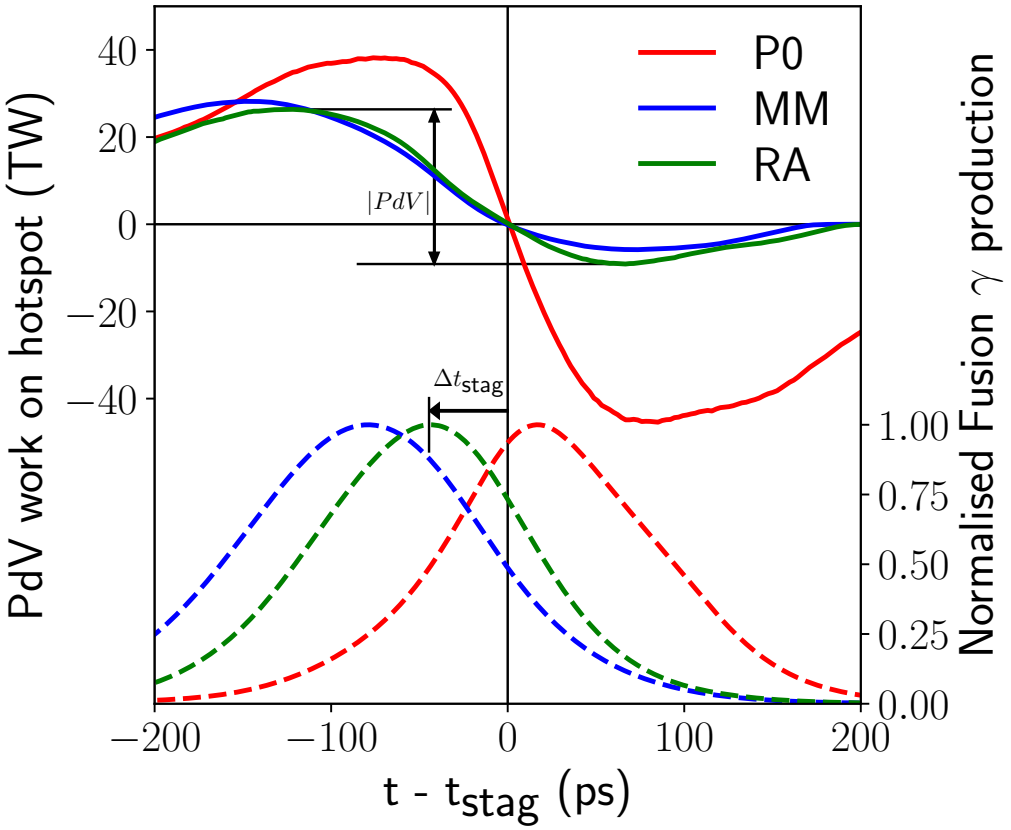

Figure 5.4: The PdV work on the 1 keV hotspot for each simulation type are shown in solid lines and in dashed lines are the normalised DT reaction rates. The simulations are high foot implosions which are symmetric (P0), perturbed with multimode (MM) or driven with radiation drive asymmetries (RA). Also shown are the time difference between bang time and stagnation, Δt_{stag}, and the peak-to-trough PdV work, $|PdV|$, for the RA case.

To find correlations between the mechanical work and burn pulse, principal component analysis (PCA) was utilised. This technique constructs the correlation matrix of the data and performs an eigen-decomposition. However, rather than looking at the directions (eigenvectors) with the highest variance within the data we will look for the highly correlated data i.e. the directions with the lowest eigenvalues. The yield, burn

width, t_{PdV} and Δt_{stag} were taken from 6 simulations (3 high foot and 3 HDC implosions) and PCA was performed. For both the high foot and HDC design, symmetric, low mode radiation asymmetries and multimode cases were considered. From PCA, it was found that 99% of the data variance lay in the first two directions. Therefore the remaining two directions are highly correlated, potentially revealing physical connections between the data coordinates. These two relationships are as follows:

$$\Delta\hat{t}_{\text{stag}} = k\hat{t}_{PdV} \qquad k = -0.882 \ , \tag{5.3}$$

$$\Delta\hat{t}_{\text{burn}} = k_1\hat{t}_{PdV} + k_2\hat{Y} \qquad \begin{cases} k_1 = 1.548 \ , \\ k_2 = 1.204 \ , \end{cases} \tag{5.4}$$

where $\hat{x}$ denotes the standardised quantity i.e. $\hat{x} = (x - \mu_x)/\sigma_x$ where μ_x and σ_x are the population mean and standard deviation of variable x. Firstly we find that the timescale over which PdV work is done is directly proportional to the time difference between bang time and stagnation. As the PdV work is a source of heating for the hotspot, a slower rate will allow energy loss mechanisms, such as radiative losses, more time leading to early burn truncation. Secondly we find the burn width is proportional to a linear combination of yield and PdV work timescale. The dependence on yield, at first counter intuitive, comes from the fact the two capsule designs used in the simulations are different sizes. Purely from hydrodynamic scaling, the smaller capsules will give lower yields, smaller hotspots and shorter burn durations. More interestingly, we see the burn width is proportional to the PdV work timescale. If the hotspot is compressively heated over a longer period this will extend the burn. The asynchronous stagnation of perturbed implosions cause an increased t_{PdV}. Therefore a possible explanation for long experimental burn widths is that not all perturbation sources are accounted for in simulations.

Detailed 3D high fidelity hydrodynamics simulations come closest to matching the experimental observables when all known perturbation modes are included [37]. An active area of research in both indirect and direct drive is looking into 3D drive asymmetries brought about by laser balance or target placement issues [63, 114, 137]. These drive asymmetries may account for the difference in simulated and experimental burn widths. From this investigation principal component analysis has proved itself a powerful tool and it could be used in a combined analysis of different diagnostic measurements.

Using γ-ray energy gating, both the fusion and carbon γ-ray production rates have been measured [30]. Neglecting the neutron time of flight between the source and the ablator ($\sim$ 1 ps), the instantaneous yield of carbon γ-rays for a spherical capsule is given by:

$$Y_{C\gamma}(t) = \int 4\pi r^2 dr \ \frac{\rho_C(r)}{m_C} \int dE \ \sigma(E)\phi_n(r,t,E) \ . \tag{5.5}$$

Similar to the carbon γ images, we will only consider the scattering of primary DT

neutrons and invoke energy separability:

$$Y_{C\gamma}(t) \approx \int 4\pi r^2 dr \frac{\rho_C(r)}{m_C} \langle\sigma\rangle \phi_n(r,t) \ . \tag{5.6}$$

If the neutron source is a point source then $\phi_n(r) \propto 1/r^2$ and the yield is directly proportional to the areal density. However, as with many examples in this work, the neutron averaged areal density is not equal to the line integrated areal density. Introducing a extended source flux factor, $F_n(r,t)Y_n(t) \equiv 4\pi r^2 \phi_n(r,t)$, we arrive at:

$$Y_{C\gamma}(t) \approx \frac{\langle\sigma\rangle}{m_C} Y_n(t) \int dr \rho_C(r) F_n(r,t) \ . \tag{5.7}$$

For most analyses, $F_n(r,t)$ is taken as 1 and the carbon γ yield is directly proportional to the product of the carbon areal density and neutron yield – this is known as the monoenergetic instantaneous point source or MIPS model [84]. However, one can calculate an approximate $F_n(r,t)$ by assuming a uniform extended neutron source of radius $R(t)$:

$$F_n(r,t) = \frac{3r}{2R^3} \left(rR - (r^2 - R^2) \ln \left[\frac{r+R}{\sqrt{r^2 - R^2}} \right] \right) \ , \tag{5.8}$$

$$F_n(r,t) \lim_{r\to\infty} = 1, \quad F_n(r,t) \lim_{r\to R} = \frac{3}{2} \ . \tag{5.9}$$

The function F_n quantifies the increase in flux due to the increased solid angle subtended by the source at distance r, compared to a point source. This modifies the carbon γ yield formula given by Eq. 5.7 as follows:

$$Y_{C\gamma}(t) \approx \frac{\langle\sigma\rangle}{m_C} \langle\rho_C L\rangle(t) \cdot Y_n(t), \quad \rho_C R \leq \langle\rho_C L\rangle \leq \frac{3}{2} \rho_C R \ . \tag{5.10}$$

Therefore the carbon γ yield can be increased due to the higher average chord length through the ablator given by an extended source. Estimates of $\rho_C R$ based on a point source model will be too high by at most 50%.

Without significant alpha heating, the carbon areal density is still increasing throughout the fusing period and peak compression is reached after bang time. Thus it is expected that the peak carbon γ signal will be reached after bang time for a symmetric case. Areal density asymmetries which disrupt the hotspot will alter both the fusion and carbon γ-ray histories. As the time between peak neutron production and peak areal density increases, an increasing delay between fusion and carbon γ-ray peaks will be observed. With hotspot self-heating, thermonuclear burn can continue during re-expansion [174] and therefore for these cases the carbon γ peak will occur before bang time. Time shifts between fusion and carbon γ peaks have been observed experimentally [122].

Figure 5.5 presents the γ-ray histories from the multimode case and the symmetric simulation from which the multimode simulation was initialised. Both exclude alpha heating. For the symmetric case, peak carbon γ signal occurred $\sim$ 15 ps after bang

time. The time difference between peak fusion and carbon γ production was 30 ps for the multimode case. Meaney *et al.* report average peak delays of $\sim$ 15 ps in experiments at NIF [122]. As discussed earlier, the increased PdV work timescale leads to an increased time delay between bang time and stagnation. Stagnation defined as the zero of mechanical work on the hotspot should be well correlated with the peak areal density. Therefore the larger time difference between peak fusion and carbon γ production in the multimode case is a direct result of the increased PdV work timescale brought about by the perturbations. The symmetric case was also run with alpha heating included and the carbon γ-ray signal peaks 10 ps before bang time. This shows that burn had continued through re-expansion, a signature of robust ignition and propagating burn, details of which can be found in Tong *et al.* [174].

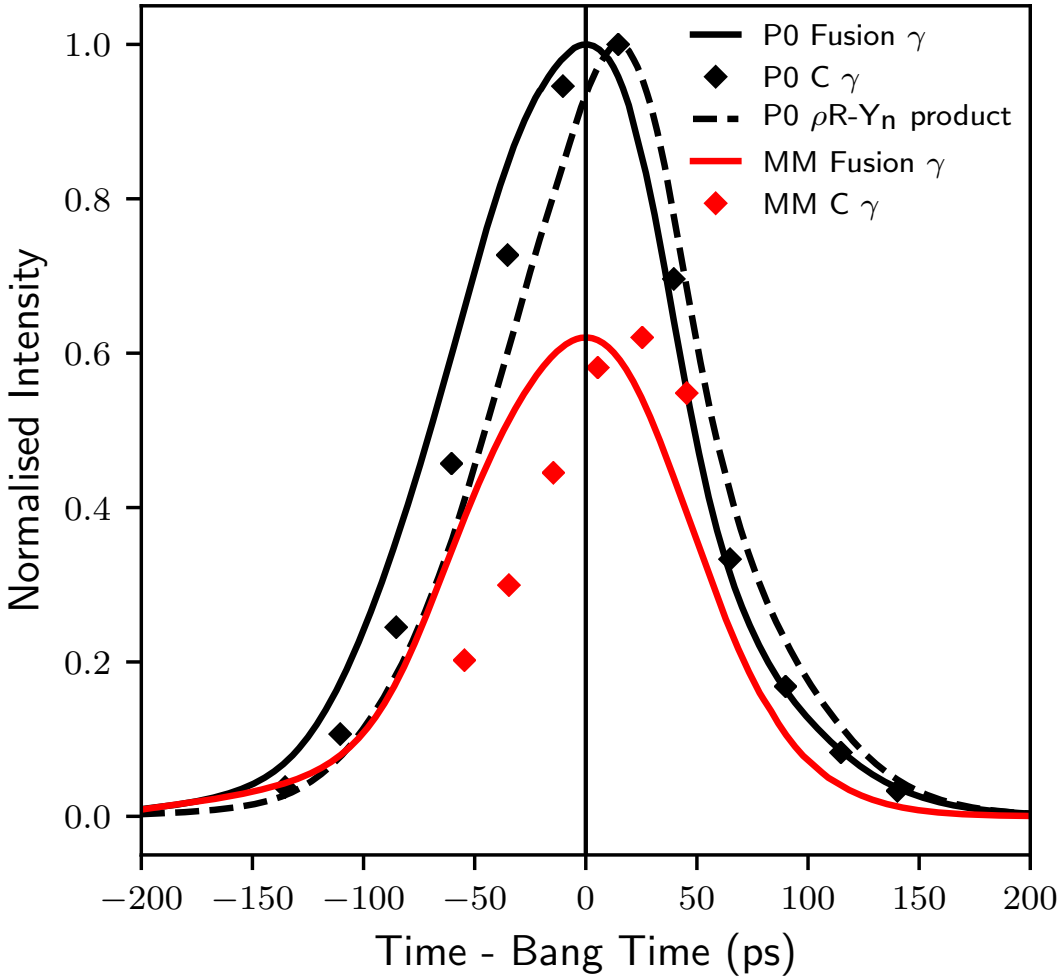

Figure 5.5: Time histories of $\mathrm{D(T},\gamma)$ and $\mathrm{C}(n,n_1\gamma)$ yields for a symmetric implosion (P0) and the multimode simulation (MM). It is observed that in both cases the peak carbon γ signal was reached after bang time. For the multimode simulation, a more significant time shift in carbon γ signal is observed. The fusion γ signals are normalised to the P0 peak value, the carbon γ signals peaks match their respective fusion γ signals. The dashed line shows the evolution of the product of ablator areal density and fusion reaction rate in the symmetric simulation.

As shown in Eq. 5.10, the time evolution of the carbon γ signal should be equal to

$Y_n \cdot \rho_C R$ within a simplified point source model. This can easily be calculated for the symmetric case and is displayed in the Fig. 5.5. We note a $\sim 10\%$ discrepancy between this simplified model and the carbon γ yield calculated via the inverse ray trace method.

First we will consider the correction from an extended source. When the hotspot is large compared to the thickness of remaining ablator then $\langle \rho_C L \rangle \rightarrow 3\rho_C R/2$ (within the uniform source model). This explains why the carbon γ production is higher than the simplified model prediction at early times. As the ratio of hotspot radius to ablator thickness decreases $\langle \rho_C L \rangle \rightarrow \rho_C R$.

An additional effect not considered in Eq. 5.10 but included in the AKED calculation is attenuation. Primary DT neutrons are scattered by the fuel and ablator altering their energy and direction. This modified the total neutron flux seen by the ablator and therefore alters the carbon γ production rate. If we first ignore the scattered neutrons, then attenuation just acts to dilute the neutron flux in the ablator. Therefore as the areal density of the fuel increases as the capsule converges the degree of attenuation will increase. This will act to reduce the carbon γ yield relative to the unattenuated case. This is indeed seen in the results. In reality a fraction of the neutrons scattered prior to exiting the fuel will inelastically scatter off the ablator producing γ-rays which the simulation does not account for. Hence the real signal is expected to lie between the extremes of no attenuation with a point source, given by the areal density burn rate product, and full attenuation with an extended source, given by the inverse ray trace model.

6 Conclusions

6.1 Neutron Spectroscopy

In Section 3.1, the effect of ion velocities on the spectrum of backscattered neutron energies was investigated theoretically and through numerical neutron transport calculations [42, 43]. The work in this thesis showed for the first time that the shape of the backscatter edge is dependent on the scattering rate weighted ion velocity distribution. Hydrodynamic conditions throughout the capsule dictate the form of this distribution and hence these conditions can be inferred from spectroscopic analysis. The mean, $\bar{v}$, and variance, Δ_v^2, of the distribution are given by averaged fluid velocity and the sum of the averaged temperature and fluid velocity variance respectively. Since the neutrons scatter in dense DT fuel which has a low neutron and photon emittance, the backscatter edge presents an avenue to probe regions of the stagnating capsule currently unmeasured. Diagnosing these conditions allows inference of hydrodynamic quantities relevant to capsule performance. For example, from $\bar{v}$ the rate of mechanical work done on the hotspot by the imploding shell during neutron production can be calculated. The Δ_v value can be converted to an inferred scatter weighted temperature, with the effect of fluid velocity variance included. Measurement of both the nD and nT edge would allow separation of the thermal and non-thermal contributions to the variance in the scattering ion velocity.

In order to fit the shape of nT backscatter edge, a spectral model for the background was developed. This includes single and double scattering terms, and the attenuated primary TT neutrons. The model was tested on synthetic data produced by the neutron transport code Minotaur[42] and showed good agreement at current direct drive ICF experimental areal densities. For LILAC simulations of the triple picket shot 87653 and the single picket shot 89224, the model and neutron transport result were within 1% of each other at all energies of the fitting region. Using a single Gaussian model for the scattering ion velocity distribution, best fit values for $\bar{v}$ and Δ_v were all within 10% of theoretical values. Numerical results suggest that to analyse at areal densities $\gtrsim 0.75$ g/cm^2 (DSR $\sim 3.8\%$) may require the inclusion of more spectral backgrounds and attenuation effects. The cumulants for the scattering triton velocity distribution were calculated for a large ensemble of 1D LILAC simulations. Large correlations were observed between the cumulants of the hotspot, shocked shell and free-falling shell indicating a more fundamental underlying relationship. For example, the total Δ_v was seen to be strongly correlated with the hotspot areal density. Future work will aim to construct a simple model which can explain these strong correlations. This will allow

more detailed information to be extracted from the backscatter edge measurements.

Analysis of experimental backscatter edge data would be possible using the same forward fitting technique currently used for neutron time-of-flight spectra [74]. The nT and nD edges occur in the vicinity of the DD peak so instrumental characterisation at these energies would be mutually beneficial for these spectral signals. Analysis of experimental nT backscatter edge data at OMEGA is in progress, for which the author has provided analysis tools [117].

For 3D perturbed implosions different lines of sight would measure the conditions of different regions of the capsule. Asymmetries in dense fuel conditions could therefore be inferred. Four neutron spectrometers are sufficient to characterise the DT neutron birth spectrum needed to analyse the edge. Future investigation is required for the treatment of large areal density asymmetries in the detailed spectral model. However, functional fits based on a simplified backscatter model including an *ad-hoc* background were able to account for the areal density asymmetry. With the use of anti-podal primary and nT edge spectral measurements, this model inferred birth spectral moments and shell velocity means and variances for a P1 implosion. Differences between the anti-podal edge measurements quantified the large residual kinetic energy and asymmetric deceleration brought about by the P1 drive. The effect of temperature on scattering was not included in this calculation but a separate analysis showed that asymmetry in the scattered weighted temperature was present.

In Section 3.2, we showed that the DSR range in the spectrum can exhibit significant slope changes in the presence of areal density asymmetries. By comparison to 1D spectra, areal densities within different angular ranges were calculated for a P2 simulation. Experimental spectral data measuring down to 10 MeV exists [74] and a comparison of inferred areal densities, FNADs and neutron images would test the viability of this analysis. Measuring the primary spectrum, backscatter edges and DSR range, and hence the inferred hotspot and shell velocities and areal density asymmetries, would allow for a more complete description of low mode perturbations.

In Section 3.3.1, the viability of using the secondary DT spectrum in pre-magnetised spherical implosions as a measure of fast ion magnetisation was explored. Conditions for an exploding pusher target were considered in order to minimise the fuel areal density, and hence minimise slowing of the fast tritons created in DD reactions. It was shown for a 2 kT magnetic field that the magnetised triton paths created significant asymmetry in the measured secondary DT spectrum. There was also an increase in secondary DT yield. The level of asymmetry and yield increase was dependent on the burn time, i.e. how long the stagnation conditions could survive. For 100 and 200 ps burn durations the secondary DT yield increased by 1.5 and 2.2 times compared to the unmagnetised case. These two timescales are approximately 2 and 4 times the triton time of flight across the fuel. The anisotropy in the secondary neutron spectrum also increased with increasing burn duration. However, an anisotropic spectrum can also be obtained from shape asymmetry in the fuel. A 33% P2 shape asymmetry was shown to give similar anisotropy in the secondary spectrum to the 100 ps magnetised burn case.

There was not an associated increase in secondary DT yield for the unmagnetised P2 case. Secondary spectral signals indicating areal density asymmetry on unmagnetised targets have been observed experimentally at NIF [106]. Therefore, it may be possible to estimate the average magnetic field strength with measurements of secondary yield, secondary spectra and X-ray imaging.

In Section 3.3.2, the spectrum of high energy neutrons created by tertiary DT reactions was shown to be sensitive to the temperature and density profiles of the hotspot. In particular, the alpha knock on component is dependent on the energy at which alpha particles reach the dense DT fuel layer. The slowing of alphas is reduced if the hotspot is more transparent. This increases the high energy yield of alpha-mediated tertiaries, altering the neutron spectrum shape. One way in which to increase the hotspot transparency is to flatten the temperature and density profile within the central hotspot. The neutron-mediated tertiaries are less sensitive to this profile effect. Thus, the high energy neutron spectra above $\sim$ 19 MeV become close to equal for different hotspot profiles. The alpha-mediated tertiaries are of particular interest as they present a direct measurement of alpha collisions, and hence alpha heating.

6.1.1 Future Work

The backscatter edge shape has been well described through the scattering rate weighted ion velocity distribution. However, understanding of the various contributions to the ion velocity distribution requires further work. The ensemble of LILAC simulations revealed that the hotspot, shocked shell and free-falling shell contributions to the velocity distribution are highly correlated. The return shock plays a key role in setting the conditions in the hotspot and shocked shell. However, other processes are occurring which prevent a purely static shock based analysis. A few possible examples are the subsonic compression post-shock, thermal flux from the hotspot and the time evolution of the shock and free-falling shell. A more fundamental understanding of the stagnation process will greatly benefit the backscatter edge measurement. This will be gained through numerical modelling and simplified analytic models.

The current spectral model for the backscatter edge cannot capture areal density asymmetries without the inclusion of *ad-hoc* backgrounds. Therefore, further development of the model is required. This will require the drawing of areal density asymmetry data from other diagnostics to feed into the model. Separately, extension of the model to higher areal densities will require additional considerations such as triple scattering. A surrogate background model developed from a database of 1D neutron spectra may be an efficient route to including the multiple backgrounds. This analysis will also benefit the spectral slope analysis in the presence of areal density asymmetries.

While the static model discussed in 3.3.1 gives a good first estimate, the capability to perform magnetised secondary spectra calculations in line with the hydrodynamics is currently being developed and tested by Dr Brian Appelbe. This will allow the secondary spectral signals from hydrodynamic simulations of proposed magnetised target

designs to be investigated.

Modelling of tertiary spectra is in its nascent stages and there are many avenues for further work. Development of the codes used to model tertiaries will be discussed later in Section 6.5. On the theoretical side, previous models for the tertiary spectrum were local [77, 78]. However, results presented here show that profile effects modify the spectrum highlighting the non-local nature. Therefore, a simple theoretical model including the finite range of alphas is required. Separately, the backscatter edge measurement samples the same region as the neutron-mediated tertiaries. A combined analysis would remove some of the unknowns present in the tertiary analysis. For example, the finite temperature of the shell alters the stopping power of knocked on ions – the backscatter edge could provide a measurement/constraint on this.

6.2 Neutron Imaging

Primary neutron imaging was investigated in Section 4.1.1. It has been shown that spatially varying attenuation does not affect shape analysis using the 17% contour. Since the 17% contour is the primary shape analysis method in use for neutron imaging, this result ensures confidence in its interpretation. This was tested for both idealised 1D and perturbed 3D conditions. While the attenuation factor varied by a few tens of percent over a few μm for the 3D perturbed case, the contour position was moved by only < 3 μm. Three dimensional reconstruction techniques using multiple lines of sight were tested on synthetic primary images. The technique developed by Volegov *et al.* [177–179] produced encouraging results on synthetic images created by AKED. However, further analysis investigating the effects of differential attenuation is required.

In Section 4.1.2, the use of activation diagnostics to measure areal density asymmetries was shown to have limited resolution due to the extended hotspot. A simple test case showed that the angular resolution ($\Delta\theta$) on areal density asymmetries is dependent on the shell to hotspot radius ratio (R_s/R_h): $\Delta\theta \propto \sin^{-1}(R_h/R_s)$. Therefore, the neutron-averaged areal density, as seen by the FNADs, will have less high mode content than the centre-point areal density. For a multimode simulation, the high mode perturbations were not resolvable by the FNADs due to the extended nature of the hotspot. Hotspot velocity appears as an additional low mode signal, further reducing the ability to measure high mode areal density variation. Theoretically, scattered neutron imaging is better suited to resolve high mode areal density asymmetries. However, it is limited by low image resolution in experiment.

In Section 4.2, it was shown that multiple energy-gated neutron images and the fluence compensation technique allow a detailed description of shell conditions. Multiple energy gates probe different angular ranges and hence localised features such as high mode spikes and the tent scar can be isolated in this scheme. For a simulation with a single spike perturbation, fluence compensated images faithfully recovered the areal density conditions near bang time. Performing the gating on a single line of sight would allow such features to be imaged with the same projection characteristics - this capability has

already been proven with the 6-12 MeV and 13-17 MeV gates on one NIS line of sight. The recent increase in neutron yields [50, 108] may allow for sufficient signal-to-noise ratio in narrower energy gates. In collaboration with Volegov *et al.* [179], scattered neutron images of the multimode simulation were used in a density reconstruction. The perturbation structure and density values were in modest agreement, with the reconstructed mass 20% lower than simulated [179]. These are encouraging results given that only a single scattered neutron image was used in the reconstruction.

In Section 4.3, combined imaging and spectroscopic analysis has been shown to aid in diagnosing different failure mechanisms and understanding the correlation between hotspot flows, shell asymmetries and drive imbalances. The particular examples considered had very similar spectroscopic signals. However, primary and fluence compensated imaging revealed that one was due to bulk motion of both shell and hotspot whilst the other had a more localised out-flowing or aneurysm of the hotspot. Since the remedies to these two failure mechanisms could be very different, it is important to differentiate between them.

6.2.1 Future Work

We expect that reconstruction techniques will become more reliable as additional imaging lines of sight are being constructed. The effect of an increased number of lines of sight can be readily tested using synthetic data. While tomography potentially leaves 17% contour and fluence compensation 2D analysis behind, new metrics and analysis of the reconstructed 3D volumes are required in order to compare prediction and experiment. Separately, analysis involving multiple energy gates on a single line of sight may allow more accurate inferred conditions without the assumptions and degeneracy of tomographic techniques.

6.3 Gamma Ray Measurements

In Section 5.1, an investigation was carried out to produce simulated images of remaining carbon-based ablator using the 4.4 MeV γ-ray produced by inelastic scattering of primary DT neutrons. The third line of sight of NIS will soon be upgraded to image the carbon γ rays – the ~ 10 μm resolution reported for the neutron imaging [176, 179] was used as an estimate for the γ imaging resolution[1]. Carbon γ imaging was shown to be an effective method to image the ablator areal density for both spherical and asymmetric implosions. The ablator features closest to the hotspot have an increased signal. This allows the feed-through of ablator perturbations to hotspot and dense fuel morphology to be investigated. For a multimode simulation, a spatial resolution of 10 μm on a time integrated image was sufficient to observe the perturbed structure. A simulation using realistic perturbation sources [120] showed that low mode radiation drive asymmetries

[1] One of the main limiting factors on the neutron image resolution is the neutrons long mean free path in the aperture materials (> 3 cm) therefore requiring specialised thick aperture arrays [176, 179], an issue which will persist with γ imaging.

can be imaged and resolved at 10 μm. However, the fine scale ablator mix induced by the fill tube defect does not give a strong enough carbon γ signal to overcome imaging spatial resolution. A combination of high fidelity simulations, which accurately capture mix dynamics [37], and synthetic carbon γ images can be used in future to find the required spatial resolution to resolve the fill tube mix.

In Section 5.2, the time series of DT fusion γ production were analysed for a number of radiation hydrodynamics simulations performed by Chimera. Comparison between the PdV work performed on the hotspot and the burn history revealed some correlations. The time between stagnation (PdV work = 0) and bang time was found to be proportional to the timescale over which the PdV work was performed. In other words, a rapid compression of the hotspot brought the stagnation and bang time closer. This is intuitive as this gives loss mechanisms, such as radiative cooling, less time over which to operate – the energy loss is therefore reduced. A second strong correlation was found between the burn width, PdV work timescale and yield. The yield dependence is purely from hydrodynamic scaling, as the smaller capsules will give lower yields, smaller hotspots and shorter burn durations. The PdV work timescale sets the heating rate of the hotspot. A prolonged heating rate will extend the burn time at the expense of a lower peak fusion rate. Hydrodynamic simulations which under-predict the burn width are likely missing perturbation sources which cause a more asynchronous stagnation. As understanding of the experiment has improved, additional perturbations such as 3D drive asymmetries have been analysed. When included in simulation, these perturbations generally bring the simulated and experimental burn widths into closer agreement.

The time series of carbon γ-rays were also consider in Section 5.2. The carbon γ-ray production rate is, to first order, proportional to the product of neutron yield and ablator areal density. Comparison of time series of DT fusion and carbon γ-ray production showed a delay between the peaks. The length of this delay changed depending on the degree of burn truncation. Symmetric and multimode simulations showed 15 and 30 ps delays respectively. Similar delays ($\sim$ 15 ps) between fusion and carbon γ-ray peaks have been systematically observed in experiments at NIF [122]. The simulation results indicate that the delay between stagnation and bang time increases for asymmetric implosions. The same conclusion was made independently from analysis of the fusion γ-rays.

6.3.1 Future Work

In a similar fashion to the scattered neutron images, the carbon γ-ray images can be used to reconstruct the remaining ablator density given a source distribution. The images contain information of carbon distribution in all 4π, unlike the restricted angular range of the scattered neutron images. This makes the reconstruction easier as there are no blind spots, but more degenerate as more solutions could create the observed image. Synthetic data created using techniques described in this work could be used to

determine if the current reconstruction techniques for scattered neutron images can be applied to carbon γ-ray images without modification.

Recent experimental developments in the measurements of the DT fusion γ-ray histories has greatly increased the time resolution possible to $\sim$10 ps [66]. Features beyond the centroid and width of the production rate can now be resolved. Therefore, a more extensive simulation study of DT fusion γ-ray histories including higher moments (such as skew and kurtosis) would allow more information to be inferred from experimental measurements. Similarly features of the carbon γ-ray signal, such as the width, could be explored to extract time resolved ablator density properties. Foremost, developing analysis to extract the ablator areal density as a function of time using the fusion and carbon γ-ray history.

6.4 Outlook

Diagnosing failure mechanisms in current ICF experiments is key in improving future experimental performance. The list of potential sources of perturbations and asymmetries is constantly evolving. Existing measurements can be used to identify and remove/minimise these sources. However, these measurements do not give a complete picture of the experiment and failure mechanisms can be missed or misidentified. Novel measurements are vital in both constraining known mechanisms and revealing new degradation sources. To date, the majority of measurements are focussed on the conditions within the hotspot. This is due to its central importance in the hotspot ignition scheme but also due to its high emittance of observable signals. The properties of the dense DT fuel are relatively poorly measured, similarly for the remaining ablator in indirect drive experiments. This is due to the low emittance of these regions. Instead scattering measurements must be relied on, which currently are used to infer areal density [84, 95] but do not measure hydrodynamics conditions such as fluid velocity and temperature. As preheating of the fuel and fuel-ablator mix are proposed as degradation mechanisms [58], hotspot measurements cannot currently directly measure these effects. Therefore, efforts towards increasing the capabilities of nuclear measurements, such as the backscatter edge analysis, is required in order to better understand the dominant degradation mechanisms at play.

Combining measurements allows more information to be extracted than analysis of the measurements separately. In the field of ICF, a Bayesian analysis using multiple measurements has been developed to infer stagnation conditions during Magnetic Linear Inertial Fusion (MagLIF) experiments at Z [103]. Integrating a similar framework to spherical ICF experiments would allow assumptions used in analysis of individual measurements to be relaxed. For example, the conversion of DSR to areal density is found from 1D neutron transport calculations so cannot account for the effects of asymmetries. By the inclusion of FNADS and neutron images, the fuel morphology could be included in the DSR to areal density measurement. In recent years, Artificial Intelligence (AI) techniques have started to enter the areas of ICF design and experiments.

These generally involved design optimisation [70, 76] and/or calibrating simulation to experimental data [58, 70, 87]. AI also has great potential in pure experimental data analysis, for example genetic algorithms have been used in X-ray spectroscopy [67]. For complex systems, it is often the case that it is difficult to construct a simple model to solve the inverse problem [99]. However, it is possible to perform a large number of calculations of the forward problem for various input conditions. Bayesian inference (using Markov chain Monte Carlo or similar) presents a way to construct a method which can use these forward calculations to fit experimental data and estimate with uncertainties the input conditions. Doing large numbers of calculations of the forward problem however can be prohibitively computationally expensive; in these situations using a machine learned emulator can speed up calculations. This is relevant to many of the nuclear measurements discussed in this thesis.

One of the primary aims of this research has been to expand the number of measurable quantities in ICF experiments. However, measurements in ICF tend to be averaged in some sense, usually temporal and/or spatial integration has been performed. Therefore potentially vital information about the time evolution and spatial profiles is still missing. For example, the burn-average ion temperature can be approximately measured but the cooling rate of the hotspot cannot. A similar problem exists with lack of measurements on spatial gradients. To access this information one needs to include higher order terms in the current analysis or to combine diagnostic information. An example of the former is to measure the kurtosis of the DT peak and therefore have a measurement of the variance of the ion temperature, see Eq. 2.77. An example of the latter is the analysis proposed and performed by Divol *et al.* [48] which uses primary neutron imaging tomography and spectral analysis to reconstruct spatially resolved 3D ion temperature maps.

As experiments towards magnetised ICF on NIF start, the role of nuclear measurements in diagnosing the effects of the magnetic fields needs to be investigated. In this work we presented the use of secondary DT spectra in diagnosing magnetic fields in low areal density targets. However, these techniques are not viable for high gain layered implosions as the triton stopping distance becomes too short. Direct measurements of the magnetic field strength with nuclear observables will become increasingly difficult. Indirect measurements, such as increased temperature and change in capsule shape, can be performed but will rely on some additional model to extract a magnetic field strength.

The measurements presented in this thesis have been given in the context of ICF. However, some of the techniques are applicable in other high energy density physics experiments. These experiments commonly involve the shock compression of materials to high densities. Ions and electrons can behave very differently at shock fronts and therefore separate measurements of ionic and electronic conditions are valuable. As the radiative properties are dominated by the electrons, it is often difficult to measure the ionic contribution. Nuclear measurements can be used to focus on the ions. With the use of an external neutron source, the backscatter edge could be used to infer velocities and temperatures of the ions.

Capsule implosions have been used to study nuclear fusion reactions at conditions relevant to stellar and Big Bang nucleosynthesis. Nuclear measurements are relied on in these cases to measure the yield and spectrum of fusion products [27, 28, 96, 193, 194]. ICF experiments also more accurately recreate the astrophysical environment in terms of plasma conditions. In more traditional accelerator experiments, the target is cold and hence has bound electron screening of the nucleus. Separately, the high neutron flux environment of a DT capsule allows neutron-induced reactions to be studied. Light nuclei provide a good test bed for fundamental nuclear theory. For example, accurate modelling of nucleon-nucleon and 3-nucleon interactions is needed to gain agreement with measurements of the D(n,2n)p reaction [52, 158]. Heavier nuclei (atomic mass $>$ 56) are also of interest as their neutron-capture reactions have astrophysical relevance. The slow (s) and rapid (r) neutron-capture processes account for all the neutron rich heavy elements observed in the universe [9]. While directly measuring these processes is extremely difficult due to their high temperature and number density requirements, nuclear physics problems which affect these processes could be investigated using ICF experiments [31]. One such effect is the thermal excitation of nuclear states altering the neutron-capture cross section. This will require temperatures in the tens of keV range [31] – this would be possible in the case of a strongly igniting DT capsule.

6.5 Future Work in Numerical Modelling

In order to continue using simulated data to inform experimental analysis, continued development of simulation tools to improve accuracy is required. We will discuss two facets of the ongoing research in numerical modelling of ICF implosions at Imperial College. These are improvements to the calculation of radiative properties used in radhydro simulations and the transport models used to post process the radhydro simulations to calculate the nuclear observables.

6.5.1 Minotaur

While Minotaur is currently the most comprehensive code at Imperial College for producing neutron spectra from 1D hydrodynamics simulations, there are several avenues for further work. Currently, the computation time is dominated by the calculation of transfer cross sections including the effects of fluid velocity and temperature. Either some increase in efficiency of the calculation is needed or the creation of tables which could be loaded to reduce run time. Since we are working with neutron energies much higher than those of the scattering ions, some suitable expansion may allow an increased efficiency. Alternatively, the scattering matrices are sparse, see Fig. 2.9, and therefore the tables would be easily compressed. The inclusion of ion velocities to inelastic processes is also currently neglected. Relativistic corrections have proved important in matching physical neutron spectra and therefore should be an aim to include these in Minotaur. Fast ion transport is in a less developed state than the neutron transport

in Minotaur. Given interesting preliminary results in high energy neutron spectra, see Section 3.3, development of the fast ion transport would allow a wider range of research paths. A key update would be to include stopping power models that can handle partially degenerate and coupled plasmas. This would aid in modelling the tertiary neutrons.

6.5.2 AKED

In order to make AKED efficient enough for 3D calculations, many simplifying steps have been taken. An important new addition to AKED would be the inclusion of inelastic scattering such as D(n,2n), allowing some accuracy to be recovered at lower neutron energies. The ray trace algorithm also traces between cell centres, albeit with some angular smoothing (see Appendix B.3), which can cause some grid effects. A subgrid or stochastic sampling of the starting and finishing points of a ray may be used to eliminate this.

6.5.3 SpK

A proposed improvement to SpK is to implement and develop a model for IPD and pressure ionisation which is self consistent i.e. the shift in continuum and loss of bound states are calculated from the same model. This non-ideal plasma behaviour can be formulated in terms of an interacting fluid description of structure factors and radial distribution functions[2]. Work from Lin *et al.* [110] describes a method to calculate IPD from the static structure factor. Work from Iglesias *et al.* [93] describes how to calculate a microfields distribution from a radial distribution function. Combining these methods within SpK with a interacting fluid model, such as hyper-netted chain or mean spherical approximation, would be a step in the direction of self-consistent non-ideal behaviour.

[2]The radial distribution function, $g(r)$ is related to the static structure factor, $S(q)$, through a Fourier transform, $S(q) = 1 + n\mathcal{F}(g)$.

Appendices

A Theory Appendices

A.1 Statistical Mechanics

A.1.1 Microfield Distribution

The microfields problem was originally approached by Holtsmark when considering the distribution of gravitational forces acting on a particle due to all neighbouring particles. The same analysis can be used in plasmas due to the same radial dependence of Newton's law of gravitation and Coloumb's force law. Since many derivations in the literature aim to provide a more general microfield distribution, the Holtsmark result is often quoted without derivation. A detailed derivation will therefore be given here for reference.

We first assume that particles are uniformly distributed in space d^3r, the distribution of force, $W(\vec{F})$, at the origin is then given by:

$$W(\vec{F}) = \int \prod_i^N \frac{d^3 r_i}{V} \delta\left(\vec{F} - \sum_i^N \vec{F}_i(\vec{r}_i)\right) \ , \tag{A.1}$$

where V is the volume of the space, r_i is the position of the i-th particle and F_i is the force due to the i-th particle. Using the Fourier transform identity:

$$\delta(\vec{x}) = \frac{1}{(2\pi)^3} \int d^3k \exp\left[-i\vec{k}\cdot\vec{x}\right] \ , \tag{A.2}$$

we then arrive at:

$$W(\vec{F}) = \frac{1}{(2\pi)^3} \int d^3k \exp\left[-i\vec{k}\cdot\vec{F}\right] \int \prod_i^N \frac{d^3 r_i}{V} \exp\left[i\vec{k}\cdot\sum_i^N \vec{F}_i(\vec{r}_i)\right] \ , \tag{A.3}$$

$$W(\vec{F}) \equiv \frac{1}{(2\pi)^3} \int d^3k \exp\left[-i\vec{k}\cdot\vec{F}\right] T(\vec{k}) \ . \tag{A.4}$$

Since the interparticle force only depends on the separation, $T(\vec{k})$ can be written as a power of a single integral:

$$T(\vec{k}) = \int \prod_i^N \frac{d^3 r_i}{V} \exp\left[i\vec{k}\cdot\sum_i^N \vec{F}_i(\vec{r}_i)\right] = \left(\int \frac{d^3x}{V} \exp\left[i\vec{k}\cdot\vec{F}(x)\right]\right)^N \ . \tag{A.5}$$

The common statistical mechanics trick of adding and subtracting 1 will then be used to obtain a convergent result in the thermodynamic limit ($N \to \infty$, $V \to \infty$, $n = N/V =$

const.):

$$T(\vec{k}) = \left\{1 - \int \frac{d^3x}{V}\left(1 - \exp\left[i\vec{k}\cdot\vec{F}(x)\right]\right)\right\}^N = \left\{1 - \frac{1}{N}\int d^3x\ n\left(1 - \exp\left[i\vec{k}\cdot\vec{F}(x)\right]\right)\right\}^N ,$$
$$T(\vec{k}) = \exp\left[-n\int d^3x\ \left(1 - \exp\left[i\vec{k}\cdot\vec{F}(x)\right]\right)\right] . \tag{A.6}$$

If we now specify the form of the force as inverse square $\vec{F} = A\vec{x}/x^3$, then $T(k)$ can be found through integration:

$$\int d^3x\ \left(1 - \exp\left[i\vec{k}\cdot\vec{F}(x)\right]\right) = 4\pi\int_0^\infty dx\left[x^2 - \frac{x^4}{kA}\sin\left(\frac{kA}{x^2}\right)\right] = \frac{4}{15}\left(2\pi k|A|\right)^{3/2} ,$$
$$T(k) = \exp\left[-n\frac{4}{15}\left(2\pi k|A|\right)^{3/2}\right] . \tag{A.7}$$

Using the isotropy of the system to integrate out the angular dimensions in k-space [21], we define the probability of finding a field strength, $F = \left|\vec{F}\right|$:

$$P(F) = 4\pi F^2 W(\vec{F}) =$$
$$\frac{2F}{\pi}\int_0^\infty dk\ k\sin(kF)\exp\left[-\frac{2\sqrt{2\pi}}{5}\left(k|A|\left[\frac{4\pi n}{3}\right]^{2/3}\right)^{3/2}\right] . \tag{A.8}$$

Finally the Holtsmark distribution is commonly written in terms of the reduced dimensionless microfield parameter $\beta = F/F_0$ and integration variable $y = kF_0$:

$$P_H(\beta) = \frac{2\beta}{\pi}\int_0^\infty dy\ y\sin(y\beta)\exp\left(-\frac{2\sqrt{2\pi}}{5}y^{3/2}\right), \tag{A.9}$$

$$F_0 = |A|\left[\frac{4\pi n}{3}\right]^{2/3} = \frac{|A|}{r_0^2} , \tag{A.10}$$

where r_0 is the interparticle separation and therefore F_0 represents the force at the interparticle separation. A plot of the functional forms of the Holtsmark distribution and its cumulative are shown in Fig. A.1. The constant $2\sqrt{2\pi}/5 = 1.002651...$ is often dropped due to its proximity to 1.

The assumption of uniformly distributed particles used in deriving the Holtsmark distribution is the same as an ideal gas approximation. In reality the repulsive forces between charged particles reduce the probability of finding particles in close proximity. Therefore microfield distributions in real plasmas are more peaked at lower field strengths. There are many models which aim to capture this behaviour [85] of which APEX is a notable example [92, 93]. APEX calculates the microfield distribution based on the pair correlation function, $g(r)$, which can be calculated from statistical fluid equations.

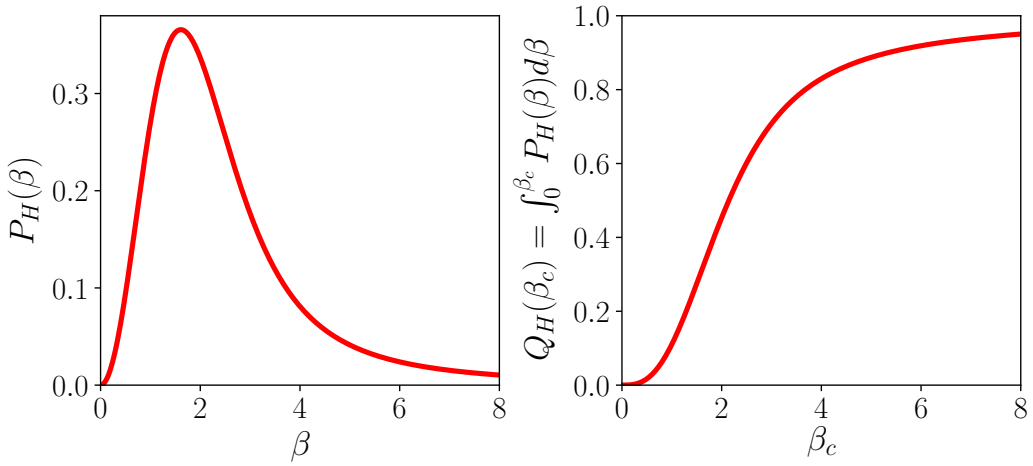

Figure A.1: The Holtsmark distribution and its cumulative as a function of the dimensionless microfield parameter β

A.2 Scattering Kinematics

A.2.1 Beam Target Geometry

We will consider a general $2 \rightarrow 2$ body interaction for species $i + j \rightarrow k + l$ where energy Q is released (negative Q gives absorbed energy). In the beam target (BT) frame, species i is our beam and species j our target. We will solve for the properties of species k without loss of generality. As with most kinematics problems, transforming to the centre of mass (CoM) frame greatly simplifies the analysis, see Fig. A.2 for the geometry of the two frames.

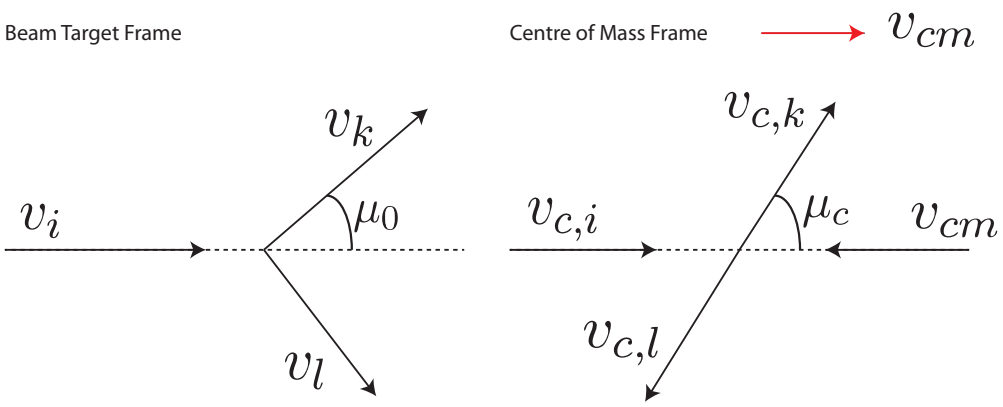

Figure A.2: Diagram showing the $2 \rightarrow 2$ scattering geometry in the beam target and centre of mass frames. Relevant velocities and angles are defined in the figure. Note in the centre of mass frame that the target particle j is moving at the centre of mass velocity as it is stationary in the lab frame.

Firstly we will consider the classical case ($v \ll c$ and $E = p^2/2m$), using energy and

momentum conservation in the CoM frame to solve for the energy of k:

$$E_{c,i} + E_{c,j} + Q = E_{c,k} + E_{c,l} \ , \tag{A.11}$$

$$m_i + m_j = m_k + m_l \ , \tag{A.12}$$

$$\vec{p}_{c,i} = -\vec{p}_{c,j} \text{ and } \vec{p}_{c,k} = -\vec{p}_{c,l} \ , \tag{A.13}$$

$$E_{c,k} = \frac{m_{lk} m_i}{m_k m_{ij}} E_{c,i} \left(1 + \frac{Q}{E^*}\right) \ , \tag{A.14}$$

where we defined the reduced mass $1/m_{ij} = 1/m_i + 1/m_j$ and the total CoM energy pre collision $E^* = E_{c,i} + E_{c,j} = \frac{m_i}{m_{ij}} E_{c,i}$. From here we will derive the first "mass parameter", a, relating the BT and CoM frame energies:

$$\vec{v}_{cm} = \frac{m_{ij}}{m_j} \vec{v}_i \rightarrow \vec{p}_{c,i} = \frac{m_{ij}}{m_i} \vec{p}_i, \tag{A.15}$$

$$E_{c,i} = \left(\frac{m_{ij}}{m_i}\right)^2 E_i, \ E^* = \frac{m_{ij}}{m_i} E_i \ , \tag{A.16}$$

$$E_{c,k} = \frac{m_{lk} m_{ij}}{m_k m_i} \left(1 + \frac{Q}{E^*}\right) E_i \equiv a^2 E_i \ . \tag{A.17}$$

Next we find the energy of the outgoing particle in the BT frame and along the way define the second "mass parameter", b. The outgoing energy is found as a function of incoming energy and CoM scattering cosine:

$$\frac{1}{2} m_k v_{cm}^2 = \frac{1}{2} m_k \left(\frac{m_{ij}}{m_j}\right)^2 v_i^2 = \frac{m_{ij}^2 m_k}{m_j^2 m_i} E_i \equiv b^2 E_i \ , \tag{A.18}$$

$$E_k = \frac{1}{2} m_k v_k^2 = \frac{1}{2} m_k (\vec{v}_{c,k} + \vec{v}_{cm})^2 = E_{c,k} + m_k \vec{v}_{c,k} \cdot \vec{v}_{cm} + \frac{1}{2} m_k v_{cm}^2 \ , \tag{A.19}$$

$$= a^2 E_i + m_k v_{c,k} v_{cm} \mu_c + b^2 E_i = \left(a^2 + 2ab\mu_c + b^2\right) E_i \ , \tag{A.20}$$

this allows the slowing down kernel, $g = \partial \mu_c / \partial E_k$, to be found:

$$g = \frac{\partial \mu_c}{\partial E_k} = \frac{1}{2abE_i} = \frac{2}{((a+b)^2 - (a-b)^2) E_i} = \frac{2}{E_{k,max} - E_{k,min}} \ . \tag{A.21}$$

The maximum and minimum energy of the outgoing particle occur at $\mu_c = +1$ and $\mu_c = -1$ respectively. Finally the BT frame scattering cosine, μ_0^*, is related to the incoming and outgoing energies:

$$E_{c,k} = \frac{1}{2} m_k (\vec{v}_k - \vec{v}_{cm})^2 = E_k - m_k \vec{v}_k \cdot \vec{v}_{cm} + b^2 E_i \ , \tag{A.22}$$

$$m_k \vec{v}_k \cdot \vec{v}_{cm} = 2b\sqrt{E_k E_i} \mu_0^* = E_k + b^2 E_i - a^2 E_i \ , \tag{A.23}$$

$$\mu_0^* = \frac{1}{2b} \left[\sqrt{\frac{E_k}{E_i}} - (a^2 - b^2) \sqrt{\frac{E_i}{E_k}}\right] \ . \tag{A.24}$$

Combining Eqs. A.20 and A.24 one can find a relationship between BT and CoM scat-

tering cosines and evaluate the Jacobian:

$$\mu_c = \frac{b}{a}\left[\mu_0^{*2} - 1 + \mu_0^*\sqrt{\mu_0^{*2} - 1 + a^2/b^2}\right] , \tag{A.25}$$

$$\frac{\partial \mu_c}{\partial \mu_0^*} = \frac{b}{a}\left[2\mu_0^* + \frac{2\mu_0^{*2} - 1 + a^2/b^2}{\sqrt{\mu_0^{*2} - 1 + a^2/b^2}}\right] . \tag{A.26}$$

In the following sections pre collision motion of the target will be included and a relativistic treatment of elastic scattering will be given.

A.2.2 Classical Lab Frame Scattering Kinematics

This section will use the notation and results outlined in the previous section, subscript BT will be used to identify BT frame quantities.

In the lab frame, target species j is no longer stationary thus altering the velocity of the CoM. Therefore, we must define additional angles between the projectile and target in the problem:

$$\mu' \equiv \frac{\vec{v}_i \cdot \vec{v}_j}{v_i v_j},\ \mu \equiv \frac{\vec{v}_k \cdot \vec{v}_j}{v_k v_j} . \tag{A.27}$$

The BT in and outgoing energies can be simply related to lab frame equivalents through frame transforms:

$$E_{\mathrm{BT},i} = \frac{1}{2}m_i(\vec{v}_i - \vec{v}_j)^2 = E_i + \frac{m_i}{m_j}E_j - 2\sqrt{\frac{m_i}{m_j}}\sqrt{E_i E_j}\mu' , \tag{A.28}$$

$$E_{\mathrm{BT},k} = \frac{1}{2}m_k(\vec{v}_k - \vec{v}_j)^2 = E_k + \frac{m_k}{m_j}E_j - 2\sqrt{\frac{m_k}{m_j}}\sqrt{E_k E_j}\mu . \tag{A.29}$$

These can be used to find the CoM scattering cosine by subbing into the expression:

$$\mu_c = \frac{1}{2ab}\frac{E_{\mathrm{BT},k}}{E_{\mathrm{BT},i}} - (a^2 + b^2) = \frac{1}{2ab}\frac{E_k + \frac{m_k}{m_j}E_j - 2\sqrt{\frac{m_k}{m_j}}\sqrt{E_k E_j}\mu}{E_i + \frac{m_i}{m_j}E_j - 2\sqrt{\frac{m_i}{m_j}}\sqrt{E_i E_j}\mu'} - (a^2 + b^2) . \tag{A.30}$$

For the lab frame scattering cosine it is simpler to re-derive from energy and momentum conservation in the lab frame than to transform the BT scattering cosine. We eliminate species l from the conservation equations and rearrange for μ_0^* to obtain:

$$\mu_0^* = \mu_{\mathrm{BT},0}^* + \sqrt{\frac{m_j E_j}{m_k E_k}}\mu' - \sqrt{\frac{m_j E_j}{m_i E_i}}\mu + \frac{m_l - m_j}{2\sqrt{m_i m_k}}\frac{E_j}{\sqrt{E_i E_k}} , \tag{A.31}$$

$$\mu_{\mathrm{BT},0}^* = \frac{1}{2b}\left[\sqrt{\frac{E_k}{E_i}} - (a^2 - b^2)\sqrt{\frac{E_i}{E_k}}\right] . \tag{A.32}$$

If we are considering reactions where species l and j are the same then the final term in Eq. A.31 vanishes, e.g. for neutron scattering.

The slowing down kernel is also needed to bring the differential cross section from the

CoM to lab frame.

$$g = \frac{\partial \mu_c}{\partial E_k} = \frac{\partial \mu_c}{\partial E_{\mathrm{BT},k}} \frac{\partial E_{\mathrm{BT},k}}{\partial E_k} = \frac{1}{2abE_{\mathrm{BT},i}} \left(1 - \sqrt{\frac{m_k E_j}{m_j E_k}} \mu\right) \ . \tag{A.33}$$

Finally the cross section must be altered to account for the change in flux due to the change in relative velocity. The factor is introduced to the cross section so that the collision operator is given by the product of the scattering kernel and lab frame incident flux:

$$\sigma(E) \rightarrow \frac{|\vec{v}_i - \vec{v}_j|}{v_i} \sigma(E) \ . \tag{A.34}$$

A.2.3 Relativistic Lab Frame Scattering Kinematics

Natural units ($c = 1$) will be used in the following section leading to following relativistic definitions:

$$\gamma = \frac{1}{\sqrt{1 - \beta^2}} \ , \tag{A.35}$$

$$\vec{p} = \gamma M \vec{\beta} \ , \tag{A.36}$$

$$E = \sqrt{M^2 + p^2} = \gamma M \ , \tag{A.37}$$

$$K = E - M = (\gamma - 1) M \ , \tag{A.38}$$

$$M^* = \sqrt{\sum E^2 - \left| \sum \vec{p} \right|^2} \ , \tag{A.39}$$

where γ, $\vec{p}$, M, $\vec{\beta}$, E, K and M^* denote the Lorentz factor, 3-momentum, rest mass, velocity, energy, kinetic energy and invariant mass respectively.

Relativistic corrections to scattering kinematics are required to very accurately describe the post collision velocities at MeV particle kinetic energies. In particular, this analysis will be of interest for the elastic scattering of DT fusion neutrons. We will therefore focus on the kinematics of the incoming and outgoing neutron.

Similar to the analysis in the previous two sections, the quantities that will be required for the scattering analysis are the scattering cosines, in the lab and centre of mass frames, and the slowing downing kernel[169]. These are given by the following definitions:

$$\mu^* \equiv \frac{\vec{p}'_n \cdot \vec{p}_n}{p'_n p_n}, \ \mu_c \equiv \frac{\vec{p}'_{c,n} \cdot \vec{p}_{c,n}}{p^2_{c,n}}, \ g \equiv \left| \frac{\partial \mu_c}{\partial E_n} \right| \ . \tag{A.40}$$

As before, subscript c denotes centre of mass frame quantities, primed quantities are pre-collision and unprimed quantities are post-collision. We also need to define the various angles between neutron and ion:

$$\mu' \equiv \frac{\vec{p}'_n \cdot \vec{p}'_i}{p'_n p'_i}, \ \mu \equiv \frac{\vec{p}_n \cdot \vec{p}'_i}{p_n p'_i} \ . \tag{A.41}$$

We will proceed in this analysis by finding the properties of the centre of mass frame,

using the invariant mass to link to the lab frame:

$$\vec{\beta}_c = \frac{\vec{p}'_n + \vec{p}'_i}{E'_n + E'_i},\ \gamma_c = \frac{1}{\sqrt{1-\beta_c^2}}\ , \tag{A.42}$$

$$p_{c,n}^2 = \frac{1}{4}\left(M^* + \frac{M_n^2 - M_i^2}{M^*}\right)^2 - M_n^2\ , \tag{A.43}$$

$$M^{*2} = M_n^2 + M_i^2 + 2E'_nE'_i - 2p'_np'_i\mu'\ , \tag{A.44}$$

where β_c is the velocity of centre of mass frame and γ_c is the equivalent Lorentz factor. The lab and centre of mass frame 3-momenta can then be related via a Lorentz boost of $\vec{\beta}_c$:

$$\vec{p}'_{c,n} = \vec{p}'_n + \left[\left(\frac{\gamma_c - 1}{\beta_c^2}\right)\vec{\beta}_c\cdot\vec{p}'_n - \gamma_c E'_n\right]\vec{\beta}_c\ , \tag{A.45}$$

$$\vec{p}_{c,n} = \vec{p}_n + \left[\left(\frac{\gamma_c - 1}{\beta_c^2}\right)\vec{\beta}_c\cdot\vec{p}_n - \gamma_c E_n\right]\vec{\beta}_c\ . \tag{A.46}$$

Combining the above equations and the energy-momentum conservation laws, the following expressions are found:

$$\mu^* = \frac{E_n(E'_n + E'_i) + \frac{1}{2}\left(M_i^2 - M_n^2 - M^{*2}\right) - p'_ip_n\mu}{p'_np_n}\ , \tag{A.47}$$

$$\mu_c = \frac{\gamma_c^2}{p_{c,n}^2}\left[\left(E'_n\vec{\beta}_c + \vec{p}'_n\right)\cdot\left(E_n\vec{\beta}_c + \vec{p}_n\right) + \vec{\beta}_c\cdot\vec{p}'_n\vec{\beta}_c\cdot\vec{p}_n - \beta_c^2p'_np_n\mu^*\right]\ , \tag{A.48}$$

$$g = \frac{E'_i - p'_i\mu/\beta_n}{p_{c,n}^2}\ . \tag{A.49}$$

To show the order of correction, we will consider the relativistic expression for μ^* for $\beta_i = 0$:

$$\mu^* = \frac{E_nE'_n + M_i(E_n - E'_n) - M_n^2}{p'_np_n} = \frac{1}{\beta'_n\beta_n}\left[1 - \frac{1}{\gamma_n\gamma'_n} + A_i\left(\frac{1}{\gamma'_n} - \frac{1}{\gamma_n}\right)\right]\ . \tag{A.50}$$

We can solve this quadratic[1] for either β_n or $\gamma_n - 1$, picking positive roots:

$$\frac{\beta_n}{\beta'_n} = \frac{\left(\frac{A_i}{\gamma'_n} + 1\right)\mu^* + \left(A_i + \frac{1}{\gamma'_n}\right)\sqrt{\mu^{*2} + A_i^2 - 1}}{A_i^2 + 2\frac{A_i}{\gamma'_n} + \frac{1}{\gamma'^2_n}(1 - \mu^{*2}) + \mu^{*2}}\ , \tag{A.51}$$

$$\frac{\gamma_n - 1}{\gamma'_n - 1} = \frac{K_n}{K'_n} = \frac{\frac{1-\gamma'_n}{2}(A_i - 1)^2 + \frac{1+\gamma'_n}{2}\left(\mu^* + \sqrt{\mu^{*2} + A_i^2 - 1}\right)^2}{(A_i + \gamma'_n)^2 - (\gamma'^2_n - 1)\mu^{*2}}\ , \tag{A.52}$$

where $A_i = M_i/M_n$ as before. We see that these equations reduce to the more familiar classical expressions for $\gamma'_n = 1$. Of particular interest is the kinematic edge at $\mu^* = -1$,

[1] The route I took involved many factorisations, rearrangements and cancellations to reach these rather pleasing final results. I imagine this is the kind of algebra a textbook might label as *an exercise for the reader.*

the relativistic equations give the following results:

$$\frac{\beta_n}{\beta'_n}(\mu^* = -1) = \frac{A_i^2 - 1}{A_i^2 + 2\frac{A_i}{\gamma'_n} + 1} = \frac{A_i - 1}{A_i + 1} \cdot \left[1 + \frac{2A_i}{(A_i+1)^2}\left(\frac{1}{\gamma'_n} - 1\right)\right]^{-1} , \tag{A.53}$$

$$\frac{K_n}{K'_n}(\mu^* = -1) = \frac{(A_i - 1)^2}{A_i^2 + 2A_i\gamma'_n + 1} = \left(\frac{A_i - 1}{A_i + 1}\right)^2 \cdot \left[1 + \frac{2A_i}{(A_i+1)^2}\left(\gamma'_n - 1\right)\right]^{-1} . \tag{A.54}$$

The terms in the square brackets are the relativistic corrections to the backscatter edge velocity and kinetic energy. For $K'_n = 14$ MeV, the incoming neutron Lorentz factor $\gamma'_n \approx 1.015$ leads to a correction factor of 0.993 (0.994) for D (T) backscatter giving downshifts of a few tens of keV to the backscattered neutron.

A.3 Quantum Mechanical Scattering Problem

The aim of this appendix is to show how nuclear potentials are related to the differential and total scattering cross sections. The basics of the quantum mechanical scattering problem are laid out while hinting at the true complexity of the full analysis.

Spinless solutions, $\psi(\vec{r})$, of the Schrödinger equation for a central potential $V(r)$ can be decomposed into spherical harmonics, $Y_{lm}(\hat{r})$, and the radial Schrödinger equation formed:

$$\psi(\vec{r}) = \sum_{lm} C_{lm} \frac{u_l(r)}{kr} Y_{lm}(\hat{r}) , \tag{A.55}$$

$$\left[\frac{d^2}{d\rho^2} + 1 - \frac{l(l+1)}{\rho^2}\right] u_l(\rho) = U(\rho) u_l(\rho) , \tag{A.56}$$

$$U(\rho) = \frac{V(r)}{E}, \; E = \frac{\hbar^2 k^2}{2m}, \; \rho = kr . \tag{A.57}$$

In the absence of the potential, Eq. A.56 is the Ricatti-Bessel function which permits solutions, $\hat{j}_l(\rho) = \rho j_l(\rho)$ and $\hat{n}_l(\rho) = \rho n_l(\rho)$ where j_l and n_l are the spherical Bessel functions. Constructing a normalised linear combination using a mixing phase shift δ_l:

$$u_l(\rho) = \cos\delta_l \hat{j}_l(\rho) + \sin\delta_l \hat{n}_l(\rho) . \tag{A.58}$$

As long as the potential decays sufficiently fast, solutions must asymptote to this free particle solution.

Now if we consider the scattering problem, we have state of definite linear momentum (i.e. plane wave) incident on the scattering potential. The probability of scattering into a given solid angle is then found through the outgoing flux at a distance much larger than the effective radius of the potential. The incoming plane wave solution can be shown to be given by [13]:

$$e^{i\vec{k}\cdot\vec{r}} = \sum_l (2l+1) i^l j_l(kr) P_l(\cos\theta) \xrightarrow[r\to\infty]{} \frac{1}{kr} \sum_l (2l+1) i^l \sin\left(kr - l\pi/2\right) P_l(\cos\theta) , \tag{A.59}$$

where P_l are the Legendre polynomials and θ is the angle between $\vec{k}$ and $\vec{r}$.

The total wavefunction must have the asymptotic form which satisfies the large r radial Schrödinger equation given in Eq. A.58:

$$\psi(\vec{r}) \underset{r\to\infty}{\Longrightarrow} \sum_{lm} C_{lm}(\cos\delta_l j_l(kr) + \sin\delta_l n_l(kr))Y_{lm}(\hat{r}) \ , \tag{A.60}$$

$$= \frac{1}{kr}\sum_{lm} C_{lm}\sin\left(kr - l\pi/2 + \delta_l\right)Y_{lm}(\hat{r}) \ . \tag{A.61}$$

The naming of δ_l as a phase shift is now clear, it is the phase difference between the incident and scattered waves. The scattered wave is the difference between this total wavefunction and the incident plane wave. By requiring that the scattered wave is purely outgoing, the coefficients C_{lm} can be solved for and the following partial wave solution is found [13, 59]:

$$\psi_{\text{scat}}(\vec{r}) = \psi(\vec{r}) - e^{i\vec{k}\cdot\vec{r}} \underset{r\to\infty}{\Longrightarrow} \frac{e^{ikr}}{kr}\sum_l (2l+1)e^{i\delta_l}\sin\delta_l P_l(\cos\theta) \equiv \frac{e^{ikr}}{r}f(\theta) \ . \tag{A.62}$$

Thus the differential and total cross section can be written in terms of the phase shifts, δ_l, introduced by the potential:

$$\frac{d\sigma}{d\Omega} = |f(\theta)|^2 = \left(\frac{4\pi}{k}\right)^2 \sum_{l,l'}(2l+1)(2l'+1)e^{i(\delta_l-\delta_{l'})}\sin\delta_l\sin\delta_{l'}P_lP_{l'} \ , \tag{A.63}$$

$$\sigma = \frac{4\pi}{k^2}\sum_l (2l+1)\sin^2\delta_l \ . \tag{A.64}$$

The partial-wave analysis gives an exact procedure to solve the scattering problem at all energies. The phase shifts can be calculated for a specified $V(r)$ or found by fitting to experimental data. The former is done by invoking the continuity of the wavefunction, $u_l(\rho)$, at the potential radius R:

$$\tan\delta_l = -\frac{kR\hat{j}_l'(kR) - \hat{j}_l(kR)\mathcal{L}}{kR\hat{n}_l'(kR) - \hat{n}_l(kR)\mathcal{L}}, \ \mathcal{L} \equiv \left(\frac{R}{u_l(k,r)}\frac{du_l(k,r)}{dr}\right)_{r=R} \ , \tag{A.65}$$

here we have ignored spin which introduces a spin-orbit interaction term to the Hamiltonian. A more complex expression for $f(\theta,\phi)$ is needed with spin dependent phase shifts δ_L^J [13]. Fitting experimental data is generally aided by the phenomenological R-matrix analysis described in the following references [13, 45].

B Numerics Appendices

B.1 Primary Fusion Reactions Spectral Cumulants

This appendix will summarise the key results of the paper "Relativisitic calculation of fusion product spectra for thermonuclear plasmas" by Ballabio *et al.*. The mean and variance of the fusion product energy spectra are used within numerical calculations within this thesis. Natural units ($c = 1$) will be used in this appendix.

First the reaction rate weighted average is defined as follows:

$$\langle f(K, v_{cm})\rangle = \frac{\int K dK \int v_{cm}^2 dv_{cm} f(K, v_{cm})\sigma(K)A}{\int K dK \int v_{cm}^2 dv_{cm}\sigma(K)A} \ , \tag{B.1}$$

$$A = \exp\left[-\frac{K}{T}\right]\exp\left[-\frac{(m_1+m_2)v_{cm}^2}{2T}\right] \ . \tag{B.2}$$

By expanding expressions for energy and momentum in terms of velocity, one can derive expressions for the mean and variance of the outgoing particle.

$$\langle E\rangle = \alpha_0 + \alpha_K\langle K\rangle + \alpha_V\langle v_{cm}^2\rangle + ... \ , \tag{B.3}$$

$$\langle E^2 - \langle E\rangle^2\rangle = \beta_0\langle v_{cm}^2\rangle + \beta_{V2}\left(\langle v_{cm}^4\rangle - \langle v_{cm}^2\rangle^2\right) + \ , \tag{B.4}$$

$$\beta_{K2}\left(\langle K^2\rangle - \langle K\rangle^2\right) + \beta_{VK}\langle v_{cm}^2\rangle\langle K\rangle + ... \ , \tag{B.5}$$

where the coefficients α and β are functions of the particle masses only. We will use the reaction notation $1 + 2 \rightarrow 3 + 4$, where 3 is the outgoing particle:

$$\alpha_0 = \frac{(m_1+m_2)^2 + m_3^2 - m_4^2}{2(m_1+m_2)} - m_3, \ \alpha_K = \frac{(m_1+m_2)^2 - m_3^2 + m_4^2}{2(m_1+m_2)^2} \ ,$$

$$\alpha_V = \frac{(m_1+m_2)^2 + m_3^2 - m_4^2}{4(m_1+m_2)} \ ,$$

$$\beta_0 = \frac{1}{3}\alpha_0(\alpha_0 + 2m_3), \ \beta_{V2} = \frac{1}{4}m_3^2, \ \beta_{K2} = \left(\frac{m_4}{m_3+m_4}\right)^2, \ \beta_{VK} = \frac{2m_3m_4}{3(m_3+m_4)} \ .$$

The averages of K and v_{cm}^2 can be readily calculated from the definition in Eq. B.1, although the averages of v_{cm}^2 have a particularly simple form:

$$\langle v_{cm}^{2n}\rangle = (2n+1)!!\left(\frac{T}{m_1+m_2}\right)^n \ . \tag{B.6}$$

By noting the definition of the reactivity $\langle\sigma v\rangle$ (as shown in Eq. 2.72), the K averages

can be shown to be given by [11]:

$$\langle K^n \rangle = T^2 \langle K^{n-1} \rangle \frac{d}{dT} \ln \left(T^{\frac{3}{2}} \langle \sigma v \rangle \langle K^{n-1} \rangle \right) \ . \tag{B.7}$$

For DT and DD, Bosch and Hale [18] provide analytic formulae for the reactivity therefore allowing for analytic, albeit complex, expressions for the K averages.

These above expressions work for any $2 \rightarrow 2$ body thermonuclear reaction with massive reactants and products.

B.2 Transfer Cross Sections in Minotaur

In Minotaur differential cross sections dependent on material conditions, fluid velocity and temperature, need to be integrated over to form transfer cross sections. This can be a numerically intensive task so analytic expressions are sought for where possible.

For temperature alone, the cross section is of the form given in Eq. 2.91, which shall be repeated here:

$$\frac{d^2\sigma}{d\Omega dE} \approx \frac{1}{2\pi} \frac{d\sigma}{d\mu_c} \left| \frac{\partial \mu_c}{\partial E} \right| D(\mu_0, E, E') \ , \tag{B.8}$$

$$D(\mu_0, E, E') = \frac{2\sqrt{EE'}}{A} \sqrt{\frac{1}{4\pi T \kappa^2}} \exp \left[-\frac{1}{4T\kappa^2} \left(\epsilon - \kappa^2 \right)^2 \right] \ , \tag{B.9}$$

$$\epsilon \equiv E' - E, \ \kappa^2 \equiv \frac{1}{A} \left(E' + E - 2\mu_0 \sqrt{EE'} \right) \ . \tag{B.10}$$

As it is only a function of the scattering cosine, the I*-method can be used. Additionally, the D function can be integrated analytically over μ_0 reducing calculation time considerably. From Mathematica, the integral over μ_0 between μ_0^{dw} and μ_0^{up} is given by:

$$\begin{aligned} &\int_{\mu_0^{dw}}^{\mu_0^{up}} D(\mu_0, E, E') d\mu_0 = \\ &-\frac{1}{2} \left[e^{\frac{\epsilon - |\epsilon|}{2T}} \left(1 + \operatorname{erf} \left(\frac{\kappa^2 - |\epsilon|}{2\kappa\sqrt{T}} \right) \right) + e^{\frac{\epsilon + |\epsilon|}{2T}} \left(\operatorname{erf} \left(\frac{\kappa^2 + |\epsilon|}{2\kappa\sqrt{T}} \right) - 1 \right) \right]_{\mu_0^{dw}}^{\mu_0^{up}} \ , \end{aligned} \tag{B.11}$$

where in the limit of $T \rightarrow 0$, the top-hat function between the beam-target kinematic limits is retrieved. If we consider the typical ICF relevant conditions $E/T \gg 1$, then the second term can be neglected as $(\kappa^2 + |\epsilon|)/\kappa > 0$ for all energies and angles so the argument of the error function is far into the tail. The level of upscatter can be calculated from $D(\mu_0, E, E')$ over the whole angular range, for $E' = 14$ MeV and $T = 10$ keV it was found to be 0.07% and 0.08% for nD and nT respectively. Therefore upscatter can be neglected at ICF relevant temperatures.

For fluid velocity alone, the cross section is of the form given in Eq. 2.95, which shall

be repeated here:

$$\frac{d^2\sigma}{d\Omega dE} = \frac{1}{2\pi}\frac{d\sigma}{d\mu_c}\frac{2}{1-\alpha}\frac{\left(1-\sqrt{\frac{E_i'}{AE}}\mu\right)}{\left(E'-2\sqrt{\frac{E'E_i'}{A}}\mu'+\frac{E_i'}{A}\right)}\delta(\mu_0-\mu_0^*)\ , \tag{B.12}$$

$$\mu_0^* = \frac{1}{2}\left[(A+1)\sqrt{\frac{E}{E'}}-(A-1)\sqrt{\frac{E'}{E}}\right]+\sqrt{\frac{AE_i'}{E}}\mu'-\sqrt{\frac{AE_i'}{E'}}\mu\ . \tag{B.13}$$

As it is a function of lab frame neutron directions, the expression for μ_0^* must be inserted into the angular transition probability before integration. The ATP can then be analytically integrated over μ and then numerically integrated over the remaining degrees of freedom [166]. The analytical integral over μ between μ^{dw} and μ^{up} is performed in the reduced variable y domain:

$$\int_{\mu^{dw}}^{\mu^{up}} I(\mu',\mu,\mu_0^*)d\mu = \int_{\mu^{dw}}^{\mu^{up}} \frac{1}{\pi\sqrt{A+B\mu-C\mu^2}}d\mu\ , \tag{B.14}$$

$$\frac{1}{\sqrt{C}}\int_{y^{dw}}^{y^{up}}\frac{1}{\pi\sqrt{1-y^2}}dy = \frac{1}{\pi\sqrt{C}}\left(\arcsin(y^{up})-\arcsin(y^{dw})\right)\ , \tag{B.15}$$

where we have completed the square in order to form the reduced variable y:

$$\beta_i' \equiv \frac{v_i'}{v_n'} = \sqrt{\frac{E_i'}{AE'}},\ \beta_i \equiv \frac{v_i'}{v_n} = \sqrt{\frac{E_i'}{AE}}\ ,$$

$$A = 1-\mu'^2-(\mu_{BT,0}^*+A\beta_i\mu')^2\ , \tag{B.16}$$

$$B = 2\mu'(1+A\beta_i')(\mu_{BT,0}^*+A\beta_i\mu')\ , \tag{B.17}$$

$$C = 1+2A\beta_i'\mu'+A^2\beta_i'^2\ , \tag{B.18}$$

$$y = \frac{\mu-\frac{B}{2C}}{\sqrt{\frac{A}{C}+\frac{B^2}{4C^2}}}, \tag{B.19}$$

$$y(v_i=0) = \frac{\mu-\mu'\mu_{BT,0}^*}{\sqrt{1-\mu'^2}\sqrt{1-\mu_{BT,0}^{*2}}}\ . \tag{B.20}$$

The transfer cross section is then found from the product of the ATP, differential cross section and Jacobian. This method was benchmarked at the backscatter edge by comparing numerical results to direct integration of the double differential cross section with colinear ion and neutron velocities.

Finally if both temperature and fluid velocity are non-zero then the product I and D must be integrated over. Unfortunately this must be done numerically over all degrees of freedom. A Gaussian-Legendre adaptive Gaussian quadrature routine is used to ensure converged results. Now that no analytic integration can be done, the singularities in $I(y)$ at $y = \pm 1$ are problematic. The variable transform $y = \sin(x)$ removes these

singularities so integration is performed in the x-domain ($-\frac{\pi}{2} < x < \frac{\pi}{2}$):

$$\int I(\mu', \mu, \mu_0) D(\mu_0, E', E, \mu', \mu, E_i') d\mu_0 = \frac{1}{\pi} \int D(x[\mu_0, E', E, \mu', \mu, E_i']) dx \ , \quad \text{(B.21)}$$

as D is strongly peaked the integration domain is split into 3, two regions either sides of the peak and one that encloses the peak:

$$\int_{x^{dw}}^{x^{up}} D(x)dx = \int_{x^{dw}}^{x_{peak}-N_\sigma\sigma_x} D(x)dx + \int_{x_{peak}-N_\sigma\sigma_x}^{x_{peak}+N_\sigma\sigma_x} D(x)dx + \int_{x_{peak}+N_\sigma\sigma_x}^{x^{up}} D(x)dx \ ,$$

$$\mu_{0,peak} = \frac{E' + E - A\epsilon}{2\sqrt{E'E}}, \ \sigma_{\mu_0} = \sqrt{\frac{A^2 T\epsilon}{2E'E}}, \quad \text{(B.22)}$$

$$\epsilon = E' - E - 2\sqrt{\frac{E'E_i'}{A}}\mu' + 2\sqrt{\frac{EE_i'}{A}}\mu, \quad \text{(B.23)}$$

$$\kappa^2 = \frac{1}{A}\left(E' + E - 2\mu_0\sqrt{EE'}\right) \ . \quad \text{(B.24)}$$

A value of $N_\sigma = 4$ was chosen as this generally causes the integrated regions outside the peak to be close to zero and thus quickly neglected by adaptive integration. If the peak lay outside the integration region the limits and the number of regions was altered appropriately. An approximate analytic method of calculating the integral in the x-domain would greatly improve calculation time.

B.3 Raytracing in AKED

AKED performs raytracing and line integrals on 3D regular Cartesian grids. Efficient algorithms are required to handle the large grid sizes and high number of rays needed to perform scattering calculations. In this appendix we will discuss the raytracing implemented in AKED, this has been improved compared to older versions of the code [115]. These improvements were aimed to address the overall computational efficiency of the code and 'grid-imprint' effects.

B.3.1 Cardinal directions and grid rotations

We will refer to the basis vectors of the Cartesian grid as the cardinal directions. Ray tracing along cardinal directions is trivial and the preferred method of calculation. Line integrals are simply for-loop sums over the cardinal direction and their total path length through the grid is the same. The grid can be reoriented via rotation followed by interpolation, see Fig. B.1.

The cardinal directions can then be orientated with the imaging coordinates. While some error is introduced during the interpolation this is compensated by the speed up gained in ray tracing along the detector direction. Rays will not intersect grid cell edges and imaging pixel coordinates match the data grid coordinates. There is potential to domain split the grid and rays between processors as each ray needs only the information in a single row of the grid. This has not been pursued as scattering breaks this simplicity

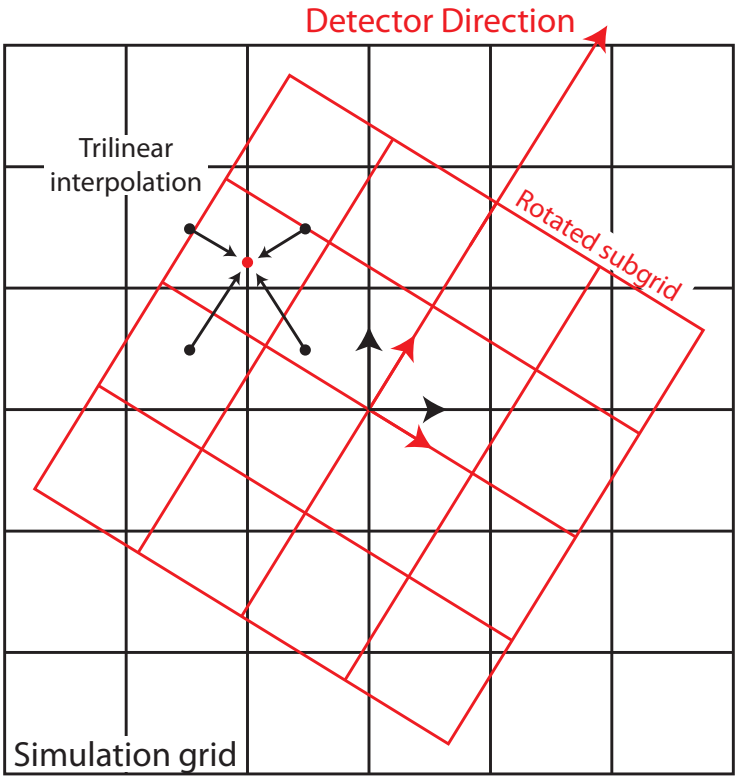

Figure B.1: Diagram showing how a rotated subgrid is formed. The axes are oriented with the detector and trilinear interpolation from the hydrodynamic simulation grid is performed to fill in the new grid.

- however rotated domain splitting could be employed in problems without scattering e.g. X-ray imaging/spectroscopy.

B.3.2 Non-cardinal directions

Scattering calculations must include rays travelling in non-cardinal directions in order to fully explore the space. These rays cut through grid cells in chords with varying chord length. However solving the line equation in each cell is relatively expensive. Since the grids on which AKED works are regular the line equation needs only to be solved a single time. Defining the line equation with the coordinate origin at the ray origin:

$$\vec{r} = p\vec{\lambda} \tag{B.25}$$

Where p is the path length travelled and $\vec{\lambda}$ is the normalised ray direction. The distances to the nearest cell boundaries in each cardinal direction can be found simply ($p_i = \Delta_i/\lambda_i$) for regular grid spacings Δ_i. The algorithm for the marching the rays is then:

- Find the path lengths, q_i, required to move into the next grid cell in each direction

$$q_i = p_i^0 + n_i p_i \ , \tag{B.26}$$

where p_i^0 are the path lengths to exit the initial starting cell as the origin may not lie at a cell boundary. n_i are the number of steps taken in each direction and therefore all n_i are initially 0.

- The smallest value of q_i is found as this will give the smallest chord to move. Then n_i is incremented by 1 for the direction i corresponding to the smallest q_i. The path length taken in this step is $q_{i,\min} - p$. The grid coordinates of the ray can also be incremented in a similar way to n_i. In the special cases were 2 or 3 of the q_i's are equal then the ray has reached a cell vertex and multiple n_i must be incremented.

- This procedure is repeated until the ray exits the grid

A schematic of this algorithm on a 2D grid is shown in Fig. B.2.

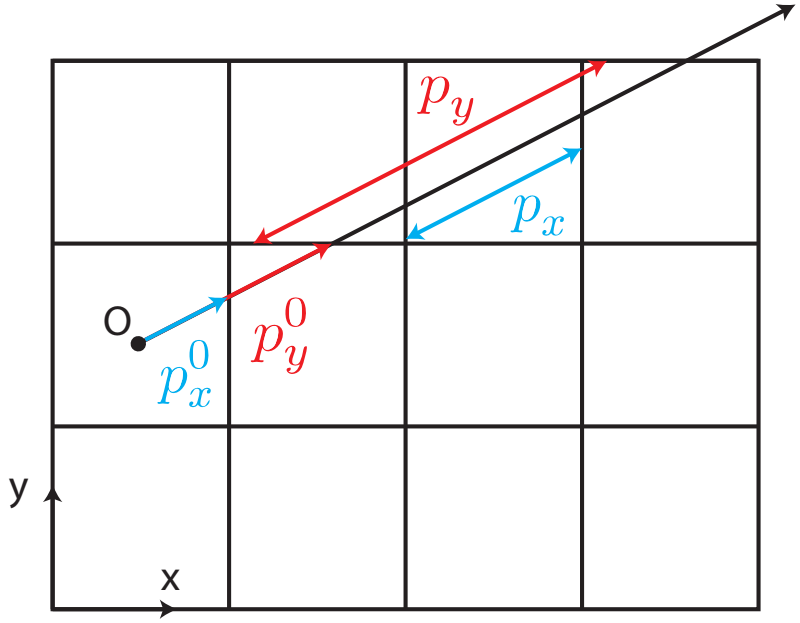

Figure B.2: Diagram showing a non-cardinal direction ray trace with the marching path lengths p_i shown. In this example the stepping order is $(x, y, x, x, y, ...)$ with path length values $p = (p_x^0, p_y^0, p_x^0 + p_x, p_x^0 + 2p_x, p_y^0 + p_y, ...)$

The simplicity of the regular grid allows this efficient algorithm which leads to reduced computation time spent in the ray trace.

B.3.3 Angular averaging

In a scattering calculation emitter and scatterer cells are paired up and a ray connecting their centres is considered. For large separations, any small change in the ray direction would disconnect the emitter and scatterer cell. Therefore a single ray along the line of centres is a good approximation. However for emitters and scatterers in close proximity this is not true. The line connecting any two points within the cells can vary from the line of centres by a large degree. The magnitude of this effect will depend on the

parameter $a = R/\Delta$ where R is the emitter-scatterer separation and Δ the grid cell size. One could subdivide the cells N times and consider many rays for each sub-cell pairing but this is computationally expensive (order N^2). Instead a single ray will be considered but with an approximate averaging of the scattering angle over many ray directions. The weighting function $W(\theta_s, a)$ is approximated by considering the fractional illumination of a circle by another circle both with radius Δ and separated by distance R. This configuration is shown in Fig. B.3 as well as angular definitions.

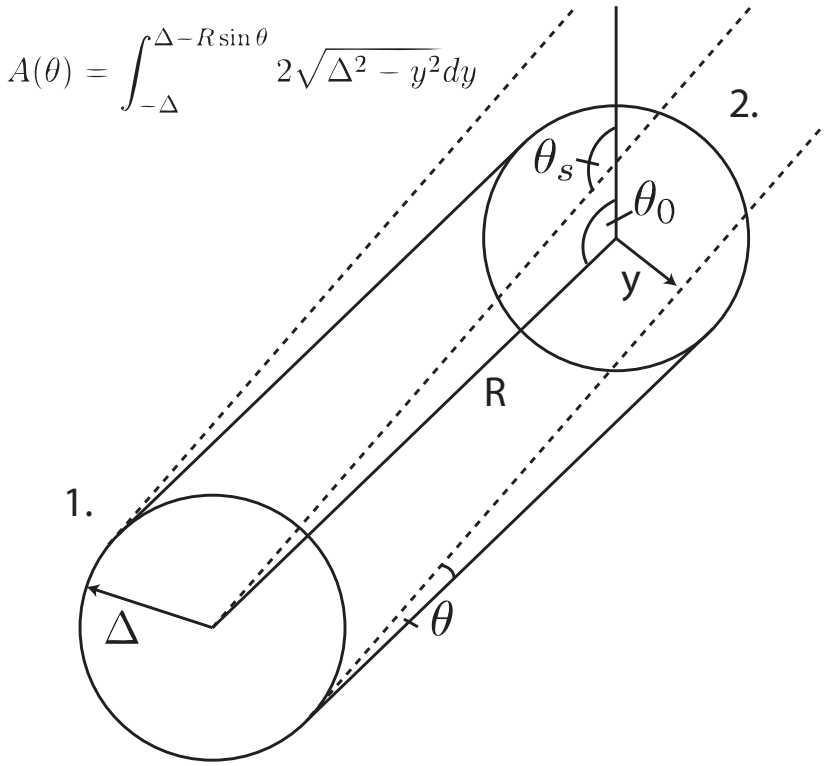

Figure B.3: Diagram showing the geometric system used to estimate the angular average weighting function. Circle 1 (the emitter) uniformly illuminates circle 2 (the scatterer), the area which is illuminated at chord angle θ is given by $A(\theta)$. The scattering angle between scatterer-emitter-detector is given by $\theta_s = \theta_0 + \theta$ where θ_0 is the scattering angle for the ray connecting grid cell centres.

The weighting function is taken as the normalised distribution of illuminated area:

$$W(\theta_s, a) = \frac{A(\theta)}{\int d\theta A(\theta)} \ , \tag{B.27}$$

$$W(\theta_s, a) = \frac{\Delta^2}{\int d\theta A(\theta)} \left[(1-x)\sqrt{2x - x^2} + \arcsin(1-x) + \frac{\pi}{2}\right] \ , \tag{B.28}$$

$$x = a\sin(\theta) = a\sin(\theta_s - \theta_0) \ . \tag{B.29}$$

The maximum chord angle permitted is given by $\theta_{\max} = \arcsin(2/a)$ and thus the weighting function becomes more peaked as the emitter and scatterer draw further apart. Hence at sufficient high a the angular averaging can be neglected, a limit of

$a > 10$ is used in AKED. While considerable simplification has been used to obtain the weighting function, it is vast improvement over the single ray treatment. Due to the cubic grid, connecting cell centres causes certain angles to be emphasized. This causes peaks to appear in the scattered neutron spectrum - similar to Bragg diffraction in crystals. The benefits of angular averaging are evident when comparing the scattered neutron spectrum with and without the angular averaging as shown in Fig. B.4.

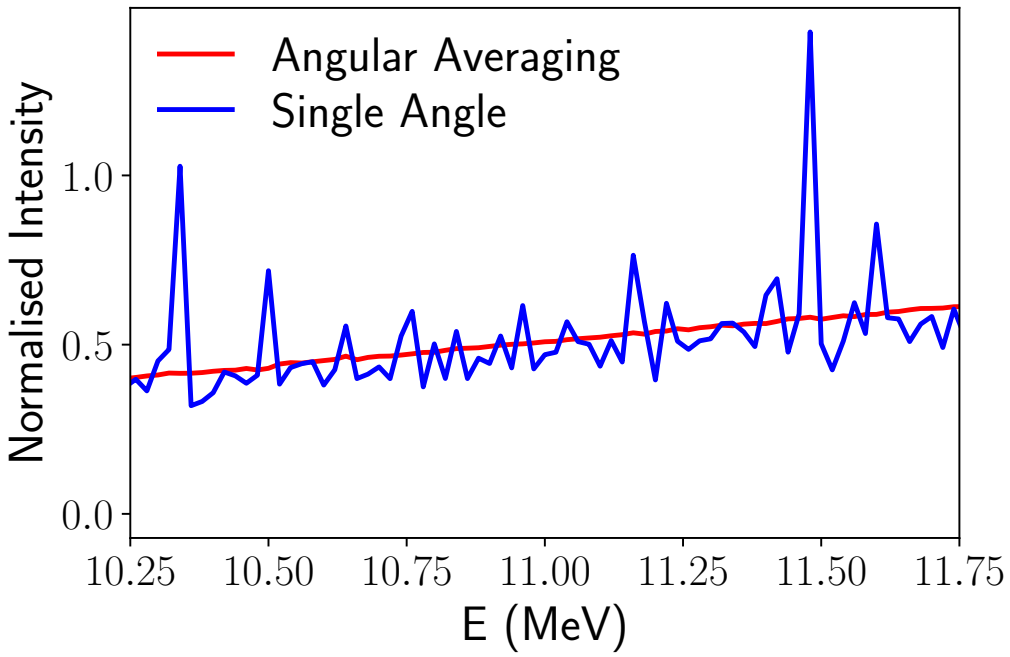

Figure B.4: Comparing the singly scattered neutron spectrum over a restricted angular range for a single angle and angular averaging treatment.

C Results Appendices

C.1 Optimal Neutron Spectrometer Arrangement

When measuring neutron spectra properties are resolved to the detector line of sight. To measure the underlying properties, multiple measurements of their components must be combined. There is therefore an optimal arrangement which minimises the error in the combined measurement. To begin we will consider the measurement of a linear combination of isotropic and vector properties. This is relevant for the centroid shift of primary DT and DD peaks:

$$\vec{m} = A \cdot \vec{b} \ , \tag{C.1}$$

$$\vec{b} = \begin{bmatrix} k \\ v_x \\ v_y \\ v_z \end{bmatrix} \ , \tag{C.2}$$

where $\vec{m}$ is a vector of measured centroid shifts, A is the matrix of projections to detector lines of sight and $\vec{b}$ is the vector containing the isotropic and vector components. With 4 unknowns, we need 4 detectors to fully determine the system. For 4 detectors, the projection matrix is given by:

$$A = \begin{bmatrix} 1 & \Omega_x^1 & \Omega_y^1 & \Omega_z^1 \\ 1 & \Omega_x^2 & \Omega_y^2 & \Omega_z^2 \\ 1 & \Omega_x^3 & \Omega_y^3 & \Omega_z^3 \\ 1 & \Omega_x^4 & \Omega_y^4 & \Omega_z^4 \end{bmatrix} \ , \tag{C.3}$$

$$\Omega^i = \begin{bmatrix} \Omega_x^i \\ \Omega_y^i \\ \Omega_z^i \end{bmatrix} = \begin{bmatrix} \sin(\theta^i)\cos(\phi^i) \\ \sin(\theta^i)\sin(\phi^i) \\ \cos(\theta^i) \end{bmatrix} \ . \tag{C.4}$$

Altering the detector arrangement changes the line of sight vectors Ω^i. The error in the inferred vector $\vec{b}$ is given by:

$$\mathrm{Var}\left(\vec{b}\right) = A^{-1}\mathrm{Var}\left(\vec{m}\right)\left(A^{-1}\right)^T \ . \tag{C.5}$$

We will now assume that the spectrometers all have the same measurement error (σ_m) such that $\mathrm{Var}\left(\vec{m}\right) = \sigma_m^2 I$, where I is the identity matrix. The determinant of covariance matrix is a measure of the total uncertainty in the inferred quantities. Therefore we

must aim to minimise this. Using the properties of determinants:

$$\left|\mathrm{Var}\left(\vec{b}\right)\right| = \frac{\sigma_m^2}{|A|^2} \,, \tag{C.6}$$

therefore we must aim to maximise the determinant of the projection matrix, A. Using that the determinant of a 3x3 matrix with columns $\vec{a}$, $\vec{b}$ and $\vec{c}$ is the signed volume of the parallelepied, V_{abc}, defined by the vectors $\vec{a}$, $\vec{b}$ and $\vec{c}$:

$$|A| = V_{234} - V_{134} + V_{124} - V_{123} \,. \tag{C.7}$$

Therefore we aim to maximise the volume enclosed by the line of sight vectors. For 4 detectors, this creates a tetrahedron with total volume $V = |A| = 16/3\sqrt{3}$. In this case, the covariance matrix of $\vec{b}$ is given by:

$$\mathrm{Var}\left(\vec{b}\right) = \frac{\sigma_m^2}{4}\begin{bmatrix}1&0&0&0\\0&3&0&0\\0&0&3&0\\0&0&0&3\end{bmatrix}, \quad \left|\mathrm{Var}\left(\vec{b}\right)\right| = \frac{27}{256}\sigma_m^2 = \frac{\sigma_m^2}{V^2} \,. \tag{C.8}$$

As we can see, the tetrahedral arrangement also ensures no covariance between inferred quantities.

Now we consider the optimal detector arrangement if we have additional detectors (for a total of N) and therefore have an overdetermined system. Since we are overdetermined, the normal equation must now be solved in order to minimise the least squares distance to the data:

$$A^T \cdot \vec{m} = A^T A \cdot \vec{b} \,, \tag{C.9}$$

$$\vec{b} = \left(A^T A\right)^{-1} \cdot A^T \cdot \vec{m} = A^+ \cdot \vec{m} \,. \tag{C.10}$$

The error propagation follows a similar format but with the pseudo inverse, A^+, rather than the square matrix inverse:

$$\mathrm{Var}\left(\vec{b}\right) = A^+ \mathrm{Var}\left(\vec{m}\right)\left(A^+\right)^T = \sigma_m^2 A^+\left(A^+\right)^T \,, \tag{C.11}$$

$$\left|\mathrm{Var}\left(\vec{b}\right)\right| = \sigma_m^2\left|A^+\left(A^+\right)^T\right| = \frac{\sigma_m^2}{|A^T A|} \,. \tag{C.12}$$

Since A is not square, the determinant cannot be split further. However, the square 4x4 $A^T A$ matrix has a simple form in terms of the detector lines of sight components:

$$A^T A = \begin{bmatrix}1&1&\cdots\\ \vec{\Omega}^1&\vec{\Omega}^2&\cdots\end{bmatrix}\begin{bmatrix}1&\vec{\Omega}^1\\1&\vec{\Omega}^2\\\vdots&\vdots\end{bmatrix} = \begin{bmatrix}N & \sum_i \Omega_x^i & \sum_i \Omega_y^i & \sum_i \Omega_z^i \\ \sum_i \Omega_x^i & \sum_i \Omega_x^{i2} & \sum_i \Omega_x^i\Omega_y^i & \sum_i \Omega_x^i\Omega_z^i \\ \sum_i \Omega_y^i & \sum_i \Omega_x^i\Omega_y^i & \sum_i \Omega_y^{i2} & \sum_i \Omega_y^i\Omega_z^i \\ \sum_i \Omega_z^i & \sum_i \Omega_x^i\Omega_z^i & \sum_i \Omega_y^i\Omega_z^i & \sum_i \Omega_z^{i2} \,.\end{bmatrix} \tag{C.13}$$

The determinant of this matrix must again be maximised to minimise the inference uncertainty. We also note that if we want no covariance between inferred quantities then $A^T A$ must be diagonal. This requires that:

$$\sum_i \Omega_x^i = \sum_i \Omega_y^i = \sum_i \Omega_z^i = \sum_i \Omega_x^i \Omega_y^i = \sum_i \Omega_x^i \Omega_z^i = \sum_i \Omega_y^i \Omega_z^i = 0 \ . \tag{C.14}$$

These above conditions are indeed satisfied by the tetrahedral arrangement for 4 spectrometers. For 5 detectors, the lines of sight which satisfy these conditions form a square pyramid with $A^T A$ of:

$$A^T A = \begin{bmatrix} 5 & 0 & 0 & 0 \\ 0 & \frac{15}{8} & 0 & 0 \\ 0 & 0 & \frac{15}{8} & 0 \\ 0 & 0 & 0 & \frac{5}{4} \end{bmatrix}, \ \mathrm{Var}\left(\vec{b}\right) = \frac{\sigma_m^2}{15} \begin{bmatrix} 3 & 0 & 0 & 0 \\ 0 & 8 & 0 & 0 \\ 0 & 0 & 8 & 0 \\ 0 & 0 & 0 & 12 \end{bmatrix} \ . \tag{C.15}$$

Interestingly, while there are no covariances, the errors are not equal for each vector component. The x and y components are treated equally, as the pyramid is rotationally symmetric around z, however the z component has a larger error.

A similar analysis can be performed if measuring a symmetric matrix component, this is relevant for the width of the primary DT and DD peaks. For each line of sight k, the measured value is given by:

$$m^k = \left(\vec{\Omega}^k\right)^T \cdot B \cdot \vec{\Omega}^k \ , \tag{C.16}$$

$$B = \begin{bmatrix} b_{xx} & b_{xy} & b_{xz} \\ b_{xy} & b_{yy} & b_{yz} \\ b_{xz} & b_{yz} & b_{zz} \end{bmatrix} \ . \tag{C.17}$$

Since B is a 3x3 symmetric matrix there are 6 unknowns and therefore at least 6 measurements are required. Any isotropic component can be added by addition to the diagonal of B. Therefore the isotropic component cannot be separated from the matrix component and the number of unknowns remains as 6. A more suitable form of the above equation can be found if we can diagonalise B:

$$m^k = \left(\vec{\Omega}^k\right)^T \cdot S^T \cdot D \cdot S \cdot \vec{\Omega}^k = \left(\vec{\omega}^k\right)^T \cdot D \cdot \vec{\omega}^k \ , \tag{C.18}$$

$$\vec{\omega} = S \cdot \vec{\Omega} \ . \tag{C.19}$$

The elements of D are the values which are measured along the principal axes of B. In terms of inferred ion temperature, the largest and smallest values in D give the maximum and minimum inferred temperatures. The projection matrix S projects the line of sight vectors to the principal axes basis of B. Therefore $\vec{\omega}$ are the projected line of sight vectors. In this form our 6 unknowns are split into 3 which form the elements of D and 3 which rotate/reflect the line of sight basis into the principal axis basis through

orthonormal matrix S.

The error propagation analysis will be more complex in this case so will not be pursued here.

C.2 Simplified Backscatter Edge Fitting Model

Early development of the theory of the backscatter edge spectral shape was reported in the Crilly *et al.* [42]. At this time, an ad-hoc background model was invoked rather than the physically based model shown in Section 3.1. The differential cross section of nT was also assumed isotropic and therefore a very restrictive fitting range had to be used to accommodate these assumptions. However this model does allow more freedom in the shape of backgrounds and therefore is, currently, more successful when considering spectra from implosions with large areal density asymmetries. However, despite the differences, the progression from the model presented below and the model presented in Section 3.1 is clear.

For elastic scattering with an isotropic centre-of-mass differential cross section and stationary scatterer, the energy spectrum at the backscatter edge can be approximated by:

$$\begin{aligned} I_{bs}(E) &\approx \int_0^\infty dE' \frac{d\sigma}{d\Omega_c} g(E') Q_b(E') \int d\mu \delta(\mu - \mu^*) \ , \\ &= \int_0^\infty dE' \frac{\sigma(E')}{4\pi} g(E') Q_b(E') \int d\mu \delta(\mu - \mu^*) \ , \\ &= \int_E^{E/\alpha} dE' \frac{\sigma(E')}{4\pi} g(E') Q_b(E') \ , \\ \mu^* &= \frac{1}{2}\left[(A+1)\sqrt{\frac{E}{E'}} - (A-1)\sqrt{\frac{E'}{E}}\right] \ , \\ \alpha &= \left(\frac{A-1}{A+1}\right)^2 \ , \ g(E') = \frac{2}{(1-\alpha)\,E'} \ . \end{aligned}$$

The backscatter energy reduction factor, α, is given above for the case of negligible fluid velocity of the scattering medium. The functional form of the integral can be approximated for a Gaussian birth spectrum, $Q_b(E')$, with a mean a and variance b^2. If the birth spectrum is strongly peaked (i.e. $b \ll a$) then the slowing down kernel [169], $g(E')$, can be expanded about a and the elastic scattering cross section taken as linear

in energy, i.e. $\sigma \approx \sigma_m E + \sigma_c$.

$$\begin{aligned}
&\text{Let } x = \frac{E' - a}{b} \ , \\
&\sigma(E') \approx \sigma_m E' + \sigma_c \rightarrow (\sigma_m a + \sigma_c) + \sigma_m b x \ , \\
&g(E') \rightarrow \frac{2}{1-\alpha}\left(a + bx\right)^{-1} \approx \frac{2}{(1-\alpha)a}\left(1 - \frac{b}{a}x + \frac{b^2}{a^2}x^2\right) \ , \\
&I_{bs}(E) \propto \int_{\frac{E-a}{b}}^{\frac{E-\alpha a}{\alpha b}} dx \left[(\sigma_m a + \sigma_c) - \frac{b}{a}\sigma_c x\right] \exp\left[-\frac{x^2}{2}\right] + \mathcal{O}\left(\frac{b^2}{a^2}\right) \ .
\end{aligned}$$

There is no σ_m contribution to the first order in b/a term due to cancellation in the product of the cross section and slowing down kernel. These approximations allow the integral to be performed analytically. To first order in b/a, this produces:

$$I_{bs}(E) \propto (\sigma_m a + \sigma_c)\sqrt{\frac{\pi}{2}}\left[\text{erf}\left(\frac{E - \alpha a}{\sqrt{2}\alpha b}\right) + 1\right] + \frac{b}{a}\sigma_c e^{-\frac{(E-\alpha a)^2}{2(\alpha b)^2}} \ . \tag{C.20}$$

Hence information about the mean and variance of the birth spectrum are stored in the form of the backscatter edge. Therefore, there is inherent slope to the edge shape even for stationary scattering ions.

By using Minotaur, this fit was tested on spectra produced by an isobaric hotspot model [172]. Figure C.1 shows the simulated nT edge and a best fit. The effect of fluid and thermal velocities on the broadening on the birth spectra was included. The effects of fluid and thermal velocities on the edge will be investigated in the following discussion and therefore will be neglected here. A limited energy range around the edge must be used for two reasons. Firstly, the assumption of isotropic centre-of-mass frame scattering will affect the spectral shape above the edge, this will constrain the upper limit of the fitting region. Secondly, using a small energy range will limit the variation in the background sources; over this range they can assumed to be constant, this will constrain the lower limit of the fitting region. For these conditions, it should be noted that the background signal is relatively constant around the nT edge. The fit was performed from 3.3 MeV up to the peak value of the backscatter edge. Fits extended to higher energy and those which only included a limited section of the edge performed poorly. In these scenarios, the height of the edge was poorly constrained which had a knock on effect on the best fit mean and variance. Hence the fitting region adopted extended from the peak of the edge down to $\geq$ 200 keV below the centre of the edge. From the edge fit the mean and standard deviation of the birth spectrum were calculated to be 14.03 and 0.145 respectively. The primary spectrum moments gave values of 14.05 and 0.147, thus the fit produced good agreement. Since Minotaur does not included the approximations used to obtain Eq. C.20, the good fit validates the choices made.

Often significant fluid velocity, v_f, is present in the scattering medium so it is required to extend this spectral backscatter edge fit to moving scatterers. By considering only co-

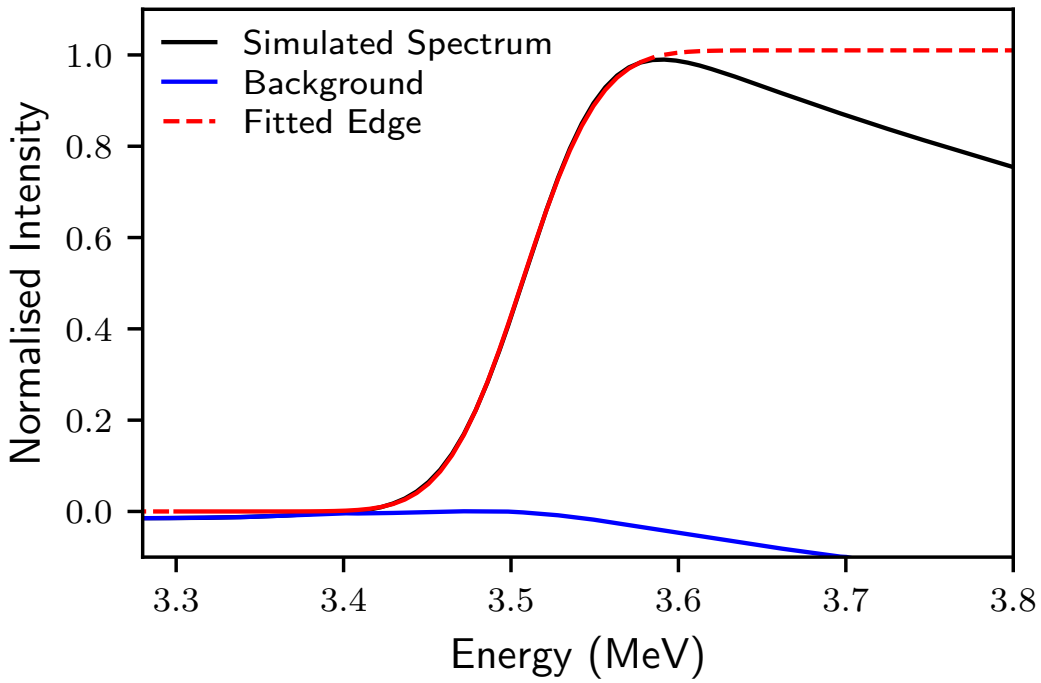

Figure C.1: Plot showing a simulated nT edge with backgrounds from scattering from D, multiple scattering, ablator scattering, deuteron break-up and TT primary neutrons. The edge fit is of the form given in Eq. C.20 plus a constant to fit the background. The solid red line shows the region over which a non-linear least-squares fit was performed. The dashed line shows the value of the fitting function, Eq. C.20, beyond this region.

linear collisions between neutrons and the scattering ions we can reformulate to include fluid velocity effects through the energy reduction factor α:

$$\alpha(v_f \neq 0) = \left(\frac{A-1}{A+1-2Av_f/v_n}\right)^2 , \tag{C.21}$$

$$\text{replacing } \alpha(v_f = 0) \rightarrow \alpha(v_f) \text{ in Eq. C.20 .}$$

This will allow a single average shell velocity to be inferred by fitting the backscatter edge. As an extension we will assume that scattering ion velocities sampled by the backscattering neutrons are normally distributed with mean and variance: $\bar{v}$ and Δ_v^2. We can see here the link with the more detailed analysis in terms of the scattering rate weighted ion velocity distribution. This allows us to calculate the expected value of the backscattered spectrum for a range of scattering ion velocities. The total backscatter shape is simply the sum of edges shifted by variable scattering medium velocity. This will cause an additional shift and smoothing of the resultant edge shape. Expanding α

to first order in v_f/v_n we find:

$$\langle I_{bs}(E)\rangle = \frac{1}{\sqrt{2\pi\Delta_v^2}}\int_{-\infty}^{+\infty} dv_f I_{bs}(E,v_f)\exp\left[-\frac{(v_f-\bar{v})^2}{2\Delta_v^2}\right] , \tag{C.22}$$

$$\langle I_{bs}(E)\rangle \propto (\sigma_m a+\sigma_c)\sqrt{\frac{\pi}{2}}\left[\mathrm{erf}\,(z)+1\right]+\frac{b}{a}\sigma_c e^{-z^2} , \tag{C.23}$$

$$c \equiv \frac{E-\alpha_0 a - 4A\bar{v}/(A+1)}{\sqrt{2}\alpha_0 b} , \; m \equiv \frac{4AE}{\sqrt{2}(A+1)\alpha_0 b}\frac{\Delta_v}{v_n} , \tag{C.24}$$

$$z \equiv \frac{c}{\sqrt{2m^2+1}} , \tag{C.25}$$

where $\alpha_0 = \alpha(v_f = 0)$. Comparing to Eq. C.20, we see the additional shape changes due to the $\bar{v}$ and Δ_v. Figure C.2 compares the results of this simple model with the more detailed model of Section 3.1, without consideration of backgrounds.

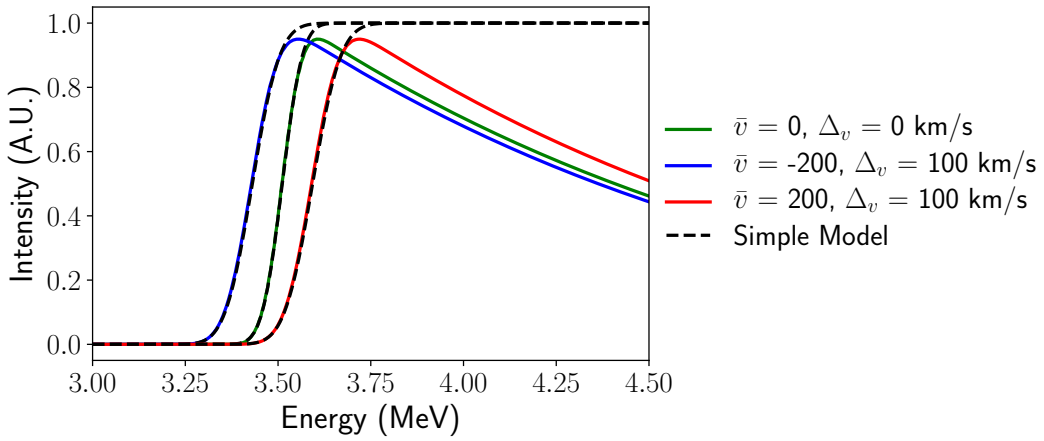

Figure C.2: A comparison between models with and without the effect of the differential cross section included. The simple model replicates the more detailed detailed model up to a certain point beyond which the shape of differential cross section alters the shape of the nT scattering signal drastically. Therefore, simple model, if used, must consider only a very limited range of energies.

A more sophisticated model which can handle both the areal density asymmetries and the physical shape of the signal and background is required to replace the two models considered in this work.

Bibliography

[1] Fay Ajzenberg-Selove and C Langell Busch. "Energy levels of light nuclei A= 11–12". *Nuclear Physics A*, 336(1):1–154, 1980. 40

[2] Michael J. Antal and Clarence E. Lee. "Charged particle mass and energy transport in a thermonuclear plasma". *Journal of Computational Physics*, 20(3):298 – 312, 1976. ISSN 0021-9991. doi: https://doi.org/10.1016/0021-9991(76)90083-8. 72

[3] B Appelbe and J Chittenden. "The production spectrum in fusion plasmas". *Plasma Physics and Controlled Fusion*, 53(4):045002, 2011. ISSN 0741-3335. doi: 10.1088/0741-3335/53/4/045002. 61, 64, 81, 93

[4] B. Appelbe and J. Chittenden. "Quasi-monoenergetic spectra from reactions in a beam-target plasma". *Physics of Plasmas*, 19(7):073115, 2012. doi: 10.1063/1.4739767. 91

[5] B. Appelbe and J. Chittenden. "Relativistically correct DD and DT neutron spectra". *High Energy Density Physics*, 11:30 – 35, 2014. ISSN 1574-1818. doi: https://doi.org/10.1016/j.hedp.2014.01.003. 36, 62, 64, 81, 93, 104, 116

[6] B. Appelbe and J. Chittenden. "The effects of ion temperature on the energy spectra of $\mathrm{T} + \mathrm{T} \rightarrow 2\mathrm{n} + \alpha$ reaction products". *High Energy Density Physics*, 19: 29 – 37, 2016. ISSN 1574-1818. doi: https://doi.org/10.1016/j.hedp.2016.02.002. 12, 69, 81, 109

[7] B. Appelbe, J. Pecover, and J. Chittenden. "The effects of magnetic field topology on secondary neutron spectra in Magnetized Liner Inertial Fusion". *High Energy Density Physics*, 22:27 – 36, 2017. ISSN 1574-1818. doi: https://doi.org/10.1016/j.hedp.2017.01.005. 123

[8] Stefano Atzeni and Jürgen Meyer-ter Vehn. "The Physics of Inertial Fusion: BeamPlasma Interaction, Hydrodynamics, Hot Dense Matter". Oxford University Press, Oxford, 2004. ISBN 9780198562641. doi: 10.1093/acprof:oso/9780198562641.001.0001. 21, 22, 23, 24

[9] Jean Audouze and Sylvie Vauclair. "An Introduction to Nuclear Astrophysics: the Formation and the Evolution of Matter in the Universe", volume 18. Springer Science & Business Media, 2012. 160

[10] H. Azechi, M. D. Cable, and R. O. Stapf. "Review of secondary and tertiary reactions, and neutron scattering as diagnostic techniques for inertial confinement fusion targets". *Laser and Particle Beams*, 9(1):119–134, 1991. doi: 10.1017/S0263034600002378. 122

[11] L Ballabio, J K Allne, and G Gorini. "Relativistic Calculation of Fusion Product Spectra". *Nuclear Fusion*, 38(11), 1998. ISSN 00295515. doi: 10.1088/0029-5515/38/11/310. 62, 81, 88, 104, 173

[12] George I Bell and Samuel Glasstone. "Nuclear reactor theory". 1970. 66, 67, 75, 76, 77, 78, 86

[13] Carlos A Bertulani. "Introduction to nuclear reactions". Graduate student series on physics. Institute of Physics, Bristol, 2004. ISBN 0750309326. 59, 170, 171

[14] R. Betti, K. Anderson, V. N. Goncharov, R. L. McCrory, D. D. Meyerhofer, S. Skupsky, and R. P. J. Town. "Deceleration phase of inertial confinement fusion implosions". *Physics of Plasmas*, 9(5):2277–2286, 2002. doi: 10.1063/1.1459458. 24, 25, 27, 29, 96, 108

[15] D. L. Bleuel, C. B. Yeamans, L. A. Bernstein, R. M. Bionta, J. A. Caggiano, D. T. Casey, G. W. Cooper, O. B. Drury, J. A. Frenje, C. A. Hagmann, R. Hatarik, J. P. Knauer, M. Gatu Johnson, K. M. Knittel, R. J. Leeper, J. M. McNaney, M. Moran, C. L. Ruiz, and D. H. G. Schneider. "Neutron activation diagnostics at the National Ignition Facility (invited)". *Review of Scientific Instruments*, 83 (10):10D313, 2012. doi: 10.1063/1.4733741. 38, 39, 118, 130, 132, 134

[16] T.R Boehly, D.L Brown, R.S Craxton, R.L Keck, J.P Knauer, J.H Kelly, T.J Kessler, S.A Kumpan, S.J Loucks, S.A Letzring, F.J Marshall, R.L McCrory, S.F.B Morse, W Seka, J.M Soures, and C.P Verdon. "Initial performance results of the OMEGA laser system". *Optics Communications*, 133(1):495 – 506, 1997. ISSN 0030-4018. doi: https://doi.org/10.1016/S0030-4018(96)00325-2. 33

[17] David Borland and Russell M Taylor Ii. "Rainbow color map (still) considered harmful". *IEEE computer graphics and applications*, 27(2):14–17, 2007. 16, 133

[18] H.-S. Bosch and G.M. Hale. "Improved formulas for fusion cross-sections and thermal reactivities". *Nuclear Fusion*, 32(4):611, 1992. 59, 97, 173

[19] A. Bose, R. Betti, D. Shvarts, and K. M. Woo. "The physics of long- and intermediate-wavelength asymmetries of the hot spot: Compression hydrodynamics and energetics". *Physics of Plasmas*, 24(10):102704, 2017. doi: 10.1063/1.4995250. 34

[20] P. A. Bradley, D. C. Wilson, F. J. Swenson, and G. L. Morgan. "ICF ignition capsule neutron, gamma ray, and high energy x-ray images". *Review of Scientific Instruments*, 74(3):1824–1827, 2003. doi: 10.1063/1.1534930. 146

[21] A. A. Broyles. "Stark Fields from Ions in a Plasma". *Phys. Rev.*, 100:1181–1187, Nov 1955. doi: 10.1103/PhysRev.100.1181. 164

[22] C. R. Brune, J. A. Caggiano, D. B. Sayre, A. D. Bacher, G. M. Hale, and M. W. Paris. "*R*-matrix description of particle energy spectra produced by low-energy ^{3}H +^{3} H reactions". *Phys. Rev. C*, 92:014003, Jul 2015. doi: 10.1103/PhysRevC.92.014003. 70

[23] H Brysk. "Fusion neutron energies and spectra". *Plasma Physics*, 15(7):611, 1973. 36, 38, 62, 64, 81, 88, 104

[24] Bengt G Carlson. "Solution of the transport equation by Sn approximations". Technical report, Los Alamos Scientific Lab., N. Mex., 1955. 75

[25] D. T. Casey, P. L. Volegov, F. E. Merrill, D. H. Munro, G. P. Grim, O. L. Landen, B. K. Spears, D. N. Fittinghoff, J. E. Field, and V. A. Smalyuk. "Fluence-compensated down-scattered neutron imaging using the neutron imaging system at the National Ignition Facility". *Review of Scientific Instruments*, 87(11):10–14, 2016. ISSN 10897623. doi: 10.1063/1.4960065. 37, 134, 135, 137

[26] D. T. Casey, C. A. Thomas, K. L. Baker, B. K. Spears, M. Hohenberger, S. F. Khan, R. C. Nora, C. R. Weber, D. T. Woods, O. A. Hurricane, D. A. Callahan, R. L. Berger, J. L. Milovich, P. K. Patel, T. Ma, A. Pak, L. R. Benedetti, M. Millot, C. Jarrott, O. L. Landen, R. M. Bionta, B. J. MacGowan, D. J. Strozzi, M. Stadermann, J. Biener, A. Nikroo, C. S. Goyon, N. Izumi, S. R. Nagel, B. Bachmann, P. L. Volegov, D. N. Fittinghoff, G. P. Grim, C. B. Yeamans, M. Gatu Johnson, J. A. Frenje, N. Rice, C. Kong, J. Crippen, J. Jaquez, K. Kangas, and C. Wild. "The high velocity, high adiabat, "Bigfoot" campaign and tests of indirect-drive implosion scaling". *Physics of Plasmas*, 25(5):056308, 2018. doi: 10.1063/1.5019741. 31

[27] DT Casey, JA Frenje, M Gatu Johnson, MJ-E Manuel, N Sinenian, AB Zylstra, FH Séguin, CK Li, RD Petrasso, V Yu Glebov, et al. "Measurements of the T (t, 2 n) He 4 Neutron Spectrum at Low Reactant Energies from Inertial Confinement Implosions". *Physical review letters*, 109(2):025003, 2012. 70, 111, 160

[28] DT Casey, DB Sayre, CR Brune, VA Smalyuk, CR Weber, RE Tipton, JE Pino, GP Grim, BA Remington, D Dearborn, et al. "Thermonuclear reactions probed at stellar-core conditions with laser-based inertial-confinement fusion". *Nature Physics*, 13(12):1227–1231, 2017. 160

[29] John I. Castor. "Radiation Hydrodynamics". Cambridge University Press, 2004. doi: 10.1017/CBO9780511536182. 43

[30] C Cerjan, DB Sayre, OL Landen, JA Church, W Stoeffl, EM Grafil, HW Herrmann, NM Hoffman, and Y Kim. "Gamma Reaction History ablator areal den-

sity constraints upon correlated diagnostic modeling of National Ignition Facility implosion experiments". *Physics of Plasmas*, 22(3):032710, 2015. 143, 148

[31] Ch J Cerjan, L Bernstein, L Berzak Hopkins, RM Bionta, DL Bleuel, JA Caggiano, WS Cassata, CR Brune, D Fittinghoff, J Frenje, et al. "Dynamic high energy density plasma environments at the national ignition facility for nuclear science research". *Journal of Physics G: Nuclear and Particle Physics*, 45(3):033003, 2018. 160

[32] Charles Cerjan, Paul T. Springer, and Scott M. Sepke. "Integrated diagnostic analysis of inertial confinement fusion capsule performance". *Physics of Plasmas*, 20(5):056319, 2013. doi: 10.1063/1.4802196. 104

[33] M.B. Chadwick, P. Obložinský, M. Herman, N.M. Greene, R.D. McKnight, D.L. Smith, P.G. Young, R.E. MacFarlane, G.M. Hale, S.C. Frankle, A.C. Kahler, T. Kawano, R.C. Little, D.G. Madland, P. Moller, R.D. Mosteller, P.R. Page, P. Talou, H. Trellue, M.C. White, W.B. Wilson, R. Arcilla, C.L. Dunford, S.F. Mughabghab, B. Pritychenko, D. Rochman, A.A. Sonzogni, C.R. Lubitz, T.H. Trumbull, J.P. Weinman, D.A. Brown, D.E. Cullen, D.P. Heinrichs, D.P. McNabb, H. Derrien, M.E. Dunn, N.M. Larson, L.C. Leal, A.D. Carlson, R.C. Block, J.B. Briggs, E.T. Cheng, H.C. Huria, M.L. Zerkle, K.S. Kozier, A. Courcelle, V. Pronyaev, and S.C. van der Marck. "ENDF/B-VII.0: Next Generation Evaluated Nuclear Data Library for Nuclear Science and Technology". *Nuclear Data Sheets*, 107(12), 2006. ISSN 0090-3752. doi: https://doi.org/10.1016/j.nds.2006.11.001. Evaluated Nuclear Data File ENDF/B-VII.0. 38, 59, 60, 66, 111

[34] J. P. Chittenden, B. D. Appelbe, F. Manke, K. McGlinchey, and N. P.L. Niasse. "Signatures of asymmetry in neutron spectra and images predicted by three-dimensional radiation hydrodynamics simulations of indirect drive implosions". *Physics of Plasmas*, 23(5), 2016. ISSN 10897674. doi: 10.1063/1.4949523. 13, 32, 33, 44, 81, 82, 113

[35] A. R. Christopherson, R. Betti, S. Miller, V. Gopalaswamy, O. M. Mannion, and D. Cao. "Theory of ignition and burn propagation in inertial fusion implosions". *Physics of Plasmas*, 27(5):052708, 2020. 108

[36] O. Ciricosta, S. M. Vinko, H.-K. Chung, B.-I. Cho, C. R. D. Brown, T. Burian, J. Chalupský, K. Engelhorn, R. W. Falcone, C. Graves, V. Hájková, A. Higginbotham, L. Juha, J. Krzywinski, H. J. Lee, M. Messerschmidt, C. D. Murphy, Y. Ping, D. S. Rackstraw, A. Scherz, W. Schlotter, S. Toleikis, J. J. Turner, L. Vysin, T. Wang, B. Wu, U. Zastrau, D. Zhu, R. W. Lee, P. Heimann, B. Nagler, and J. S. Wark. "Direct Measurements of the Ionization Potential Depression in a Dense Plasma". *Phys. Rev. Lett.*, 109:065002, Aug 2012. doi: 10.1103/PhysRevLett.109.065002. 57

[37] D. S. Clark, C. R. Weber, J. L. Milovich, A. E. Pak, D. T. Casey, B. A. Hammel, D. D. Ho, O. S. Jones, J. M. Koning, A. L. Kritcher, M. M. Marinak, L. P. Masse, D. H. Munro, M. V. Patel, P. K. Patel, H. F. Robey, C. R. Schroeder, S. M. Sepke, and M. J. Edwards. "Three-dimensional modeling and hydrodynamic scaling of National Ignition Facility implosions". *Physics of Plasmas*, 26(5):050601, 2019. doi: 10.1063/1.5091449. 32, 143, 148, 157

[38] DS Clark, AL Kritcher, JL Milovich, JD Salmonson, CR Weber, SW Haan, BA Hammel, DE Hinkel, MM Marinak, MV Patel, et al. "Capsule modeling of high foot implosion experiments on the National Ignition Facility". *Plasma Physics and Controlled Fusion*, 59(5):055006, 2017. 32, 211

[39] D.S. Clark, C.R. Weber, A.L. Kritcher, J.L. Milovich, P.K. Patel, S.W. Haan, B.A. Hammel, J.M. Koning, M.M. Marinak, M.V. Patel, C.R. Schroeder, S.M. Sepke, and M.J. Edwards. "Modeling and projecting implosion performance for the National Ignition Facility". *Nuclear Fusion*, 59(3):032008, dec 2018. 32, 145, 211

[40] Cathie Clarke, Bob Carswell, RF Carswell, et al. "Principles of astrophysical fluid dynamics". Cambridge University Press, 2007. 44

[41] G. W. Cooper, C. L. Ruiz, R. J. Leeper, G. A. Chandler, K. D. Hahn, A. J. Nelson, J. A. Torres, R. M. Smelser, B. R. McWatters, D. L. Bleuel, C. B. Yeamans, K. M. Knittel, D. T. Casey, J. A. Frenje, M. Gatu Johnson, R. D. Petrasso, and J. D. Styron. "Copper activation deuterium-tritium neutron yield measurements at the National Ignition Facility". *Review of Scientific Instruments*, 83(10):10D918, 2012. doi: 10.1063/1.4746999. 38

[42] A. J. Crilly, B. D. Appelbe, K. McGlinchey, C. A. Walsh, J. K. Tong, A. B. Boxall, and J. P. Chittenden. "Synthetic nuclear diagnostics for inferring plasma properties of inertial confinement fusion implosions". *Physics of Plasmas*, 25(12): 122703, 2018. doi: 10.1063/1.5027462. 5, 15, 33, 36, 42, 92, 108, 111, 113, 114, 116, 117, 118, 119, 127, 143, 152, 183, 211

[43] A. J. Crilly, B. D. Appelbe, O. M. Mannion, C. J. Forrest, V. Gopalaswamy, C. A. Walsh, and J. P. Chittenden. "Neutron backscatter edge: A measure of the hydrodynamic properties of the dense DT fuel at stagnation in ICF experiments". *Physics of Plasmas*, 27(1):012701, 2020. doi: 10.1063/1.5128830. 5, 92, 152, 211

[44] J. Delettrez, R. Epstein, M. C. Richardson, P. A. Jaanimagi, and B. L. Henke. "Effect of laser illumination nonuniformity on the analysis of time-resolved x-ray measurements in uv spherical transport experiments". *Phys. Rev. A*, 36:3926–3934, Oct 1987. doi: 10.1103/PhysRevA.36.3926. 13, 94, 98

[45] P Descouvemont and D Baye. "The R matrix theory". *Reports on Progress in*

Physics, 73(3):036301, Feb 2010. ISSN 1361-6633. doi: 10.1088/0034-4885/73/3/036301. 171

[46] T R Dittrich, O A Hurricane, L F Berzak-Hopkins, D A Callahan, D T Casey, D Clark, E L Dewald, T Doeppner, S W Haan, B A Hammel, J A Harte, D E Hinkel, B J Kozioziemski, A L Kritcher, T Ma, A Nikroo, A E Pak, T G Parham, H-S Park, P K Patel, B A Remington, J D Salmonson, P T Springer, C R Weber, G B Zimmerman, and J L Kline. "Simulations of fill tube effects on the implosion of high-foot NIF ignition capsules". *Journal of Physics: Conference Series*, 717: 012013, may 2016. 145

[47] L Divol, A Pak, LF Berzak Hopkins, S Le Pape, NB Meezan, EL Dewald, DD-M Ho, SF Khan, AJ Mackinnon, JS Ross, et al. "Symmetry control of an indirectly driven high-density-carbon implosion at high convergence and high velocity". *Physics of Plasmas*, 24(5):056309, 2017. 145

[48] Laurent Divol. "3D isobaric hotspot reconstruction from multiple neutron and Xray views on the NIF: quantifying radiative loss impact on DT implosion and other insights". *Bulletin of the American Physical Society*, 64, 2019. 32, 130, 159

[49] R Paul Drake. "High-energy-density physics". *Phys. Today*, 63(6):28, 2010. 105

[50] M. J. Edwards and Ignition Team. "The Ignition Physics Campaign on NIF: Status and Progress". *Journal of Physics: Conference Series*, 688(1):012017, 2016. 156

[51] V. E. Fatherley, D. N. Fittinghoff, R. L. Hibbard, H. J. Jorgenson, J. I. Martinez, J. A. Oertel, D. W. Schmidt, C. S. Waltz, C. H. Wilde, and P. L. Volegov. "Aperture design for the third neutron and first gamma-ray imaging systems for the National Ignition Facility". *Review of Scientific Instruments*, 89(10):10I127, 2018. doi: 10.1063/1.5039328. 36, 40

[52] C. J. Forrest, A. Deltuva, W. U. Schröder, A. V. Voinov, J. P. Knauer, E. M. Campbell, G. W. Collins, V. Yu. Glebov, O. M. Mannion, Z. L. Mohamed, P. B. Radha, S. P. Regan, T. C. Sangster, and C. Stoeckl. "Deuteron breakup induced by 14-MeV neutrons from inertial confinement fusion". *Phys. Rev. C*, 100:034001, Sep 2019. doi: 10.1103/PhysRevC.100.034001. 70, 111, 160

[53] G. S. Fraley, E. J. Linnebur, R. J. Mason, and R. L. Morse. "Thermonuclear burn characteristics of compressed deuterium-tritium microspheres". *The Physics of Fluids*, 17(2):474–489, 1974. doi: 10.1063/1.1694739. 11, 23, 24, 26

[54] J. A. Frenje, D. T. Casey, C. K. Li, J. R. Rygg, F. H. Séguin, R. D. Petrasso, V. Yu Glebov, D. D. Meyerhofer, T. C. Sangster, S. Hatchett, S. Haan, C. Cerjan, O. Landen, M. Moran, P. Song, D. C. Wilson, and R. J. Leeper. "First measurements of the absolute neutron spectrum using the magnetic recoil spectrometer at

OMEGA (invited)". *Review of Scientific Instruments*, 79(10):10E502, 2008. doi: 10.1063/1.2956837. 36

[55] J. A. Frenje, C. K. Li, F. H. Seguin, D. T. Casey, R. D. Petrasso, D. P. McNabb, P. Navratil, S. Quaglioni, T. C. Sangster, V. Yu Glebov, and D. D. Meyerhofer. "Measurements of the Differential Cross Sections for the Elastic $n-^3$H and $n-^2$H Scattering at 14.1 MeV by Using an Inertial Confinement Fusion Facility". *Phys. Rev. Lett.*, 107:122502, Sep 2011. doi: 10.1103/PhysRevLett.107.122502. 111

[56] J.A. Frenje, R. Bionta, E.J. Bond, J.A. Caggiano, D.T. Casey, C. Cerjan, J. Edwards, M. Eckart, D.N. Fittinghoff, S. Friedrich, V.Yu. Glebov, S. Glenzer, G. Grim, S. Haan, R. Hatarik, S. Hatchett, M. Gatu Johnson, O.S. Jones, J.D. Kilkenny, J.P. Knauer, O. Landen, R. Leeper, S. Le Pape, R. Lerche, C.K. Li, A. Mackinnon, J. McNaney, F.E. Merrill, M. Moran, D.H. Munro, T.J. Murphy, R.D. Petrasso, R. Rygg, T.C. Sangster, F.H. Séguin, S. Sepke, B. Spears, P. Springer, C. Stoeckl, and D.C. Wilson. "Diagnosing implosion performance at the National Ignition Facility (NIF) by means of neutron spectrometry". *Nuclear Fusion*, 53(4):043014, 2013. 84, 118

[57] Johan Frenje, Cody Parker, Maria Gatu Johnson, Brandon Lahmann, Alexander Sandberg, Chikang Li, Fredrick Seguin, Richard Petrasso, Terance Hilsabeck, Joseph Kilkenny, et al. "The next-generation Magnetic Recoil Spectrometer for time-resolved measurement of the neutron spectrum at the National Ignition Facility (NIF)". In *APS Meeting Abstracts*, 2018. 36

[58] Jim A Gaffney, Scott T Brandon, Kelli D Humbird, Michael KG Kruse, Ryan C Nora, J Luc Peterson, and Brian K Spears. "Making inertial confinement fusion models more predictive". *Physics of Plasmas*, 26(8):082704, 2019. 158, 159

[59] S. Gasiorowicz. "Quantum physics". Wiley, 2003. ISBN 9780471057000. 171

[60] M. Gatu Johnson, D. T. Casey, J. A. Frenje, C.-K. Li, F. H. Séguin, R. D. Petrasso, R. Ashabranner, R. Bionta, S. LePape, M. McKernan, A. Mackinnon, J. D. Kilkenny, J. Knauer, and T. C. Sangster. "Measurements of collective fuel velocities in deuterium-tritium exploding pusher and cryogenically layered deuterium-tritium implosions on the NIF". *Physics of Plasmas*, 20(4):042707, 2013. doi: 10.1063/1.4802810. 32

[61] M. Gatu Johnson, J. P. Knauer, C. J. Cerjan, M. J. Eckart, G. P. Grim, E. P. Hartouni, R. Hatarik, J. D. Kilkenny, D. H. Munro, D. B. Sayre, B. K. Spears, R. M. Bionta, E. J. Bond, J. A. Caggiano, D. Callahan, D. T. Casey, T. Döppner, J. A. Frenje, V. Yu Glebov, O. Hurricane, A. Kritcher, S. LePape, T. Ma, A. Mackinnon, N. Meezan, P. Patel, R. D. Petrasso, J. E. Ralph, P. T. Springer, and C. B. Yeamans. "Indications of flow near maximum compression in layered deuterium-tritium implosions at the National Ignition Facility". *Physical Review E*, 94(2): 1–5, 2016. ISSN 24700053. doi: 10.1103/PhysRevE.94.021202. 36, 84, 96

[62] M. Gatu Johnson, B. D. Appelbe, J. P. Chittenden, A. Crilly, J. Delettrez, C. Forrest, J. A. Frenje, V. Yu. Glebov, W. Grimble, B. M. Haines, I. V. Igumenshchev, R. Janezic, J. P. Knauer, B. Lahmann, F. J. Marshall, T. Michel, F. H. Séguin, C. Stoeckl, C. Walsh, A. B. Zylstra, and R. D. Petrasso. "Impact of imposed mode 2 laser drive asymmetry on inertial confinement fusion implosions". *Physics of Plasmas*, 26(1):012706, 2019. doi: 10.1063/1.5066435. 34, 64

[63] M. Gatu Johnson, P. J. Adrian, K. S. Anderson, B. D. Appelbe, J. P. Chittenden, A. J. Crilly, D. Edgell, C. J. Forrest, J. A. Frenje, V. Yu. Glebov, B. M. Haines, I. Igumenshchev, D. Jacobs-Perkins, R. Janezic, N. V. Kabadi, J. P. Knauer, B. Lahmann, O. M. Mannion, F. J. Marshall, T. Michel, F. H. Séguin, R. Shah, C. Stoeckl, C. A. Walsh, and R. D. Petrasso. "Impact of stalk on directly driven inertial confinement fusion implosions". *Physics of Plasmas*, 27(3):032704, 2020. doi: 10.1063/1.5141607. 34, 148

[64] Z. G. Ge, Z. X. Zhao, H. H. Xia, Y. X. Zhuang, T. J. Liu, J. S. Zhang, and H. C. Wu. "The Updated Version of Chinese Evaluated Nuclear Data Library (CENDL-3.1)". *Journal of the Korean Physical Society*, 59, 2011. 60, 66, 111, 143

[65] H. Geppert-Kleinrath, H. W. Herrmann, Y. H. Kim, A. B. Zylstra, K. Meaney, F. E. Lopez, B. J. Pederson, J. Carrera, H. Khater, C. J. Horsfield, M. S. Rubery, S. Gales, A. Leatherland, A. Meadowcroft, T. Hilsabeck, J. D. Kilkenny, R. M. Malone, J. D. Hares, A. K. L. Dymoke-Bradshaw, J. Milnes, and C. McFee. "Pulse dilation gas Cherenkov detector for ultra-fast gamma reaction history at the NIF (invited)". *Review of Scientific Instruments*, 89(10):10I146, 2018. doi: 10.1063/1.5039377. 40

[66] Hermann Geppert-Kleinrath, Hans W Herrmann, Yong Ho Kim, Alex B Zylstra, K Meaney, Frank Edward Lopez, Benjamin James Pederson, J Carrera, H Khater, CJ Horsfield, et al. "Pulse dilation gas Cherenkov detector for ultra-fast gamma reaction history at the NIF". *Review of Scientific Instruments*, 89(10):10I146, 2018. 158

[67] IE Golovkin, RC Mancini, SJ Louis, RW Lee, and L Klein. "Analysis of X-ray spectral data with genetic algorithms". *Journal of Quantitative Spectroscopy and Radiative Transfer*, 75(5):625–636, 2002. 159

[68] V. N. Goncharov, J. P. Knauer, P. W. McKenty, P. B. Radha, T. C. Sangster, S. Skupsky, R. Betti, R. L. McCrory, and D. D. Meyerhofer. "Improved performance of direct-drive inertial confinement fusion target designs with adiabat shaping using an intensity picket". *Physics of Plasmas*, 10(5):1906–1918, 2003. doi: 10.1063/1.1562166. 102

[69] V. N. Goncharov, T. C. Sangster, T. R. Boehly, S. X. Hu, I. V. Igumenshchev, F. J. Marshall, R. L. McCrory, D. D. Meyerhofer, P. B. Radha, W. Seka, S. Skupsky,

C. Stoeckl, D. T Casey, J. A. Frenje, and R. D. Petrasso. "Demonstration of the Highest Deuterium-Tritium Areal Density Using Multiple-Picket Cryogenic Designs on OMEGA". *Phys. Rev. Lett.*, 104:165001, Apr 2010. doi: 10.1103/PhysRevLett.104.165001. 98

[70] V Gopalaswamy, R Betti, JP Knauer, N Luciani, D Patel, KM Woo, A Bose, IV Igumenshchev, EM Campbell, KS Anderson, et al. "Tripled yield in direct-drive laser fusion through statistical modelling". *Nature*, 565(7741):581–586, 2019. 98, 159

[71] Hans Griem. "Spectral line broadening by plasmas". Elsevier, 2012. 52, 55

[72] G. P. Grim, N. Guler, F. E. Merrill, G. L. Morgan, C. R. Danly, P. L. Volegov, C. H. Wilde, D. C. Wilson, D. S. Clark, D. E. Hinkel, O. S. Jones, K. S. Raman, N. Izumi, D. N. Fittinghoff, O. B. Drury, E. T. Alger, P. A. Arnold, R. C. Ashabranner, L. J. Atherton, M. A. Barrios, S. Batha, P. M. Bell, L. R. Benedetti, R. L. Berger, L. A. Bernstein, L. V. Berzins, R. Betti, S. D. Bhandarkar, R. M. Bionta, D. L. Bleuel, T. R. Boehly, E. J. Bond, M. W. Bowers, D. K. Bradley, G. K. Brunton, R. A. Buckles, S. C. Burkhart, R. F. Burr, J. A. Caggiano, D. A. Callahan, D. T. Casey, C. Castro, P. M. Celliers, C. J. Cerjan, G. A. Chandler, C. Choate, S. J. Cohen, G. W. Collins, G. W. Cooper, J. R. Cox, J. R. Cradick, P. S. Datte, E. L. Dewald, P. Di Nicola, J. M. Di Nicola, L. Divol, S. N. Dixit, R. Dylla-Spears, E. G. Dzenitis, M. J. Eckart, D. C. Eder, D. H. Edgell, M. J. Edwards, J. H. Eggert, R. B. Ehrlich, G. V. Erbert, J. Fair, D. R. Farley, B. Felker, R. J. Fortner, J. A. Frenje, G. Frieders, S. Friedrich, M. Gatu-Johnson, C. R. Gibson, E. Giraldez, V. Y. Glebov, S. M. Glenn, S. H. Glenzer, G. Gururangan, S. W. Haan, K. D. Hahn, B. A. Hammel, A. V. Hamza, E. P. Hartouni, R. Hatarik, S. P. Hatchett, C. Haynam, M. R. Hermann, H. W. Herrmann, D. G. Hicks, J. P. Holder, D. M. Holunga, J. B. Horner, W. W. Hsing, H. Huang, M. C. Jackson, K. S. Jancaitis, D. H. Kalantar, R. L. Kauffman, M. I. Kauffman, S. F. Khan, J. D. Kilkenny, J. R. Kimbrough, R. Kirkwood, J. L. Kline, J. P. Knauer, K. M. Knittel, J. A. Koch, T. R. Kohut, B. J. Kozioziemski, K. Krauter, G. W. Krauter, A. L. Kritcher, J. Kroll, G. A. Kyrala, K. N. La Fortune, G. LaCaille, L. J. Lagin, T. A. Land, O. L. Landen, D. W. Larson, D. A. Latray, R. J. Leeper, T. L. Lewis, S. LePape, J. D. Lindl, R. R. Lowe-Webb, T. Ma, B. J. MacGowan, A. J. MacKinnon, A. G. MacPhee, R. M. Malone, T. N. Malsbury, E. Mapoles, C. D. Marshall, D. G. Mathisen, P. McKenty, J. M. McNaney, N. B. Meezan, P. Michel, J. L. Milovich, J. D. Moody, A. S. Moore, M. J. Moran, K. Moreno, E. I. Moses, D. H. Munro, B. R. Nathan, A. J. Nelson, A. Nikroo, R. E. Olson, C. Orth, A. E. Pak, E. S. Palma, T. G. Parham, P. K. Patel, R. W. Patterson, R. D. Petrasso, R. Prasad, J. E. Ralph, S. P. Regan, H. Rinderknecht, H. F. Robey, G. F. Ross, C. L. Ruiz, F. H. Séguin, J. D. Salmonson, T. C. Sangster, J. D. Sater, R. L. Saunders, M. B. Schneider, D. H. Schneider, M. J. Shaw, N. Simanovskaia, B. K.

Spears, P. T. Springer, C. Stoeckl, W. Stoeffl, L. J. Suter, C. A. Thomas, R. Tommasini, R. P. Town, A. J. Traille, B. Van Wonterghem, R. J. Wallace, S. Weaver, S. V. Weber, P. J. Wegner, P. K. Whitman, K. Widmann, C. C. Widmayer, R. D. Wood, B. K. Young, R. A. Zacharias, and A. Zylstra. "Nuclear imaging of the fuel assembly in ignition experiments". *Physics of Plasmas*, 20(5):056320, 2013. doi: 10.1063/1.4807291. 36, 37, 38, 127, 129

[73] G. P. Grim, R. Rundberg, M. M. Fowler, A. C. Hayes, G. Jungman, M. Boswell, A. Klein, J. Wilhelmy, A. Tonchev, and C. B. Yeamans. "Measurement of reaction-in-flight neutrons using thulium activation at the National Ignition Facility". In Perry M. Bell and Gary P. Grim, editors, *Target Diagnostics Physics and Engineering for Inertial Confinement Fusion III*, volume 9211, pages 29 – 41. International Society for Optics and Photonics, SPIE, 2014. doi: 10.1117/12.2066249. 125

[74] R. Hatarik, D. B. Sayre, J. A. Caggiano, T. Phillips, M. J. Eckart, E. J. Bond, C. Cerjan, G. P. Grim, E. P. Hartouni, J. P. Knauer, J. M. Mcnaney, and D. H. Munro. "Analysis of the neutron time-of-flight spectra from inertial confinement fusion experiments". *Journal of Applied Physics*, 118(18):184502, 2015. doi: 10.1063/1.4935455. 35, 108, 153

[75] R. Hatarik, R. C. Nora, B. K. Spears, M. J. Eckart, G. P. Grim, E. P. Hartouni, A. S. Moore, and D. J. Schlossberg. "Using multiple neutron time of flight detectors to determine the hot spot velocity". *Review of Scientific Instruments*, 89 (10):10I138, 2018. doi: 10.1063/1.5039372. 32, 36, 39, 64, 116, 139

[76] PW Hatfield, SJ Rose, and RHH Scott. "The blind implosion-maker: Automated inertial confinement fusion experiment design". *Physics of Plasmas*, 26(6):062706, 2019. 159

[77] A. C. Hayes, Gerard Jungman, A. E. Schulz, M. Boswell, M. M. Fowler, G. Grim, A. Klein, R. S. Rundberg, J. B. Wilhelmy, D. Wilson, C. Cerjan, D. Schneider, S. M. Sepke, A. Tonchev, and C. Yeamans. "Reaction-in-flight neutrons as a test of stopping power in degenerate plasmas". *Physics of Plasmas*, 22(8):082703, 2015. doi: 10.1063/1.4928104. 125, 155

[78] AC Hayes, ME Gooden, E Henry, Gerard Jungman, JB Wilhelmy, RS Rundberg, C Yeamans, G Kyrala, C Cerjan, DL Danielson, et al. "Plasma stopping-power measurements reveal transition from non-degenerate to degenerate plasmas". *Nature Physics*, pages 1–6, 2020. 125, 155

[79] C. A. Haynam, P. J. Wegner, J. M. Auerbach, M. W. Bowers, S. N. Dixit, G. V. Erbert, G. M. Heestand, M. A. Henesian, M. R. Hermann, K. S. Jancaitis, K. R. Manes, C. D. Marshall, N. C. Mehta, J. Menapace, E. Moses, J. R. Murray, M. C. Nostrand, C. D. Orth, R. Patterson, R. A. Sacks, M. J. Shaw, M. Spaeth, S. B.

Sutton, W. H. Williams, C. C. Widmayer, R. K. White, S. T. Yang, and B. M. Van Wonterghem. "National Ignition Facility laser performance status". *Appl. Opt.*, 46(16):3276–3303, Jun 2007. doi: 10.1364/AO.46.003276. 30

[80] Per Helander and Dieter J Sigmar. "Collisional transport in magnetized plasmas", volume 4. Cambridge university press, 2005. 71

[81] H. W. Herrmann, N. Hoffman, D. C. Wilson, W. Stoeffl, L. Dauffy, Y. H. Kim, A. McEvoy, C. S. Young, J. M. Mack, C. J. Horsfield, M. Rubery, E. K. Miller, and Z. A. Ali. "Diagnosing inertial confinement fusion gamma ray physics (invited)". *Review of Scientific Instruments*, 81(10):10D333, 2010. doi: 10.1063/1.3495770. 40

[82] H. W. Herrmann, Y. H. Kim, A. B. Zylstra, H. Geppert-Kleinrath, K. D. Meaney, C. S. Young, F. E. Lopez, V. E. Fatherley, B. J. Pederson, J. A. Oertel, J. E. Hernandez, J. Carrera, H. Khater, M. S. Rubery, C. J. Horsfield, S. Gales, A. Leatherland, T. Hilsabeck, J. D. Kilkenny, R. M. Malone, and S. H. Batha. "Progress on next generation gamma-ray Cherenkov detectors for the National Ignition Facility". *Review of Scientific Instruments*, 89(10):10I148, 2018. doi: 10.1063/1.5039378. 40

[83] D. J. Hoarty, P. Allan, S. F. James, C. R. D. Brown, L. M. R. Hobbs, M. P. Hill, J. W. O. Harris, J. Morton, M. G. Brookes, R. Shepherd, J. Dunn, H. Chen, E. Von Marley, P. Beiersdorfer, H. K. Chung, R. W. Lee, G. Brown, and J. Emig. "Observations of the Effect of Ionization-Potential Depression in Hot Dense Plasma". *Phys. Rev. Lett.*, 110:265003, Jun 2013. doi: 10.1103/PhysRevLett.110.265003. 57

[84] N. M. Hoffman, H. W. Herrmann, Y. H. Kim, H. H. Hsu, C. J. Horsfield, M. S. Rubery, E. K. Miller, E. Grafil, W. Stoeffl, J. A. Church, C. S. Young, J. M. Mack, D. C. Wilson, J. R. Langenbrunner, S. C. Evans, T. J. Sedillo, V. Yu. Glebov, and T. Duffy. "Measurement of areal density in the ablators of inertial-confinement-fusion capsules via detection of ablator (n, n'γ) gamma-ray emission". *Physics of Plasmas*, 20(4):042705, 2013. doi: 10.1063/1.4799799. 40, 143, 149, 158

[85] CF Hooper Jr. "Low-frequency component electric microfield distributions in plasmas". *Physical Review*, 165(1):215, 1968. 164

[86] Joseph D Huba. "NRL plasma formulary". Technical report, NAVAL RESEARCH LAB WASHINGTON DC PLASMA PHYSICS DIV, 2006. 43

[87] Kelli D Humbird, Jayson Luc Peterson, BK Spears, and RG McClarren. "Transfer learning to model inertial confinement fusion experiments". *IEEE Transactions on Plasma Science*, 2019. 159

[88] D. G. Hummer. "The atomic internal partition function". *AIP Conference Proceedings*, 168(1):1–14, 1988. doi: 10.1063/1.37180. 57

[89] DG Hummer and Dimitri Mihalas. "The equation of state for stellar envelopes. I-an occupation probability formalism for the truncation of internal partition functions". *The Astrophysical Journal*, 331:794–814, 1988. 57

[90] O. A. Hurricane, D. A. Callahan, D. T. Casey, P. M. Celliers, C. Cerjan, E. L. Dewald, T. R. Dittrich, T. Döppner, D. E. Hinkel, L. F. B. Hopkins, J. L. Kline, S. Le Pape, T. Ma, A. G. Macphee, J. L. Milovich, A. Pak, H.-S. Park, P. K. Patel, B. A. Remington, J. D. Salmonson, P. T. Springer, and R. Tommasini. "Fuel gain exceeding unity in an inertially confined fusion implosion". *Nature*, 506:343–348, 2014. 11, 32

[91] O. A. Hurricane, D. A. Callahan, D. T. Casey, E. L. Dewald, T. R. Dittrich, T. Döppner, S. Haan, D. E. Hinkel, L. F. Berzak Hopkins, O. Jones, A. L. Kritcher, S. Le Pape, T. Ma, A. G. Macphee, J. L. Milovich, J. Moody, A. Pak, H.-S. Park, P. K. Patel, J. E. Ralph, H. F. Robey, J. S. Ross, J. D. Salmonson, B. K. Spears, P. T. Springer, R. Tommasini, F. Albert, L. R. Benedetti, R. Bionta, E. Bond, D. K. Bradley, J. Caggiano, P. M. Celliers, C. Cerjan, J. A. Church, R. Dylla-Spears, D. Edgell, M. J. Edwards, D. Fittinghoff, M. A. Barrios Garcia, A. Hamza, R. Hatarik, H. Herrmann, M. Hohenberger, D. Hoover, J. L. Kline, G. Kyrala, B. Kozioziemski, G. Grim, J. E. Field, J. Frenje, N. Izumi, M. Gatu Johnson, S. F. Khan, J. Knauer, T. Kohut, O. Landen, F. Merrill, P. Michel, A. Moore, S. R. Nagel, A. Nikroo, T. Parham, R. R. Rygg, D. Sayre, M. Schneider, D. Shaughnessy, D. Strozzi, R. P. J. Town, D. Turnbull, P. Volegov, A. Wan, K. Widmann, C. Wilde, and C. Yeamans. "Inertially confined fusion plasmas dominated by alpha-particle self-heating". *Nature*, 12:800–806, 2016. 25, 134

[92] CA Iglesias, FJ Rogers, R Shepherd, A Bar-Shalom, MS Murillo, DP Kilcrease, Annette Calisti, and RW Lee. "Fast electric microfield distribution calculations in extreme matter conditions". *Journal of Quantitative Spectroscopy and Radiative Transfer*, 65(1-3):303–315, 2000. 164

[93] Carlos A Iglesias, Hugh E DeWitt, Joel L Lebowitz, David MacGowan, and William B Hubbard. "Low-frequency electric microfield distributions in plasmas". *Physical Review A*, 31(3):1698, 1985. 161, 164

[94] C Jennings. "Radiation Transport Effects in Wire Array Z-Pinches and Magneto-Hydrodynamic Modelling Techniques". PhD thesis, Imperial College London, 2005. 47

[95] M. Gatu Johnson, J. A. Frenje, D. T. Casey, C. K. Li, F. H. Séguin, R. Petrasso, R. Ashabranner, R. M. Bionta, D. L. Bleuel, E. J. Bond, J. A. Caggiano, A. Carpenter, C. J. Cerjan, T. J. Clancy, T. Doeppner, M. J. Eckart, M. J. Edwards, S. Friedrich, S. H. Glenzer, S. W. Haan, E. P. Hartouni, R. Hatarik, S. P. Hatchett, O. S. Jones, G. Kyrala, S. Le Pape, R. A. Lerche, O. L. Landen, T. Ma,

A. J. MacKinnon, M. A. McKernan, M. J. Moran, E. Moses, D. H. Munro, J. McNaney, H. S. Park, J. Ralph, B. Remington, J. R. Rygg, S. M. Sepke, V. Smalyuk, B. Spears, P. T. Springer, C. B. Yeamans, M. Farrell, D. Jasion, J. D. Kilkenny, A. Nikroo, R. Paguio, J. P. Knauer, V. Yu Glebov, T. C. Sangster, R. Betti, C. Stoeckl, J. Magoon, M. J. Shoup, G. P. Grim, J. Kline, G. L. Morgan, T. J. Murphy, R. J. Leeper, C. L. Ruiz, G. W. Cooper, and A. J. Nelson. "Neutron spectrometry-An essential tool for diagnosing implosions at the National Ignition Facility (invited)". *Review of Scientific Instruments*, 83(10), 2012. ISSN 00346748. doi: 10.1063/1.4728095. 36, 108, 118, 119, 158

[96] M Gatu Johnson, CJ Forrest, DB Sayre, A Bacher, J-L Bourgade, CR Brune, JA Caggiano, DT Casey, JA Frenje, V Yu Glebov, et al. "Experimental Evidence of a Variant Neutron Spectrum from the T (t, 2 n) α Reaction at Center-of-Mass Energies in the Range of 16–50 keV". *Physical review letters*, 121(4):042501, 2018. 70, 160

[97] Thomas B Kaiser. "Laser ray tracing and power deposition on an unstructured three-dimensional grid". *Physical Review E*, 61(1):895, 2000. 45

[98] Mehran Kardar. "Statistical Physics of Particles". Cambridge University Press, 2007. doi: 10.1017/CBO9780511815898. 42

[99] MF Kasim, TP Galligan, Jacob Topp-Mugglestone, Gianluca Gregori, and SM Vinko. "Inverse Problem Instabilities in Large-Scale Plasma Modelling". *arXiv preprint arXiv:1805.08301*, 2018. 159

[100] AJ Kemp and J Meyer-ter Vehn. "An equation of state code for hot dense matter, based on the QEOS description". *Nuclear Instruments and Methods in Physics Research Section A: Accelerators, Spectrometers, Detectors and Associated Equipment*, 415(3):674–676, 1998. 49

[101] Y. Kim, J. M. Mack, H. W. Herrmann, C. S. Young, G. M. Hale, S. Caldwell, N. M. Hoffman, S. C. Evans, T. J. Sedillo, A. McEvoy, J. Langenbrunner, H. H. Hsu, M. A. Huff, S. Batha, C. J. Horsfield, M. S. Rubery, W. J. Garbett, W. Stoeffl, E. Grafil, L. Bernstein, J. A. Church, D. B. Sayre, M. J. Rosenberg, C. Waugh, H. G. Rinderknecht, M. Gatu Johnson, A. B. Zylstra, J. A. Frenje, D. T. Casey, R. D. Petrasso, E. Kirk Miller, V. Yu Glebov, C. Stoeckl, and T. C. Sangster. "D-T gamma-to-neutron branching ratio determined from inertial confinement fusion plasmas". *Physics of Plasmas*, 19(5):056313, 2012. doi: 10.1063/1.4718291. 40

[102] P. F. Knapp, P. F. Schmit, S. B. Hansen, M. R. Gomez, K. D. Hahn, D. B. Sinars, K. J. Peterson, S. A. Slutz, A. B. Sefkow, T. J. Awe, E. Harding, C. A. Jennings, M. P. Desjarlais, G. A. Chandler, G. W. Cooper, M. E. Cuneo, M. Geissel, A. J. Harvey-Thompson, J. L. Porter, G. A. Rochau, D. C. Rovang, C. L. Ruiz, M. E. Savage, I. C. Smith, W. A. Stygar, and M. C. Herrmann. "Effects of magnetization

on fusion product trapping and secondary neutron spectra". *Physics of Plasmas*, 22(5):056312, 2015. doi: 10.1063/1.4920948. 123

[103] Patrick Knapp, Michael Glinsky, Matthew Evans, Stephanie Hansen, Christopher Jennings, Eric Harding, Matthew Weis, Stephen Slutz, Matt Gomez, Kelly Hahn, et al. "Bayesian Parameter Estimation for Data Integration in ICF Experiments". In *APS Meeting Abstracts*, 2018. 158

[104] Dietrich Kremp, Manfred Schlanges, and Wolf-Dietrich Kraeft. "Quantum statistics of nonideal plasmas", volume 25. Springer Science & Business Media, 2006. 51, 53

[105] AL Kritcher, D Clark, S Haan, SA Yi, AB Zylstra, DA Callahan, DE Hinkel, LF Berzak Hopkins, OA Hurricane, OL Landen, et al. "Comparison of plastic, high density carbon, and beryllium as indirect drive NIF ablators". *Physics of Plasmas*, 25(5):056309, 2018. 31

[106] B Lahmann, JA Frenje, M Gatu Johnson, FH Seguin, CK Li, RD Petrasso, E Hartouni, C Yeamans, H Rinderknecht, D Sayre, et al. "Using X-Ray Images and Secondary DT Neutrons to Diagnose Convergence and hot-spot asymmetries in implosions at the NIF". *Bulletin of the American Physical Society*, 64, 2019. 154

[107] K. D. Lathrop. "Ray Effects in Discrete Ordinates Equations". *Nuclear Science and Engineering*, 32(3):357–369, 1968. 85

[108] S. Le Pape, L. F. Berzak Hopkins, L. Divol, A. Pak, E. L. Dewald, S. Bhandarkar, L. R. Bennedetti, T. Bunn, J. Biener, J. Crippen, D. Casey, D. Edgell, D. N. Fittinghoff, M. Gatu-Johnson, C. Goyon, S. Haan, R. Hatarik, M. Havre, D. D-M. Ho, N. Izumi, J. Jaquez, S. F. Khan, G. A. Kyrala, T. Ma, A. J. Mackinnon, A. G. MacPhee, B. J. MacGowan, N. B. Meezan, J. Milovich, M. Millot, P. Michel, S. R. Nagel, A. Nikroo, P. Patel, J. Ralph, J. S. Ross, N. G. Rice, D. Strozzi, M. Stadermann, P. Volegov, C. Yeamans, C. Weber, C. Wild, D. Callahan, and O. A. Hurricane. "Fusion Energy Output Greater than the Kinetic Energy of an Imploding Shell at the National Ignition Facility". *Phys. Rev. Lett.*, 120:245003, Jun 2018. doi: 10.1103/PhysRevLett.120.245003. 30, 31, 156

[109] Elmer Eugene Lewis and Warren F Miller. "Computational methods of neutron transport". 1984. 75, 77, 78

[110] Chengliang Lin, Gerd Röpke, Wolf-Dietrich Kraeft, and Heidi Reinholz. "Ionization-potential depression and dynamical structure factor in dense plasmas". *Physical Review E*, 96(1):013202, 2017. 161

[111] John Lindl. "Development of the indirect-drive approach to inertial confinement fusion and the target physics basis for ignition and gain". *Physics of plasmas*, 2 (11):3933–4024, 1995. 22, 24, 44

[112] Malcolm S Longair. "High energy astrophysics". Cambridge University Press, 2011. 54, 55

[113] JJ MacFarlane. "VISRAD—A 3-D view factor code and design tool for high-energy density physics experiments". *Journal of Quantitative Spectroscopy and Radiative Transfer*, 81(1-4):287–300, 2003. 33

[114] B MacGowan, O Landen, D Casey, C Young, P Michel, D Callahan, J-M di Nicola, D Mariscal, T Ma, J Milovich, et al. "Understanding 3D Asymmetries In X-ray Drive At The National Ignition Facility Using a Simple View Factor Metric". *APS*, 2019:JO7–010, 2019. 142, 148

[115] F. Manke. "Inertial Fusion Diagnostic Modelling". Master's thesis, Imperial College London, 2015. 5, 175

[116] O. M. Mannion, V. Yu. Glebov, C. J. Forrest, J. P. Knauer, V. N. Goncharov, S. P. Regan, T. C. Sangster, C. Stoeckl, and M. Gatu Johnson. "Calibration of a neutron time-of-flight detector with a rapid instrument response function for measurements of bulk fluid motion on OMEGA". *Review of Scientific Instruments*, 89(10):10I131, 2018. doi: 10.1063/1.5037324. 32, 34, 35, 36, 64, 96, 112, 116, 139

[117] O. M. Mannion, A. J. Crilly, C. J. Forrest, B. D. Appelbe, Z. L. Mohamed, V. Yu. Glebov, V. Gopalaswamy, V. N. Goncharov, J. P. Knauer, T. C. Sangster, T. C. Stoeckl, J. P. Chittenden, and S. P. Regan. "First temperature and velocity measurements of the dense fuel layer in inertial confinement fusion experiments". 2020. submitted. 112, 153

[118] OM Mannion, JP Knauer, V Yu Glebov, CJ Forrest, A Liu, ZL Mohamed, MH Romanofsky, TC Sangster, C Stoeckl, and SP Regan. "A suite of neutron time-of-flight detectors to measure hot-spot motion in direct-drive inertial confinement fusion experiments on OMEGA". *Nuclear Instruments and Methods in Physics Research Section A: Accelerators, Spectrometers, Detectors and Associated Equipment*, page 163774, 2020. 36, 116

[119] K McGlinchey. "Radiation-Hydrodynamics Simulations of the Impact of Instabilities and Asymmetries of Inertial Confinement Fusion". PhD thesis, Imperial College London, 2017. 5, 32, 44, 47, 144

[120] K McGlinchey, BD Appelbe, AJ Crilly, JK Tong, CA Walsh, and JP Chittenden. "Diagnostic signatures of performance degrading perturbations in inertial confinement fusion implosions". *Physics of Plasmas*, 25(12):122705, 2018. 5, 32, 33, 145, 146, 156

[121] K. D. Meaney, Y. H. Kim, H. Geppert-Kleinrath, H. W. Herrmann, L. Berzak Hopkins, and N. M. Hoffman. "Diagnostic signature of the compressibility of the inertial-confinement-fusion pusher". *Phys. Rev. E*, 101:023208, Feb 2020. doi: 10.1103/PhysRevE.101.023208. 40, 143

[122] Kevin Meaney. "Gamma measured ablator areal density observations, trends and time shifts on the National Ignition Facility". *Bulletin of the American Physical Society*, 64, 2019. 149, 150, 157

[123] F. E. Merrill, D. Bower, R. Buckles, D. D. Clark, C. R. Danly, O. B. Drury, J. M. Dzenitis, V. E. Fatherley, D. N. Fittinghoff, R. Gallegos, G. P. Grim, N. Guler, E. N. Loomis, S. Lutz, R. M. Malone, D. D. Martinson, D. Mares, D. J. Morley, G. L. Morgan, J. A. Oertel, I. L. Tregillis, P. L. Volegov, P. B. Weiss, C. H. Wilde, and D. C. Wilson. "The neutron imaging diagnostic at NIF (invited)". *Review of Scientific Instruments*, 83(10):10D317, 2012. doi: 10.1063/1.4739242. 36

[124] Dimitri Mihalas, Werner Dappen, and DG Hummer. "The equation of state for stellar envelopes. II-Algorithm and selected results". *The Astrophysical Journal*, 331:815–825, 1988. 57

[125] A. S. Moore, D. J. Schlossberg, E. P. Hartouni, D. Sayre, M. J. Eckart, R. Hatarik, F. Barbosa, J. Root, C. Waltz, B. Beeman, M. S. Rubery, and G. P. Grim. "A fused silica Cherenkov radiator for high precision time-of-flight measurement of DT γ and neutron spectra (invited)". *Review of Scientific Instruments*, 89(10): 10I120, 2018. doi: 10.1063/1.5039322. 35, 40

[126] R. M. More, K. H. Warren, D. A. Young, and G. B. Zimmerman. "A new quotidian equation of state (QEOS) for hot dense matter". *The Physics of fluids*, 31(10): 3059–3078, 1988. 49

[127] R.M. More. "Pressure Ionization, Resonances, and the Continuity of Bound and Free States". volume 21 of *Advances in Atomic and Molecular Physics*, pages 305 – 356. Academic Press, 1985. 56

[128] JE Morel. "Fokker-Planck calculations using standard discrete ordinates transport codes". *Nuclear Science and Engineering*, 79(4):340–356, 1981. 84, 85

[129] JE Morel. "Diffusion-limit asymptotics of the transport equation, the P1/3 equations, and two flux-limited diffusion theories". *Journal of Quantitative Spectroscopy and Radiative Transfer*, 65(5):769–778, 2000. 47

[130] Takamasa Mori, Masayuki Nakagawa, and Makoto. Sasaki. "One-, two- and three-dimensional transport codes using multi-group double-differential form cross sections", 1988. 66, 80

[131] D. H. Munro, J. E. Field, R. Hatarik, J. L. Peterson, E. P. Hartouni, B. K. Spears, and J. D. Kilkenny. "Impact of temperature-velocity distribution on fusion neutron peak shape". *Physics of Plasmas*, 24(5):056301, 2017. doi: 10.1063/1.4976857. 64, 88

[132] David H. Munro. "Interpreting inertial fusion neutron spectra". *Nuclear Fusion*, 56(3):036001, 2016. ISSN 0029-5515. doi: 10.1088/0029-5515/56/3/036001. 36, 39, 62, 88, 89, 93, 94, 104, 116

[133] T. J. Murphy. "The effect of turbulent kinetic energy on inferred ion temperature from neutron spectra". *Physics of Plasmas*, 21(7):072701, 2014. doi: 10.1063/1.4885342. 96

[134] N. P. L. Niasse. "Development of a Pseudo Non-LTE Model for Z-Pinch Simulations". PhD thesis, Imperial College London, 2012. 5, 44, 55, 56

[135] M. Nocente, J. Källne, M. Salewski, M. Tardocchi, and G. Gorini. "Gamma-ray emission spectrum from thermonuclear fusion reactions without intrinsic broadening". *Nuclear Fusion*, 55(12):123009, oct 2015. doi: 10.1088/0029-5515/55/12/123009. 40

[136] William F Noh and Paul Woodward. "SLIC (simple line interface calculation)". In *Proceedings of the fifth international conference on numerical methods in fluid dynamics June 28–July 2, 1976 Twente University, Enschede*, pages 330–340. Springer, 1976. 145

[137] Ryan Nora. "Modeling the 3D structure of ignition experiments at the NIF". *Bulletin of the American Physical Society*, 64, 2019. 148

[138] R. K. Osborn. "Some Characteristics of the Thermal Neutron Scattering Probability". *Nuclear Science and Engineering*, 3(1):29–37, 1958. doi: 10.13182/NSE58-A25443. 67

[139] H.-S. Park, O. A. Hurricane, D. A. Callahan, D. T. Casey, E. L. Dewald, T. R. Dittrich, T. Döppner, D. E. Hinkel, L. F. Berzak Hopkins, S. Le Pape, T. Ma, P. K. Patel, B. A. Remington, H. F. Robey, J. D. Salmonson, and J. L. Kline. "High-Adiabat High-Foot Inertial Confinement Fusion Implosion Experiments on the National Ignition Facility". *Phys. Rev. Lett.*, 112:055001, Feb 2014. doi: 10.1103/PhysRevLett.112.055001. 31

[140] LJ Perkins, DD-M Ho, BG Logan, GB Zimmerman, MA Rhodes, DJ Strozzi, DT Blackfield, and SA Hawkins. "The potential of imposed magnetic fields for enhancing ignition probability and fusion energy yield in indirect-drive inertial confinement fusion". *Physics of Plasmas*, 24(6):062708, 2017. 45

[141] L. A. Pickworth, B. A. Hammel, V. A. Smalyuk, H. F. Robey, L. R. Benedetti, L. Berzak Hopkins, D. K. Bradley, J. E. Field, S. W. Haan, R. Hatarik, E. Hartouni, N. Izumi, S. Johnson, S. Khan, B. Lahmann, O. L. Landen, S. Le Pape, A. G. MacPhee, N. B. Meezan, J. Milovich, S. R. Nagel, A. Nikroo, A. E. Pak, R. Petrasso, B. A. Remington, N. G. Rice, P. T. Springer, M. Stadermann,

K. Widmann, and W. Hsing. "Visualizing deceleration-phase instabilities in inertial confinement fusion implosions using an "enhanced self-emission" technique at the National Ignition Facility". *Physics of Plasmas*, 25(5):054502, 2018. doi: 10.1063/1.5025188. 32

[142] L. A. Pickworth, B. A. Hammel, V. A. Smalyuk, H. F. Robey, R. Tommasini, L. R. Benedetti, L. Berzak Hopkins, D. K. Bradley, M. Dayton, S. Felker, J. E. Field, S. W. Haan, B. Haid, R. Hatarik, E. Hartouni, D. Holunga, M. Hoppe, N. Izumi, S. Johnson, S. Khan, T. Kohut, B. Lahmann, O. L. Landen, S. LePape, A. G. MacPhee, E. Marley, N. B. Meezan, J. Milovich, S. R. Nagel, A. Nikroo, A. E. Pak, R. Petrasso, B. A. Remington, N. G. Rice, H. A. Scott, P. T. Springer, M. Stadermann, C. Walters, K. Widmann, and W. W. Hsing. "Development of new platforms for hydrodynamic instability and asymmetry measurements in deceleration phase of indirectly driven implosions on NIF". *Physics of Plasmas*, 25(8):082705, 2018. doi: 10.1063/1.5039744. 32

[143] A. Poquérusse. "Approximation rationnelle simplifiée des fonctions de Holtsmark et connexes". *The European Physical Journal D - Atomic, Molecular, Optical and Plasma Physics*, 10(2):307–308, Apr 2000. ISSN 1434-6079. doi: 10.1007/s100530050553. 57

[144] William H Press, Saul A Teukolsky, Brian P Flannery, and William T Vetterling. "Numerical recipes in Fortran 77: volume 1, volume 1 of Fortran numerical recipes: the art of scientific computing". Cambridge University Press, 1992. 85

[145] S. P. Regan, V. N. Goncharov, I. V. Igumenshchev, T. C. Sangster, R. Betti, A. Bose, T. R. Boehly, M. J. Bonino, E. M. Campbell, D. Cao, T. J. B. Collins, R. S. Craxton, A. K. Davis, J. A. Delettrez, D. H. Edgell, R. Epstein, C. J. Forrest, J. A. Frenje, D. H. Froula, M. Gatu Johnson, V. Yu. Glebov, D. R. Harding, M. Hohenberger, S. X. Hu, D. Jacobs-Perkins, R. Janezic, M. Karasik, R. L. Keck, J. H. Kelly, T. J. Kessler, J. P. Knauer, T. Z. Kosc, S. J. Loucks, J. A. Marozas, F. J. Marshall, R. L. McCrory, P. W. McKenty, D. D. Meyerhofer, D. T. Michel, J. F. Myatt, S. P. Obenschain, R. D. Petrasso, P. B. Radha, B. Rice, M. J. Rosenberg, A. J. Schmitt, M. J. Schmitt, W. Seka, W. T. Shmayda, M. J. Shoup, A. Shvydky, S. Skupsky, A. A. Solodov, C. Stoeckl, W. Theobald, J. Ulreich, M. D. Wittman, K. M. Woo, B. Yaakobi, and J. D. Zuegel. "Demonstration of Fuel Hot-Spot Pressure in Excess of 50 Gbar for Direct-Drive, Layered Deuterium-Tritium Implosions on OMEGA". *Phys. Rev. Lett.*, 117:025001, Jul 2016. doi: 10.1103/PhysRevLett.117.025001. 11, 211

[146] Sean Regan, Owen Mannion, Chad Forrest, James Knauer, Riccardo Betti, Michael Campbell, Duc Cao, Vladimir Glebov, Valeri Goncharov, Steven Ivancic, et al. "Hot-Spot Flow Velocity in Laser-Direct-Drive Inertial Confinement Fusion Implosions". *Bulletin of the American Physical Society*, 2019. 34

[147] H. G. Rinderknecht, M. J. Rosenberg, A. B. Zylstra, B. Lahmann, F. H. Séguin, J. A. Frenje, C. K. Li, M. Gatu Johnson, R. D. Petrasso, L. F. Berzak Hopkins, J. A. Caggiano, L. Divol, E. P. Hartouni, R. Hatarik, S. P. Hatchett, S. Le Pape, A. J. Mackinnon, J. M. McNaney, N. B. Meezan, M. J. Moran, P. A. Bradley, J. L. Kline, N. S. Krasheninnikova, G. A. Kyrala, T. J. Murphy, M. J. Schmitt, I. L. Tregillis, S. H. Batha, J. P. Knauer, and J. D. Kilkenny. "Using multiple secondary fusion products to evaluate fuel ρR, electron temperature, and mix in deuterium-filled implosions at the NIF". *Physics of Plasmas*, 22(8):082709, 2015. doi: 10.1063/1.4928382. 123

[148] Hans G. Rinderknecht, R. Bionta, G. Grim, R. Hatarik, H. Khater, D. Schlossberg, and C. Yeamans. "Velocity correction for neutron activation diagnostics at the NIF". *Review of Scientific Instruments*, 89(10):10I125, 2018. doi: 10.1063/1.5038734. 40, 132, 134, 139

[149] James William Rohlf. "Modern Physics from α to Z°". New York (N.Y.) : Wiley, 1st ed. edition, 1994. ISBN 0471572705. 20

[150] S J Rose. "Calculations of the radiative opacity of laser-produced plasmas". *Journal of Physics B: Atomic, Molecular and Optical Physics*, 25(7):1667–1681, apr 1992. doi: 10.1088/0953-4075/25/7/034. 56

[151] Carl A Rouse. "Ionization Equilibrium Equation of State.". *The Astrophysical Journal*, 134:435, 1961. 56

[152] J. J. Ruby, A. Pak, J. E. Field, T. Ma, B. K. Spears, L. R. Benedetti, D. K. Bradley, L. F. Berzak Hopkins, D. T. Casey, T. Döppner, D. Eder, D. Fittinghoff, G. Grim, R. Hatarik, D. E. Hinkel, N. Izumi, J. D. Kilkenny, S. F. Khan, J. P. Knauer, A. L. Kritcher, F. E. Merrill, J. D. Moody, S. R. Nagel, H.-S. Park, J. D. Salmonson, D. B. Sayre, D. A. Callahan, W. W. Hsing, O. A. Hurricane, P. K. Patel, and M. J. Edwards. "Spatially resolved X-ray emission measurements of the residual velocity during the stagnation phase of inertial confinement fusion implosion experiments". *Physics of Plasmas*, 23(7):072701, 2016. doi: 10.1063/1.4956468. 32, 142

[153] George B Rybicki and Alan P Lightman. "Radiative processes in astrophysics". John Wiley & Sons, 2008. 54, 55

[154] T. C. Sangster, V. N. Goncharov, P. B. Radha, V. A. Smalyuk, R. Betti, R. S. Craxton, J. A. Delettrez, D. H. Edgell, V. Yu. Glebov, D. R. Harding, D. Jacobs-Perkins, J. P. Knauer, F. J. Marshall, R. L. McCrory, P. W. McKenty, D. D. Meyerhofer, S. P. Regan, W. Seka, R. W. Short, S. Skupsky, J. M. Soures, C. Stoeckl, B. Yaakobi, D. Shvarts, J. A. Frenje, C. K. Li, R. D. Petrasso, and F. H. Séguin. "High-Areal-Density Fuel Assembly in Direct-Drive Cryogenic Implosions". *Phys. Rev. Lett.*, 100:185006, May 2008. doi: 10.1103/PhysRevLett.100.185006. 98

[155] T. C. Sangster, V. N. Goncharov, R. Betti, T. R. Boehly, D. T. Casey, T. J. B. Collins, R. S. Craxton, J. A. Delettrez, D. H. Edgell, R. Epstein, K. A. Fletcher, J. A. Frenje, Y. Yu. Glebov, D. R. Harding, S. X. Hu, I. V. Igumenschev, J. P. Knauer, S. J. Loucks, C. K. Li, J. A. Marozas, F. J. Marshall, R. L. McCrory, P. W. McKenty, D. D. Meyerhofer, P. M. Nilson, S. P. Padalino, R. D. Petrasso, P. B. Radha, S. P. Regan, F. H. Seguin, W. Seka, R. W. Short, D. Shvarts, S. Skupsky, V. A. Smalyuk, J. M. Soures, C. Stoeckl, W. Theobald, and B. Yaakobi. "Shock-tuned cryogenic-deuterium-tritium implosion performance on Omega". *Physics of Plasmas*, 17(5):056312, 2010. doi: 10.1063/1.3360928. 98

[156] P. F. Schmit, P. F. Knapp, S. B. Hansen, M. R. Gomez, K. D. Hahn, D. B. Sinars, K. J. Peterson, S. A. Slutz, A. B. Sefkow, T. J. Awe, E. Harding, C. A. Jennings, G. A. Chandler, G. W. Cooper, M. E. Cuneo, M. Geissel, A. J. Harvey-Thompson, M. C. Herrmann, M. H. Hess, O. Johns, D. C. Lamppa, M. R. Martin, R. D. McBride, J. L. Porter, G. K. Robertson, G. A. Rochau, D. C. Rovang, C. L. Ruiz, M. E. Savage, I. C. Smith, W. A. Stygar, and R. A. Vesey. "Understanding Fuel Magnetization and Mix Using Secondary Nuclear Reactions in Magneto-Inertial Fusion". *Phys. Rev. Lett.*, 113:155004, Oct 2014. doi: 10.1103/PhysRevLett.113.155004. 123

[157] R. H. H. Scott, D. S. Clark, D. K. Bradley, D. A. Callahan, M. J. Edwards, S. W. Haan, O. S. Jones, B. K. Spears, M. M. Marinak, R. P. J. Town, P. A. Norreys, and L. J. Suter. "Numerical Modeling of the Sensitivity of X-Ray Driven Implosions to Low-Mode Flux Asymmetries". *Phys. Rev. Lett.*, 110:075001, Feb 2013. doi: 10.1103/PhysRevLett.110.075001. 122

[158] H. R. Setze, C. R. Howell, W. Tornow, R. T. Braun, D. E. González Trotter, A. H. Hussein, R. S. Pedroni, C. D. Roper, F. Salinas, I. Šlaus, B. Vlahović, R. L. Walter, G. Mertens, J. M. Lambert, H. Witała, and W. Glöckle. "Cross-section measurements of neutron-deuteron breakup at 13.0 MeV". *Phys. Rev. C*, 71:034006, Mar 2005. doi: 10.1103/PhysRevC.71.034006. 160

[159] Mark Sherlock. "A Monte-Carlo method for coulomb collisions in hybrid plasma models". *Journal of Computational Physics*, 227(4):2286–2292, 2008. 90

[160] V A Smalyuk, C R Weber, O L Landen, S Ali, B Bachmann, P M Celliers, E L Dewald, A Fernandez, B A Hammel, G Hall, A G MacPhee, L Pickworth, H F Robey, N Alfonso, K L Baker, L F Berzak Hopkins, L Carlson, D T Casey, D S Clark, J Crippen, L Divol, T Döppner, M J Edwards, M Farrell, S Felker, J E Field, S W Haan, A V Hamza, M Havre, M C Herrmann, W W Hsing, S Khan, J Kline, J J Kroll, S LePape, E Loomis, B J MacGowan, D Martinez, L Masse, M Mauldin, J L Milovich, A S Moore, A Nikroo, A Pak, P K Patel, J L Peterson, K Raman, B A Remington, N Rice, M Schoff, and M Stadermann. "Review of hydrodynamic instability experiments in inertially confined fusion implosions on

National Ignition Facility". *Plasma Physics and Controlled Fusion*, 62(1):014007, oct 2019. doi: 10.1088/1361-6587/ab49f4. 142

[161] V.A. Smalyuk, H.F. Robey, D.T. Casey, D.S. Clark, T. Döppner, S.W. Haan, B.A. Hammel, A.G. MacPhee, D. Martinez, J.L. Milovich, J.L. Peterson, L. Pickworth, J.E. Pino, K. Raman, R. Tipton, C.R. Weber, K.L. Baker, B. Bachmann, L.F. Berzak Hopkins, E. Bond, J.A. Caggiano, D.A. Callahan, P.M. Celliers, C. Cerjan, S.N. Dixit, M.J. Edwards, S. Felker, J.E. Field, D.N. Fittinghoff, N. Gharibyan, G.P. Grim, A.V. Hamza, R. Hatarik, M. Hohenberger, W.W. Hsing, O.A. Hurricane, K.S. Jancaitis, O.S. Jones, S. Khan, J.J. Kroll, K.N. Lafortune, O.L. Landen, T. Ma, B.J. MacGowan, L. Masse, A.S. Moore, S.R. Nagel, A. Nikroo, A. Pak, P.K. Patel, B.A. Remington, D.B. Sayre, B.K. Spears, M. Stadermann, R. Tommasini, C.C. Widmayer, C.B. Yeamans, J. Crippen, M. Farrell, E. Giraldez, N. Rice, C.H. Wilde, P.L. Volegov, and M. Gatu Johnson. "Mix and hydrodynamic instabilities on NIF". *Journal of Instrumentation*, 12(06):C06001–C06001, jun 2017. doi: 10.1088/1748-0221/12/06/c06001. 32, 142

[162] Brian K Spears, MJ Edwards, S Hatchett, J Kilkenny, J Knauer, A Kritcher, J Lindl, D Munro, P Patel, HF Robey, et al. "Mode 1 drive asymmetry in inertial confinement fusion implosions on the National Ignition Facility". *Physics of Plasmas*, 21(4):042702, 2014. 32

[163] Lyman Spitzer and Richard Härm. "Transport Phenomena in a Completely Ionized Gas". *Phys. Rev.*, 89:977–981, Mar 1953. doi: 10.1103/PhysRev.89.977. 44

[164] John C Stewart and Kedar D Pyatt Jr. "Lowering of ionization potentials in plasmas". *The Astrophysical Journal*, 144:1203, 1966. 56

[165] James M Stone, Dimitri Mihalas, and Michael L Norman. "ZEUS-2D: A radiation magnetohydrodynamics code for astrophysical flows in two space dimensions. III-The radiation hydrodynamic algorithms and tests". *The Astrophysical Journal Supplement Series*, 80:819–845, 1992. 47

[166] Mary M Tai. "A mathematical model for the determination of total area under glucose tolerance and other metabolic curves". *Diabetes care*, 17(2):152–154, 1994. 174

[167] A. Takahashi and D. Rusch. "Fast rigorous numerical method for the solution of the anisotropic neutron transport problem and the NITRAN system for fusion neutronics application. Pt. 1". Technical report, 1979. 66, 78, 79

[168] A. Takahashi and D. Rusch. "Fast rigorous numerical method for the solution of the anisotropic neutron transport problem and the NITRAN system for fusion neutronics application. Pt. 2". Technical report, 1979. 66, 79

[169] Akito Takahashi, Junji Yamamoto, Mituo Ebisuya, and Kenji Sumita. "Method for calculating anisotropic neutron transport using scattering kernel without polynomial expansion". *Journal of Nuclear Science and Technology*, 16(1):1–15, 1979. 64, 75, 78, 79, 94, 168, 183

[170] Yasuo Tanaka and Yôrô Ôno. "Shock Waves in Degenerate Plasma Gases". *Progress of Theoretical Physics*, 27(6):1280–1282, 1962. 105

[171] S Taylor. "A Computational Study of the Stagnation Phase in Inertial Confinement Fusion: Hotspot Energetics, Diagnostics, and Burn Propagation". PhD thesis, Imperial College London, 2013. 25, 44, 125, 128, 137

[172] S. Taylor and J. P. Chittenden. "Effects of perturbations and radial profiles on ignition of inertial confinement fusion hotspots". *Physics of Plasmas*, 21(6): 062701, 2014. doi: 10.1063/1.4879020. 83, 84, 184

[173] S. Taylor, B. Appelbe, N. P. L. Niasse, and J. P. Chittenden. "Effect of perturbations on yield in ICF targets – 4π 3D hydro simulations". *EPJ Web of Conferences*, 59:04009, 2013. doi: 10.1051/epjconf/20135904009. 83

[174] J.K. Tong, K. McGlinchey, B.D. Appelbe, C.A. Walsh, A.J. Crilly, and J.P. Chittenden. "Burn regimes in the hydrodynamic scaling of perturbed inertial confinement fusion hotspots". *Nuclear Fusion*, 59(8):086015, jun 2019. doi: 10.1088/1741-4326/ab22d4. 5, 24, 33, 44, 97, 113, 149, 150

[175] A Trkov, M Herman, DA Brown, et al. "ENDF-6 formats manual". *Brookhaven National Laboratory*, 2012. 80

[176] P. L. Volegov, C. R. Danly, D. N. Fittinghoff, N. Guler, F. E. Merrill, and C. H. Wilde. "Self characterization of a coded aperture array for neutron source imaging". *Review of Scientific Instruments*, 85(12):123506, 2014. doi: 10.1063/1.4902978. 142, 156

[177] P. L. Volegov, C. R. Danly, F. E. Merrill, R. Simpson, and C. H. Wilde. "On three-dimensional reconstruction of a neutron/x-ray source from very few two-dimensional projections". *Journal of Applied Physics*, 118(20), 2015. ISSN 10897550. doi: 10.1063/1.4936319. 5, 37, 130, 155

[178] P. L. Volegov, C. R. Danly, D. Fittinghoff, V. Geppert-Kleinrath, G. Grim, F. E. Merrill, and C. H. Wilde. "Three-dimensional reconstruction of neutron, gamma-ray, and x-ray sources using spherical harmonic decomposition". *Journal of Applied Physics*, 122(17):175901, 2017. doi: 10.1063/1.4986652. 37

[179] P. L. Volegov, S. H. Batha, V. Geppert-Kleinrath, C. R. Danly, F. E. Merrill, C. H. Wilde, D. C. Wilson, D. T. Casey, D. Fittinghoff, B. Appelbe, J. P. Chittenden, A. J. Crilly, and K. McGlinchey. "Density determination of the thermonuclear

fuel region in inertial confinement fusion implosions". *Journal of Applied Physics*, 127(8):083301, 2020. doi: 10.1063/1.5123751. 5, 130, 139, 142, 145, 155, 156, 211

[180] P. L. Volegov, S. H. Batha, et al. "Density determination of the thermonuclear fuel region in inertial confinement fusion implosions". *Journal of Applied Physics*, In Review. 37

[181] C. A. Walsh, J. P. Chittenden, K. McGlinchey, N. P.L. Niasse, and B. D. Appelbe. "Self-Generated Magnetic Fields in the Stagnation Phase of Indirect-Drive Implosions on the National Ignition Facility". *Physical Review Letters*, 118(15): 1–5, 2017. ISSN 10797114. doi: 10.1103/PhysRevLett.118.155001. 5, 16, 45, 128, 129

[182] C. A. Walsh, J. P. Chittenden, D. W. Hill, and C. Ridgers. "Extended-magnetohydrodynamics in under-dense plasmas". *Physics of Plasmas*, 27(2): 022103, 2020. doi: 10.1063/1.5124144.

[183] CA Walsh, K McGlinchey, JK Tong, BD Appelbe, A Crilly, MF Zhang, and JP Chittenden. "Perturbation modifications by pre-magnetisation of inertial confinement fusion implosions". *Physics of Plasmas*, 26(2):022701, 2019. 45

[184] Christopher Walsh. "Extended magneto-hydrodynamic effects in indirect-drive inertial confinement fusion experiments". PhD thesis, Imperial College London, 2018. 5, 45

[185] CR Weber, DS Clark, A Pak, N Alfonso, B Bachmann, LF Berzak Hopkins, T Bunn, J Crippen, L Divol, T Dittrich, et al. "Mixing in ICF implosions on the National Ignition Facility caused by the fill-tube". *Physics of Plasmas*, 27(3): 032703, 2020. 145

[186] F. Weilacher, P. B. Radha, and C. Forrest. "Three-dimensional modeling of the neutron spectrum to infer plasma conditions in cryogenic inertial confinement fusion implosions". *Physics of Plasmas*, 25(4):042704, 2018. doi: 10.1063/1.5016856. 75

[187] Mark D. Wilke, Steven H. Batha, Paul A. Bradley, Robert D. Day, David D. Clark, Valerie E. Fatherley, Joshua P. Finch, Robert A. Gallegos, Felix P. Garcia, Gary P. Grim, Steven A. Jaramillo, Andrew J. Montoya, Michael J. Moran, George L. Morgan, John A. Oertel, Thomas A. Ortiz, Jeremy R. Payton, Peter Pazuchanics, Derek W. Schmidt, Adelaida C. Valdez, Carl H. Wilde, and Doug C. Wilson. "The National Ignition Facility Neutron Imaging System". *Review of Scientific Instruments*, 79(10):10E529, 2008. doi: 10.1063/1.2987984. 36

[188] K. M. Woo, R. Betti, D. Shvarts, O. M. Mannion, D. Patel, V. N. Goncharov, K. S. Anderson, P. B. Radha, J. P. Knauer, A. Bose, V. Gopalaswamy, A. R.

Christopherson, E. M. Campbell, J. Sanz, and H. Aluie. "Impact of three-dimensional hot-spot flow asymmetry on ion-temperature measurements in inertial confinement fusion experiments". *Physics of Plasmas*, 25(10):102710, 2018. doi: 10.1063/1.5048429. 31, 64

[189] X-5 Monte Carlo Team. "MCNP – A General Monte Carlo N-Particle Transport Code, Version 5". Technical Report LA-UR-03-1987, Los Alamos National Laboratory, 2003. 75

[190] C. B. Yeamans and D. L. Bleuel. "The Spatially Distributed Neutron Activation Diagnostic FNADs at the National Ignition Facility". *Fusion Science and Technology*, 72(2):120–128, 2017. doi: 10.1080/15361055.2017.1320499. 38, 118, 130, 133

[191] C. B. Yeamans, D. L. Bleuel, and L. A. Bernstein. "Enhanced NIF neutron activation diagnostics". *Review of Scientific Instruments*, 83(10):10D315, 2012. doi: 10.1063/1.4739230. 38, 118, 130, 133

[192] Ya B Zel'Dovich and Yu P Raizer. "Physics of shock waves and high-temperature hydrodynamic phenomena". Courier Corporation, 2002. 46, 54, 56, 105

[193] A. B. Zylstra, J. A. Frenje, M. Gatu Johnson, G. M. Hale, C. R. Brune, A. Bacher, D. T. Casey, C. K. Li, D. McNabb, M. Paris, R. D. Petrasso, T. C. Sangster, D. B. Sayre, and F. H. Séguin. "Proton Spectra from ^{3}He + T and ^{3}He +^{3} He Fusion at Low Center-of-Mass Energy, with Potential Implications for Solar Fusion Cross Sections". *Phys. Rev. Lett.*, 119:222701, Nov 2017. doi: 10.1103/PhysRevLett.119.222701. 160

[194] AB Zylstra, Hans W Herrmann, M Gatu Johnson, Yong Ho Kim, JA Frenje, G Hale, CK Li, M Rubery, M Paris, A Bacher, et al. "Using Inertial Fusion Implosions to Measure the T+ He 3 Fusion Cross Section at Nucleosynthesis-Relevant Energies". *Physical review letters*, 117(3):035002, 2016. 160

Permissions

Figure #	Reference #	Copyright Holder	Permissions #
1.7	[38]	Creative Commons (CC-BY) License	-
1.7	[39]	IoP Publishing	1
1.8	[145]	APS Publishing	2

Table of figure, reference and permission numbers as well as the copyright holder for copyrighted material reproduced in this thesis. Permissions are printed in the following pages in the order laid out by the permissions number in the above table.

Material is reproduced from a number of AIP publications for which the author of this thesis was also an author on the publication (in bold):

- "Synthetic nuclear diagnostics for inferring plasma properties of inertial confinement fusion implosions", Physics of Plasmas 25, 122703 (2018), **A. J. Crilly**, B. D. Appelbe, K. McGlinchey, C. A. Walsh, J. K. Tong, A. B. Boxall and J. P. Chittenden [42]

- "Neutron backscatter edge: A measure of the hydrodynamic properties of the dense DT fuel at stagnation in ICF experiments", Physics of Plasmas 27, 012701 (2020), **A. J. Crilly**, B. D. Appelbe, O. M. Mannion, C. J. Forrest, V. Gopalaswamy, C. A. Walsh and J. P. Chittenden [43]

- "Density determination of the thermonuclear fuel region in inertial confinement fusion implosions", Journal of Applied Physics 127, 083301 (2020), P. L. Volegov, S. H. Batha, V. Geppert-Kleinrath, C. R. Danly, F. E. Merrill, C. H. Wilde, D. C. Wilson, D. T. Casey, D. Fittinghoff, B. Appelbe, J. P. Chittenden, **A. J. Crilly**, and K. McGlinchey [179]

The author has followed the AIP rights and permissions advice: "Authors do not need permission from AIP Publishing to reuse your own AIP Publishing article in your thesis or dissertation (please format your credit line: "Reproduced from [FULL CITATION], with the permission of AIP Publishing")"

Figure permissions

EDVARDSEN, Miriam <M.Edvardsen@iaea.org>

Wed 18/03/2020 08:51

To: Crilly, Aidan <a.crilly16@imperial.ac.uk>

Dear Aiden,

Following your request for permission to reuse material:

Figure 4, from “Modeling and projecting implosion performance for the National Ignition Facility”, Nucl. Fusion 59, No. 3, 032008 (2019), by D.S. Clark et al.

The IAEA is pleased to grant permission for the figure listed above to be reproduced to the extent and for the purposes detailed in your email. Please could you also notify the corresponding author.

Best regards,
Miriam

Ms Miriam EDVARDSEN | Publications Assistant (Marketing and Sales) |
Publishing section | Division of Conference and Document Services | Department of Management |
International Atomic Energy Agency | Vienna International Centre, PO Box 100, 1400 Vienna, Austria |
Email: **M.Edvardsen@iaea.org** | T: (+43-1) 2600-22530 | F : (+43-1) 2600-22529 |

Follow us on www.iaea.org

ATOMS FOR PEACE AND DEVELOPMENT

American Physical Society
Reuse and Permissions License

16-Mar-2020

This license agreement between the American Physical Society ("APS") and Aidan Crilly ("You") consists of your license details and the terms and conditions provided by the American Physical Society and SciPris.

Licensed Content Information

License Number:	**RNP/20/MAR/023789**
License date:	16-Mar-2020
DOI:	10.1103/PhysRevLett.117.025001
Title:	Demonstration of Fuel Hot-Spot Pressure in Excess of 50 Gbar for Direct-Drive, Layered Deuterium-Tritium Implosions on OMEGA
Author:	S. P. Regan et al.
Publication:	Physical Review Letters
Publisher:	American Physical Society
Cost:	USD $ 0.00

Request Details

Does your reuse require significant modifications: No

Specify intended distribution locations:	Worldwide
Reuse Category:	Reuse in a thesis/dissertation
Requestor Type:	Student
Items for Reuse:	Figures/Tables
Number of Figure/Tables:	1
Figure/Tables Details:	Figure 1b
Format for Reuse:	Print and Electronic
Total number of print copies:	Up to 1000

Information about New Publication:

University/Publisher:	Imperial College London
Title of dissertation/thesis:	Simulation of Nuclear Observables in Inertial Confinement Fusion Experiments
Author(s):	Aidan Crilly
Expected completion date:	Mar. 2020

License Requestor Information

Name:	Aidan Crilly
Affiliation:	Individual
Email Id:	ac116@ic.ac.uk
Country:	United Kingdom

American Physical Society
Reuse and Permissions License

TERMS AND CONDITIONS

The American Physical Society (APS) is pleased to grant the Requestor of this license a non-exclusive, non-transferable permission, limited to Print and Electronic format, provided all criteria outlined below are followed.

1. You must also obtain permission from at least one of the lead authors for each separate work, if you haven't done so already. The author's name and affiliation can be found on the first page of the published Article.
2. For electronic format permissions, Requestor agrees to provide a hyperlink from the reprinted APS material using the source material's DOI on the web page where the work appears. The hyperlink should use the standard DOI resolution URL, http://dx.doi.org/{DOI}. The hyperlink may be embedded in the copyright credit line.
3. For print format permissions, Requestor agrees to print the required copyright credit line on the first page where the material appears: "Reprinted (abstract/excerpt/figure) with permission from [(FULL REFERENCE CITATION) as follows: Author's Names, APS Journal Title, Volume Number, Page Number and Year of Publication.] Copyright (YEAR) by the American Physical Society."
4. Permission granted in this license is for a one-time use and does not include permission for any future editions, updates, databases, formats or other matters. Permission must be sought for any additional use.
5. Use of the material does not and must not imply any endorsement by APS.
6. APS does not imply, purport or intend to grant permission to reuse materials to which it does not hold copyright. It is the requestor's sole responsibility to ensure the licensed material is original to APS and does not contain the copyright of another entity, and that the copyright notice of the figure, photograph, cover or table does not indicate it was reprinted by APS with permission from another source.
7. The permission granted herein is personal to the Requestor for the use specified and is not transferable or assignable without express written permission of APS. This license may not be amended except in writing by APS.
8. You may not alter, edit or modify the material in any manner.
9. You may translate the materials only when translation rights have been granted.
10. APS is not responsible for any errors or omissions due to translation.
11. You may not use the material for promotional, sales, advertising or marketing purposes.
12. The foregoing license shall not take effect unless and until APS or its agent, Aptara, receives payment in full in accordance with Aptara Billing and Payment Terms and Conditions, which are incorporated herein by reference.
13. Should the terms of this license be violated at any time, APS or Aptara may revoke the license with no refund to you and seek relief to the fullest extent of the laws of the USA. Official written notice will be made using the contact information provided with the permission request. Failure to receive such notice will not nullify revocation of the permission.
14. APS reserves all rights not specifically granted herein.
15. This document, including the Aptara Billing and Payment Terms and Conditions, shall be the entire agreement between the parties relating to the subject matter hereof.